



HAL
open science

Ternary blend ink formulations for fabricating organic solar cells via inkjet printing

Thomas Kraft

► **To cite this version:**

Thomas Kraft. Ternary blend ink formulations for fabricating organic solar cells via inkjet printing. Micro and nanotechnologies/Microelectronics. Université de Limoges; Queen's university (Kingston, Canada), 2015. English. NNT : 2015LIMO0027 . tel-02637919

HAL Id: tel-02637919

<https://theses.hal.science/tel-02637919v1>

Submitted on 28 May 2020

HAL is a multi-disciplinary open access archive for the deposit and dissemination of scientific research documents, whether they are published or not. The documents may come from teaching and research institutions in France or abroad, or from public or private research centers.

L'archive ouverte pluridisciplinaire **HAL**, est destinée au dépôt et à la diffusion de documents scientifiques de niveau recherche, publiés ou non, émanant des établissements d'enseignement et de recherche français ou étrangers, des laboratoires publics ou privés.

**TERNARY BLEND INK FORMULATIONS FOR FABRICATING
ORGANIC SOLAR CELLS VIA INKJET PRINTING**

by

Thomas M. Kraft

A thesis submitted to the Department of Chemistry

In conformity with the requirements for
the degree of Doctor of Philosophy

Queen's University

Kingston, Ontario, Canada

(May, 2015)

Copyright ©Thomas M. Kraft, 2015

UNIVERSITÉ DE LIMOGES

Ecole Doctorale n° 521 : Sciences et Ingénierie pour l'Information, Mathématiques
(S2I)

Faculté de Sciences et Techniques de Limoges

XLIM - Département MINACOM

Thèse N° xx/2015

Thèse

pour obtenir le grade de

DOCTEUR DE L'UNIVERSITÉ DE LIMOGES

Discipline : Electronique des Hautes Fréquences, Photonique et Systèmes

Présentée et soutenue le 27 mai 2015 à Kingston par

Thomas KRAFT

**Ternary Blend Ink Formulations for Fabricating Organic
Solar Cells via Inkjet Printing**

Thèse dirigée par Prof. Jean-Michel NUNZI et Prof. Bernard RATIER

JURY :

Rapporteurs

Olivier Lebel, *Assistant Professor, Royal Military College of Canada*

Guillaume Wantz, *Maître de Conférences HDR, Université de Bordeaux*

Examineurs

Anne Petitjean, *Associate Professor, Queen's University*

Thierry Trigaud, *Maître de Conférences, Université de Limoges*

Jean-Michel Nunzi, *Professor, Queen's University*

Bernard Ratier, *Professeur, Université de Limoges*

Président du jury

Naraig Manjikian, *Associate Professor, Queen's University*

Abstract

Two approaches were followed to achieve increased control over properties of the photo-active layer (PAL) in solution processed polymer solar cells (PSCs). This was accomplished by either (1) the addition of functionalized single-walled carbon nanotubes (SWCNTs) to improve the charge transport properties of the device or (2) the realization of dual donor polymer ternary blends to achieve colour-tuned devices.

In the first component of the study, P3HT:PC₆₁BM blends were doped with SWCNTs with the ambition to improve the morphology and charge transport within the PAL. The SWCNTs were functionalized with alkyl chains to increase their dispersive properties in solution, increase their interaction with the P3HT polymer matrix, and to disrupt the metallic characteristic of the tubes, which ensures that the incorporated SWCNTs are primarily semi-conducting. P3HT:PCBM:CNT composite films were characterized and prepared for use as the photoactive layer within the inverted solar cell. The CNT doping acts to increase order within the active layer and improve the active layer's charge transport properties (conductivity) as well as showed some promise to increase the stability of the device. The goal is that improved charge transport will allow high level polymer solar cell (PSC) performance as the active layer thickness and area are increased, which is an important consideration for large-area inkjet printing.

The use of ternary blends (two donor polymers with a fullerene acceptor) in bulk-heterojunction (BHJ) photovoltaic devices on plastic substrates was investigated as a future means to colour-tune ink-jet printed PSCs. The study involved the blending of two of the three chosen donor polymers [red (P3HT), blue (B1), and green (G1)] with PC₆₁BM. Through external quantum efficiency (EQE) measurements, it was shown that even devices with blends exhibiting poor efficiencies, caused by traps, both polymers were able to contribute to the photovoltaic (PV) effect. However, traps were avoided to create a parallel-like BHJ (PBHJ) when two polymers were chosen with suitable physical compatibility

(harmonious solid state mixing), and appropriate HOMO-HOMO energy band alignment. The parallel diode model was used to describe the PV circuit of devices with the B1:G1:PC₆₁BM ternary blend.

Résumé

L'objectif final de la thèse est l'impression de la couche photo-active ternaire d'une cellule solaire organique en utilisant deux approches: l'une concerne l'apport de nanotubes de carbone (SWCNT) pour améliorer les propriétés de transport, l'autre concerne la préparation de mélanges ternaires de matériaux pour contrôler la couleur des cellules.

Les encres pour la couche active incluant des SWCNT fonctionnalisés sont composées d'un donneur d'électron (polymère) (poly(3-hexylthiophène), [P3HT]) et d'un accepteur d'électron ([6,6]-phényl-C₆₁-butanoate de méthyle [PC₆₁BM]) et ont été développées pour la fabrication de cellules inversées. Ces cellules sont réalisées sur substrats de verre pour l'optimisation de leurs performances, puis sur substrats plastiques pour les applications. Diverses couches d'interfaces ont été testées, qui incluent l'oxyde de zinc (ZnO, couches obtenues par pulvérisation ionique (IBS) ou à partir de solutions de nanoparticules) pour la couche de transport d'électrons et le PEDOT:PSS, le P3MEET, le V₂O₅ et le MoO₃ pour la couche de transport de trous. Des essais ont été effectués avec et sans CNT afin d'étudier leur impact sur les performances. Des résultats similaires sont obtenus dans les deux cas. Il était attendu que les CNT améliorent les performances, ce qui n'a pas été observé pour le moment. Des travaux supplémentaires sont donc nécessaires au niveau de la formulation de la couche active.

Avec trois polymères de couleur rouge (P3HT), bleue (B1) et verte (G1), nous avons préparé des mélanges ternaires efficaces permettant l'obtention de couleurs jusque là indisponibles. Nous avons fait une étude sur le piégeage et les mécanismes de diodes parallèles associés aux mélanges. En général, nous avons constaté que les mélanges ternaires de polymères bleu et vert peuvent être décrits par un mécanisme de diodes parallèles, sans entraîner de perte de performances, ce qui n'est pas possible pour les systèmes P3HT:B1:PCBM et P3HT:G1:PCBM qui se piègent mutuellement.

L'objectif final du projet est l'impression de la couche photo-active ternaire d'une cellule solaire organique, composites ternaires (polymère:polymères:acceptor) ou dopés avec les SWCNT. Cette étape nécessite encore des développements futurs.

Acknowledgements

Throughout my PhD studies, I have been conducting research on two continents; whether it be in Canada at Queen's University or France at the Université de Limoges.

This rewarding journey was made possible through the support of my supervisors; Profs. Jean-Michel Nunzi and Bernard Ratier. I would like to thank Prof. Ratier for his creative investigative approach and guidance throughout the project. His thorough scientific method and enthusiastic energy provided me inspiration to explore numerous avenues of the project. Also, I thank Prof. Nunzi for his continual never ending support which began with my MSc studies at Queen's. Prof. Nunzi's vision has driven my academic career and led me throughout graduate school. My successful PhD studies would not have been possible without their support.

I would also like to thank Drs. Thierry Trigaud, Bruno Lucas, and Johann Bouclé from the XLIM Research Institute, as well as Prof. Erwin Buncel from Queen's University. From the moment I first arrived in France in 2011, Dr. Trigaud has not only been there for me as a role model, but has helped me tremendously in all aspects of the cotutelle experience. Furthermore, my research would not have been possible without the positive research environment provided by all those I worked with at the University of Limoges' XLIM Research Institute and within the Department of Chemistry at Queen's University. I am thankful for my group members in the Organic Electronics Group (OPTOPLAST) at XLIM, as well as those in Prof. Nunzi's group at Queen's, who were always there to discuss and help resolve any research challenges and tasks that arose.

I am grateful for the financial support provided through the "Conventions Industrielles de Formation par la Recherche" (CIFRE) scholarship which was jointly funded by the Association Nationale de la Recherche et de la Technologie (ANRT, France) and the French solar company, DisaSolar. I am also thankful for funding that was awarded by the French Embassy in Canada's Office of Science and Technology (France), the Province of Ontario (Ontario Graduate Scholarship, Canada),

and the Natural Sciences and Engineering Research Council's Photovoltaic Innovation Network (NSERC PVIN, Canada).

Additionally, I acknowledge those I was fortunate to have collaborated with in Canada and throughout Europe. I thank Prof. Carlos Silva (*Department of Physics, University of Montreal*) for use of his equipment to perform time correlated single photon counting (TCSPC), as well as Prof. Jenny Nelson (*Department of Physics, Imperial College London*) for the ability to use her laboratory's Kelvin probe force microscope (KPFM). I would also like to thank Dr. Andrea Liskova (*Department of Chemical Engineering, Queen's University*) for the use of Thermogravimetric Analysis (TGA), Prof. Robert Knobel (*Department of Physics, Queen's University*) for use of the SonoPlot GIX microplotter, Cyril Guines (*XLIM, Université de Limoges*) for help in the clean room, the team at Ceradrop (Limoges, France) for help with inkjet printing, and all team members at DisaSolar. I would especially like to acknowledge work done at XLIM in collaboration with my officemates (Claudio Cristoferi, Richard Garuz, and Martin Schirr-Bonnans) who worked together with me on numerous projects in France.

Throughout my time as a graduate student I have been endlessly supported by my loving family. I would specifically like to thank my Mum and Dad (Deborah and Jouni), my Grandpa (M.O.), and my beloved fiancée (Riitta) for their eternal love and support.

Thank You!

Statement of Originality

I hereby certify that all of the work described within this thesis is the original work of the author. Any published (or unpublished) ideas and/or techniques from the work of others are fully acknowledged in accordance with the standard referencing practices.

Thomas M. Kraft

May, 2015

Table of Contents

Abstract	iii
Résumé	v
Acknowledgements	vii
Statement of Originality	ix
List of Figures	xiv
List of Tables	xxii
List of Abbreviations	xxiii
Chapter 1 Introduction.....	1
1.1 Solar Cells: An Introduction.....	1
1.1.1 Current solar cell technologies	4
1.1.2 Organic Photovoltaics	7
1.1.3 Solar Cell Characterization.....	11
1.2 Ternary Polymer Solar Cells	12
1.2.1 Charge Transport Mechanisms in Ternary Solar Cells.....	13
1.3 Carbon Nanotubes	24
1.3.1 Properties of single-walled carbon nanotubes	24
1.3.2 Properties of multi-walled carbon nanotubes	27
1.4 Modification of Carbon Nanotubes	27
1.4.1 Functionalization of Carbon Nanotubes	27
Covalent Functionalization.....	28
Non-Covalent Functionalization.....	29
1.4.2 Polymer/Carbon Nanotube Composites for Photovoltaic Cells	30
1.5 Printable Photovoltaics.....	34
1.5.1 Inkjet printable films in polymer solar cells	36
Electron Transport Layer (e.g. ZnO)	36
Active Layer (e.g. <i>P3HT:PCBM</i>)	37
Hole Transport Layer (e.g. PEDOT:PSS)	38
1.6 Research Objectives	39
1.6.1 CNT-doped PSCs	39
1.6.2 Colour-tuned ternary PSCs.....	39
Chapter 2 Experimental.....	41

2.1 Materials.....	41
2.2 Instruments	41
2.3 Carbon nanotube functionalization.....	42
2.3.1 Purification of single-walled carbon nanotubes (step 1)	43
2.3.2 Carboxylation of SWCNTs (step 2)	43
2.3.3 Acyl chloride functionalized SWCNTs (step 3).....	43
2.3.4 Esterification of SWCNTs (step 4).....	44
2.4 Solar Cell Fabrication Methods.....	44
2.4.1 Etching of indium tin oxide (ITO) layer.....	44
2.4.2 Preparation of polymer composites for BHJ active layer	46
2.4.2.1 Polymer and fullerene solutions	46
2.4.2.2 Polymer, PCBM, and CNT solutions	46
2.4.3 Solar Cell Fabrication.....	47
Inverted devices.....	47
Chapter 3 Results and Discussion	50
3.1 Carbon Nanotube doped polymer solar cells.....	50
3.1.1 Functionalization of SWCNTs	50
3.1.2 Carbon-nanotube doped polymer films	53
3.1.3 Carbon Nanotube-doped Polymer Solar Cells.....	55
Fabrication without SWCNTs	55
Fabrication with SWCNTs	55
3.1.4 Inkjet printing of CNT-doped active layers.....	56
3.2 Ternary blend active layers	59
Donor:donor:acceptor photovoltaics	60
3.2.1 Photovoltaic performance of ternary blends.....	61
J(V) characteristics	63
P3HT:B1:PCBM.....	63
P3HT:G1:PCBM	63
B1:G1:PCBM	64
External Quantum Efficiency (EQE).....	69
External quantum efficiency (EQE) versus incident photon energy	72
Photocurrent vs. Effective Voltage (J_{ph} vs. $(V_{bi}-V)$).....	74
3.2.2 Morphology of ternary blend active layers.....	78

3.2.3 Equivalent circuit of the parallel diode.....	80
3.2.4 Mismatch factor of active layers	83
Chapter 4 Conclusions and Future Work	85
4.1 Functionalized SWCNTs.....	85
4.2 Colour-tuned ternary blend PSCs.....	85
References	87
Appendices A-G.....	94
Appendix A Colour variation of photo-active layers	95
Binary Active Layer Blends	95
P3HT:acceptor.....	95
B1:acceptor.....	95
G1:acceptor.....	96
Ternary Active Layer Blends	96
Colourimetry	97
Appendix B UV-vis Absorption Spectroscopy	99
Binary blends (P3HT, B1, and G1 with PC ₆₁ BM, PC ₇₁ BM, or ICBA)	99
Binary polymer:polymer blends	100
Ternary blends (P3HT, B1, and G1 with PC ₆₁ BM).....	102
Appendix C Photoluminescence Spectroscopy of Polymer Films	104
Neat polymer films	104
Binary polymer:polymer blends	105
P3HT:B1.....	105
P3HT:G1	107
B1:G1	108
Time Correlated Single Photon Counting (TCSPC) of polymer films.....	111
Appendix D Comparison of EQE and active layer absorption.....	114
Binary blends.....	114
P3HT	114
B1	114
G1	116
Ternary blends.....	117
P3HT:B1:PC ₆₁ BM	117
P3HT:G1:PC ₆₁ BM.....	118

B1:G1:PC ₆₁ BM.....	120
B1:G1:PC ₇₁ BM.....	121
Appendix E J(V) characteristics of photo-active layer blends	123
J(V) characteristics of cells with 0.18 cm ² active area.....	123
J(V) characteristics of cells with 2 cm ² active area.....	123
J(V) curves.....	124
0.18 cm ² active areas	124
2 cm ² active areas.....	131
Intensity variation of ternary blends	135
Appendix F Thermogravimetric analysis (TGA) of esterified SWCNTs.....	142
Unidym SWCNTs (esterified tubes and reference)	142
BuckyUSA SWCNTs (esterified tubes and reference).....	142
Comparison of both varieties esterified with 1-decanol.....	143
Comparison of both varieties esterified with 1-dodecanol	143
Comparison of both varieties esterified with 1-tetradecanol.....	144
Visual solubility test of functionalized single-walled carbon nanotubes (f-SWCNTs).....	145
Appendix G Preliminary effects of CNT doping.....	149
Effects of CNT doping on P3HT fluorescence decay	149
Stability investigation of CNT-doped PSCs.....	151

List of Figures

Figure 1-1: Comparison of emerging (red) solar cell record efficiencies achieved in the laboratory (National Renewable Energy Laboratory (USA)).	1
Figure 1-2: Comparison of world record solar cell efficiencies determined by the NREL.	2
Figure 1-3: Summary of material conductivities[3]	3
Figure 1-4: The average solar spectrum at the surface of the earth with traditional inorganic semiconductor band gaps indicated [1].	5
Figure 1-5: Interpenetrating network of donor and acceptor active layer in BHJ cell (left) and general polymer solar cell composition (right).	8
Figure 1-6: Geometry of [6,6]-phenyl-C ₆₁ -butyric acid methyl ester (PC ₆₁ BM)	9
Figure 1-7: Photo-induced charge transfer within BHJ solar cell.	9
Figure 1-8: Structure of BHJ solar cell with Al back electrode	10
Figure 1-9: Reverse BHJ solar cell with high work function back electrode (Ag)	11
Figure 1-10: Current versus voltage curve for a standard P3HT:PCBM inverted photovoltaic cell on a glass substrate. Architecture: glass/ITO/ZnO/P3HT:PCBM/PEDOT:PSS/Ag	12
Figure 1-11: Charge transport mechanism for the transport of charges in a ternary BHJ device. Arrows denote electron (red) and hole (blue) migration.	14
Figure 1-12: Energy transport mechanism for the transport of charges in a ternary BHJ device. Arrows denote electron (red) and hole (blue) migration.	15
Figure 1-13: Parallel diode mechanism for the transport of charges in a ternary BHJ device. Arrows denote electron (red) and hole (blue) migration.	17
Figure 1-14: Description of carbon nanotube formation [39]	25
Figure 1-15: Armchair (A) and zigzag (B) single-walled carbon nanotube morphologies	26
Figure 2-1 Reaction scheme for the esterification of single walled carbon nanotubes.	42
Figure 2-2: Masking of ITO film on glass or plastic substrates.	45
Figure 2-3: ITO mask (yellow) for etching on 12mm x 12 mm substrates and its corresponding dimensions.	45
Figure 2-4: Polymer solar cell with silver back electrode.	47
Figure 2-5: AFM image of a ZnO nanoparticle film deposited via spin coating.	48
Figure 2-6: Physical vapour deposition of the Ag electrode (left) and removal of the device from the shadow mask (right), prior to removal of excess polymer.	49

Figure 3-1: Representation of the functionalized SWCNTs.....	50
Figure 3-2: Comparison of unfunctionalized Unidym (black dotted line) SWCNTs with tubes that have been functionalized with decanoic acid (green solid line).	51
Figure 3-3: Thermogravimetric analysis of Unidym SWCNT's functionalized with decanoic acid. The TGA results show a 30.1% weight loss due to functional group degradation.....	51
Figure 3-4: Comparison of c-AFM determined topography and current (relative to conductivity) of pristine and doped P3HT:PC ₆₁ BM films. Active layer films doped with 0.25 wt% and 0.5 wt% functionalized SWCNTs (Unidym, R = 14).	54
Figure 3-5: Evolution of the efficiency and J _{SC} of a non-doped and CNT-doped PSCs under constant illumination.	56
Figure 3-6: Interferometry of P3HT:PCBM films deposited via a microplotter with: 1) 0.5 wt % unmodified BuckyUSA; 2) 0.5 wt% f-SWCNTs (BuckyUSA, R=12); 3) 5 wt% f-SWCNTs (BuckyUSA, R=12); and 4) undoped P3HT:PCBM control.	58
Figure 3-7: UV-vis absorption (A, solid line) and emission spectra (PL, dotted line) of the three polymer films on glass (P3HT, B1, and G1) . Excitation for photoluminescence was performed by a 509.2 nm laser.	61
Figure 3-8: Device architecture of ternary blend OPVs	62
Figure 3-9: Image of completed devices (without Ag electrode) with 12 different active layer blends. Three binary blends (polymer:PC ₆₀ BM) and nine ternary blends (P1:P2:PC ₆₀ BM).	62
Figure 3-10: Evolution of (1) V _{OC} and (2) J _{SC} in P1:P2:PCBM ternary blends with respect to the relative donor polymer ratio.	64
Figure 3-11: Photoluminescence emission spectra of <i>polymer1:polymer2</i> blends (60 nm film on glass) as well as the neat polymer films, with a 509.2 nm excitation source. PL spectra for 1) P3HT:B1; 2) P3HT:G1; and 3) B1:G1 blends.	66
Figure 3-12: Energy levels (HOMO and LUMO) of active layer materials in ternary blends.....	69
Figure 3-13: External quantum efficiency of B1:G1:PCBM blends (solid) and the binary blends; B1:PCBM and G1:PCBM (dotted).....	70
Figure 3-14: External quantum efficiency of P3HT:B1:PCBM blends (solid) and the binary blends; P3HT:PCBM and B1:PCBM (dotted).	71
Figure 3-15: External quantum efficiency of P3HT:G1:PCBM blends (solid) and the binary blends; P3HT:PCBM and G1:PCBM (dotted).....	71
Figure 3-16: Normalized EQE of P3HT:B1:PCBM ternary devices (open squares) compared to the absorption spectra of the neat polymer films (solid line).	72

Figure 3-17: Normalized EQE of P3HT:G1:PCBM ternary devices (open squares) compared to the absorption spectra of the neat polymer films (solid line).	73
Figure 3-18: Normalized EQE of B1:G1:PCBM ternary devices (open squares) compared to the absorption spectra of the neat polymer films (solid line).	73
Figure 3-19: Illumination intensity dependence of J_{sc} for all 12 active layers. A) ternary and binary sub-blends for P3HT and G1; B) ternary and binary sub-blends for P3HT and B1; C) ternary and binary sub-blends for B1 and G1.....	75
Figure 3-20: Photocurrent density vs. effective voltage at different light intensities for B1:G1 blend (50% G1).[1 Sun=100 mW/cm ²].....	76
Figure 3-21: J_{ph} vs. $(V_{bi}-V)$ for P3HT:B1:PCBM blend at 1 sun (100 mW/cm ²).....	77
Figure 3-22: J_{ph} vs. $(V_{bi}-V)$ for the P3HT:G1:PCBM blend at 1 sun (100 mW/cm ²).....	77
Figure 3-23: J_{ph} vs. $(V_{bi}-V)$ for the B1:G1:PCBM blend at 1 sun (100 mW/cm ²).....	78
Figure 3-24: AFM phase images (1 x 1 μm^2) of the binary and ternary blends: (1) P3HT:PCBM; (2) B1:PCBM; (3) G1:PCBM; (4) P3HT:B1:PCBM; (5) P3HT:G1:PCBM; (6) B1:G1:PCBM.....	79
Figure 3-25: Illustration of the parallel diode model to approximate the equivalent circuit in a parallel BHJ polymer solar cell.	80
Figure 3-26: Equivalent circuit model of the parallel diode mechanism.....	81
Figure 3-27: Theoretical J(V) curves (dotted line) for the 3 ternary systems at 1:1 polymer ratios (50% P2) using the parallel diode model. The fitted results are compared to the experimental results (blue squares).....	82
Figure 3-28: Comparison of experimental and modeled J(V) curves for B1:G1:PCBM blends. Experimental results (squares) and parallel diode model fits (dotted line) for 20, 50, and 80 wt% G1 relative to B1.	83
Figure 3-29: Normalized irradiance of the ATLAS solar simulator at Xlim (used through a window in the glovebox) and the irradiance of the sun (AM 1.5G).....	83
Figure 0-1: Image of transmitted light through a PET/ITO/ZnO/P3HT:acceptor/PEDOT:PSS substrate.....	95
Figure 0-2: Image of transmitted light through a PET/ITO/ZnO/B1:acceptor/PEDOT:PSS substrate.....	95
Figure 0-3: Image of transmitted light through a PET/ITO/ZnO/G1:acceptor/PEDOT:PSS substrate.....	96
Figure 0-4: Image of transmitted light through a PET/ITO/ZnO/polymer:polymer:acceptor/PEDOT:PSS substrate.	96
Figure 0-5: Colourimetry of the binary polymer:acceptor blends and the 50% ternary blends (P1:P2:[60]PCBM).....	97

Figure 0-6: UV-vis absorption of P3HT binary active layers with PC ₆₁ BM, PC ₇₁ BM, or ICBA.	99
Figure 0-7: UV-vis absorption of B1 binary active layers with PC ₆₁ BM, PC ₇₁ BM, or ICBA.	99
Figure 0-8: UV-vis absorption of G1 binary active layers with PC ₆₁ BM, PC ₇₁ BM, or ICBA.	100
Figure 0-9: UV-vis absorption of P3HT:B1 binary blend films (60 nm films).....	100
Figure 0-10: UV-vis absorption of P3HT:G1 binary blend films (60 nm films).....	101
Figure 0-11: UV-vis absorption of B1:G1 binary blend films (60 nm films).....	101
Figure 0-12: UV-vis absorption of P3HT:B1:PC ₆₁ BM ternary active layers (80%, 50% and 20% relative P3HT:B1 concentrations) and their corresponding binary blends (dotted).	102
Figure 0-13: UV-vis absorption of P3HT:G1:PC ₆₁ BM ternary active layers (80%, 50% and 20% relative P3HT:G1 concentrations) and their corresponding binary blends (dotted).	102
Figure 0-14: UV-vis absorption of B1:G1:PC ₆₁ BM ternary active layers (80%, 50% and 20% relative B1:G1 concentrations) and their corresponding binary blends (dotted).	103
Figure 0-15: UV-vis absorption of B1:G1:PC ₆₁ BM ternary active layers (50, 30, 20, 10, 5, and 1 wt% relative B1:G1 concentrations).	103
Figure 0-16: UV-vis absorption (A) and emission spectra (PL) of a P3HT film (60 nm). Excitation for photoluminescence was performed by a 509.2 nm laser.	104
Figure 0-17: UV-vis absorption (A) and emission spectra (PL) of a B1 film (60 nm). Excitation for photoluminescence was performed by a 509.2 nm laser.	104
Figure 0-18: UV-vis absorption (A) and emission spectra (PL) of a G1 film (60 nm). Excitation for photoluminescence was performed by a 509.2 nm laser.	105
Figure 0-19: UV-vis absorption (A) and emission spectra (PL) of a P3HT:B1 (4:1) film (60 nm). Excitation for photoluminescence was performed by a 509.2 nm laser.	105
Figure 0-20: UV-vis absorption (A) and emission spectra (PL) of a P3HT:B1 (1:1) film (60 nm). Excitation for photoluminescence was performed by a 509.2 nm laser.	106
Figure 0-21: UV-vis absorption (A) and emission spectra (PL) of a P3HT:B1 (1:4) film (60 nm). Excitation for photoluminescence was performed by a 509.2 nm laser.	106
Figure 0-22: UV-vis absorption (A) and emission spectra (PL) of a P3HT:G1 (4:1) film (60 nm). Excitation for photoluminescence was performed by a 509.2 nm laser.	107
Figure 0-23: UV-vis absorption (A) and emission spectra (PL) of a P3HT:G1 (1:1) film (60 nm). Excitation for photoluminescence was performed by a 509.2 nm laser.	107
Figure 0-24: UV-vis absorption (A) and emission spectra (PL) of a P3HT:G1 (1:4) film (60 nm). Excitation for photoluminescence was performed by a 509.2 nm laser.	108

Figure 0-25: UV-vis absorption (A) and emission spectra (PL) of a B1:G1 (9:1) film (60 nm). Excitation for photoluminescence was performed by a 509.2 nm laser.	108
Figure 0-26: UV-vis absorption (A) and emission spectra (PL) of a B1:G1 (4:1) film (60 nm). Excitation for photoluminescence was performed by a 509.2 nm laser.	109
Figure 0-27: UV-vis absorption (A) and emission spectra (PL) of a B1:G1 (1:1) film (60 nm). Excitation for photoluminescence was performed by a 509.2 nm laser.	109
Figure 0-28: UV-vis absorption (A) and emission spectra (PL) of a B1:G1 (1:4) film (60 nm). Excitation for photoluminescence was performed by a 509.2 nm laser.	110
Figure 0-29: UV-vis absorption (A) and emission spectra (PL) of a B1:G1 (1:9) film (60 nm). Excitation for photoluminescence was performed by a 509.2 nm laser.	110
Figure 0-30: Photoluminescence TCSPC at 750 nm of neat P3HT, B1 and G1 polymer films with a 509.2 nm excitation laser.	111
Figure 0-31: Photoluminescence TCSPC at 750 nm of neat P3HT and B1 films and their binary blends (P3HT:B1) with a 509.2 nm excitation laser.	112
Figure 0-32: Photoluminescence TCSPC at 750 nm of neat P3HT and G1 films and their binary blends (P3HT:G1) with a 509.2 nm excitation laser.	112
Figure 0-33: Photoluminescence TCSPC at 750 nm of neat B1 and G1 films and their binary blends (B1:G1) with a 509.2 nm excitation laser.	113
Figure 0-34: Comparison of the UV-visible optical absorption (A) of a P3HT and P3HT:PC ₆₁ BM film with the external quantum efficiency (EQE) of a solar cell with a P3HT:PC ₆₁ BM active layer.	114
Figure 0-35: Comparison of the UV-visible optical absorption (A) of a B1 and B1:PC ₆₁ BM film with the external quantum efficiency (EQE) of a solar cell with a B1:PC ₆₁ BM active layer.	114
Figure 0-36: Comparison of the UV-visible optical absorption (A) of a B1:PC ₇₁ BM film with the external quantum efficiency (EQE) of a solar cell with a B1:PC ₇₁ BM active layer.	115
Figure 0-37: Comparison of the UV-visible optical absorption (A) of a B1:ICBA film with the external quantum efficiency (EQE) of a solar cell with a B1:ICBA active layer.	115
Figure 0-38: Comparison of the UV-visible optical absorption (A) of a G1 and G1:PC ₆₁ BM film with the external quantum efficiency (EQE) of a solar cell with a G1:PC ₆₁ BM active layer.	116
Figure 0-39: Comparison of the UV-visible optical absorption (A) of a G1:PC ₇₁ BM film with the external quantum efficiency (EQE) of a solar cell with a G1:PC ₇₁ BM active layer.	116
Figure 0-40: Comparison of the UV-visible optical absorption (A) of a P3HT:B1 (4:1) and P3HT:B1:PC ₆₁ BM (4:1:10) film with the external quantum efficiency (EQE) of a solar cell with a P3HT:B1:PC ₆₁ BM (4:1:10) active layer.	117

Figure 0-41: Comparison of the UV-visible optical absorption (A) of a P3HT:B1 (1:1) and P3HT:B1:PC ₆₁ BM (1:1:4) film with the external quantum efficiency (EQE) of a solar cell with a P3HT:B1:PC ₆₁ BM (1:1:4) active layer.....	117
Figure 0-42: Comparison of the UV-visible optical absorption (A) of a P3HT:B1 (1:4) and P3HT:B1:PC ₆₁ BM (1:4:10) film with the external quantum efficiency (EQE) of a solar cell with a P3HT:B1:PC ₆₁ BM (1:4:10) active layer.....	118
Figure 0-43: Comparison of the UV-visible optical absorption (A) of a P3HT:G1 (4:1) and P3HT:G1:PC ₆₁ BM (4:1:10) film with the external quantum efficiency (EQE) of a solar cell with a P3HT:G1:PC ₆₁ BM (4:1:10) active layer.	118
Figure 0-44: Comparison of the UV-visible optical absorption (A) of a P3HT:G1 (1:1) and P3HT:G1:PC ₆₁ BM (1:1:4) film with the external quantum efficiency (EQE) of a solar cell with a P3HT:G1:PC ₆₁ BM (1:1:4) active layer.	119
Figure 0-45: Comparison of the UV-visible optical absorption (A) of a P3HT:G1 (1:4) and P3HT:G1:PC ₆₁ BM (1:4:10) film with the external quantum efficiency (EQE) of a solar cell with a P3HT:G1:PC ₆₁ BM (1:4:10) active layer.	119
Figure 0-46: Comparison of the UV-visible optical absorption (A) of a B1:G1 (4:1) and B1:G1:PC ₆₁ BM (4:1:10) film with the external quantum efficiency (EQE) of a solar cell with a B1:G1:PC ₆₁ BM (4:1:10) active layer.	120
Figure 0-47: Comparison of the UV-visible optical absorption (A) of a B1:G1 (1:1) and B1:G1:PC ₆₁ BM (1:1:4) film with the external quantum efficiency (EQE) of a solar cell with a B1:G1:PC ₆₁ BM (1:1:4) active layer.	120
Figure 0-48: Comparison of the UV-visible optical absorption (A) of a B1:G1 (1:4) and B1:G1:PC ₆₁ BM (1:4:10) film with the external quantum efficiency (EQE) of a solar cell with a B1:G1:PC ₆₁ BM (1:4:10) active layer.	121
Figure 0-49: Comparison of the UV-visible optical absorption (A) of a B1:PC ₇₁ BM (blue dots) and G1:PC ₇₁ BM (green dots) film with the external quantum efficiency (EQE) of a solar cell with a B1:G1:PC ₇₁ BM (1:1:4) active layer.	121
Figure 0-50: J(V) curve and characteristics for a PSC on plastic with the following architecture: PET/ITO/ZnO/P3HT:PC ₆₁ BM/PEDOT:PSS/Ag.....	124
Figure 0-51: J(V) curve and characteristics for a PSC on plastic with the following architecture: PET/ITO/ZnO/B1:PC ₆₁ BM/PEDOT:PSS/Ag.....	124
Figure 0-52: J(V) curve and characteristics for a PSC on plastic with the following architecture: PET/ITO/ZnO/G1:PC ₆₁ BM/PEDOT:PSS/Ag	125

Figure 0-53: J(V) curve and characteristics for a PSC on plastic with the following architecture: PET/ITO/ZnO/B1:PC ₇₁ BM/PEDOT:PSS/Ag.....	125
Figure 0-54: J(V) curve and characteristics for a PSC on plastic with the following architecture: PET/ITO/ZnO/G1:PC ₇₁ BM/PEDOT:PSS/Ag	126
Figure 0-55: J(V) curve and characteristics for a PSC on plastic with the following architecture: PET/ITO/ZnO/P3HT:G1:PC ₆₁ BM (4:1:10)/PEDOT:PSS/Ag.....	126
Figure 0-56: J(V) curve and characteristics for a PSC on plastic with the following architecture: PET/ITO/ZnO/P3HT:G1:PC ₆₁ BM (1:1:4)/PEDOT:PSS/Ag.....	127
Figure 0-57: J(V) curve and characteristics for a PSC on plastic with the following architecture: PET/ITO/ZnO/P3HT:G1:PC ₆₁ BM (1:4:10)/PEDOT:PSS/Ag.....	127
Figure 0-58: J(V) curve and characteristics for a PSC on plastic with the following architecture: PET/ITO/ZnO/B1:G1:PC ₆₁ BM (4:1:10)/PEDOT:PSS/Ag.....	128
Figure 0-59: J(V) curve and characteristics for a PSC on plastic with the following architecture: PET/ITO/ZnO/B1:G1:PC ₆₁ BM (1:1:4)/PEDOT:PSS/Ag.....	128
Figure 0-60: J(V) curve and characteristics for a PSC on plastic with the following architecture: PET/ITO/ZnO/B1:G1:PC ₆₁ BM (1:4:10)/PEDOT:PSS/Ag.....	129
Figure 0-61: J(V) curve and characteristics for a PSC on plastic with the following architecture: PET/ITO/ZnO/P3HT:B1:PC ₆₁ BM (4:1:10)/PEDOT:PSS/Ag	129
Figure 0-62: J(V) curve and characteristics for a PSC on plastic with the following architecture: PET/ITO/ZnO/P3HT:B1:PC ₆₁ BM (1:1:4)/PEDOT:PSS/Ag	130
Figure 0-63: J(V) curve and characteristics for a PSC on plastic with the following architecture: PET/ITO/ZnO/P3HT:B1:PC ₆₁ BM (1:4:10)/PEDOT:PSS/Ag	130
Figure 0-64: J(V) curve and characteristics for a PSC on plastic with the following architecture: PET/ITO/ZnO/B1:G1:PC ₇₁ BM (1:1:4)/PEDOT:PSS/Ag.....	131
Figure 0-65: J(V) curve and characteristics for a 2 cm ² PSC on plastic with the following architecture: PET/ITO/ZnO/P3HT:PC ₆₁ BM/PEDOT:PSS/Ag.....	131
Figure 0-66: J(V) curve and characteristics for a 2 cm ² PSC on plastic with the following architecture: PET/ITO/ZnO/B1:PC ₆₁ BM/PEDOT:PSS/Ag.....	132
Figure 0-67: J(V) curve and characteristics for a 2 cm ² PSC on plastic with the following architecture: PET/ITO/ZnO/G1:PC ₆₁ BM/PEDOT:PSS/Ag	132
Figure 0-68: J(V) curve and characteristics for a 2 cm ² PSC on plastic with the following architecture: PET/ITO/ZnO/P3HT:PC ₇₁ BM/PEDOT:PSS/Ag.....	133

Figure 0-69: J(V) curve and characteristics for a 2 cm ² PSC on plastic with the following architecture: PET/ITO/ZnO/G1:PC ₇₁ BM/PEDOT:PSS/Ag	133
Figure 0-70: J(V) curve and characteristics for a 2 cm ² PSC on plastic with the following architecture: PET/ITO/ZnO/P3HT:G1:PC ₆₁ BM/PEDOT:PSS/Ag.....	134
Figure 0-71: J(V) curve and characteristics for a 2 cm ² PSC on plastic with the following architecture: PET/ITO/ZnO/B1:G1:PC ₇₁ BM/PEDOT:PSS/Ag.....	134
Figure 0-72: TGA results for Unidym SWCNTs: non-esterified reference (<i>unidym dry</i>), and those esterified with 1-decanol (<i>trial 1, solid</i>), 1-dodecanol (<i>trial 5, ---</i>), and 1-tetradecanol (<i>trial 4, - - -</i>).	142
Figure 0-73: TGA results for BuckyUSA SWCNTs: non-esterified reference (<i>BuckyUSA CNT untreated</i>), and those esterified with 1-decanol (<i>trial 6, - - -</i>), 1-dodecanol (<i>trial 2, solid</i>), and 1-tetradecanol (<i>trial 3, ---</i>).....	142
Figure 0-74: TGA results for SWCNTs esterified with 1-decanol: Unidym (<i>trial 1</i>) and BuckyUSA (<i>trial 6</i>).	143
Figure 0-75: TGA results for SWCNTs esterified with 1-dodecanol: Unidym (<i>trial 5</i>) and BuckyUSA (<i>trial 2</i>).	143
Figure 0-76: TGA results for SWCNTs esterified with 1-decanol: Unidym (<i>trial 4</i>) and BuckyUSA (<i>trial 3</i>).	144
Figure 0-77: Photoluminescence TCSPC of P3HT films with various functionalized SWCNT concentrations (wt%) at 730 nm.....	150
Figure 0-78: Evolution of V _{OC} of CNT-doped PSCs under constant illumination.	151
Figure 0-79: Evolution of J _{SC} of CNT-doped PSCs under constant illumination.	152
Figure 0-80: Evolution of the FF of CNT-doped PSCs under constant illumination.	152
Figure 0-81: Evolution of the efficiency of CNT-doped PSCs under constant illumination.	153

List of Tables

Table 1-1: Literature summary of ternary systems involving two donor polymers. Relevant details and corresponding HOMO and LUMO energy levels are included.....	22
Table 3-1: Degree of carbon nanotube functionalization (%) calculated by thermogravimetric analysis.....	53
Table 3-2: Influence of CNT doping (Unidym, R = 14) on P3HT:PCBM film's measured current. RMS roughness and current determined for a 10 x 10 μm^2 surface area.....	54
Table 3-3: Average results for non-doped and SWCNT-doped OPVs (12 devices each), with standard deviation in brackets.....	56
Table 3-4: Rheological properties of a variety of active layer inks.....	57
Table 3-5: J(V) characteristics for the ternary (P3HT:B1) blend and its corresponding binary blends.....	63
Table 3-6: J(V) characteristics for the ternary (P3HT:G1) blend and its corresponding binary blends.....	63
Table 3-7: J(V) characteristics for the ternary (B1:G1) blend and its corresponding binary blends....	64
Table 3-8: RMS roughness (nm) of the AFM topology of the binary active layers and ternary blends with equal donor polymer ratios.....	79
Table 3-9: Calculated mismatch factors (M) for a variety of active layers in inverted devices with the following architecture: PET/ZnO/active layer/PEDOT:PSS/Ag.....	84
Table 0-1 J(V) characteristics of 0.18 cm^2 PV devices on plastic with the following architecture: PET/ITO/ZnO/active layer/PEDOT:PSS/Ag.....	123
Table 0-2: J(V) characteristics of 2 cm^2 PV devices on plastic with the following architecture: PET/ITO/ZnO/active layer/PEDOT:PSS/Ag.....	123
Table 0-3: J(V) characteristics for a P3HT:[60]PCBM cell as illumination intensity is varied.....	136
Table 0-4: J(V) characteristics for a G1:[60]PCBM cell as illumination intensity is varied.....	137
Table 0-5: J(V) characteristics for a P3HT:G1:[60]PCBM cell as illumination intensity is varied ...	138
Table 0-6: J(V) characteristics for a P3HT:B1:[60]PCBM cell as illumination intensity is varied ...	139
Table 0-7: J(V) characteristics for a B1:G1:[60]PCBM cell as illumination intensity is varied.....	140

List of Abbreviations

Abbreviation	full name
AFM	atomic force microscopy
AM1.5G	Air Mass 1.5 Global
B1:G1:PCBM	polymer composite of B1 and G1 matrix with PC ₆₁ BM
B1:PCBM	polymer composite of B1 matrix with PC ₆₁ BM
BHJ	bulk-heterojunction
c-AFM	conductive AFM
CNT	carbon nanotube
CT	charge transfer
DMF	N, N-dimethylformamide
DMSO	dimethyl sulfoxide
DoF	degree of functionalization
DSSC	dye-sensitized solar cell
DTBT	poly(benzodithiophenedithienylbenzothiadiazole)
DTffBT	poly(benzodithiophene–dithienyldifluorobenzothiadiazole)
DTPyT	poly(benzodithiophene–dithienylthiadiazolopyridine)
e-	electron
EQE	external quantum efficiency
ERC	electron cyclotron resonance
ETL	electron transport layer
FET	field effect transistor
FF	fill factor
f-SWCNT	functionalized SWCNT
G1:PCBM	polymer composite of G1 matrix with PC ₆₁ BM
h+	hole
HOMO	highest occupied molecular orbital
HTL	hole transport layer
I	current
IBS	ion-beam sputtering
ICBA	indene-C ₆₀ bisadduct

ITO	indium tin oxide
J	current density
J _{mp}	current density at maximum power point
J _{sc}	short circuit current density
LBG	low band gap
LUMO	lowest unoccupied molecular orbital
MDMO PPV	poly[2-methoxy-5-(3',7'-dimethyloctyloxy)-1,4-phenylenevinylene]
MEH PPV	poly(2-methoxy-5-(2'-ethyl-hexyloxy)- 1,4-phenylene vinylene)
MWCNT	multi-walled carbon nanotube
NREL	national renewable energy laboratory
OLED	organic light-emitting diode
OPV	organic photovoltaic
P3HT	poly(3-hexylthiophene)
P3HT:B1:PCBM	polymer composite of P3HT and B1 matrix with PC61BM
P3HT:G1:PCBM	polymer composite of P3HT and G1 matrix with PC61BM
P3HT:PCBM	polymer composite of P3HT matrix with PC61BM
P3HT ₇₅ -co-EHT ₂₅	poly(3-hexylthiophene-co-3-(2-ethylhexyl)thiophene
P3HTT-DPP-10%	poly(3-hexylthiophene-thiophene-diketopyrrolopyrrole
P3OT	poly(3-octylthiophene)
PAL	photo-active layer
PAT	poly(alkylthiophene)
PBDTT-DPP	poly{2,6-4,8-di(5-ethylhexylthienyl)benzo[1,2-b;3,4 b]dithiophene-alt-5-dibutyloctyl-3,6-bis(5-bromothiophene 2-yl)pyrrolo[3,4-c]pyrrole-1,4-dione }
PBDTT-SeDPP	poly{2,6'-4,8-di(5-ethylhexylthienyl)benzo[1,2-b;3,4-b]dithiophenealt-2,5-bis(2-butyloctyl)-3,6 bis(selenophene-2-yl)pyrrolo[3,4-c]pyrrole-1,4-dione }
PBDTTT-C	poly[4,8-bis-substitutedbenzo[1,2-b:4,5-b]dithiophene-2,6 diyl-alt-4-substituted-thieno[3,4-b]thiophene-2,6-diyl]
PBHJ	parallel bulk-heterojunction
PC ₆₁ BM (PCBM)	[6,6]-phenyl-C61-butyric acid methyl ester
PC ₇₁ BM	[6,6]-phenyl-C71-butyric acid methyl ester

PCDTBT	poly[N-9'-heptadecanyl-2,7-carbazole-alt-5,5-(4',7'-di-2-thienyl-2',1',3'-benzothiadiazole)]
PCE	power conversion efficiency (η)
PCPDTBT (aka C-PCPDTBT)	Poly[2,6-(4,4-bis-(2-ethylhexyl)-4 <i>H</i> -cyclopenta [2,1- <i>b</i> ;3,4- <i>b'</i>]dithiophene)- <i>alt</i> -4,7(2,1,3-benzothiadiazole)]
PEDOT:PSS	Poly(3,4-ethylenedioxythiophene)-poly(styrenesulfonate)
PET	poly(ethylene terephthalate)
PID2	poly-3-oxothieno[3,4- <i>d</i>]isothiazole-1,1-dioxide/benzodithiophene
PL	photoluminescence
Pmax	maximum power point
PPEI-EI	poly(propionylethylenimine-co-vinyl alcohol
PSBTBT (aka Si-PCPDTBT)	poly[(4,4'-bis(2-ethylhexyl)-dithienol[3,2- <i>b</i> :2',3'- <i>d</i>]silole)-2,6-diyl-alt-(2,1,3-benzothiadiazole)-4,7-diyl]
PSC	polymer solar cell
PTB7	polythieno[3,4- <i>b</i>]-thiophene/benzodithiophene
PVA-VA	poly(vinyl acetate-co-vinyl alcohol)
PVD	physical vapour deposition
PVP	polyvinyl pyrrolidone
RF	radio frequency
RMS	root mean square
rr-P3HT	regioregular poly(3-hexylthiophene)
SDBS	sodium dodecyl benzene sulphonate
SDS	sodium dodecyl sulphate
SiNc	silicon naphthalocyanine bis(trihexylsilyloxiide)
SiPc	silicon phthalocyanine bis(trihexylsilyloxiide)
Si-PCPDTBT (aka PSBTBT)	poly[2,1,3-benzothiadiazole-4,7-diyl[4,4-bis(2-ethylhexyl)-4 <i>H</i> -cyclopenta [2,1- <i>b</i> :3,4- <i>b'</i>]dithiophene-siloe 2,6-diyl]]
S-P3MEET	sulfonated poly(thiophene-3-[2-(2-methoxyethoxy)ethoxy]-2,5-diyl)
SWCNT	single-walled carbon nanotube
TAZ	poly(benzodithiophenedithienylbenzotriazole
TCSPC	time correlated single photon counting
Tg	glass transition temperature

TGA	thermogravimetric analysis
THF	tetrahydrofuran
V	voltage
V_{mpp}	voltage at maximum power point
Voc	open circuit voltage

Chapter 1

Introduction

1.1 Solar Cells: An Introduction

Solar cells have seen vast improvements since the notion of harvesting direct electrical energy from the sun was first discovered in France in 1839 by the father-son team of Antoine César and Alexandre-Edmond Becquerel [1]. At present, there are numerous types of solar cells that include but are not limited to crystalline silicon cells (blue), thin film technologies (green), multijunction concentrators (purple), and emerging photovoltaics (red) (Figure 1-2). The record efficiencies of these photovoltaic technologies was determined and subsequently displayed in Figure 1-1 (enlarged region to emphasize emerging PV technologies), which was produced by the USA National Renewable Energy Laboratory (NREL) (full figure found on page 2, Figure 1-2). Of particular interest, are the emerging photovoltaics (PV) that include the polymer organic PV devices, which have seen a dramatic improvement over the last five years.

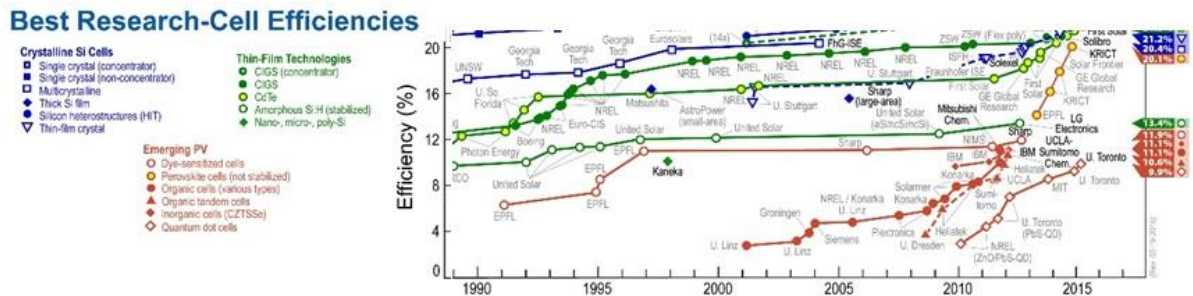


Figure 1-1: Comparison of emerging (red) solar cell record efficiencies achieved in the laboratory (National Renewable Energy Laboratory (USA)).

Best Research-Cell Efficiencies

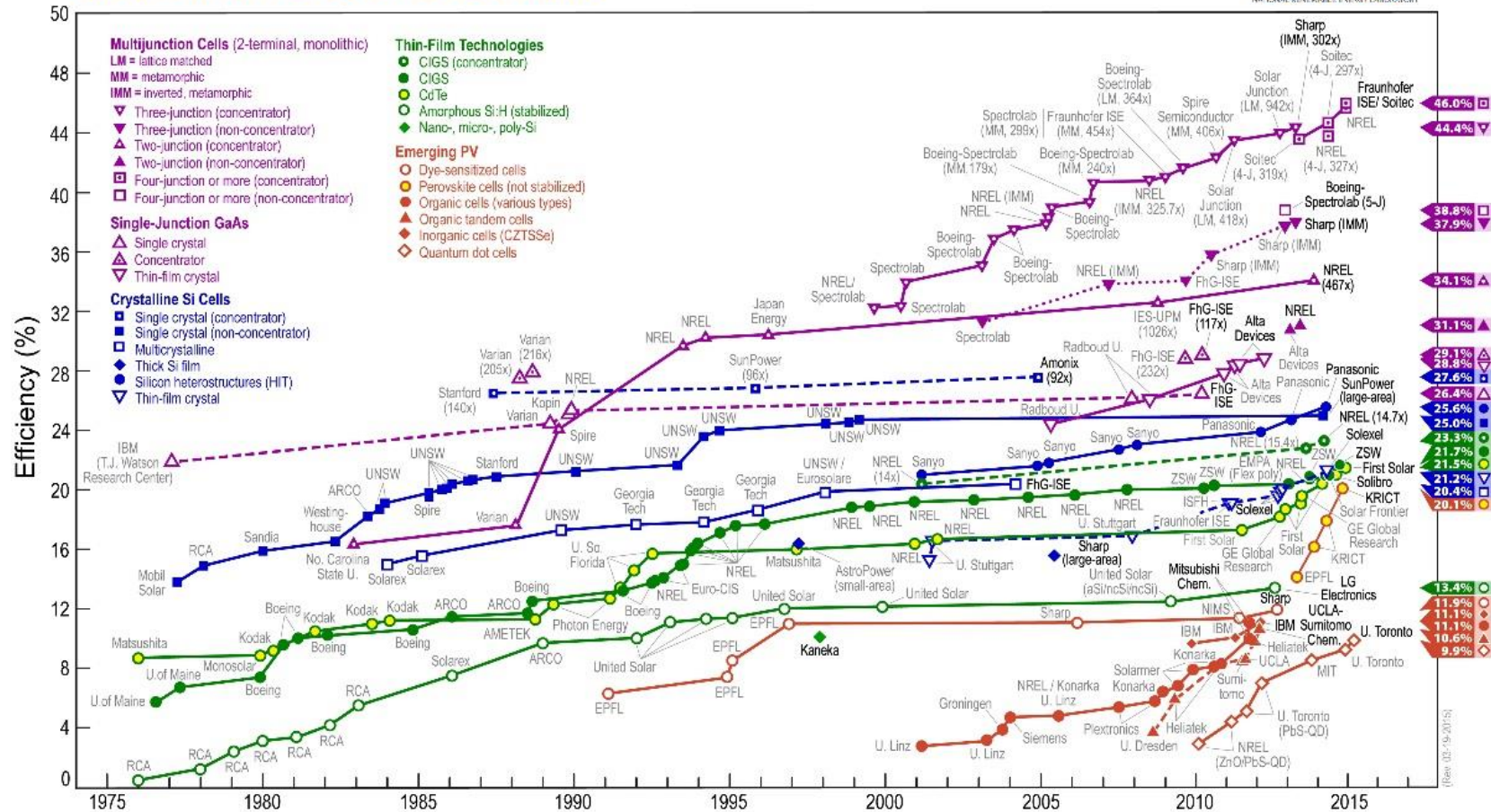


Figure 1-2: Comparison of world record solar cell efficiencies determined by the NREL.

Although the cell designs may vary, there is one component that they all have in common; the ability to convert photons into electricity. This phenomenon, in which light interacts with a solid semiconductor, is known as the photovoltaic effect.

Semiconductors can be defined loosely by either their energy gap (energy difference between the valence and conduction band energy levels, HOMO-LUMO band gap) or their resistivity. The energy gap of a semiconductor lies in the range of 0 eV - 4 eV and its resistivity (inverse of conductivity) is between $10^{-2} - 10^9 \Omega\text{cm}$ [2].

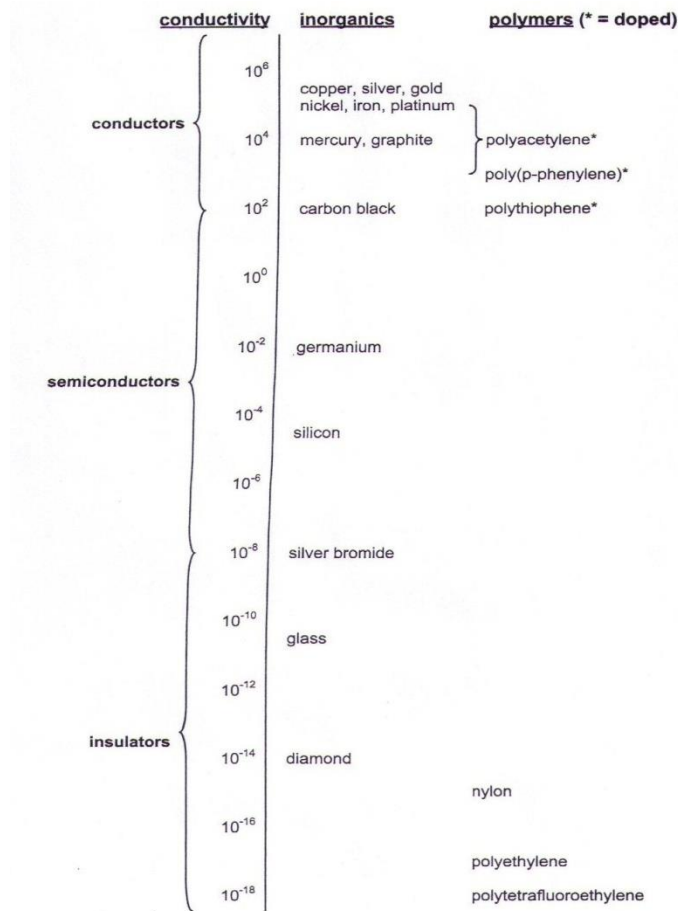


Figure 1-3: Summary of material conductivities [3]

The band gap energy of a semiconductor lies between that of a metal (0 eV band gap) and an insulator (band gap greater than 3 eV). The semiconductors electronic properties can be altered via doping to

prepare either an n-type or p-type semiconductor. Essentially, an n-type semiconductor has a majority of free electrons, whereas the majority of free carriers in a p-type semiconductor are holes (a hole is what is left in the absence of an electron) [2]. Electrons in the semiconductor's conduction band and holes in its valence band are known as free carriers due to their ability to carry electrical current. The electronic characteristic of the semiconducting material within the solar cell is of paramount importance for the ability to convert sunlight into electricity (photovoltaic activity).

The photovoltaic effect describes the fundamental interaction of light with matter to produce electricity. Light with photon energy greater than the band gap is absorbed by a semiconductor material. Within the semiconductor, electrons and holes are formed by the optical excitation provided by light. It is necessary for an internal electric field to separate the electrons and holes so that they do not recombine within the semiconductor. The electric field, which exerts a force on electrically charged particles, is created when holes and electrons form a band opposite one another on either side of the junction. The holes (from the p-type region) form a band in a small area in the n-type region and the electrons (from the n-type region) in the p-type material. To generate electricity, the electrons and holes must pass out of the material into the external circuit via opposite electrodes. This fundamental process in photovoltaic cells can occur through various mechanisms depending on cell type and morphology.

1.1.1 Current solar cell technologies

There are several different solar cell junctions (interfaces) in which holes and electrons are separated. These designs include the homojunction, heterojunction, heteroface junction (buried homojunction), metal-semiconductor junction (Schottky barrier), p-i-n junction, semiconductor-electrolyte junction, and the bulk-heterojunction (multiple junctions within the active layer). The most common cell morphologies are fabricated with crystalline silicon, amorphous silicon, gallium arsenide and other III-V materials, cadmium telluride and other II-VI materials, copper indium deselenide and other I-III-VI materials, and various organic compounds.

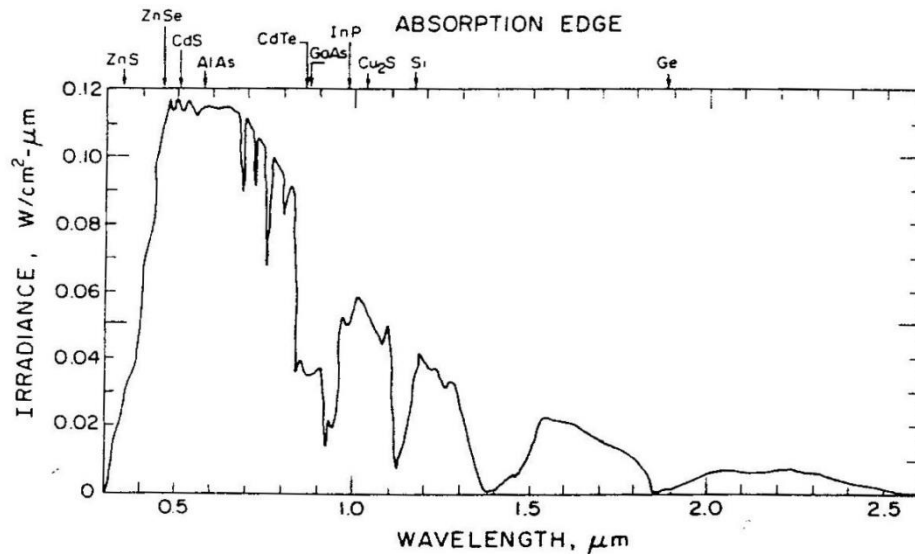


Figure 1-4: The average solar spectrum at the surface of the earth with traditional inorganic semiconductor band gaps indicated [1].

The majority of solar cells currently in mass production are composed of crystalline silicon. Silicon is non-toxic, stable, highly abundant in the earth's crust, and has dominated semiconductor applications for over half a century. The Si p-n homojunction cell was the only solar cell widely available to consumers in the early 1980s. The homojunction cell contains one semiconductor material in which there are two fractions, doped either p-type or n-type. Silicon is commonly doped with boron (acceptor impurity) to form a p-type semiconductor and phosphorous (donor impurity from PH_3) is the dopant used to prepare the n-type material. When light hits the silicon, photoexcitation creates free minority carrier electrons in the p-type portion and free minority carrier holes in the n-type portion. The free carriers diffuse toward the junction and pass over it, as long as they are not removed by recombination before arriving at the junction. The carriers are then collected by the junction's electric field and pass into the external circuit after they have traveled through the other region of the semiconductor. The p-n junction of the homojunction is similar to that of the p-n heterojunction, the major difference being that the heterojunction is composed of two different semiconductor materials; one that is p-type and the other n-type. A common combination used in heterojunction cells is the n-

type semiconductor CdS and the p-type CdTe. In 1976, the n-CdS/p-CdTe cell reached efficiencies of 6 – 7% by Bube and in 1993 Ferekides' group was able to produce an all thin-film n-CdS/p-CdTe cell that had a 15.8% efficiency. Although the efficiency of these types of cells is high, there are major drawbacks related to cost, fabrication, and health. Not only are the inorganic materials needed for the solar cells expensive but many heavy metals, like cadmium, are toxic. An alternative to the inorganic materials are organic conjugated polymers.

The unique electronic properties of conjugated polymers allow them to be used for various electronic applications which include xerography, multi-element sensors, batteries, and organic electronics [4]. Organic electronics, also known as soft electronics, can be fabricated with conjugated polymers or small molecules to create field effect transistors (FET), organic light emitting diodes (OLED), and organic photovoltaic devices (OPV). Their use in such devices is enabled by the semiconducting electronic characteristic of the conjugated polymers.

Semiconducting polymers have an unsaturated carbon based backbone with alternating single and double bonds [5]. Each carbon atom has one electron in a p_z orbital that is not involved in the σ -bond. The p_z orbitals between adjacent carbon atoms overlap to create a π -system, which can host a delocalized π -electron cloud along the polymer backbone. The molecular energy levels of the π -band (HOMO) and the π^* -band (LUMO) provide a critical characteristic of the polymer. The energy difference between the HOMO and LUMO is equivalent to the optical band gap, which is responsible for various characteristics including absorption, photoluminescence, and the photo-induced charge transfer (essential to the bulk-heterojunction (BHJ) solar cell).

The electronic transport properties of a conjugated polymer are affected by several intrinsic and extrinsic properties. Intrinsic molecular level properties include ionization potentials, electron affinity, coulomb correlations, and, as previously mentioned, the HOMO-LUMO π -bands. The HOMO-LUMO band gap energy can also be described as the energy difference between the valence band and the conduction band ($E_G = E_V - E_C$). The energy associated with the valence band is equivalent to the

ionization potential (energy required to remove an electron from the highest occupied state to vacuum) and the energy of the conduction band is equivalent to the electron affinity (energy gained when an electron is added to the lowest unoccupied state from vacuum). Extrinsic properties that have an effect on a polymer's transport properties include crystallinity, morphology, disorder, intermolecular interactions, and impurities [5]. Consequently, both intrinsic and extrinsic properties can be controlled by carefully engineering the polymer's structure (e.g. backbone and side chains).

1.1.2 Organic Photovoltaics

Organic photovoltaics (OPVs) are an emerging technology that uses organic compounds in order to decrease cost and increase ease of processing solar cells. These solar cells provide the promise of ultra-low cost, production via continuous printing process, and large area coverage (i.e. roof tops). Organic solar cells have the potential to be semitransparent, flexible and extremely light weight, which makes them an ideal candidate for personal use (i.e. incorporation into cell phones and clothing). The efficiencies of OPVs have seen great improvements throughout the last decade, from less than 1% to over 10%.

The most mature OPV is the dye-sensitized solar cell (DSSC) that uses an organic dye to absorb light and undergo a fast electron transfer to a nanostructure oxide (e.g. TiO_2). The largest disadvantage of the DSSCs is that hole transport is normally achieved by a liquid electrolyte. Another type of OPV that does not rely on a liquid electrolyte, and is more promising for large scale applications is the solid-state bulk-heterojunction device (BHJ), which is a conjugated polymer based solar cell [6]. Furthermore, this intermixed donor-acceptor BHJ provides a route to a more effective PV device compared to the classic bilayer heterojunction [7].

Currently, Mitsubishi Chemicals holds the world record for preparing a polymer solar cell (PSC) with an overall efficiency of 11.1 % (certified by the National Renewable Energy Laboratory in 2014, Figure 1-1). The polymer OPV contains a bulk-heterojunction (BHJ) within the cell's active

layer that undergoes a photoinduced charge transfer phenomenon. One of the seminal works to study this phenomena was performed by Morita *et al.* in 1992, in which they investigated the charge transfer between poly-3-alkylthiophenes (PATs) and a Buckminsterfullerene (C_{60}) [8]. It was shown that not only was the photoluminescence of the polythiophene quenched by C_{60} but also that the fullerene changed the inter-band and intra-gap optical absorption of the polymer film. They explained how the C_{60} is used as a p-dopant in a conducting polymer matrix, while being n-type doped itself. The fullerene passes from a neutral (C_{60}) to negatively charged state (C_{60}^{-1}), while creating a positively charged polaron (P^+) in the PAT chain. The BHJ active layer relies on this simple, yet intricate, phenomenon and is composed of an interpenetrating network of a donor (conjugated polymer) and an acceptor (fullerene derivatives), sandwiched between two electrodes.

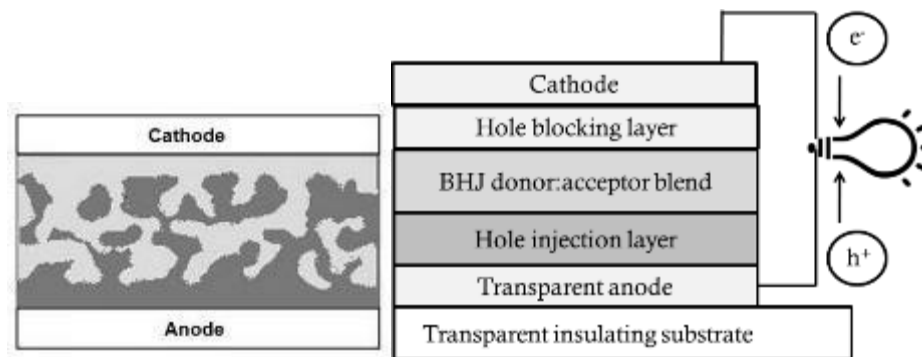


Figure 1-5: Interpenetrating network of donor and acceptor active layer in BHJ cell (left) and general polymer solar cell composition (right).

The most common buckminsterfullerene derivative is [6,6]-phenyl-C₆₁-butyric acid methyl ester (PC₆₁BM or PCBM) which is miscible with conjugated polymers, a great electron acceptor, and has good electron mobility.



Figure 1-6: Geometry of [6,6]-phenyl-C61-butyric acid methyl ester (PC₆₁BM)

For the BHJ solar cell to function, photons pass through the transparent electrode (commonly an indium tin oxide thin-film) and are absorbed by the polymer. The energy stimulates a coulombically bound electron-hole pair, known as an exciton, from the highest occupied molecular orbital (HOMO) to the lowest unoccupied molecular orbital (LUMO).

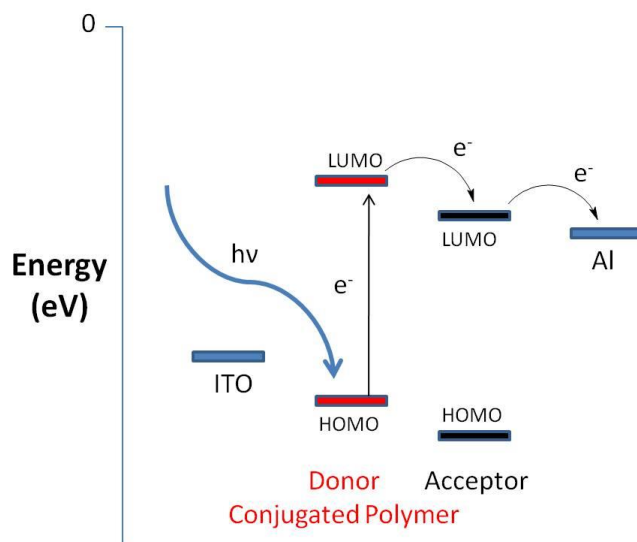


Figure 1-7: Photo-induced charge transfer within BHJ solar cell.

This is followed by exciton dissociation that occurs due to electron transfer from the LUMO of the donor to the LUMO of the acceptor. Charge transport of the hole (from the donor) to the anode and the

electron (from the acceptor) to the cathode enables the hole and electron to enter the external circuit and create electricity [9].

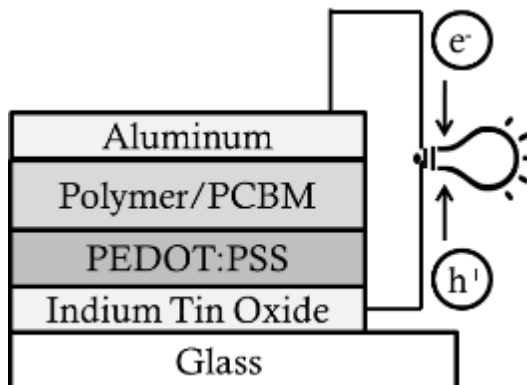


Figure 1-8: Structure of BHJ solar cell with Al back electrode

Most commonly charge extraction occurs using indium tin oxide (ITO), which has a high work function, as the positive electrode (anode) and aluminum, which is a metal with a low work function, as the negative electrode (cathode). The positive electrode (e.g. ITO) extracts the positive holes from the active layer with the help of a hole transport layer (e.g. poly(3,4-ethylenedioxythiophene) poly(styrenesulfonate) (PEDOT:PSS)), while simultaneously the negative electrode (e.g. Al) extracts the electrons.

One of the most prominent concerns for polymer photovoltaics is their performance lifetime (longevity in air). Problems can arise from both excessive sunlight and also the use of a low work function back electrode (e.g. Al) that can be easily oxidized in the presence of oxygen [10]. Not only can sunlight alter the morphology of the layers within the cell but it can also induce interfacial degradation over the cells lifetime. Potentially, the cells can be made more durable by including polymers in the BHJ layer that are designed to have an increased T_g (glass transition temperature) or induce cross linking of the polymers. The oxidation of the electrode can be reduced by either encapsulating the low work function metal (e.g. capping with a less reactive metal) or by using a metal electrode that has a higher work function. When a high work function metal (e.g. Ag) is used, the

charge extraction within the cell must be inverted. This implies that the ITO will be used to extract electrons and that the silver back electrode will collect holes. To ensure that this process works efficiently, a hole blocking layer must be added between ITO and the BHJ layer to ensure only electrons reach the negative electrode (ITO). Sean Shaheen and coworkers deposited a zinc acetate film (via spin coating) and subsequently performed a thermal conversion to form a zinc oxide (ZnO) hole blocking layer [11]. On the silver electrode a silver oxide (Ag_xO) layer forms between the organic layer and the metal electrode. The silver oxide is a p-type semiconductor with a high work function that can effectively extract holes from the cell, whose efficiency can be further increased by the introduction of a hole transport layer (PEDOT:PSS) between the silver electrode and BHJ layer.

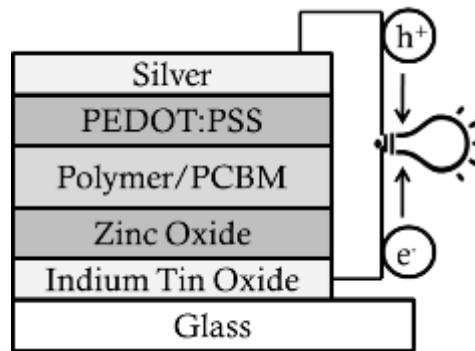


Figure 1-9: Reverse BHJ solar cell with high work function back electrode (Ag)

1.1.3 Solar Cell Characterization

The solar cell's performance can be characterized by several parameters (V_{OC} , I_{SC} , FF, and P_{max}) that can be used to calculate the cell's overall efficiency (power conversion efficiency, PCE) or external quantum efficiency (EQE) [12].

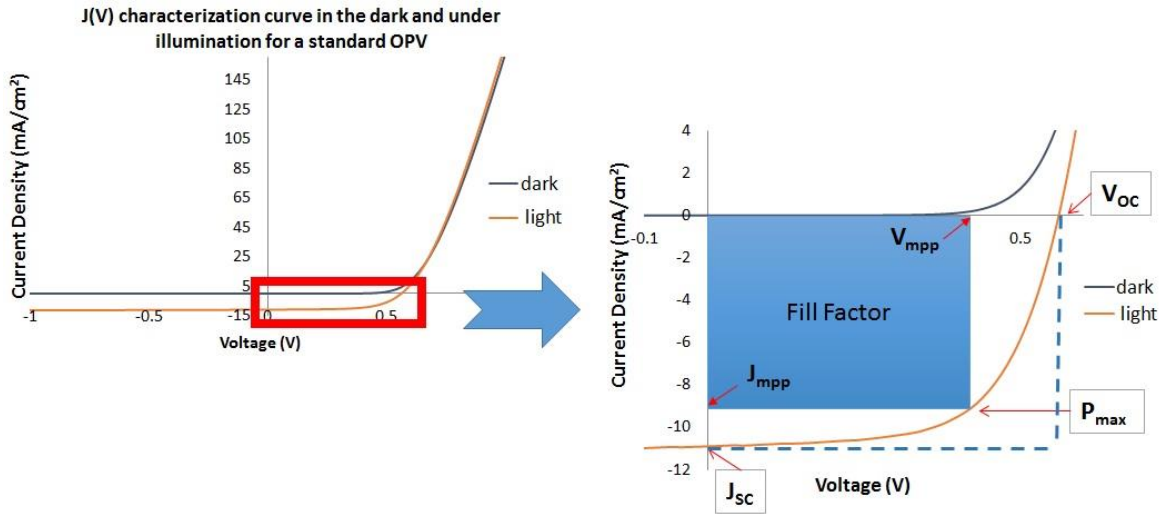


Figure 1-10: Current versus voltage curve for a standard P3HT:PCBM inverted photovoltaic cell on a glass substrate. Architecture: glass/ITO/ZnO/P3HT:PCBM/PEDOT:PSS/Ag

The PCE provides the efficiency of the cell under illumination by the standard light source, AM 1.5. The AM 1.5 is 100 mW cm^{-2} white light matching the spectral intensity distribution on the earth's surface when it is tilted at an angle of 37° . EQE is the ratio of collected charge carriers (electrons) per incident photon at a specific wavelength.

$$\text{PCE} = (V_{OC} * J_{SC} * \text{FF}) / P_{in}$$

$$\text{EQE} = (1240 * J_{SC}) / (\lambda * P_{in})$$

V_{OC} - open-circuit voltage

J_{SC} - short-circuit current density

$$\text{FF} = (J_{mpp} * V_{mpp}) / (V_{OC} * J_{SC})$$

P_{in} - incident light power

$$J_{mpp} * V_{mpp} = P_{max} - \text{maximum power output of solar cell}$$

$$hc/e = 1240 \text{ W*nm/A} \text{ --- (1eV} = 1240 \text{ nm)}$$

1.2 Ternary Polymer Solar Cells

Following the discovery of heterojunction polymer solar cells in 1986 by Tang [7] there has been tremendous advancement in the field of organic photovoltaics. This has been led by significant progress in the study of BHJ OPVs which started by the previously mentioned work observing the charge transfer between PATs [8] as well as poly(2-methoxy-5-(2'-ethyl-hexyloxy)-1,4-phenylene vinylene) (MEH-PPV) and a fullerene [6]. Currently, one of the most successful routes for preparing

organic photovoltaics consists of this polymer:fullerene active layer which was initially investigated by Heeger's group in 1995 [13].

Since 1995, there has been an array of advances in increasing the power conversion efficiency (PCE) of BHJ polymer solar cells (PSC). These advances have not only focused on improving active layer materials, but performance enhancement has also been achieved by altering the architectural design of the PSC and by introducing additives within the active layer. Hence, a ternary blend PSC strays from the traditional binary blend, and incorporates a third material in the active layer.

There have been several ternary blend PSCs investigated, which include: (1) a donor polymer with two fullerene acceptors (e.g. P3HT:ICBA:PCBM) [14], (2) a donor polymer with a fullerene acceptor and a donor dopant (small molecule [15] or polymer [16], [17]) (e.g. P3HT:PCPDTBT:PCBM), (3) two donor polymers and a fullerene acceptor [18], [19], [20] (e.g. PTB7:PBDTT-SeDPP:PCBM), and (4) variations of the donor:acceptor blend with quantum dots [21].

1.2.1 Charge Transport Mechanisms in Ternary Solar Cells

In ternary polymer solar cells, three primary charge transport mechanisms have been identified and well described by Yang *et al.* [22]. These mechanisms have been termed 1) Charge Transfer, 2) Energy Transfer, and 3) Parallel-diode; normally with one mechanism being dominant within the active layer blend.

Charge Transfer

Active layers that exhibit the charge transfer mechanism normally consist of a polymer:fullerene active layer doped with a sensitizer (dye molecule or polymer). Examples include P3HT:PCBM:SiPc (silicon phthalocyanine bis(trihexylsilyloxy)):SiNc (silicon naphthalocyanine bis(trihexylsilyloxy)) [23], and P3HT:PCBM:PCPDTBT (poly[N-9'-heptadecanyl-2,7-carbazole-alt-5,5-(4',7'-di-2-thienyl-2',1',3'-benzothiadiazole)]) [24] ternary active layers. For a charge transfer

mechanism, both donors can directly contribute to generation of free charge carriers while interacting with the acceptor (refer to Figure 1-11). In this case, the hole transport occurs through one donor domain after exciton dissociation with the acceptor.

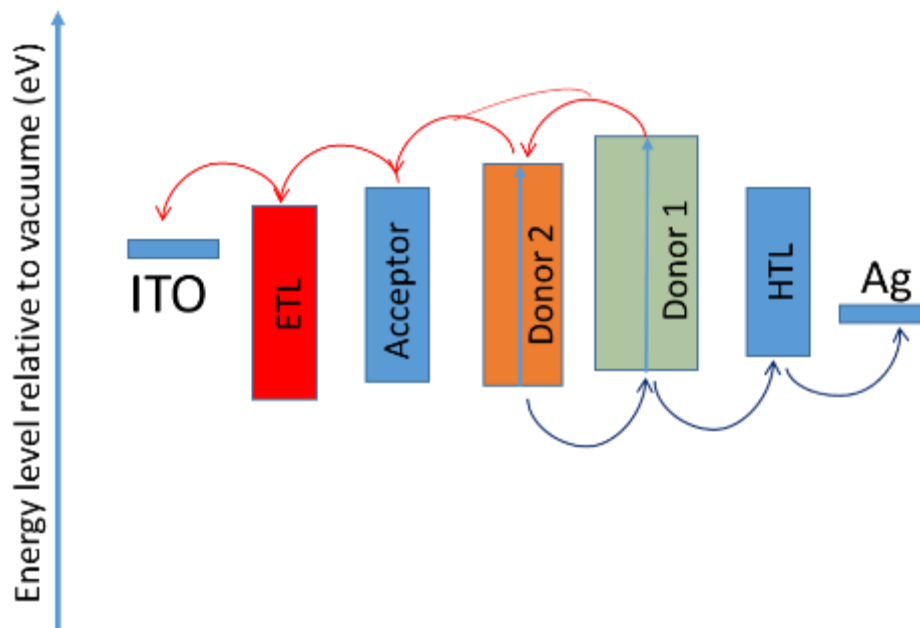


Figure 1-11: Charge transport mechanism for the transport of charges in a ternary BHJ device. Arrows denote electron (red) and hole (blue) migration.

For example, in a P3HT:PCBM blend doped with a dye sensitizer, there is increased exciton generation from the dye which dissociates at the dye:PCBM interface. The hole is subsequently transported by the P3HT phase to the anode. In general it is thought that there is a HOMO energy cascade for hole transport among donor moieties and that the V_{oc} is determined by smallest LUMO (acceptor) – HOMO (donor) energy difference. Increased efficiency is derived from a broadening in the external quantum efficiency (EQE) which in turn increases the J_{sc} . However, for efficient charge transfer between the donors, the sensitizer must be located at the donor-acceptor interface to generate additional photocurrent. Also, if the sensitizer concentration is too high, exciton traps can be created.

Energy Transfer

With the energy transfer mechanism, unlike the charge transfer mechanism, the extra absorber (dopant) does not directly generate free charge carriers (refer to Figure 1-12). It is thought that all holes are generated in one donor domain (energy acceptor), whilst the other donor acts only as a light absorber (energy donor). The energy donor (dopant absorber) transfers energy to the other donor through either Förster (long-range, resonance based) or Dexter (short range, electron-exchanged based) energy transfers. The photons absorbed by the dopant provide extra energy to generate more excitons in the primary donor and thus more holes are created. Although not affiliated directly with charge transport, the dopant increases the photovoltaic performance of the active layer, which is experimentally seen as a broadening in the EQE and increase in the J_{sc} . With the use of the energy absorber it is said that this mechanism allows cells to function closer to the Shockley-Queisser limit of a p-n junction solar cell.

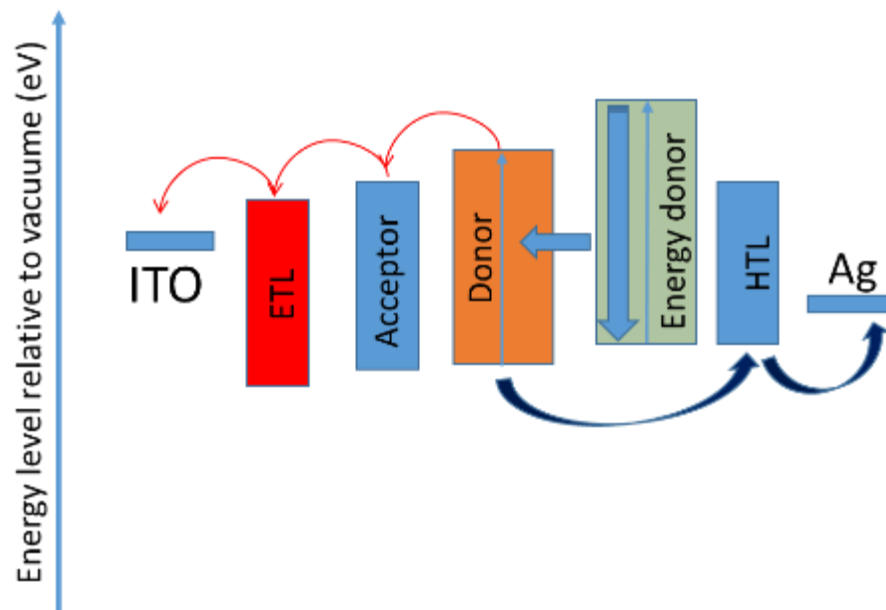


Figure 1-12: Energy transport mechanism for the transport of charges in a ternary BHJ device. Arrows denote electron (red) and hole (blue) migration.

The Shockley-Queisser limit is described by two loss mechanisms: thermalization loss, and spectrum loss [25]. Thermalization loss is caused by photons with higher energy than the absorbers band gap that first relax to the band edge prior to generation of charge carriers. While, spectrum loss is the result of photons with energy less than the donors band gap that cannot be captured to produce photoelectrons. Spectrum loss can be diminished using low band gap dopants and thermalization loss can be overcome by doping the active layer with molecules that exhibit singlet fission. These molecules exhibit fission of one high energy singlet exciton into two triplets of lower energy. Conveniently, unlike single excitons that have an approximate 10 nm diffusion length, the diffusion length of a triplet exciton is around 100 nm [22]. There are many methods to try and utilize this mechanism with one example involving the up conversion of energy from lanthanide ion dopants [26] to the primary donor. This principle enables the use of a similar method as applied in the up-conversion mechanism demonstrated in some organic light emitting diodes [27].

Parallel diode polymer solar cells

The parallel diode mechanism is significantly different from that of the charge and energy transfer mechanisms. This observation is because within the active layer there exists two independent systems working simultaneously to generate charges (refer to Figure 1-13). In the BHJ there is believed to be a parallel connection of two individual binary blend solar cells, hence termed a parallel bulk-heterojunction polymer solar cell (PBHJ PSC).

In the PBHJ neither the charge nor energy transfer mechanism plays a significant role in the photovoltaic process. Within the ternary blend, excitons are generated in each donor domain and subsequently migrate to their respective donor/acceptor interface to dissociate into free charge carriers. This mechanism should not be confused with a charge transfer mechanism in which for example a polymer:fullerene blend is sensitized with a low-band gap polymer dopant.

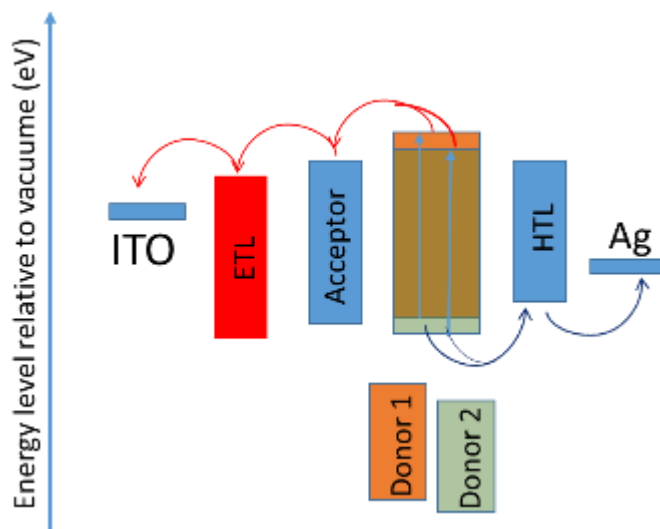


Figure 1-13: Parallel diode mechanism for the transport of charges in a ternary BHJ device. Arrows denote electron (red) and hole (blue) migration.

Two donor polymer ternary blends

A polymer-based parallel diode BHJ can be prepared by blending (1) two donor polymers with an acceptor, (2) blending a polymer and inorganic donor with an acceptor, or by (3) blending two acceptors with a donor polymer. However, focus will be on the two donor polymer:acceptor ternary blend as this provides a relatively simple route to colour tuned PSCs.

Prior to 2011, very little attention was paid to ternary blends with multiple donor polymers, let alone a parallel bulk-heterojunction active layer. Although, in 2008 an attempt was made to increase the open-circuit voltage (V_{oc}) of a P3HT:PCBM active layer by incorporating poly[2-methoxy-5-(3',7'-dimethyloctyloxy)-1,4-phenylenevinylene] (MDMO-PPV) [28]. Even though the V_{oc} of the doped P3HT:PCBM active layer was greater than the binary reference cell, this particular ternary blend exhibited charge trapping at a 1:0.5 donor polymer ratio. The next year, Campoy-Quiles and colleagues reported on an efficient ternary blend utilizing two P3HT polymers (regio-random and regio-regular) blended with PCBM [27]. The results were impressive and illustrated the possibilities of blending

polymers, however, since both polymers were polythiophenes, it is difficult to describe the system as a BHJ with two parallel diodes residing in the active layer.

In 2011, initial work on parallel diodes was reported by Ojala *et al.* in which they describe a parallel-BHJ cell prepared by blending two merocyanine dyes (donors) and a fullerene acceptor (C_{60}) [30]. A few months later, Yang *et al.* published the first paper in which the term parallel-like BHJ PSC was used in literature to describe a ternary active layer consisting of two donor polymers and a fullerene acceptor ($PC_{61}BM$) [18]. In this report, two ternary blend (polymer1:polymer2:PCBM) active layers were investigated. In the first blend, poly(benzodithiophenedithienylbenzotriazole [TAZ] and poly(benzodithiophenedithienylbenzothiadiazole) [DTBT] were used, and in the second blend poly(benzodithiophene-dithienyldifluorobenzothiadiazole) [DTffBT] was blended with poly(benzodithiophene-dithienylthiadiazolopyridine) [DTPyT]. The authors found that the V_{oc} of the ternary OPVs lie between that of the binary subcell references and also that, in general, the ternary blend J_{sc} 's can be higher than that of the binary blends. Although, this observation regarding current density is highly thickness dependent and it was not conclusively shown that a ternary blend had improved charge transport over the binary subcells. Another example of a successfully prepared parallel-BHJ PSC was accomplished by Khlyabich and coworkers in an investigation of the V_{oc} dependence on ternary blend composition. For their study, they blended a high band gap polymer (poly(3-hexylthiophene-co-3-(2-ethylhexyl)thiophene) [P3HT75-co-EHT25]) and a low band gap polymer (poly(3-hexylthiophene-thiophene-diketopyrrolopyrrole) [P3HTT-DPP-10%]) with $PC_{61}BM$ [19]. This work was elaborated by exploring the polymer1-polymer2 compatibility influence on the performance of the solar cell. In this recent study, the authors blended poly[N-9'-heptadecanyl-2,7-carbazole-alt-5,5-(4',7'-di-2-thienyl-2',1',3'-benzothiadiazole)] (PCDTBT) and P3HTT-DPP-10% with PCBM to form their ternary active layer [31]. In these blends the V_{oc} was independent of the polymer:polymer ratio and no parallel diode was formed, which was attributed to the polymers

immiscibility. However, physical incompatibility of the polymers may not be the only cause of an unsuccessful PBHJ, which can also be related to the polymers' large HOMO energy mismatch and the variation in their crystallinity. The HOMO energy levels of P3HTT-DPP-10% and PCDTBT are respectively 5.2 eV and 5.5 eV, which results in a 0.3 eV difference in HOMO level energies.

The idea of an optimal morphology of ternary polymer solar cell active layers was described by Yan *et al.* by a hierarchical interpenetrating networks model (HINM) [32]. In their study, they investigated two complementarily absorbing polymers, P3HT and poly[(4,4'-bis(2-ethylhexyl)-dithienol[3,2-b:2',3'-d]silole)-2,6-diyl-alt-(2,1,3-benzothiadiazole)-4,7-diyl] (PSBTBT), and noticed a variation in performance as the active layer film was cast from different solvents. Even though a parallel-like BHJ was not formed, they proposed a model in which ternary active layer morphology can be controlled by use of processing solvents.

In 2014, two papers involving P3HT and poly[2,1,3-benzothiadiazole-4,7-diyl[4,4-bis(2-ethylhexyl)-4H-cyclopenta [2,1-b:3,4-b']dithiophene-silole 2,6-diyl]] (Si-PCPDTBT) were published in which the authors prepared polymer sensitized ternary blends. Interestingly, Li and coworkers prepared efficient ternary blends with P3HT sensitized with 30 wt% Si-PCPDTBT [33] and Lin *et al.* prepared blends of Si-PCPDTBT sensitized with up to 5 wt% P3HT [34]. Although, the parallel mechanism is not observed in these systems, it was found that sensitization of a small amount of a second donor polymer can increase light absorption, polymer phase separation, exciton separation, and charge carrier mobilities. Another recent study, by Ameri and coworkers, investigated the importance of the ternary blend morphology and compatibility of the donor polymers [16]. They investigated both P3HT:PC₆₀BM and P3HT:ICBA active layers doped with either Si-PCPDTBT or C-PCPDTBT as an IR sensitizer. Even though both dopant polymers have similar structural and electronic properties, the Si-PCPDTBT polymer was found to be a much more effective sensitizer. It was noted that the interfacial surface energy of the polymer dopant had a significant effect on morphology and subsequent free charge carrier

transport within the active layer. Within the ternary blend both dopant polymers locate at the amorphous interfaces, but interestingly, the Si-PCPDTBT locates at the P3HT crystallites, whereas the C-PCPDTBT locates at the semi-crystalline fullerene domains. These findings led the authors to believe that the disruption of the semi-crystalline fullerene domains was worse for the charge transport of free carriers than the disruption of the polymer domains.

A recent example of a ternary blend BHJ which exhibits high efficiency at equal polymer:polymer ratios was published by Lu *et al.* [35]. This work involves the blending of poly-3-oxothieno[3,4-d]isothiazole-1,1-dioxide/benzodithiophene (PID2) and polythieno[3,4-b]-thiophene/benzodithiophene (PTB7) with PC₇₁BM. This is the first published example of a ternary blend with an efficiency greater than 8%, although it is not described as a parallel BHJ and has an open-circuit voltage that is independent of the polymer ratios. In fact, instead of a V_{oc} lying between the V_{oc} 's of the two binary subcells, the V_{oc} was determined by the smallest $LUMO_{(acceptor)}-HOMO_{(donor)}$ energy difference. The highest efficiency of the ternary blend was found in a PTB7:PID2:PC₇₁BM 9:1:15 ratio which was indeed more efficient than the two binary blend references. The ternary blend with equal quantities of both polymers achieved similar results as the PTB7 binary reference, whereas an increase in the PID2 concentration over 50% relative to PTB7 reduced the current density and overall performance of the device. It was described that this ternary system not only improves the solar cell's absorption, but that there is a cascade of hole transfer from PID2 to PTB7 to PEDOT:PSS. At 10 wt% PID2 doping, it was noted that PTB7 crystallinity was not affected, that both charge dissociation and transport were increased and that the charge recombination was suppressed.

It is important to note, that the parallel diode system is not well understood and efforts are underway to explore the various mechanisms involved in charge transport. A convincing theory has been proposed by Street and coworkers who describes the formation of an organic alloy in the ternary blend [36]. This alloy is described as having electronic alloy states that account for the V_{oc} dependence

on concentration. This is due to the variation in $\text{HOMO}_{\text{donor}}$ and $\text{LUMO}_{\text{acceptor}}$ levels as the concentration of the two donors is varied. In these blends, the charge transfer energy varies, which implies that an alloy is formed with an extensive array of delocalized energy states. This organic alloy, or PBHJ, is significantly different from a binary blend PSC doped with a low-band gap sensitizer (under charge transfer mechanism), in which the electronic states reflect properties of individual molecules. This is illustrated by the dynamic V_{oc} of the alloy which is not limited to the smallest $\text{HOMO}_{\text{donor}}$ - $\text{LUMO}_{\text{acceptor}}$ energy gap, as seen in the doped binary blends.

A study involving four systems ($2x \text{D1:D2:A}$ and $2x \text{D:A1:A2}$) was performed by Street *et al.* to help describe the multitude of possible electronic states in a ternary blend [37]. They explained that in the two donor polymer ternary blend (with dilute concentration of D2), well intermixed polymers have excitons that diffuse easily from the dilute low band gap polymer to the BHJ interface to generate mobile charges. Whereas in a system with poorly intermixed polymers, the excitons from the low band gap polymer cannot readily diffuse and do not contribute to charge generation. This paper went on to further describe two scenarios for the ternary blends: (1) well intermixed blend with alloy properties (characterized by electronic states that reflect the average composition of components), or (2) incomplete intermixing with highly localized electronic states (reflecting individual molecules unmodified by presence of two materials). In the poorly mixed case, it is described that the smaller band gap component (dopant) introduces trap states in the higher gap polymer matrix. This premise of “morphological traps” and unfavourable polymer-polymer interactions was further developed and supported by work published in 2015 by Yang Yang *et al.*[20]. This research provides insight into seven polymerA:polymerB:PC₇₁BM ternary blends, in which three illustrate trapping behaviour and the other four exhibit a parallel-like BHJ (refer to Table 1-1). Yang and coworkers, stress the need for polymers with compatible physical properties (e.g. molecular orientation and crystallinity) to avoid the molecular disorder exhibited in incompatible ternary polymer matrixes, which leads to a drop in the PV

performance. Additionally, the influence of polymer side-chain interaction was used to explain the disruption between edge-on and face-on polymers. It was found that poor polymer-polymer packing led to not only morphological traps, but also decreased crystallinity length, a disruption in long-range charge transport, as well as reduced charge carrier mobility. It was also explained that polymers with similar HOMO levels are preferable, but not strictly necessary to achieve the PBHJ. They observed that in the P3HT blends there was a hole transfer (energy transfer) from the low band gap polymer's HOMO to the HOMO of P3HT.

Table 1-1: Literature summary of ternary systems involving two donor polymers. Relevant details and corresponding HOMO and LUMO energy levels are included.

Year	Description	Polymers	HOMO (eV)	LUMO (eV)	E _g (eV)
2008	Kim et al. – trapped [28]	P3HT poly(3-hexylthiophene)	4.9	3.0	1.9
		MDMO-PPV poly[2-methoxy-5-(3',7'-dimethyloctyloxy)-1,4-phenylenevinylene]	5.3	3.0	2.3
2009	Campoy-Quiles et al – efficient at 50% ratio [29]	rr-P3HT	4.61	~ 2.6	2.0
		Random-P3HT	4.73	~ 2.5	2.23
2012	Yang et al – first PBHJ - (submitted 2011) [18]	TAZ poly(benzodithiophenedithienylbenzotriazole)	5.29	3.31	1.98
		DTBT poly(benzodithiophenedithienylbenzothiadiazole)	5.40	3.7	1.7
		DTffBT poly(benzodithiophene–dithienyldifluorobenzothiadiazole)	5.54	3.84	1.7
		DTpyT poly(benzodithiophene–dithienylthiadiazolopyridine)	5.45	3.94	1.51

	Khlyabich et al – PBHJ, received March 2012 [19]	P3HTT-DPP-10% poly(3-hexylthiophene-thiophene-diketopyrrolopyrrole)	5.2	3.69	1.51
		P3HT₇₅-co-EHT₂₅ (poly(3-hexylthiophene-co-3-(2-ethylhexyl)thiophene))	5.43	3.53	1.9
2014	Khlyabich et al – trapped – contrary to alloy theory [31]	P3HTT-DPP-10%	5.2	3.69	1.51
		PCDTBT poly[N-9'-heptadecanyl-2,7-carbazole-alt-5,5-(4',7'-di-2-thienyl-2',1',3'-benzothiadiazole)]	5.5	3.6	1.9
	Yan et al. – trapped/dependence on morphology [32]	P3HT	5.1	2.9	2.2
		PSBTBT (Si-PCPDTBT) poly[(4,4'-bis(2-ethylhexyl)-dithienol[3,2-b:2',3'-d]silole)-2,6-diyl-alt-(2,1,3-benzothiadiazole)-4,7-diyl]	5.3	3.5	1.8
	Li et al – P3HT with NIR sensitizer [33]	P3HT	5.1	3.0	2.1
		Si-PCPDTBT (PSBTBT) poly[2,1,3-benzothiadiazole-4,7-diyl[4,4-bis(2-ethylhexyl)-4H-cyclopenta [2,1-b:3,4-b']dithiophene-silole 2,6-diyl]]	5.3	3.55	1.75
	Lin et al. – P3HT sensitized [34]	Si-PCPDTBT (PSBTBT)	5.3	3.6	1.7
		P3HT	5.2	3.2	2
	Lu et al. – near PBHJ [35]	PTB7 Poly[[4.8-bis[(2-ethylhexyl)oxy]benzo[1,2-b:4,5-b]dithiophene-2,6-diyl][3-fluoro-2-[(2-ethylhexyl)carbonyl]thieno[3,4-b]thiophenediyl]]	5.15	3.31	1.84
		PID2 poly-3-oxothieno[3,4-d]isothiazole-1,1 dioxide/benzodithiophene (with 2-ethylhexyl sidechains)	5.52	3.50	2.02
2015	Yang et al. – various combinations of two donor polymer ternary blends with PC ₇₀ BM	1a) P3HT	5.03	3.05	1.98
		1b) PBDTT-SeDPP poly{2,6'-4,8-di(5-ethylhexylthienyl)benzo[1,2-b:3,4-b]dithiophenealt-2,5-bis(2-butyloctyl)-3,6 bis(selenophene-2-yl)pyrrolo[3,4-c]pyrrole-1,4-dione}	5.21	3.70	1.51

– those exhibiting traps (1-3) and PBHJs (4-7) [20]	2a) P3HT	5.03	3.05	1.98
	2b) PBDTT-DPP poly{2,6-4,8-di(5-ethylhexylthienyl)benzo[1,2-b;3,4-b]dithiophene-alt-5-dibutyl-3,6-bis(5-bromothiophene 2-yl)pyrrolo[3,4-c]pyrrole-1,4-dione}	5.25	3.63	1.62
	3a) PBDTTT-C poly[4,8-bis-substitutedbenzo[1,2-b;4,5-b]dithiophene-2,6 diyl-alt-4-substituted-thieno[3,4-b]thiophene-2,6-diyl]	5.25	3.63	1.62
	3b) Si-PCPDTBT	5.3	3.55	1.75
	4a) PBDTTT-C	5.16	3.35	1.81
	4b) PBDTT-SeDPP	5.21	3.70	1.51
	5a) PBDTTT-C	5.16	3.35	1.81
	5b) PBDTT-DPP	5.25	3.63	1.62
	6a) PTB7	5.20	3.31	1.89
	6b) PBDTT-DPP	5.25	3.63	1.62
	7a) PTB7	5.20	3.31	1.89
	7b) PBDTT-SeDPP	5.21	3.70	1.51

1.3 Carbon Nanotubes

1.3.1 Properties of single-walled carbon nanotubes

A single-walled carbon nanotube (SWCNT) is best described as a graphene sheet that has been rolled into a cylinder with a half fullerene sealing both ends. Graphene is a polyaromatic monoatomic layer consisting of sp^2 -hybridized carbon atoms arranged in hexagons (graphite is composed of multiple layers of graphene). The diameter of most SWCNT is about 1-2 nm, although there have been reports

of tubes synthesized with diameters as small as 0.4 nm (the tubular morphology is not favoured beyond 2.5 nm). The carbon nanotubes have very high aspect ratios (length/diameter) with lengths in the micrometer range (200 nm – 10 μm) [38]. The chemical reactivity of the nanotubes is more prevalent among the carbons at the tips. This increased reactivity is because these carbons are arranged in six pentagonal rings, whereas all the other carbons within the tube are involved in hexagonal rings. Unlike planar graphene, whose carbon atoms are all sp^2 -hybridized, the sp^2 -hybridized carbons in the nanotubes have a small degree of sp^3 character due to the tubes radius of curvature. This tubular morphology provides the CNTs with unique electronic behaviour that can vary depending on how the graphene sheet is rolled into a tube.

The morphology of SWCNTs can be divided into two broad categories; either chiral or achiral. A chiral carbon nanotube (just like any chiral molecule) cannot be superimposed on its own mirror image and is known as a helical nanotube. The cylindrical folding of the graphene sheet can be described by a vector (and the corresponding vector integers: n and m) and the angle of helicity (θ).

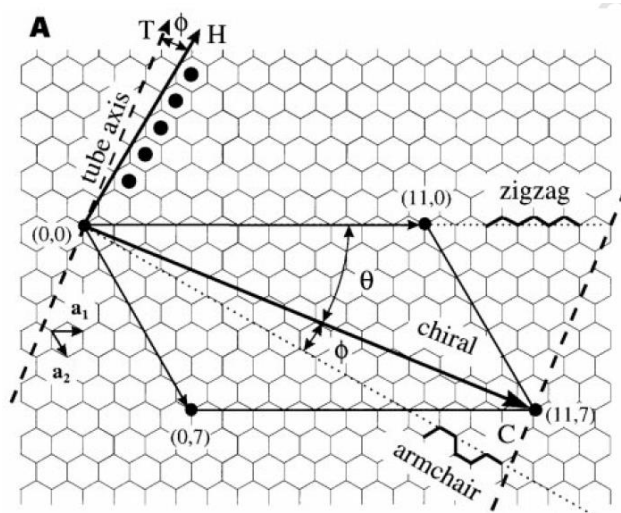


Figure 1-14: Description of carbon nanotube formation [39]

Chiral nanotubes can take various forms with an angle of helicity between 0° (zigzag type $(n,0)$) to 30° (armchair type (n,n)). Approximately one third of produced single-walled carbon nanotubes have a

metallic electronic characteristic, whereas two thirds are semiconducting [40]. As a general rule, armchair (n,n) tubes are metals (band gap = 0), zigzag (n,0) tubes are semiconducting, chiral (n,m) tubes with n-m equivalent to an integer of 3 ($n-m = 3y$; $y = \text{non-zero integer}$) are small (tiny) gap semiconductors, and all other chiral tubes are large gap semiconductors.

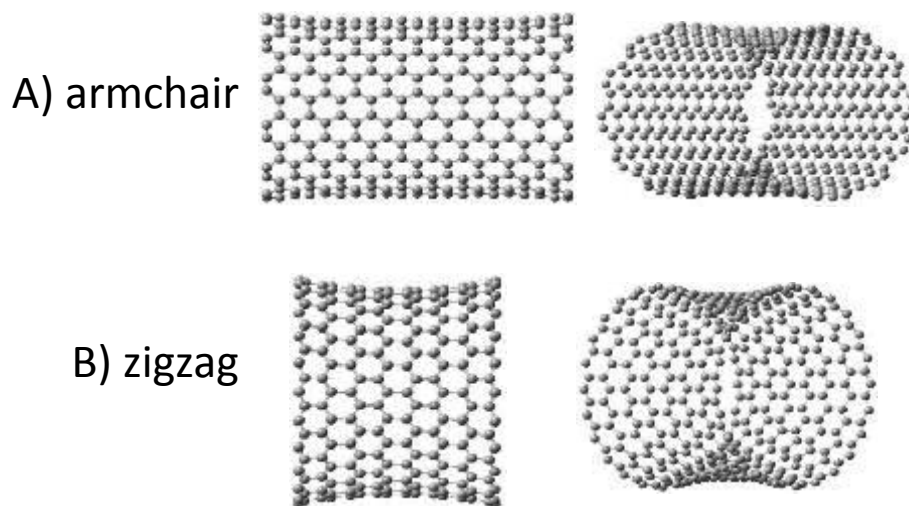


Figure 1-15: Armchair (A) and zigzag (B) single-walled carbon nanotube morphologies

However, the band gap energy of the semiconducting tubes is inversely proportional to the tube diameter. Therefore, armchair and about 1/3 of zigzag SWCNTs should be metallic with the rest being semiconducting [41]. Even though SWCNT can have unique electronic properties amongst themselves, there is a common attraction among all CNTs. This attraction, van der Waals forces, is caused by the π -electrons that interact between adjacent nanotubes. The van der Waals forces cause the native state of the SWCNT to be in ropes rather than separate tubes. Similarly, double-walled carbon nanotube (DWCNT) and multi-walled carbon nanotubes (MWCNT) can either become entangled with each other or exist as individual moieties. The ropes (also known as bundles) of single-walled carbon nanotubes exhibit hexagonal arrangements and are rather difficult to disrupt due to the van der Waals forces which provide an intertube binding energy of approximately 900 meV/nm (87 kJ/mol*nm). The diameter of the ropes can range from 5-100 nm but normally exhibit a diameter close to 30 nm [38].

1.3.2 Properties of multi-walled carbon nanotubes

As the name suggests, multi-walled carbon nanotubes can have any number of walls upwards from two layers (DWCNT). MWCNT can acquire various morphologies during synthesis and commonly fall into two categories. The morphology of the tube is described as either a concentric multi-walled carbon nanotube (c-MWCNT) or a herringbone multi-walled carbon nanotube (h-MWCNT). c-MWCNTs consist of any number of SWCNTs coaxially arranged around one another with increasing diameter (one SWCNT within a larger SWCNT). The tubes have a metallic characteristic with the outer tube primarily involved in conduction. The intertube distance between nanotubes is approximately 0.34 nm, which is slightly larger than graphite's inter-graphene sheet distance of 0.335 nm. The increase in packing distance is caused by the curvature of the nanotubes, which does not allow for planar packing. h-MWCNT's have a herringbone texture caused by the graphene sheets making an angle with respect to the nanotube axis varying the inner diameter of the CNTs. This variation in the angle of the graphene sheets distorts the tubular arrangement of the nanotubes. The angle, which determines the ultimate morphology of the MWCNTs, is controlled by the synthetic conditions (i.e. catalyst morphology, composition of atmosphere). If the angle is 0° then a c-MWCNT is formed, although if the angle is 90° the structure is no longer a tube. CNTs can be altered to carbon nanofibers when perpendicular graphene sheets (that make a 90° angle relative to the CNT axis) are incorporated in c-MWCNT and h-MWCNT structures. When this anomaly occurs, a bamboo structure is formed creating divided internal cavities within the tube.

1.4 Modification of Carbon Nanotubes

1.4.1 Functionalization of Carbon Nanotubes

The physical and electrical properties of carbon nanotubes can be exploited through covalent bonding or non-covalent interactions (i.e van der Waals and π - π stacking). These modifications can be performed to increase the tube's dispersibility in various solvents, for their incorporation in a matrix

(polymer, ceramic, metal), or with proteins to enable the tubes to cross cell membranes [42]. Nucleic acids have also been used for both non-covalent and covalent functionalization of nanotubes. Ming Zheng and colleagues from DuPont, MIT and the University of Illinois at Urbana-Champaign were among the first researchers to explore DNA wrapping of single-walled carbon nanotubes [43]. The interest in CNT functionalization has grown enormously in an effort to explore and utilize the unique electronic and physical properties of carbon nanotubes.

Covalent Functionalization

The tips and sidewalls of carbon nanotubes can be functionalized through covalent bonding, with the ends of the tubes being the most reactive. Oxidizing acids (such as HNO_3 , $\text{HNO}_3 + \text{H}_2\text{SO}_4$, H_2SO_4 in conjunction with KMnO_4) that are often used for the purification and end opening of CNTs can also functionalize the tips and defects of tubes with carboxylic ($-\text{COOH}$) and alcohol ($-\text{OH}$) groups. Oxidation of the tubes surface can allow for their electrostatically stabilized colloidal dispersion in water and ethanol [38]. Further functionalization of the tubes with organic or inorganic materials can be achieved by reacting with the $-\text{OH}$ and $-\text{COOH}$ groups. Functionalization of the nanotubes can serve to achieve enhanced solvent dispersion, self assembly, or even use as a chemical sensor.

There are numerous examples of nanotube functionalization, some workers attaching long aliphatic amines to tube ends and others attaching CNTs to each other forming macromolecules. In 1998, Smalley and coworkers connected nanotubes together in sequence by attaching $\text{NH}_2-(\text{CH}_2)_{11}-\text{SH}$ groups via an amide linkage to the tips of single-walled carbon nanotubes [44]. Subsequently gold particles were introduced to anchor the thiol chain ends which provided the link between the tubes. Not only is it possible to add functional groups to the tube ends, but sidewall functionalization can also be achieved.

When highly reactive reagents are used it is possible to covalently modify the tube walls. The reactivity of the tube's sidewall is increased as the diameter of the tube is decreased, due to increasing curvature and loss of aromaticity. The sidewalls can be functionalized in many different ways which

include fluorination, formation of carbenes and nitrenes, alkylation and arylation, 1,3-dipolar cycloaddition of azomethine ylides, solution phase ozonolysis, addition of radicals, silylation, electrochemical reactions, and attachment of polymers. Polymer grafting (involving the attachment of polymers) can be accomplished via amide linkages when the carboxyl group on the nanotube is reacted with an aminopolymer (i.e poly(propionylethylenimine-co-vinyl alcohol) (PPEI-EI). In a similar fashion highly soluble linear polymers can also be attached via ester linkages, which can be accomplished with poly(vinyl acetate-co-vinyl alcohol) (PVA-VA). This attachment of polymers can increase the solubility of the CNT in many different solvents. Polymers can also be grafted to improve the nanotube's bonding in CNT:polymer composites. Ajayan and collaborators treated SWCNTs with sec-butyllithium to create an initiator for the anionic polymerization of styrene [45]. This resulted in polystyrene grafted SWNTs prepared in a single-step.

Even though the covalent modifications of nanotubes (such as those previously mentioned) provide a means to incorporate these unique carbon structures into various applications, there is one major drawback. The downside is that covalent bond formation disrupts the native electronic structure of the tube.

Non-Covalent Functionalization

To modify carbon nanotubes, while retaining the original electronic structure, non-covalent functionalization can be used. Non-covalent modifications are particularly important when pursuing applications that exploit the unique electronic properties of CNTs. This electronically mild functionalization normally occurs via van der Waals forces between the tubes and surfactants, planar aromatics (such as pyrene), or by helical wrapping by polymers around the tube [41].

Surfactants (anionic, cationic, or non-ionic) and diblock copolymers (hydrophilic:hydrophobic) are often used to solubilize both multi-walled and single-walled carbon nanotubes in water [38]. Specifically, this can be achieved with the use of the ionic surfactant, sodium dodecyl sulphate (SDS), which coats the CNT, transfers charge to the tube surface and disperses the tubes in water by

electrostatic forces. This dispersion can be performed by addition of 1% SDS to an aqueous suspension of CNTs followed by ultrasonication. Other surfactants used to solubilise CNTs include the use of triton-X-100 with sodium dodecyl benzene sulphonate (SDBS) and a poly(acrylic acid)-CTAB (hexadecyltrimethylammonium bromide) complex to form a lamellar structure on the surface of MWCNTs [46].

Small molecules have also been used to bind non-covalently to the surface of nanotubes. One of the first research groups to try this was that of Hongjie Dai in 2001. Dai's group used a pyrene derivative to form π - π interactions between the π -orbitals of the planar pyrene and those of the CNT sidewall [47]. Other groups have used various heterocyclic polyaromatic molecules, such as porphyrins and phthalocyanines to modify the tube surface through van der Waals interactions.

Another method to functionalize CNTs without covalent bonding is by polymer wrapping. An example of this was performed in 2001 by Smalley's group, who used polyvinyl pyrrolidone (PVP) and polystyrene sulphonate (PSS) to solubilize SWCNTs [48]. This work provided a great example of how polymers are used to helically wrap around the nanotube surface to aid in the tubes possible application.

1.4.2 Polymer/Carbon Nanotube Composites for Photovoltaic Cells

Many research groups have made efforts to harness the advantageous electronic and structural properties of CNTs in PSCs. The acceptor, which must have greater electron affinity than the polymer, can be replaced by single-walled, double-walled or multi-walled nanotubes. CNTs have high surface area which provides an ideal morphological architecture for exciton dissociation. Furthermore, the nanotubes' high aspect ratio (>1000) allows for the creation of percolation pathways at low doping levels and thus provides a means for high carrier mobility and efficient charge transfer to the appropriate electrodes.

SWNTs were first used as the acceptor in the PSC's BHJ by Kymakis and Amaratunga who blended poly(3-octylthiophene) (P3OT) with 1 weight % nanotube [49]. The performance of the solar

cells was increased with respect to the open circuit voltage (V_{OC}) and short circuit current density (J_{SC}). This variation to the PSC introduced internal polymer:nanotube junctions, which allowed for exciton dissociation, and a continuous path for electron transport to the cathode. The semiconducting SWCNT has a n-type character [50] and the ability to promote charge separation and electron transport. Low efficiencies of SWCNT based solar cells can be associated with a few factors such as the presence of metallic SWCNT that short-circuit the cell (reducing the shunt resistance), impurities (mostly metal catalyst residue), SWCNT aggregation, and low charge carrier mobility in the polymer matrix. Ab initio calculations have been used to evaluate the electron charge transfer ability in such polymer–CNT heterojunctions [51]. It was found that only semiconducting SWNTs can favour the electron charge transfer. It is clearly possible to predict V_{OC} from the heterojunction energy band diagram deduced from this study which has shown that it remains very low (0.3 V) even in the most favourable configuration (with the polymer chain parallel to the CNT). This result is compatible with the experimentally measured V_{OC} for such P3HT:CNT heterojunctions [49]. Conversely, high charge transfer ability has been experimentally evidenced on nano-planar heterojunction structures consisting of highly oriented and isolated SWNTs grown by chemical vapour deposition parallel to the substrate on which was deposited a P3HT layer [52]. A heterojunction based on SWNT and P3HT was estimated to yield 3% efficiency with a surprisingly high V_{OC} of 0.5 V. This higher V_{OC} was obtained with an n-type SWNT doped by prior coating with polyethylene imine, shifting the Fermi level close to the LUMO level. The authors attributed their nano-device performance, 50–100 times higher than those obtained in P3HT:CNT blends, to the fact that no CNT aggregation was present to create a CNT:CNT junction which would hinder the effect of the isolated CNT:P3HT junction. Thus a perfect CNT dispersion in the polymer matrix seems to be mandatory for efficient devices.

Nogueira and colleagues tried to mitigate some of these potential problems by the covalent functionalization of SWCNT ends and defects with thiophene moieties [53]. The thiophene pendent groups were used to increase the dispersion of the tubes in a P3OT matrix. As eluded to previously, it

is critical that the nanotubes are dispersed homogeneously throughout the polymer matrix to achieve an optimized interfacial area for charge transfer. Hümmelgen and colleagues also used a P3OT:SWCNT composite to prepare a solar cells that reached power conversion efficiencies of 1.48% under 15.5 W/m² light [54]. The solar cell had a CNT composite layer deposited on a polybithiophene layer between the two electrodes. Pal and coworkers also used two layers within their photovoltaic devices [55]. The solar cells produced by their group had a C₆₀ layer vacuum evaporated on a spin coated MWCNT:P3HT composite. The nanotubes were used to aid in exciton dissociation and extract charges toward the ITO electrode. Fullerenes were also used by Mitra and coworkers to functionalize SWCNTs for their incorporation into a P3HT composite to be used as the active layer in a BHJ solar cell [56]. There was an improvement in both the I_{SC} and FF by taking advantage of the accepting nature of fullerene and the charge transport capability of SWNTs. Likewise, polymer photovoltaics that used CNT:P3HT composites were studied by Arranz-Andrés and Blau who used SWCNT, DWCNT, and MWCNT [57]. It was found that the CNTs induced local order of the polymer chains and that there was an increase in the power conversion efficiency (PCE), V_{OC}, I_{SC}, and FF when compared to cells without CNTs.

The carbon nanotubes within the cell should ease exciton dissociation and make charge extraction more efficient. Ternary blend composites of CNT:P3HT:PCBM were used as the active layer in BHJ cells prepared by Berson and fellow researchers [58]. They prepared dilute solutions of single- and multi-walled carbon nanotube solutions which they added to solutions of P3HT and PCBM. This ternary blend, dissolved in chlorobenzene, was spin coated to prepare the thin film active layer in various photovoltaic devices. A power conversion efficiency of 2.0% was achieved with a 1:1 P3HT:PCBM solution with 0.1 weight % MWCNTs. It was found that thermal treatment of the D-A layer was necessary to ensure high current density. The thermal annealing of the BHJ active layer produces a nanostructured morphology that reduces charge carrier recombination that can occur in the polymer composite (due to the proximity of the donor and acceptor). The polymer:CNT solutions used

to prepare the BHJ thin film must be stable and free of CNT aggregates. This is successfully achieved with conjugated polymers whose chains interact with the nanotubes via π - π stacking.

When single-walled nanotubes are used as the acceptor in the BHJ internal polymer:nanotube junctions are present which allow for the photoinduced electron transfer from the polymer to the SWNT. Kymakis and colleagues who used SWNTs as an acceptor with P3OT found that the solar cell's had an increase photoresponse and that the photocurrent increased by more than two orders of magnitude [59], [60]. The introduction of SWCNTs ensured that a bi-continuous network was present for the electrons and holes to travel to their respective electrodes. The internal electric field created within the BHJ causes the excitons to dissociate into electrons and holes which travel in opposite directions. The free holes travel through the polymer to the anode and the free electrons travel to the cathode through the nanotubes. The nanotubes' presence within the BHJ layer is critical to achieve ordered phase segregation and self-organization of the bi-continuous internal pathway. Doping of the P3HT:PCBM BHJ active layer with esterified SWCNTs (about one ester per 50 carbon atoms) was performed and resulted in an increased J_{SC} owing to improved ordering of the material [61]. Moreover, V_{OC} was also increased, thus breaking down the currently admitted necessary reduction of V_{OC} related to interface polarons or built-in field.

Significant improvement of the J_{SC} of P3HT:PCBM solar cells has been obtained by the Plastic Optoelectronics Group at the University of Limoges, by adding a small amount (0.1 wt%) of SWNTs in the solution and performing the orientation of the tubes during the annealing process [62]. The initial average cell efficiencies before annealing, around 2.5%, was enhanced to 4.4% with the application of a 10 MHz electric field. The improvement was attributed to the perpendicular orientation of the CNTs relative to the electrodes. Moreover it was found that doping the polymer matrix with CNTs increased the absorption of the composite film.

Considering the ability of CNTs to provide percolation pathways for the photogenerated charges in PSCs, there remains some speculation about what type of charge will be carried by the tubes.

For example, it has been established that neat SWCNTs carry holes [63] and that doping the CNTs with boron or nitrogen improved either the hole or electron transport respectively in P3HT:PCBM:f-SWNT BHJ solar cells [64]. Remarkably, the authors were able to balance the electron and hole mobility with B-doped CNTs, resulting in an increased V_{OC} , J_{SC} and an improvement in the PCE from 3% to 4.1%. Doping CNTs with C_{60} by chemical or microwave grafting methods to enhance electron transport was also successfully demonstrated [56].

In summary, it has been shown that by incorporating CNTs in BHJs, one can improve the polymer organization [65], charge transport, and mobility balance by providing selective hole or electron pathways. Additionally, electric field orientation and migration of the CNTs can be achieved to reinforce the above effects. Thus, an ideal polymer:PCBM:CNT layer should consist of electric field aligned and well dispersed functionalized SWNTs which provide an interdigitated structure perpendicular to the electrodes. Ideally, the electrons and holes could be driven respectively by selectively n or p-type doped CNTs, which with electric field migration (orientation) of the electron-carrying CNTs to the cathode and of the hole-carrying CNTs to the anode will improve charge collection by forming ohmic contacts with the electrodes.

1.5 Printable Photovoltaics

As previously noted, polymer photovoltaics have the potential to provide the means to achieving low cost, flexible and light weight solar cells. The current state of polymer solar cell research is promising although it lacks the industrial scale up which is necessary for the large scale production. The industrial benefit of polymer solar cells is that they can be manufactured via existing solution based printing techniques. The printing of a uniform polymer film can be performed in a number of different ways and these vary between those used for small scale tests in the lab and those used for high volume production. Common film forming techniques in the lab include spin coating, doctor blading and casting. For high volume processing it is possible to use coating techniques such as slot-die, gravure,

knife-over-edge, off-set and spray coating [66]. For enhanced processing detail, printing techniques can be used which include pad, screen and inkjet printing. Inkjet printing can not only be used for the fabrication of organic solar cells, but it can also be used for the fabrication of thin-film transistors (TFTs), light emitting diodes (LEDs), contacts and conductive structures, memory and magnetic applications, sensors and detectors, biological and pharmaceutical application and patterning (e.g. reactive etching) [67]. Moreover, inkjet printing is a useful fabrication technique for polymer solar cells as it provides a fabrication method that is highly precise with a high production rate, silent, non-impact, fully electronic operation, an additive process (ability to print multiple layers) and also preserves the solutions as the material is only dispensed when necessary [68].

One of the main challenges to be solved is the control over the inks rheological properties. These properties are specific to the desired printing method and therefore must be tuned to meet the correct specifications. In general, for inks to be compatible with the inkjet print head they must have a low viscosity (1-30 mPa*s) as well as a low surface tension (30-40 mN/m) [69]. It has been specified by other groups working with inks for inkjet printing of electronics that the viscosity range is narrower and should lie between 8-15 mPa s and that the surface tension should range from 25-35 mN/m [70]. There is an inevitable balance between ink viscosity and surface wetting to prepare pinhole-free polymer films and to avoid inks that spray from the nozzles if the viscosity is too low. Also, if the surface tension is too high droplet formation will be too difficult to occur.

An inkjet printer normally uses a piezoelectric drop on demand (DoD) print head containing numerous nozzles which depends on the size of the head. The piezoelectric DoD controls jetting by a voltage pulse that deforms the piezoelectric actuator in the ink cavity causing a volume change. The drop is subsequently ejected from the nozzle due to the pressure wave that overcomes the surface tension at the ink/air interface. Not only are the rheological properties of the inks important, but other relevant parameters to consider during ink formulation are the compatibility of the ink with the substrate, volatility and surface energy. The droplet-substrate interaction will not only affect the contact

angle and wettability of the drop but also it is important to use orthogonal solvents to prevent dissolution of other printed layers. The behaviour of the drop after it is released from the nozzle and after it contacts the substrate is crucial in forming a uniform thin film. This can have an effect on the molecular ordering of the polymer layer which will control the film's charge transport properties. Furthermore, using a mixture of solvents that solubilise the solutes within the ink and that have different boiling points can not only influence the rheological properties of the ink but will also have an impact on the morphology of the dried film.

1.5.1 Inkjet printable films in polymer solar cells

To print an inverted polymer solar cell via inkjet printing, it is necessary to print sequential layers using orthogonal solvents. In a standard inverted device architecture, four layers can be printed on an inert substrate coated with a transparent conductive electrode (e.g. ITO). These layers include the electron transport layer (e.g. ZnO), the photoactive layer (e.g. P3HT:PCBM), the hole transport layer (e.g. PEDOT:PSS), and the silver back contact electrode.

Electron Transport Layer (e.g. ZnO)

The electron transport layer separates the active layer from the cathode and aids in the transport of electrons and the blocking of holes. Materials that can be used to prepare the electron transport layer include zinc oxide (ZnO) [71], titanium oxide (TiO_x) [72], titanium dioxide (TiO_2) [73], and cesium carbonate (Cs_2CO_3) [74]. Thus far, one of the most universally used materials is zinc oxide.

Zinc oxide has a valence band at -7.7 eV and a conduction band at -4.3 eV which allows for the transport of charge from the lowest occupied molecular orbital (LUMO) of [6,6]-phenyl-C61-butyric acid methyl ester (PC_{60}BM) which lies at -3.8 eV. The ZnO then in turn is able to transport the electron to ITO (transparent cathode) which has a work function at 4.7 eV. A uniform zinc oxide layer can be deposited by several methods, although there are restrictions for large scale inkjet deposition.

Small scale deposition techniques of the oxide layer include ion-beam sputtering (IBS) and spin casting. Deposition of this electron transport interfacial layer via IBS provides a well-controlled deposition rate at room temperature, which is excellent for bench mark tests on plastic substrates. Two examples of IBS sources include electron cyclotron resonance (ERC) and radio frequency (RF), both of which were used for bench mark devices on glass and plastic in this study. The benefit of the RF IBS source was that it allows for large area, low temperature deposition of a uniform metal oxide film.

Another method for the deposition of a zinc oxide layer is via a solution processing technique that uses a solgel. The solgel is deposited using spin coating and then annealed at 300 °C in air to form zinc oxide. Initial ZnO solgel solutions used in this study comprised of zinc acetate ($Zn(O_2CCH_3)_2$) dissolved in 2-methoxyethanol:ethanolamine (96:4) [75]. The major disadvantage to the use of this solgel (surface tension = 31.6 mN/m) is the high temperature annealing necessary to form the oxide film.

For a solution processable ZnO layer that is compatible with plastic substrates the high temperature annealing step must be circumvented. To accomplish this, a ZnO nanoparticle dispersion was used.

Active Layer (e.g. *P3HT:PCBM*)

A commonly used active layer that has previously been printed via inkjet printing is comprised of poly(3-hexylthiophene) (P3HT) and PCBM. As previously mentioned the P3HT is responsible for photon absorption/exciton generation and the PCBM aids in exciton dissociation and transportation of the electron towards the cathode. To prepare an ink for inkjet printing it is important that the solution adheres to the desired rheological properties and also has solvents that aid in the desired morphology of the active layer upon evaporation.

Several research groups have attempted Inkjet printing with P3HT:PCBM solutions using solvents that include chlorobenzene [76], chlorobenzene:1,8-octanedithiol (95:5) [76], chlorobenzene:1,2-dichlorobenzene (95:5) [76], chlorobenzene:1-chloronaphthalene (95:5) [76],

chlorobenzene:tetralin (1:1) [77], chlorobenzene:1,2,4-trichlorobenzene (55:45) [78], tetralin [67], [79], 1,2-dichlorobenzene [67], 1,2-dichlorobenzene:mesitylene (2:1) [67], [79], [80], and 1,2-dichlorobenzene:chloroform (1:1) [80].

Hole Transport Layer (e.g. PEDOT:PSS)

As the name implies, the hole transport layer (HTL) functions to transport positive charge between the active layer and the anode. In an inverted cell with a silver back-electrode, the HTL transfers the hole from the polymer (along its HOMO – valence band) to silver. Common materials used as the HTL include poly(3,4-ethylenedioxythiophene):poly(styrenesulfonate) (PEDOT:PSS) [76], sulfonated poly(thiophene-3-[2-(2-methoxyethoxy)ethoxy]-2,5-diyl) (S-P3MEET) [81], tungsten oxide (WO_3) [82], molybdenum oxide (MoO_3) [82], and vanadium oxide (V_2O_5) [82], with valence band energies at -5.2 eV, -5.35 eV, -5.3 eV, -4.7 eV respectively [83]. Although difficult to print due to many factors including coagulation, solutions of PEDOT:PSS have potential for large area printing applications. Other alternatives include molybdenum oxide [84] and tungsten oxide [85] solutions, similar to the ZnO solution processed films, that involve low temperature annealing.

Top Electrode

The top electrode (a.k.a. back electrode) of the polymer solar cell can either act as a cathode or an anode depending on the interfacial layers within the cell. The common back electrode for normal cells is aluminum which has a work function of 4.1 eV. The low work function provides problems for device lifetimes due to its ease of oxidation. To avoid this problem silver is used which has a work function of 5.0 eV. Another benefit with the use of silver is its printing possibilities. There are many silver nanoparticle inks available on the market that are compatible with inkjet printing and in which appropriate conductivities can be reached with low temperature annealing.

1.6 Research Objectives

This research project will be divided into two themes: (1) doping PSCs with functionalized SWCNTs; and (2) colour-tuning the active layer through the use of ternary blends (polymer:polymer:PCBM). These two approaches will be pursued to achieve increased control over properties of the photo-active layer (PAL) in solution processed PSCs.

1.6.1 CNT-doped PSCs

As previously mentioned, it has been shown that incorporating CNTs in BHJs, one can improve the polymer organization [65], charge transport, and mobility balance by enhancing free charge carrier transport. With this in mind and to produce devices on the large scale with a reduced cost, we wish to improve PV device performance without having to alter the active layer materials.

In this study, the SWCNTs will be functionalized with alkyl chains to increase their dispersive properties in solution, increase their interaction with the P3HT polymer matrix, and to disrupt the metallic characteristic of the tubes, which ensures that the incorporated SWCNTs are primarily semi-conducting. Two varieties of SWCNTs will be purchased for the study (BuckyUSA and Unidym) and functionalized with three linear aliphatic primary alcohols (1-decanol, 1-dodecanol, and 1-tetradecanol) through an esterification reaction. Furthermore, linear chains were chosen to reduce steric disruption of the P3HT matrix. After characterization of the functionalized CNTs, the P3HT:PCBM:CNT composite films will be characterized and used as the photoactive layer within the inverted solar cell. The goal is that improved charge transport will allow high level PSC performance as the active layer thickness and area are increased, which is an important consideration for large-area inkjet printing.

1.6.2 Colour-tuned ternary PSCs

Even though low-cost synthetic routes for the mass production of conjugated polymers is being explored [86], a potential solution to achieve low-cost colour-tuned PSCs is through the use of ternary

blend active layers. This route to colour-tune PSCs was found to be very attractive for DisaSolar as it is a method to provide clients with many design options while maintaining low costs.

To attain this goal, the photo-active layer of the PSC will be prepared by blending two donor polymers and an acceptor (e.g. PCBM), with the goal of forming a parallel-like bulk heterojunction (PBHJ) PSC [18], [19], [33]. As previously addressed, in an efficient PBHJ blend, the V_{oc} lies between the V_{oc} of the individual sub-blends whereas the current density is a sum of the blends. In this manner, efficient ternary blends should provide a route for colour-tuned printable PVs while limiting the number of active layer materials.

Specifically, dual donor polymer ternary blend (D1:D2:A) solar cells made from a selection of three donor polymers and PCBM will be prepared on flexible plastic substrates. Furthermore, the goal of the study will be to: 1) tune the devices' colour without a large efficiency loss, and 2) provide evidence of limiting factors involved in the performance of dual donor:acceptor polymer photovoltaics. For the D1D2:A blends, three complimentary polymers (red, blue, green) were chosen: G1 (green), B1 (blue), and P3HT (red), based on availability determined by DisaSolar (Limoges, France). Unfortunately, the chemical structure and supplier of the two low band gap polymers (B1 and G1) is restricted and must remain unknown in accordance with the confidentiality requirements of DisaSolar and their partners. Blends of various concentrations will be analyzed in terms of colourimetry by reflectance, absorption, and fluorescence spectroscopy. The J(V) characteristics, external quantum efficiency (EQE) and photogenerated current vs. light intensity and bias polarization studies will be used to investigate the photovoltaic and charge transport properties of the blends. Additionally, equivalent circuit modelling will be implemented to provide further evidence of a parallel BHJ mechanism in the ternary blends.

Chapter 2

Experimental

2.1 Materials

Tetrahydrofuran (THF), diethyl ether, hexanes, and toluene were purchased as dry solvents stored over molecular sieves from Sigma-Aldrich. 1-decanol, 1-dodecanol, and 1-tetradecanol were used and received from Sigma-Aldrich. Dichloromethane, *o*-dichlorobenzene, chlorobenzene, bromobenzene, hexanes, ethyl acetate, dimethyl sulfoxide (DMSO), N, N-dimethylformamide (DMF), ethanol, methanol, diethyl ether (for extractions), acetone, and aqueous HCl and H₂SO₄ were used as received from Fisher.

Single-walled carbon nanotubes (SWCNTs) were used as received from Unidym (grade: P0901) and BuckyUSA (SWCNT 90). The 99% pure PC₆₁BM was purchased from SES Research (now Nanos Research).

2.2 Instruments

Optical absorption spectra were determined on an HP 8542 diode array spectrophotometer or a SAFAS200 spectrophotometer. Fluorescence measurements were primarily detected with an Edinburgh Instruments FLS980 Photoluminescence Spectrometer, but an USB2000-Ocean Optics Spectrometer was also used. Colorimetry of the polymer films was conducted via reflectance spectroscopy using an Agilent Cary 300 spectrophotometer. The thickness of evaporated films were controlled by a quartz crystal monitor and measured using a Bruker DektakXT. The film morphology was analyzed by non-contact mode Atomic Force Microscopy (AFM: CSI Nano-Observer).

The J-V characteristics were recorded in a glove box (N₂ atmosphere) with a computer-programmed Keithley 2400 source under simulated AM1.5 solar irradiance (100 mW/cm²) which was calibrated using a standard silicon solar cell. The short-circuit photocurrent spectra proportional to IPCE

(Incident Photon-to-Electron Conversion Efficiency; External Quantum Efficiency (EQE)) of the solar cells were taken under illumination from a TS-428 Acton 250 W tungsten halogen lamp supplied by a JQE 25-10M Kepco voltage unit and monochromated by an Acton SpectraPro 2150i at a 80 Hz chopping frequency. The photocurrent was detected by a Stanford Research SR530 lock-in amplifier and compared to the signal obtained under the same illumination conditions by a Hamamatsu large area photodiode whose spectral response is given by the manufacturer.

2.3 Carbon nanotube functionalization

Single-walled carbon nanotubes (sourced from two manufacturers) were functionalized with three varying lengths of carboxylic side chains: decanoic (10Cs), dodecanoic (12Cs) and tetradecanoic (14Cs) acid substituents. The single-walled carbon nanotubes in this study were purchased from both Bucky USA and Unidym. For esterification, the SWCNTs underwent four steps, starting with a nitric acid purification to remove residual metal catalyst prior to the carboxylation and esterification steps of the synthesis. The reaction scheme is shown in Figure 2-1, which follows a similar method used by Bergeret *et al.* [87].

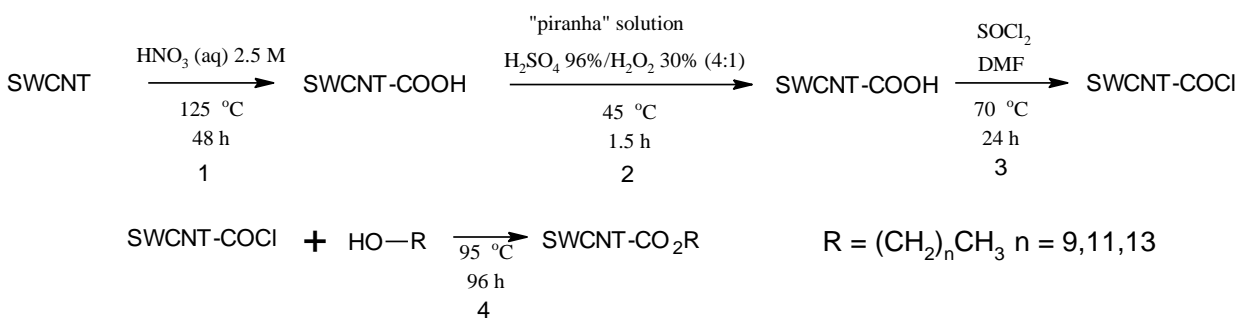


Figure 2-1 Reaction scheme for the esterification of single walled carbon nanotubes.

2.3.1 Purification of single-walled carbon nanotubes (step 1)

To ensure purity, the SWCNTs (250 mg) were stirred in 250 mL of 2.5 M nitric acid (aq.) at 125 °C for 48 h in a round bottom flask fit with a reflux condenser. After the oxidizing acid reaction mixture was cooled to room temperature, the mixture was vacuum filtered through a polyvinylidene fluoride (PVDF) millipore membrane (0.22 μm), then washed with distilled water (until filtrate was neutral), 5 mL of 0.001 M NaOH (aq.), and finally another 100 mL of distilled water. The remaining black solid was dried in a vacuum overnight at 70 °C, resulting in a 75 % yield (188 mg).

2.3.2 Carboxylation of SWCNTs (step 2)

In the previous step, the CNTs were purified of their metal catalysts and underwent a degree of oxidation. However, in this step, further oxidation is carried out. The purified SWCNTs (188 mg) were added to 150 mL of freshly prepared “piranha solution” (conc. $\text{H}_2\text{SO}_4:\text{H}_2\text{O}_2$ 30%, 4:1) which was cooled in an ice bath. The mixture, which was stirred in a round bottom flask fitted with a reflux condenser, was vigorously stirred at 45 °C for 1.5 h. After cooling to room temperature, the reaction mixture was carefully poured into an Erlenmeyer flask containing 150 g of ice. After cooling for 15 minutes, the mixture was vacuum filtered through a PVDF (0.22 μm) Millipore membrane and washed with 500 mL of distilled water. The remaining black solid was dried in a vacuum overnight at 70 °C, resulting in a 86 % yield (160.8 mg). It is recommended that solid state Fourier transform infrared spectroscopy (FT-IR) be performed on the carboxylated CNTs to ensure the presence of relevant functional groups.

2.3.3 Acyl chloride functionalized SWCNTs (step 3)

The carboxylated SWCNTs (160.8 mg) were stirred in 3 mL of DMF in a round bottom flask (with reflux condenser) under argon gas. To form the acyl chloride, thionyl chloride (SOCl_2 , 15 mL) was added dropwise via syringe. The reaction mixture subsequently stirred at 70 °C for a 24 hour period.

After cooling to room temperature, the mixture was vacuum filtered through a PVDF (0.22 μm) Millipore membrane and washed with anhydrous THF (3 x 15 mL). The remaining black solid was dried in a vacuum overnight at 80 °C, resulting in a 94 % yield (150.8 mg).

2.3.4 Esterification of SWCNTs (step 4)

In a flame dried round bottom flask (with condenser) containing the dried SWCNT-COCl black solid (150.8 mg), R-OH (~ 15 mL) was added in excess. Subsequently, the reaction mixture was stirred at 95 °C for 96 h under Ar (g). After cooling to room temperature, the mixture was vacuum filtered through a PVDF (0.22 μm) Millipore membrane and washed with ethanol (warmed to 60 °C). The filtered black solid was removed from the filter membrane and dried under high vacuum to produce the desired esterified SWCNTs (SWCNT-CO₂(CH₂)_nCH₃) (170 mg). This four step procedure, results in an overall average crude product yield of 66%. Note, it is recommended that the FT-IR spectra of the CNTs following carboxylation (step 2) be compared to the esterified product (step 4). This is done to ensure that the majority of the carboxylic acid moieties have been converted to the ester.

2.4 Solar Cell Fabrication Methods

2.4.1 Etching of indium tin oxide (ITO) layer

The first step in preparing a bulk-heterojunction solar cell is to etch the ITO substrate (transparent and electrically conducting). Glass and plastic substrates were purchased that have a thin layer of ITO deposited on one side. To avoid short circuits in the completed solar cell the ITO electrode needed to be etched. Firstly, the desired ITO etching surface was masked with masking tape to produce the negative of the intended design. Subsequently, a resin (nail polish) was coated over the exposed surface to mask the ITO for etching (Figure 2-2). Before completing resin deposition, the three

longitudinal (side A) strips of masking tape were removed so that a T pattern can be formed. Upon drying of the resin, the remaining five strips (side B) of masking tape were removed.

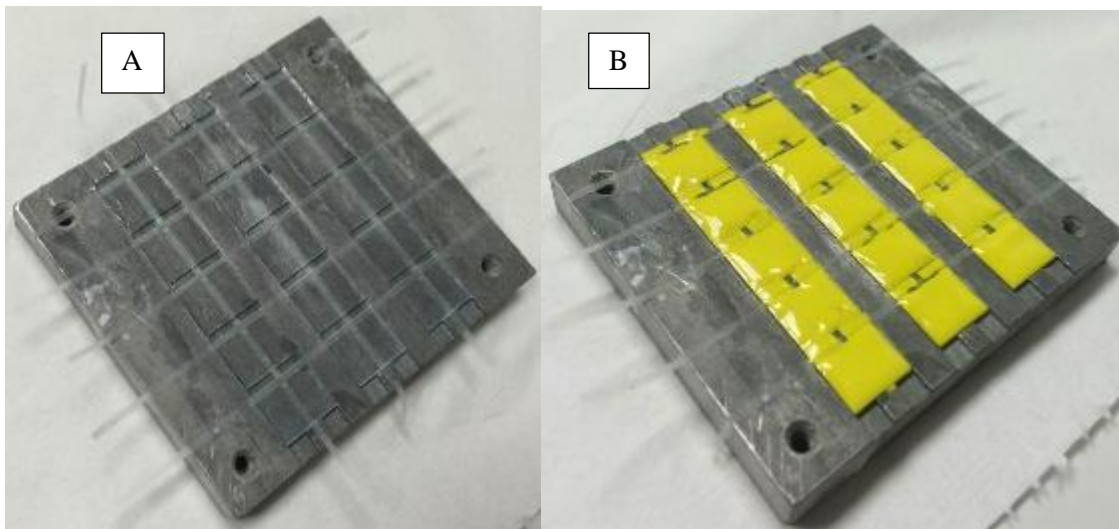


Figure 2-2: Masking of ITO film on glass or plastic substrates.

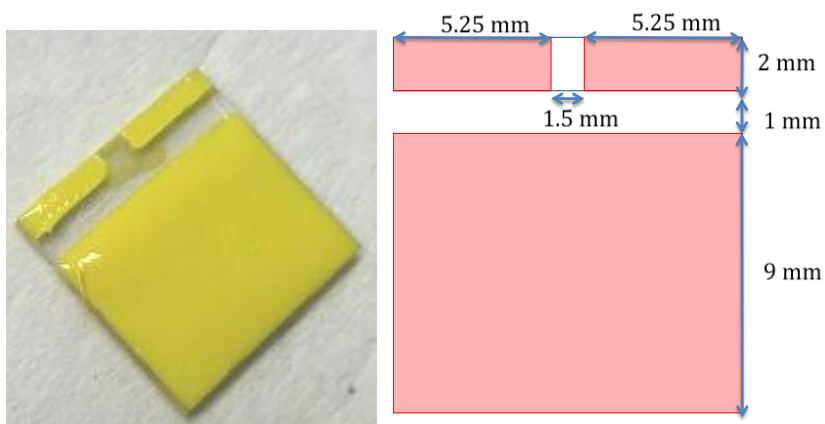


Figure 2-3: ITO mask (yellow) for etching on 12mm x 12 mm substrates and its corresponding dimensions.

The resin coated ITO substrates were placed in 2 M HCl (aq) heated to 90 °C for approximately 5 minutes. Subsequently, the slide was rinsed thoroughly with distilled water and then the masking resin was removed with acetone. The slide was washed with a cotton pad soaked in acetone then rinsed with iso-propanol and dried under a stream of nitrogen.

2.4.2 Preparation of polymer composites for BHJ active layer

2.4.2.1 Polymer and fullerene solutions

Solutions of polymer:fullerene derivatives were prepared using 1,2-dichlorobenzene as solvent (e.g. with 30 mg/mL P3HT and 24 mg/mL PCBM). Preparation of the active layer solution began by preparing solutions of the polymer and fullerene components separately. This was done to ensure that the solutes were well solubilized and to ensure homogeneity of the active layer. After the sub-components were well mixed, they were all blended together and stirred at 60 °C in the glove box.

2.4.2.2 Polymer, PCBM, and CNT solutions

Prior to the preparation of the polymer:PCBM:SWCNT solutions a CNT dispersion was needed. A single-walled carbon nanotube solution was prepared to ensure that the SWNTs were fully dispersed in the solvent and that the final polymer:PCBM:SWCNT would contain a precise CNT concentration. To achieve this concentration, SWCNTs (0.422 mg) were dispersed via sonication in 1,2-dichlorobenzene (20 mL).

Solutions of the P3HT were prepared using 1,2-dichlorobenzene:CNT as solvent (30 mg/mL). The solution was filtered with a 0.45 µm filter tip into a new vial that contained [C₆₁]PCBM (24 mg). The polymer:PCBM:SWCNT mixture was stirred constantly prior to use.

2.4.3 Solar Cell Fabrication

Inverted devices

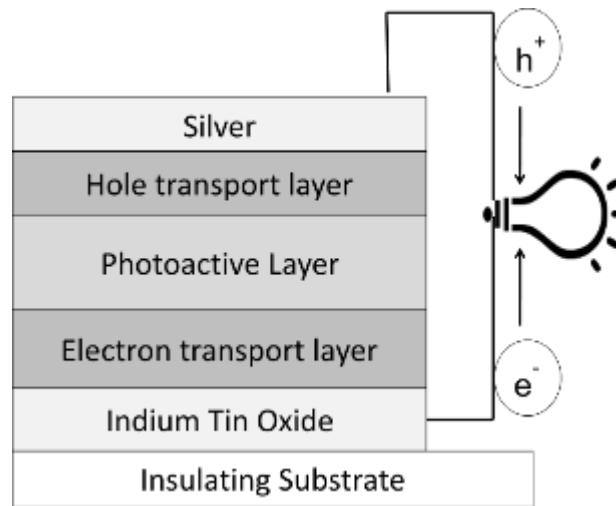


Figure 2-4: Polymer solar cell with silver back electrode.

Solar cell devices were fabricated using an inverted geometry on poly(ethylene terephthalate) (PET) substrates with ITO as the cathode and silver as the anode (or ITO/glass substrates). The devices were prepared with the following architecture: PET/ITO/ZnO/polymer:PCBM/PEDOT:PSS/Ag. Prior to device fabrication, ITO coated PET substrates ($12 \times 12 \text{ mm}^2$, $15 \Omega/\square$, VisonTek) were etched with HCl (aq) to prepare a substrate suitable for two 0.18 cm^2 rectangular electrodes. The etched PET substrates were sequentially cleaned by sonication in acetone, ethanol, and isopropyl alcohol followed by drying with a stream of nitrogen. After undergoing a UV/ O_3 treatment (10 mins) a thin layer of ZnO nanoparticles was spin coated (speed = 2200 rpm, acceleration = 2000 rpm/s, duration = 30 s) on the

substrates and then after the electrode contact edges were cleaned the film was dried on a hotplate at 115 °C for 15 mins in air.

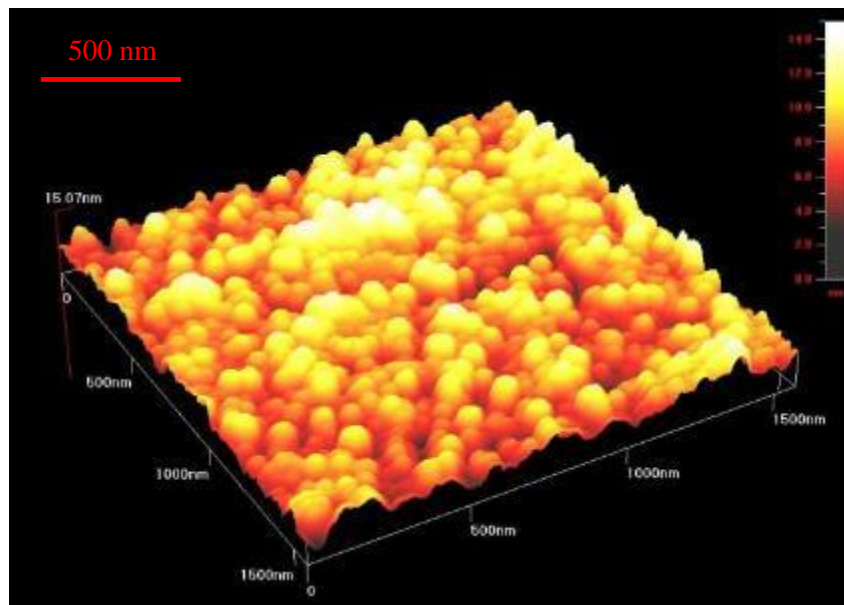


Figure 2-5: AFM image of a ZnO nanoparticle film deposited via spin coating.

In a nitrogen filled glove box, separate solutions of polymers and PC₆₁BM were prepared in 1,2-dichlorobenzene. After a UV/O₃ treatment (10 mins) of the ZnO film, the polymer:PC₆₁BM active layer was spin coated (speed = 1000 rpm, acceleration = 500 rpm/s, duration = 50 s) and dried at room temperature under an atmosphere of N₂ (g). After a low temperature annealing at 90 °C under N₂ to ensure the excess solvent has evaporated, a thin 20 nm film of PEDOT:PSS (Heraeus RD Clevious F010) was spin coated using a two-step process ((a) speed = 1500 rpm, acceleration = 200 rpm/s, duration = 23 s; (b) speed = 3000 rpm, acceleration = 300 rpm/s, duration = 25 s) in air, followed by a low temperature annealing under N₂ at 120 °C for 2 mins. The substrates were then placed in a vacuum chamber for silver deposition at approximately 10⁻⁶Torr. The silver electrodes (100 nm) were thermally evaporated onto the PEDOT:PSS film through a rectangular shadow mask with an area of 0.18 cm². After the plastic substrates were removed from the vacuum chamber, the excess polymer was removed

from surrounding the electrodes to ensure the active area was solely associated with the Ag back electrode.



Figure 2-6: Physical vapour deposition of the Ag electrode (left) and removal of the device from the shadow mask (right), prior to removal of excess polymer.

Chapter 3

Results and Discussion

3.1 Carbon Nanotube doped polymer solar cells

3.1.1 Functionalization of SWCNTs

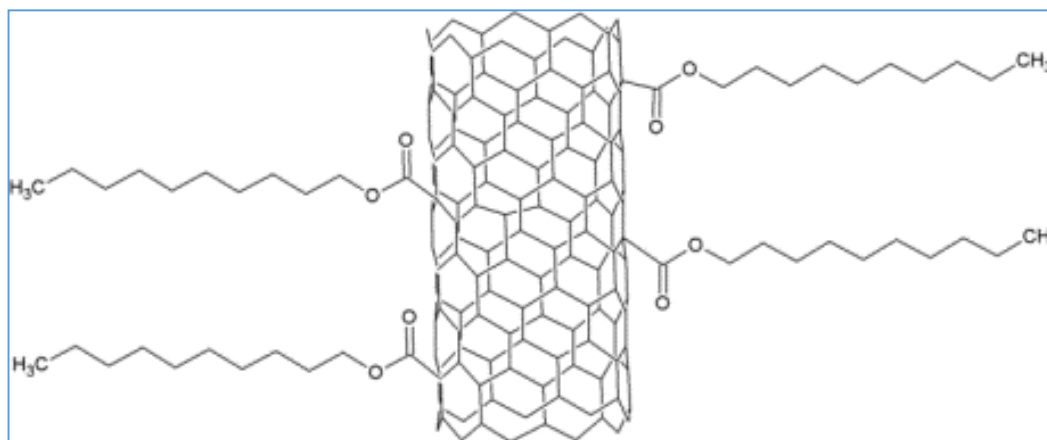


Figure 3-1: Representation of the functionalized SWCNTs.

Following the synthesis of the functionalized single-walled carbon nanotubes (SWCNTs), a thermogravimetric analysis (TGA) was performed to determine the degree of functionalization. For this analysis, it was necessary to ensure that all residual solvent and moisture was removed from the SWCNTs in a vacuum oven prior to the tests. Subsequently, to determine the degree of functionalization (DoF), the weight loss between 200 – 400°C was calculated as this represents the loss of sidewall functional groups (m_F). This weight loss is determined by calculating the relative weight loss for each sample (percentage of weight sublimed) and multiplying it by the mass of the dried CNT sample that was initially used for the analysis (~ 10 mg). For the DoF calculation, the moles of the carbon atoms in the side-chains equivalent to this weight loss was divided by the approximate moles of the initial number of carbon atoms in the CNT sample (m_i).

$$\text{DoF (\%)} = (m_F/MW_F) / (m_i/12 \text{ mg/mol}) * 100\% ; \text{ where } m_F = m_i * (\% \text{ weight loss})$$

The relevance of this weight loss can be seen by comparing the pristine CNTs to those that have been functionalized (Figure 3-2). Even though the pristine Unidym tubes show signs of step-wise solvent loss up to temperatures of 50°C, there is no significant loss between 200 - 400°C.

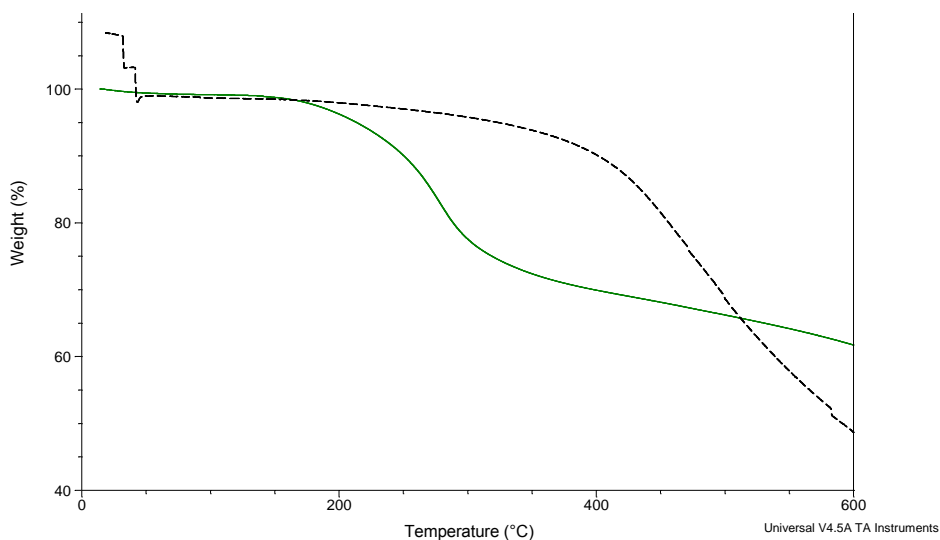


Figure 3-2: Comparison of unfunctionalized Unidym (black dotted line) SWCNTs with tubes that have been functionalized with decanoic acid (green solid line).

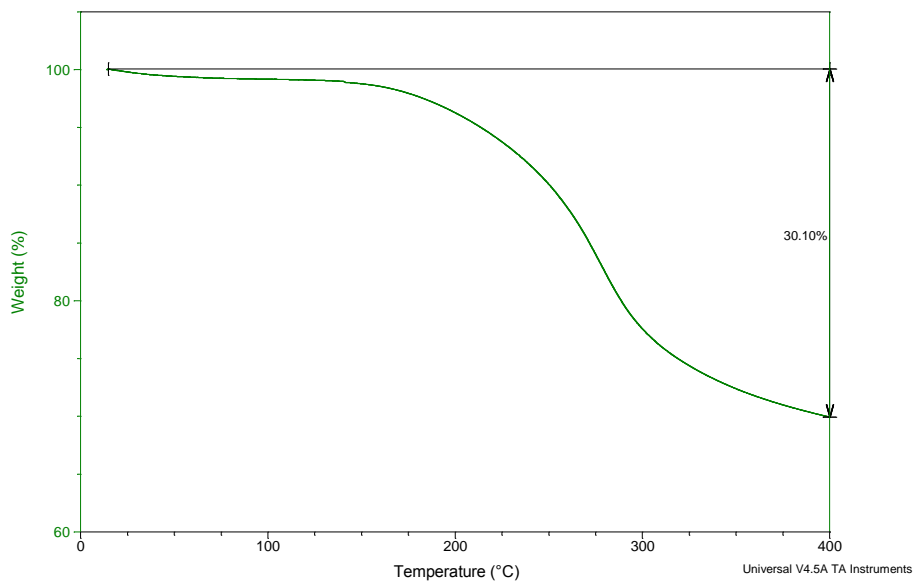


Figure 3-3: Thermogravimetric analysis of Unidym SWCNT's functionalized with decanoic acid. The TGA results show a 30.1% weight loss due to functional group degradation.

Specifically, this weight loss is associated with the degradation of the ester groups and un-esterified carboxylic acid moieties attached to the tube walls. A detailed investigation of the weight loss is presented in Figure 3-3, which shows a 30.1% weight loss from the loss of the tube's functional groups.

Table 3-1 presents a summary of the TGA results for all six varieties of functionalized SWCNTs. Unfortunately, since TGA is an irreversible destructive analysis only one trial was performed for each of the six different functionalized CNTs to conserve the product. Based on these findings, it is apparent that the CNT functionalization was dependent on the alkyl chain length. In fact, there is a clear correlation that as the alkyl tail length is increased, the DoF is decreased. For instance, the Unidym tubes with the R=10 functional group is 33% more functionalized than the tubes with R=12, and furthermore these tubes functionalized with R=12 have a DoF 23 % greater than the tubes functionalized with the R=14 alkyl chain. This variation and decrease of the DoF as chain length is increased can be attributed to the steric hindrance presented by the bulkier functional groups. It was also found that the Unidym tubes had an average DoF equivalent to 2.2%, whereas the BuckUSA tubes' DoF was 0.69%. This discrepancy in DoF may be attributed to the brand of purchased tubes' inherent reactivity which is associated with the tubes' diameter. With the Unidym tubes' slightly smaller average diameter (mean diameter = 1 nm), their reactivity was higher than those purchased from BuckyUSA (mean diameter = 1.1 nm), which is in agreement with the notion that increased strain of the sp^2 hybridized carbons, increases their relative reactivity.

Table 3-1: Degree of carbon nanotube functionalization (%) calculated by thermogravimetric analysis.

SWCNT supplier	Carbons in alkyl tail of ester functional group	TGA weight loss between 200°C-400°C (weight %)	Degree of functionalization (%) $n_{\text{ester}}/n_{\text{CNT}}$	CNT carbon atoms per ester group (approx.)
Unidym	10	30	2.8	36
BuckyUSA	10	11	0.80	125
Unidym	12	27	2.1	48
BuckyUSA	12	13	0.84	119
Unidym	14	25	1.7	60
BuckyUSA	14	8	0.43	233

3.1.2 Carbon-nanotube doped polymer films

Prior to solar cell fabrication, polymer active layer films were doped with the functionalized SWCNTs. This was done to investigate some of the properties that the carbon nanotube doping imparts on the polymer film. To investigate these properties, conductive atomic force microscopy (c-AFM) was employed to determine the average roughness and conductivity of P3HT:PC₆₁BM films doped with CNTs. For this investigation, the Unidym SWCNTs functionalized with a tetradecanoic acid moiety (R=14) were chosen to dope the P3HT active layer films. These nanotubes were functionalized with the longest alkyl chain moieties used in this study and showed a 1.7 % degree of functionalization. The P3HT:PCBM (30:24 mg/ml) films were doped with 0.25 wt% and 0.5 wt% f-SWCNTs (relative to P3HT) and compared to the neat active layer film. The films were cast from a 1,2-dichlorobenzene solution via spin coating onto clean ITO/glass substrates. It was found that the low level of CNT doping had little effect on the active layer films' roughness (topology), with all three P3HT:PCBM films having a RMS roughness of approximately 9 nm (over the 10 x 10 μm^2 sample). Although, as shown in **Table 3-2** there is a doping influence on the average conductivity, which was compared by determining the RMS current over the 100 μm^2 sample. The introduction of 0.25 wt% SWCNTs, increased the

conductivity of the film, exhibited as a current increase from 9 pA to 13 pA (+44%), and doubling of the amount of CNTs to 0.5 wt% increased this value to 19 pA (+111%). This illustrates that even though the low concentration of f-SWCNTs had an effect on the conductivity of the polymer film, they did not show significant disruption of the polymer films' topology. In summary, **Table 3-2** shows the topography and conductivity of the three films as determined by c-AFM.

Table 3-2: Influence of CNT doping (Unidym, R = 14) on P3HT:PCBM film's measured current. RMS roughness and current determined for a 10 x 10 μm^2 surface area.

CNT Concentration (wt. %)	Roughness (nm)	RMS current (pA)	Increase in current (%)
0	9	9	--
0.25	10	13	44%
0.5	8	19	111%

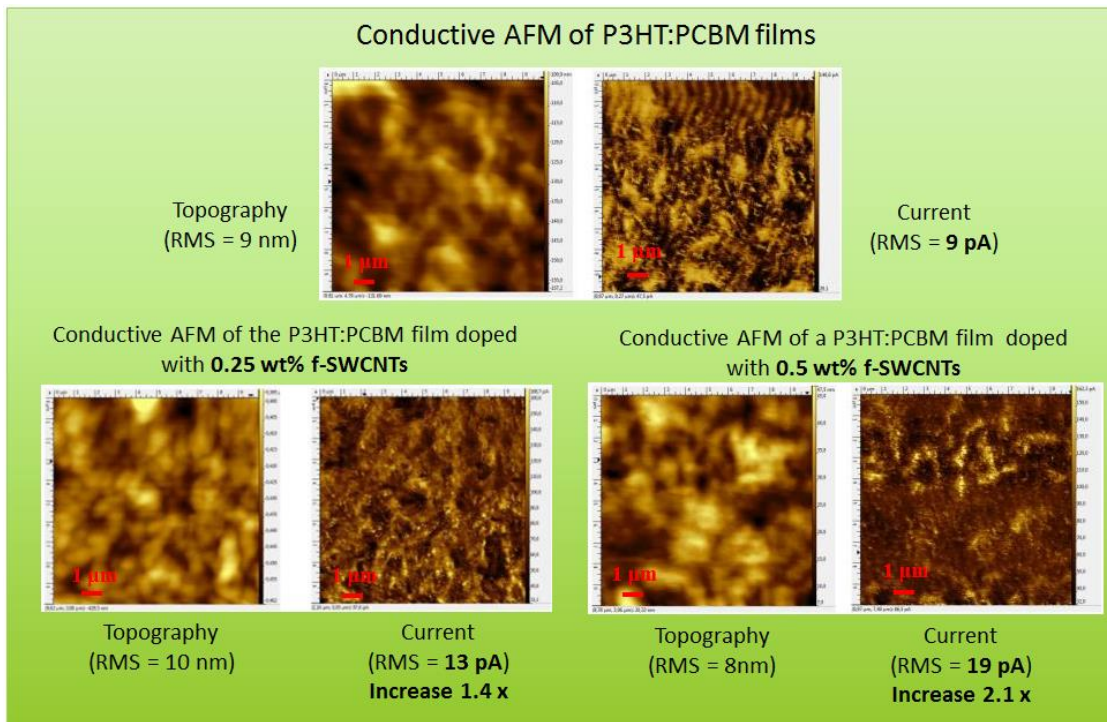


Figure 3-4: Comparison of c-AFM determined topography and current (relative to conductivity) of pristine and doped P3HT:PC₆₁BM films. Active layer films doped with 0.25 wt% and 0.5 wt% functionalized SWCNTs (Unidym, R = 14).

3.1.3 Carbon Nanotube-doped Polymer Solar Cells

Fabrication without SWCNTs

The cells fabricated in this study have provided preliminary results that provide insight into the photovoltaic activity of the prepared polymer composites (with and without SWCNTs). The devices were characterized to determine the overall efficiency (%) of each cell as well as the maximum power (P_{\max}), open-circuit voltage (V_{OC}), short-circuit current density (I_{SC}), and the cell's fill factor (FF).

The solar cell's PV function can be influenced by many factors that include the homogeneity of the cell layers, composition of electrodes, and most importantly the morphology of the active layer. Defects in the active layer film can significantly reduce the performance of a cell and can create short circuits or charge traps. Parameters that must be carefully controlled when forming the film via spin coating are solvent selection [88]–[97], concentration [98], rotation speed [99], and ratio of PCBM to polymer in the mixture [100]. With a variety of polymers it is very difficult to assume these parameters are consistent as each parameter will vary according to the polymer's physical and chemical characteristics.

Fabrication with SWCNTs

The characteristics of solar cells prepared with single-walled carbon nanotubes (SWNTs) exhibited relatively inconclusive yet promising results. For this evaluation, a P3HT:PC₆₁BM active layer was doped with 0.2 wt% functionalized SWCNTs (decane chains, R=10) in a glass/ITO/ZnO/active layer/PEDOT:PSS/Ag architecture (with a 0.18 cm² active area). Unfortunately, due to time constraints, CNT variety and concentration was not optimized for each of the *f*-SWCNTs. The results displayed in Table 3-3 display the similarity between the reference and doped devices. Although, contrary to our expectations of an improved photovoltaic performance, the lack of short circuits and reproducibility of the doped devices was promising. It was also found that the doping can increase the stability of a non-annealed device under constant illumination (results displayed in appendix and Figure 3-5). However, the results concerning stability are highly variable but do show

promise. In Figure 3-5, the results from an intensity study (constant illumination) with a P3HT:PCBM active layer doped with Unidym functionalized SWCNTs (R=10) is compared to a non-doped device. In this case, with non-annealed devices, the CNTs are able to preserve the J_{SC} within the device and increase the stability of the efficiency.

Table 3-3: Average results for non-doped and SWCNT-doped OPVs (12 devices each), with standard deviation in brackets.

Type	# of cells	V_{OC} (V)	J_{SC} (mA/cm ²)	FF (%)	η (%)	R_{ser} (Ω)	R_{sh} (Ω)
no CNTs	12	0.54 (0.04)	9.9 (1.2)	60 (6)	3.2 (0.7)	50 (17)	3386 (1088)
with CNT	12	0.53 (0.01)	9.9 (2.7)	56 (4)	2.9 (0.6)	49 (8)	2246 (818)

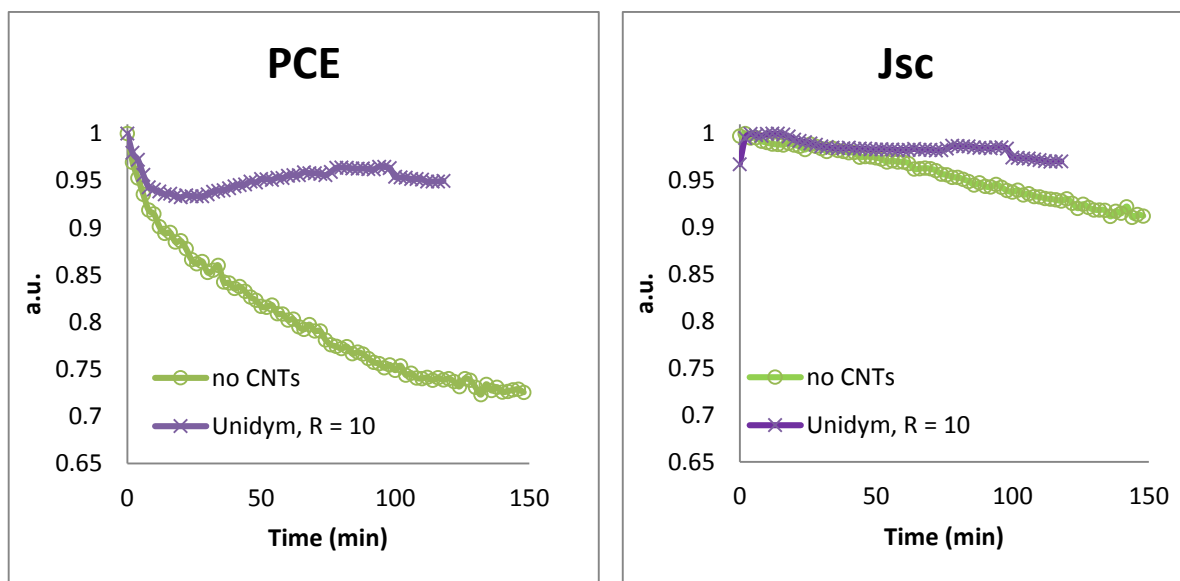


Figure 3-5: Evolution of the efficiency and J_{SC} of a non-doped and CNT-doped PSCs under constant illumination.

3.1.4 Inkjet printing of CNT-doped active layers

Even though a CNT-doped ink-jet printed active layer was not incorporated into a functioning PV device, initial steps were taken to pursue this vision. Along with other work performed for

DisaSolar, not included in this manuscript, this endeavor was not fully realized in order to pursue more pertinent avenues (i.e. colour-tuning).

Nonetheless, initial ink characterizations were performed on several different active layer inks with and without CNTs. In general, the results clearly indicate that the 0.1 wt% CNT doping did not affect the rheological properties of the active layer inks. Table 3-4 provides a summary of a collection of P3HT:PCBM active layer solutions and provides a comparison with inks containing 0.1 wt% CNT to P3HT and PCBM. (the weight % of the solute is provided in relation to the solvent mass).

Table 3-4: Rheological properties of a variety of active layer inks.

Solution	Viscosity (mPa s)	Surface Tension (mN/m)	Density (g/ml)	[P3HT] (mg/ml)
4% P3HT:PCBM(1:1) in chlorobenzene:mesitylene (2:1)	5.03	29.5	1.08	18
4% P3HT:PCBM(1:1) in chlorobenzene:toluene (9:1)	1.86	36.2	1.14	21
2% P3HT:PCBM(1:1) in 1,2-dichlorobenzene	2.26	43.96	1.42	13
2% P3HT:PCBM(1:1) In 1,2-dichlorobenzene:mesitylene (2:1)	1.92	39.8	1.29	11.5
2% P3HT:PCBM(1:1) In chlorobenzene:1,2,4-trichlorobenzene (9:1)	1.51	36.0	1.18	11.5
2% P3HT:PCBM(1:1) in 1,2-dichlorobenzene:1,2,4-trichlorobenzene (9:1)	2.72	47.13	1.47	13.2
With CNTs				
3.4% P3HT:PCBM(1:0.8):CNT (Unidym R= 10) chlorobenzene:1,2-dichlorobenzene (47:53)	2.84	34.31	1.19	23.2
3.4% P3HT:PCBM(1:0.8):CNT (Unidym, R = 14) chlorobenzene:1,2-dichlorobenzene (47:53)	2.87	35.63	1.22	23.4
3.4% P3HT:PCBM(1:0.8):CNT (Unidym, R = 12) chlorobenzene:1,2-dichlorobenzene (47:53)	3.06	35.02	1.16	23.2
3.7% P3HT:PCBM(1:0.8):CNT (Unidym, R = 10) chlorobenzene:1,2-dichlorobenzene:tetralin (47:33:20)	3.10	36.20	1.12	23.3

To investigate the feasibility to inkjet print active layers that are doped with CNTs, a SonoPlot GIX microplotter was employed. The microplotter was fixed with a 30 μm diameter glass pipette which was piezoelectrically activated and had a diameter sufficiently large to ensure that the nozzle would not

be clogged by the nanotubes. An additional benefit of using this system, was that the microplotter only uses a self-contained reservoir of 8 μL , which conserved the ink solution. Inks were prepared with a 1,2-dichlorobenzene:chlorobenzene (4:1) solvent system and the active layer of P3HT (12 mg/ml) and PCBM (10 mg/ml). A comparison of four films is presented in Figure 3-6 in which a non-doped control is compared with films doped with either the untreated BuckyUSA CNTs or the BuckyUSA tubes with the R=12 alkyl chain. Although the CNTs did not hinder the printing of the films, they did however agglomerate rather significantly during the ink deposition.

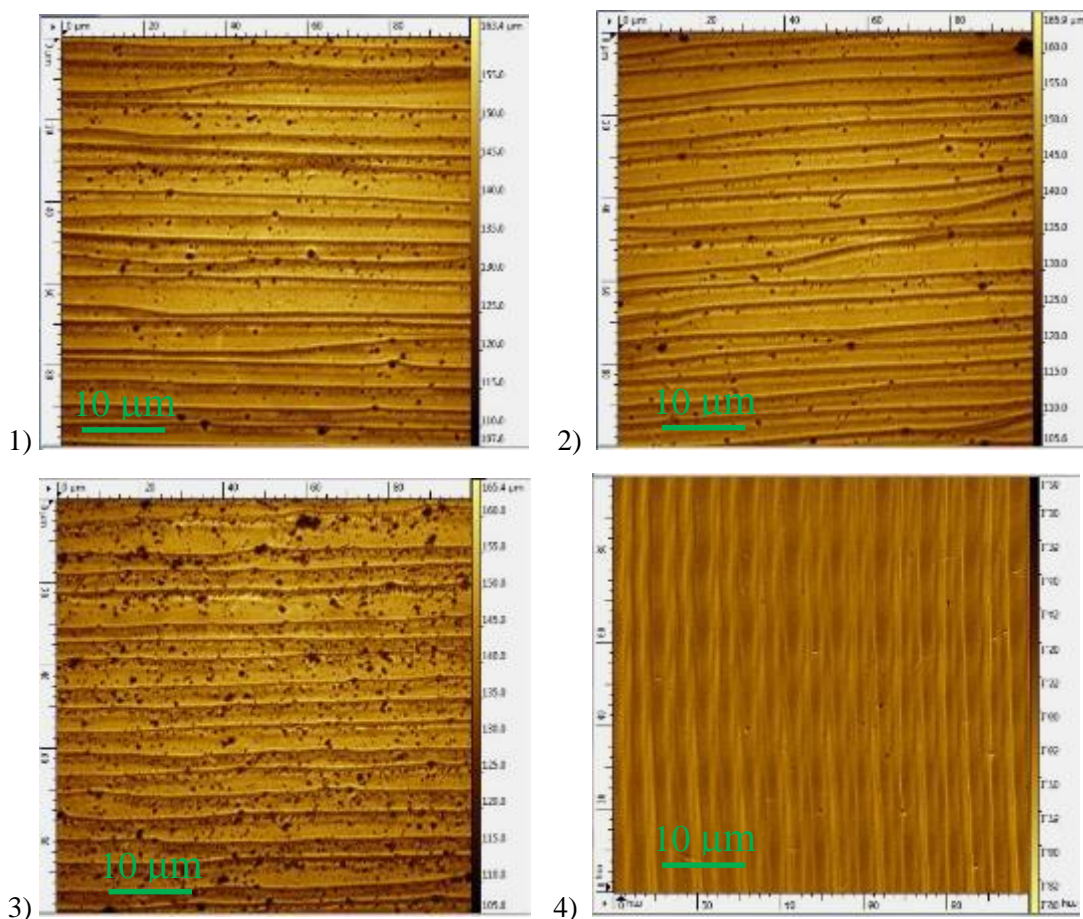


Figure 3-6: Interferometry of P3HT:PCBM films deposited via a microplotter with: 1) 0.5 wt % unmodified BuckyUSA; 2) 0.5 wt% f-SWCNTs (BuckyUSA, R=12); 3) 5 wt% f-SWCNTs (BuckyUSA, R=12); and 4) undoped P3HT:PCBM control.

3.2 Ternary blend active layers

All-solution processed polymer solar cells (PSCs) provide the means to fabricate low cost, flexible, and transparent organic photovoltaics (OPVs) through traditional printing techniques. An argument often made by naysayers is that the cost of high performance conjugated polymers is too great to sustain low-cost production and that economically viable PSCs must be limited to active layers prepared from a small number of polymers. Unfortunately, if the active layers are limited to a few polymers, hence colours, multi-coloured flexible PSCs may not be achieved.

Although, is there a solution that satisfies the need to limit active layer compounds (low-cost mass production) and also have a diverse array of colours?

Well, even though low-cost synthetic routes for the mass production of conjugated polymers is being explored [86], a potential solution to achieve low-cost colour-tuned PSCs is through the use of ternary blend active layers.

To reach this potential, the photo-active layer of these blends is prepared by blending two donor polymers and an acceptor (e.g. PCBM), with the goal of forming a parallel-like bulk heterojunction (PBHJ) PSC [18], [19], [33]. As previously addressed, in an efficient PBHJ blend, the V_{oc} lies between the V_{oc} of the individual sub-blends whereas the current density is a sum of the blends. In this manner, efficient ternary blends should provide a route for colour-tuned printable PVs while limiting the number of active layer materials. However, tuning the colour of the solar cells without efficiency degradation remains a challenge and has been proven in only a few examples of two donor (D1:D2:A devices) [18]–[20], [35], and two acceptor blends (D:A1:A2 devices) [14], [17], [36].

Our aim, is to study dual donor polymer ternary blend (D1:D2:A) solar cells made from a selection of three donor polymers and PCBM. Furthermore, the goal of the study is to: 1) tune the devices' colour without a large efficiency loss, and 2) provide evidence of limiting factors involved in the performance of dual donor:acceptor polymer photovoltaics.

Donor:donor:acceptor photovoltaics

In this study, the use of ternary blends (two donor polymers and a fullerene acceptor) in bulk-heterojunction (BHJ) photovoltaic devices is used to compare the parallel diode and trap model. The study involved the blending of various quantities of two of the three chosen complimentary donor polymers (red, green, blue) with PC₆₁BM. For the donor:donor:acceptor blends, three complementary polymers (red, blue, green) were chosen: G1 (green), B1 (blue), and P3HT (red), based on availability determined by DisaSolar (Limoges, France). The chemical structure and supplier of the two low band gap polymers (B1 and G1) are restricted and must remain unknown in accordance with the confidentiality requirements of DisaSolar and their partners. However, their approximate HOMO and LUMO energy levels have been disclosed (Figure 3-12).

Blends of various concentrations were analyzed in terms of absorption, colourimetry by reflectance spectroscopy, as well as fluorescence spectroscopy. J-V characteristics as well as external quantum efficiency (EQE) measurements were used to quantify the photovoltaic performance and charge transport properties were evaluated through photogenerated current vs. light intensity and bias polarization studies. The absorption and fluorescence of the neat polymer films is presented in Figure 3-7, with the complete study of all binary polymer:polymer blends located in the appendices (with colourimetry located in Appendix A).

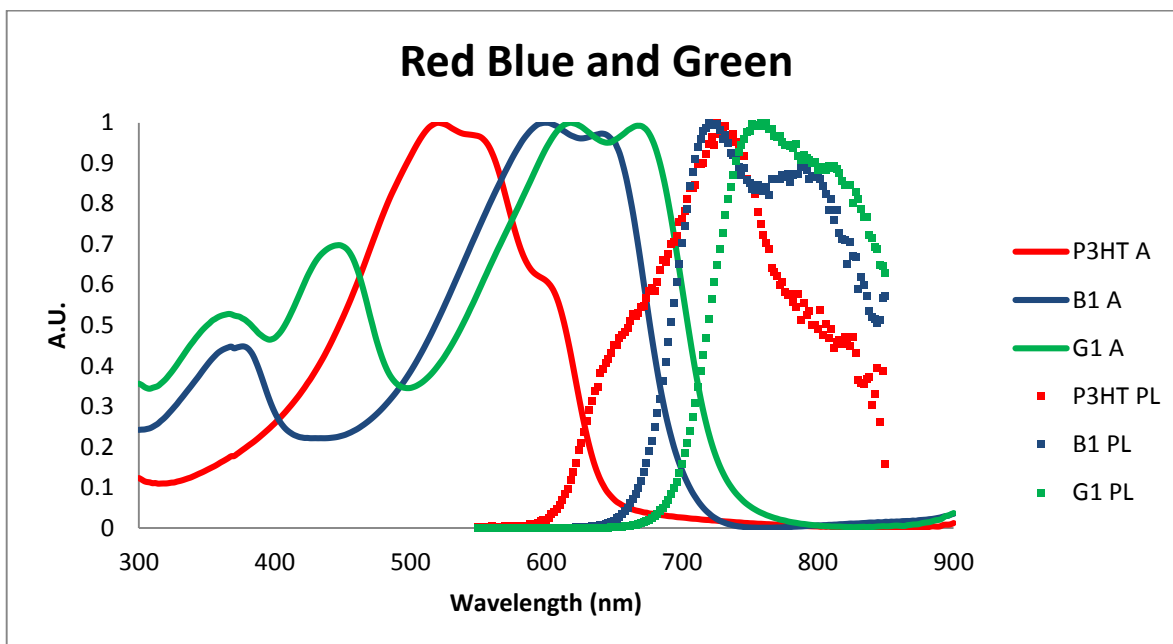


Figure 3-7: UV-vis absorption (A, solid line) and emission spectra (PL, dotted line) of the three polymer films on glass (P3HT, B1, and G1) . Excitation for photoluminescence was performed by a 509.2 nm laser.

3.2.1 Photovoltaic performance of ternary blends

Organic photovoltaic devices were prepared on ITO coated plastic substrates (polyethylene terephthalate [ITO/PET]) as described in the experimental section, with all layers spin coated sequentially on the substrate except for the Ag back electrode. The active layer was comprised of a polymer1(P1):polymer2(P2):PCBM ternary blend with various relative donor polymer concentrations, while maintaining the PCBM content constant. For each of the three ternary systems, P3HT:B1:PCBM, P3HT:G1:PCBM and B1:G1:PCBM, a minimum of three concentrations were investigated (deposited from an *ortho*-dichlorobenzene solution), however fabrication methods were not individually optimized for each scenario. These three P2 relative to P1 concentrations were 20% (4:1:10), 50% (1:1:4) and 80% (1:4:10), with a 1:2 ratio of total polymer relative to PCBM. The hole and electron transport layers, as well as the ternary active layer were deposited by spin coating on the ITO coated PET

substrate. This was followed by thermal evaporation of the silver back electrode to achieve an active area of 0.18 cm². The devices were composed of the following architecture (Figure 3-8):

PET/ITO/ZnO/polymer1(P1):polymer2(P2):PC₆₁BM/PEDOT:PSS/Ag

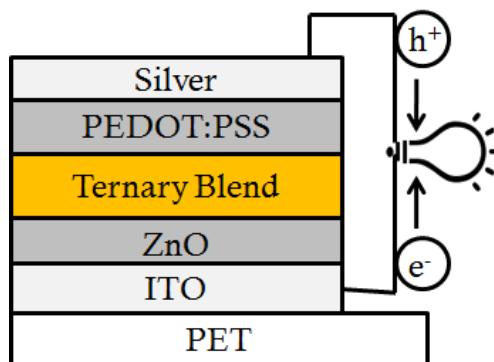


Figure 3-8: Device architecture of ternary blend OPVs


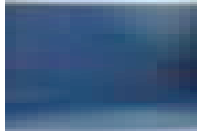
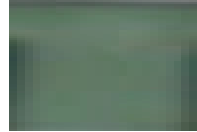

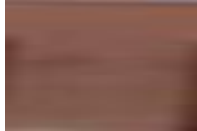

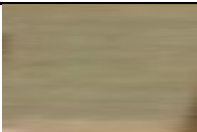
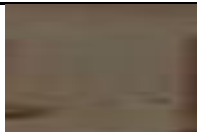
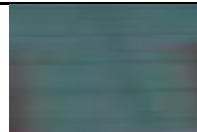
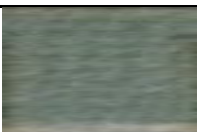

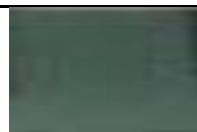
Binary Blend Photoactive Layer (PAL) – polymer:PC ₆₁ BM		
		
P3HT:PCBM	B1:PCBM	G1:PCBM
Ternary Blend PAL - polymer1:polymer2:PC ₆₁ BM		
P3HT:B1:PCBM	P3HT:G1:PCBM	B1:G1:PCBM
		
20 wt% B1	20 wt% G1	20 wt% G1
		
50 wt% B1	50 wt% G1	50 wt% G1
		
80 wt% B1	80 wt% G1	80 wt% G1

Figure 3-9: Image of completed devices (without Ag electrode) with 12 different active layer blends. Three binary blends (polymer:PC₆₀BM) and nine ternary blends (P1:P2:PC₆₀BM).

J(V) characteristics

Preliminary device characterization was performed by sweeping a voltage tension from -1.5V to +1.5V (V) and recording the output current density (J). With this preliminary characterization, the V_{oc} , J_{sc} , and FF were determined, as well as the approximation of the series and parallel resistance. The results for the most successful series are tabulated in Table 3-5 for P3HT:B1:PCBM blends, Table 3-6 for P3HT:G1:PCBM blends, and Table 3-7 for B1:G1:PCBM ternary blend devices. A comparison of V_{oc} and J_{sc} with respect to the P1:P2 concentration of the nine ternary blends and the 3 binary blends is presented in Figure 3-10.

P3HT:B1:PCBM

Table 3-5: J(V) characteristics for the ternary (P3HT:B1) blend and its corresponding binary blends.

Active Layer	V_{oc} (V)	J_{sc} (mA/cm ²)	FF (%)	PCE (%)
P3HT:[60]PCBM	0.55	8.18	53.0	2.39
P3HT:B1:[60]PCBM (4:1:10)	0.57	5.31	54.6	1.64
P3HT:B1:[60]PCBM (1:1:4)	0.60	2.71	39.9	0.65
P3HT:B1:[60]PCBM (1:4:10)	0.66	4.20	38.9	1.07
B1:[60]PCBM	0.77	11.07	53.7	4.56

P3HT:G1:PCBM

Table 3-6: J(V) characteristics for the ternary (P3HT:G1) blend and its corresponding binary blends.

Active Layer	V_{oc} (V)	J_{sc} (mA/cm ²)	FF (%)	PCE (%)
P3HT:[60]PCBM	0.55	8.18	53.0	2.39
P3HT:G1:[60]PCBM (4:1:10)	0.54	7.35	53.0	2.10
P3HT:G1:[60]PCBM (1:1:4)	0.56	4.34	40.1	0.97
P3HT:G1:[60]PCBM (1:4:10)	0.62	5.83	37.7	1.37
G1:[60]PCBM	0.71	13.72	59.4	5.78

B1:G1:PCBM

Table 3-7: J(V) characteristics for the ternary (B1:G1) blend and its corresponding binary blends.

Active Layer	V_{oc} (V)	J_{sc} (mA/cm ²)	FF (%)	PCE (%)
B1:[60]PCBM	0.77	11.07	53.7	4.56
B1:G1:[60]PCBM (4:1:10)	0.73	11.18	53.8	4.40
B1:G1:[60]PCBM (1:1:4)	0.72	11.08	64.8	5.16
B1:G1:[60]PCBM (1:4:10)	0.73	12.55	63.6	5.82
G1:[60]PCBM	0.71	13.72	59.4	5.78

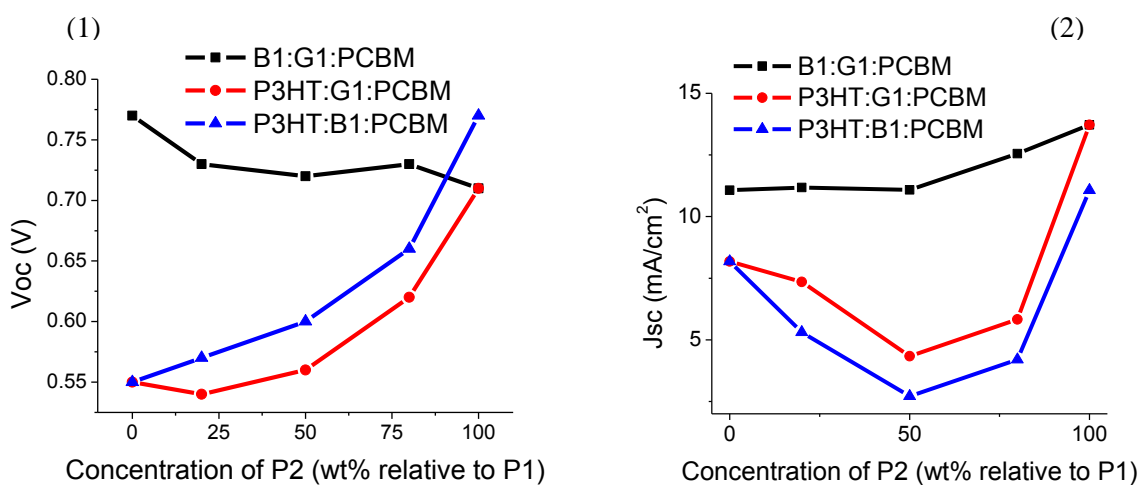


Figure 3-10: Evolution of (1) V_{oc} and (2) J_{sc} in P1:P2:PCBM ternary blends with respect to the relative donor polymer ratio.

Even though these preliminary results are essential to characterize the fabricated PV devices, they are unable to distinguish which type of charge transport mechanism is present within the ternary blend BHJ. In chapter 1.2.1, three types of charge transport mechanisms are discussed: (1) charge transfer (Figure 1-11), (2) energy transfer (Figure 1-12) and (3) parallel diode (Figure 1-13).

Although, these charge transfer mechanisms may occur simultaneously within a ternary blend, it is common for one to be the principal mechanism. In this study of dual polymer ternary blends, the energy transfer mechanism can be disregarded. This is because, in the energy transfer mechanism the polymer 1 (energy donor) would have to act as the sensitizer and would not participate in the charge

generation, which would be controlled by the second polymer. In this scenario there is no change in the D:A energy level configuration and therefore there would be no variation in the V_{OC} (which is contrary to the results). Furthermore, the V_{OC} in a ternary blend with primarily an energy transfer mechanism would be equal to the quasi-Fermi level difference between the charge transporting polymer and the acceptor (as in a binary blend). Which in fact implies that it will be close to the difference between the LUMO of the acceptor and the HOMO of the primary donor (polymer 2) with a subtraction of ΔE that can be attributed to charge transfer (CT) energy levels. Moreover, the exclusion of the energy transfer mechanism from these ternary blends, is also confirmed by the fluorescence study (Figure 3-11 and appendix for additional spectra). Figure 3-11 illustrates the photoluminescence (PL) emission spectra of the polymer films on glass with a 509.2 nm excitation source. The concentrations displayed in the figure, are those that were used in the ternary blend devices (0, 20, 50, 80, 100 % P2 relative to P1), and show the comparison between the polymer1:polymer2 blends (solid line) with the corresponding neat polymer films (dotted line). If an energy transfer from polymer 1 to polymer 2 is involved, the PL contribution of polymer 2 will be predominant on the PL spectra, however this is not the case in this study. In brief, this provides further evidence that only the charge transfer or parallel diode mechanism is present and that the energy transfer model can be reasonably disregarded.

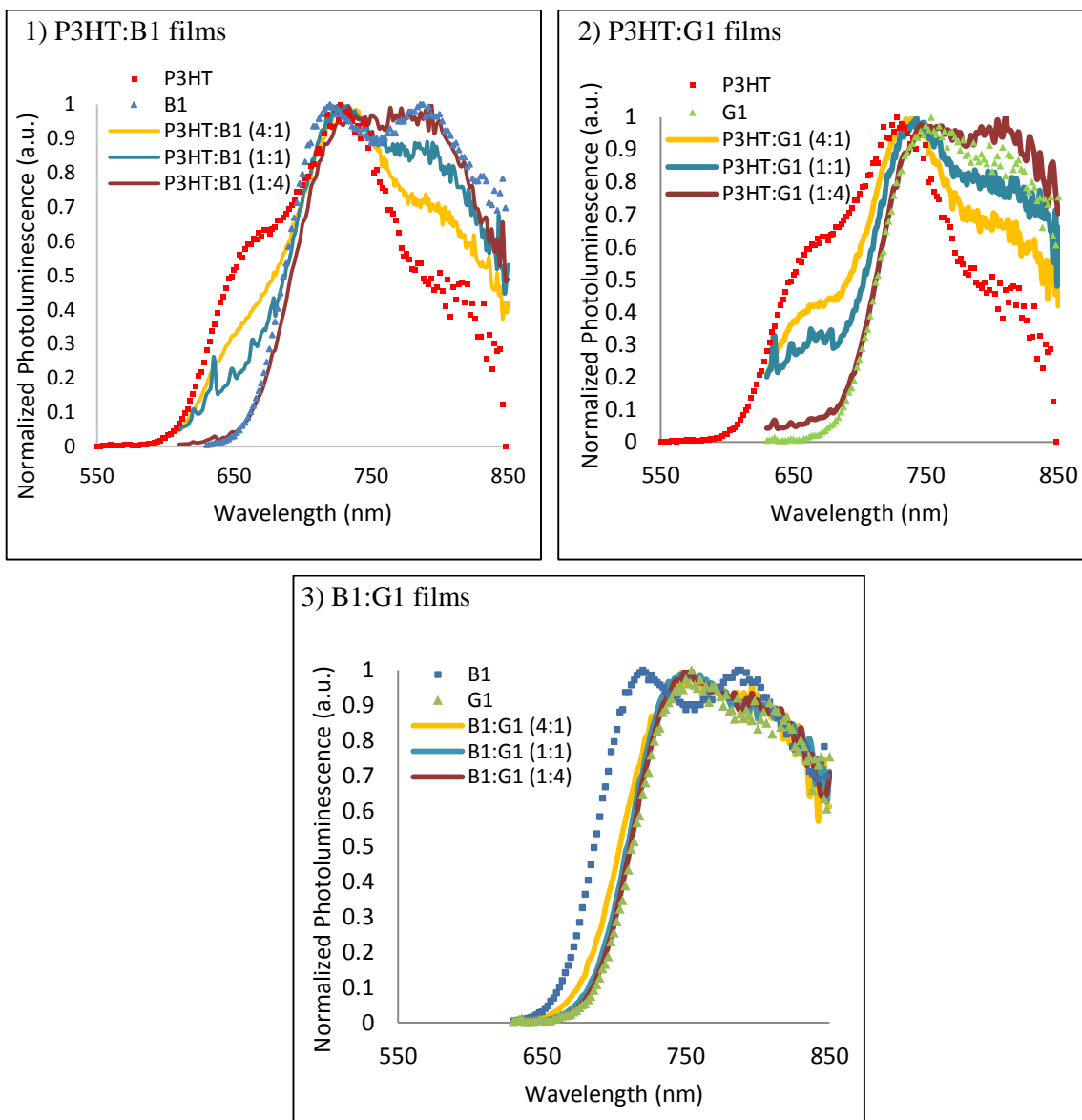


Figure 3-11: Photoluminescence emission spectra of *polymer1:polymer2* blends (60 nm film on glass) as well as the neat polymer films, with a 509.2 nm excitation source. PL spectra for 1) P3HT:B1; 2) P3HT:G1; and 3) B1:G1 blends.

While the J(V) characterization cannot identify the ternary charge transport mechanism that is present within the device, it can shed light on a possible PBHJ model. In Figure 3-10, the Jsc evolution (along with V_{OC}) is shown with the variation in P1:P2 ratio. It is clearly observed in this graph, that only the ternary BHJ made of the B1:G1:PCBM active layers can offer the possibility to tune the colour

of the device without a significant loss in J_{SC} . This implies that the B1:G1:PCBM blend is capable of attaining relatively high efficiencies as the P1:P2 ratio is varied.

In the recent report from Yang and coworkers, several key conditions were observed in order to obtain efficient ternary blend BHJ [20]. Interestingly, the authors prepared ternary blends whose efficiencies are greater than those of each of the binary sub-blends. To achieve this, the polymers must first have complementary absorption spectra in order to harvest an increased portion of the solar spectrum. This increase in the PV devices' spectral range inherently leads to a ternary blend with a larger J_{SC} . In our study, the polymer absorption spectra have a noticeable overlapping of their spectra (Figure 3-7). However, our goal was solely to colour-tune the active layer with the polymers obtained by DisaSolar, while avoiding a significant efficiency loss.

Another important parameter when dealing with two donor polymer ternary blends, is to use "compatible polymers" [101]. This will ensure that the BHJ morphology is not significantly disrupted as the polymers form a solid state polymer composite. For example, P3HT prefers to crystallize with edge-on lamellae on the substrate surface, whereas most of low band gap (LBG) polymers generally arrange face-on and are quite amorphous. This disruption of the morphology must apply in our case and certainly could explain the lower J_{SC} obtained when P3HT is used in conjunction with B1 and G1 (refer to section 3.2.2).

Finally, transport compatibility must be taken into consideration for an effective ternary blend active layer. In the blend, it must be avoided that one polymer provides traps that will lower transport properties of the other polymer. This can apply in either of the two models that have been recently described in the literature. For instance, if the two polymers form an alloy and transport is ensured via the "mutual" CT states of the alloy [31], [36], [101], there will be no traps since the HOMO levels of each polymer will not participate in the charge transport. This implies also that the blend has to be highly homogeneous, with the small individual polymer domains that are well intermixed and provide "mutual" and equivalent transport properties within the alloy blend. Similarly, this can be looked at

from the case of the parallel diode model which provides charge transport via the CT states of each of the two donor:acceptor interfaces (P1:A and P2:A systems) [102]. In this case, a suitable morphology allows each D:A diode to independently transport photogenerated charges to the electrodes without interfering with neighboring diodes. The resulting V_{OC} and J_{SC} of the device will be the result of the parallel sum of all the sub-device domains. However, charge traps can very well be present at the frontier between these diode domains.

Both of the models can be a good approximation for the B1:G1:PCBM devices which present rather homogeneous blend morphologies (see section 3.2.2). Conversely, the P3HT:P2:PCBM blends show significantly inhomogeneous films which prevent the creation of a polymer alloy.

It is important to note, that when P3HT is used in the ternary blends the lowest J_{sc} 's are obtained when the P3HT:P2 ratio is 1:1. This provides evidence that the charge transport occurs through the polymer with a higher concentration in the blend and that the highest trap densities exist when equal quantities of each polymer are present. Another interesting feature is that the J_{sc} values are more affected by a 20 % P3HT concentration in the B1 or G1 matrix than when 20 % B1 or G1 is used in the P3HT matrix. This can be explained when we look at the polymer energy levels which are illustrated in Figure 3-12: HOMO levels are located at -5.1 eV, -5.45 eV and -5.4 eV for P3HT, B1 and G1 polymers respectively.

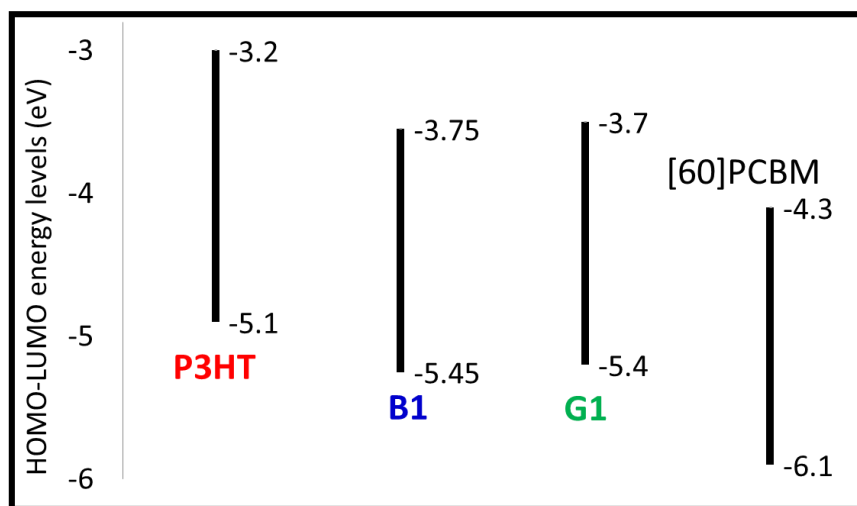


Figure 3-12: Energy levels (HOMO and LUMO) of active layer materials in ternary blends.

In the case of a B1 or G1 matrix, P3HT addition creates a sub-band gap trap state located with a minimum value of 0.35 eV and 0.3 eV respectively, for which value we have to add the CT exciton binding energy. However, in the case of a P3HT matrix, trap states created by adding the B1 or G1 polymers will only give sub-band gap trap states located at an energy value equivalent to the CT exciton binding energy.

In further experiments, we will try to show that the two polymers of the ternary blend must have similar HOMO energy levels in order to avoid the trapping effect.

External Quantum Efficiency (EQE)

The external quantum efficiency (EQE), which provides the percentage of incident photons converted to electrons (IPCE), is an important parameter to investigate when comparing different active layer compositions. In ternary blends, the EQE provides insight into the effective absorption of the active layer and the subsequent charge extraction of the device.

In the B1:G1:PCBM systems, a similar EQE curve is exhibited for all ternary blends (Figure 3-13). As the concentration of the G1 polymer is increased, so is the absorption range of the active layer. This increase in absorption, from 720 – 750 nm, in turn relates to an increase in the current produced by the device.

In the two ternary blends paired with P3HT, there is a significant loss in the EQE with respect to the binary blends. In the P3HT:B1:PCBM (Figure 3-14) and P3HT:G1:PCBM (Figure 3-15) ternary systems the quantum efficiency reduction is found with all three concentrations. Although, even as the concentration of the lower band gap polymer (B1 or G1) is increased, the increase in the effective absorption does not enhance the produced current. In fact, at 20 wt% (B1 or G1 to P3HT) the PV cell has a higher J_{sc} than the 50 and 80 wt% blends. The cause of this current loss is derived from polymer-polymer charge trapping. Furthermore, the P3HT blends do not follow a progressive pattern as the concentration of B1 or G1 increases.

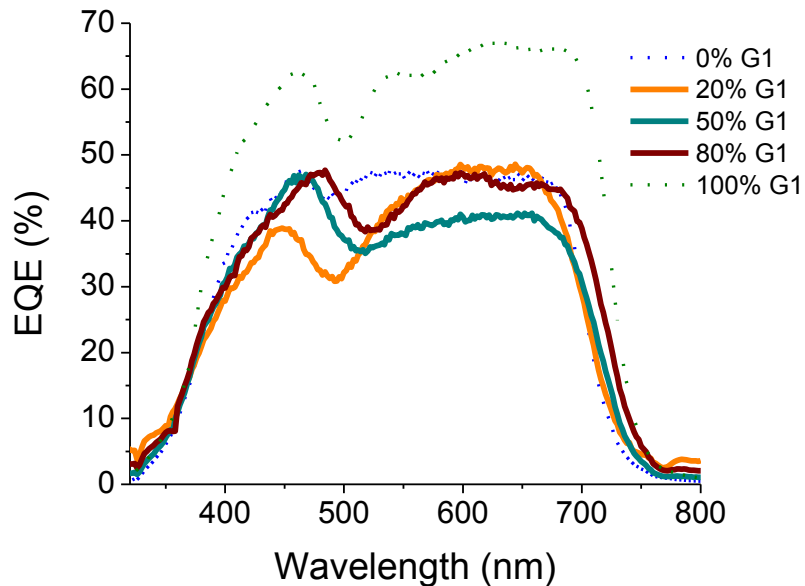


Figure 3-13: External quantum efficiency of B1:G1:PCBM blends (solid) and the binary blends; B1:PCBM and G1:PCBM (dotted).

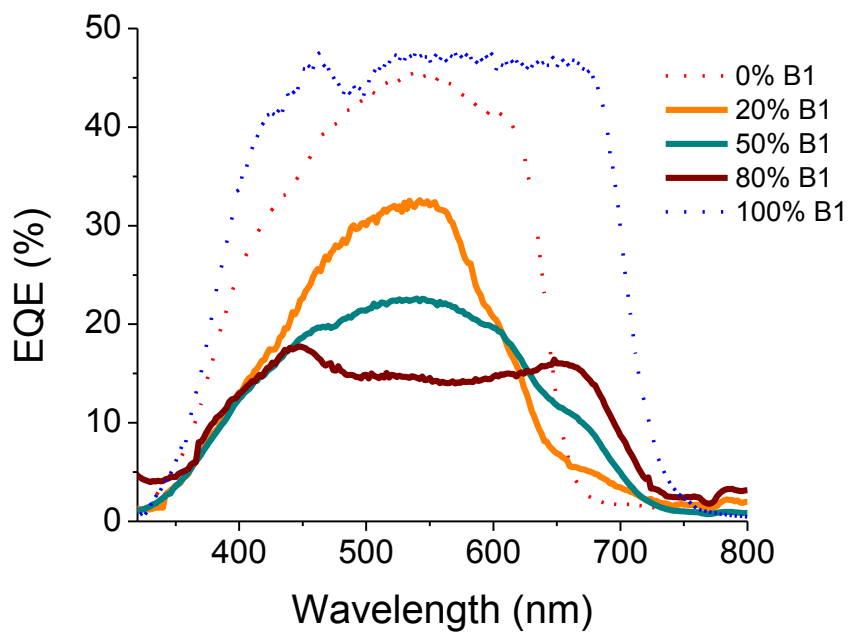


Figure 3-14: External quantum efficiency of P3HT:B1:PCBM blends (solid) and the binary blends; P3HT:PCBM and B1:PCBM (dotted).

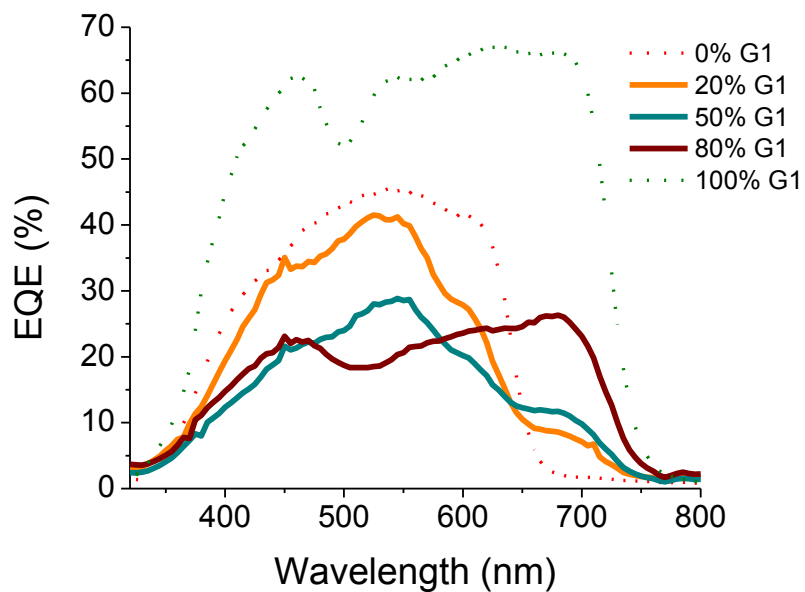


Figure 3-15: External quantum efficiency of P3HT:G1:PCBM blends (solid) and the binary blends; P3HT:PCBM and G1:PCBM (dotted).

External quantum efficiency (EQE) versus incident photon energy

Normalized EQE spectra versus photon energy is an insightful study to investigate the sub-band gap absorption of the devices, which can elucidate a CT energy state (refer to Figure 3-16, Figure 3-17, Figure 3-18). This sub-band gap absorption occurs via the CT states of each P1:PCBM or P2:PCBM (or a combination of them) which lies at a lower energy than the absorption spectra of each polymer. This particularity is an illustration of the difference between the optical and charge transport properties in an active layer blend; absorption properties are governed by the molecular scale and reflect the property of each individual polymer, whereas transport properties will result from the longer range order (or disorder) of the lattice, which comprise of both polymer donors and PCBM. The energy difference between the absorption band edge and the EQE edge can provide insight into an approximate position of the CT energy levels, which lie in the band gap. Moreover, in a "non-compatible" ternary blend it can be used to distinguish the energy depth of the traps in a polymer1 matrix doped with polymer2. Evidently, it is clearly noted that in this latter case the P3HT:P2 blends exhibit a reduction in the CT states in contrary to the B1:G1 blends.

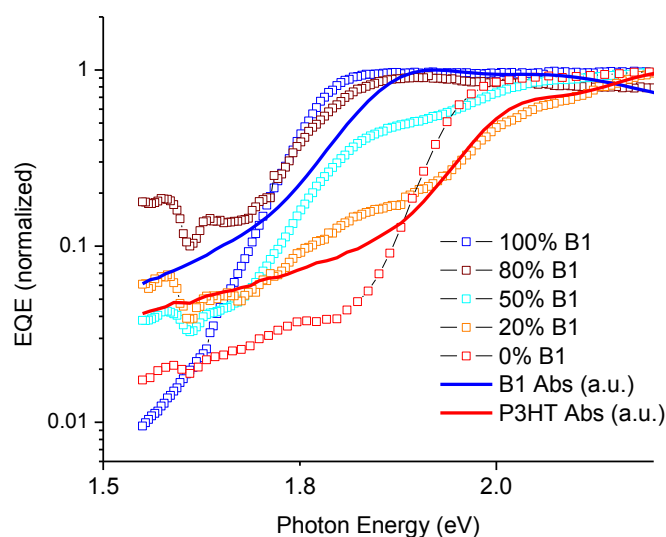


Figure 3-16: Normalized EQE of P3HT:B1:PCBM ternary devices (open squares) compared to the absorption spectra of the neat polymer films (solid line).

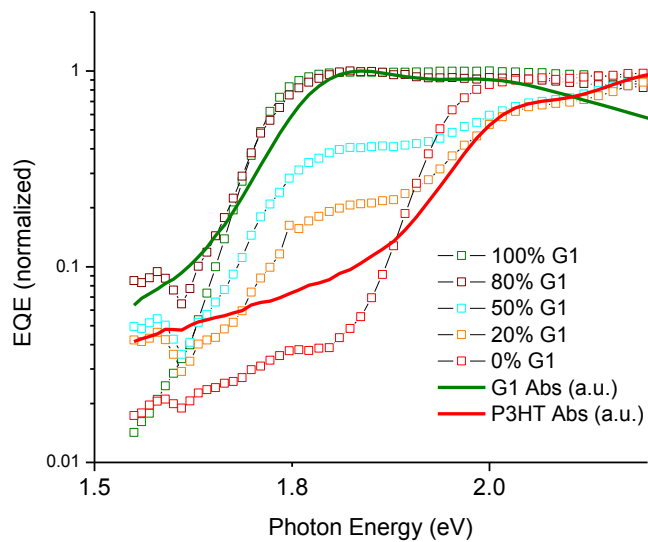


Figure 3-17: Normalized EQE of P3HT:G1:PCBM ternary devices (open squares) compared to the absorption spectra of the neat polymer films (solid line).

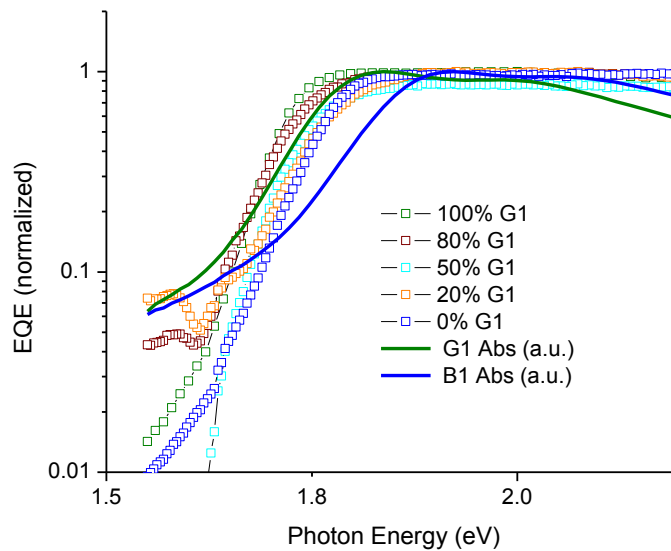


Figure 3-18: Normalized EQE of B1:G1:PCBM ternary devices (open squares) compared to the absorption spectra of the neat polymer films (solid line).

Photocurrent vs. Effective Voltage (J_{ph} vs. ($V_{bi}-V$))

To further investigate the charge transport mechanism within the blends, a bias polarisation study was performed in relation to various light intensities. The device was subjected to a voltage sweep from -10 V to 1.5 V, under one sun illumination (100 mW/cm^2) and then at progressively reduced light intensities (1 sun to dark). Through these measurements, it was shown that there was a distinct dependence between the J_{sc} and a variation in illumination intensity. This is illustrated in Figure 3-19 in which a distinct deviation from linearity is shown for the ternary blends with P3HT, whereas linear relationship is seen for all blends consisting of B1 and G1. The deviation from linearity is insufficient to determine the order of recombination, although it does indicate that in the trapped blends significant charge-density dependent losses are occurring at J_{sc} with greater illumination [103], and that these losses may be due to bimolecular recombination [35]. Furthermore, the greatest sub-linear deviation occurs in the P3HT ternary blends that have an equivalent quantity (50%) of each donor polymer (Figure 3-19, graphs A and B). This phenomenon provides further evidence that the trap density in the P3HT:P2:PCBM active layers reaches a maximum in the 50% P2 blends.

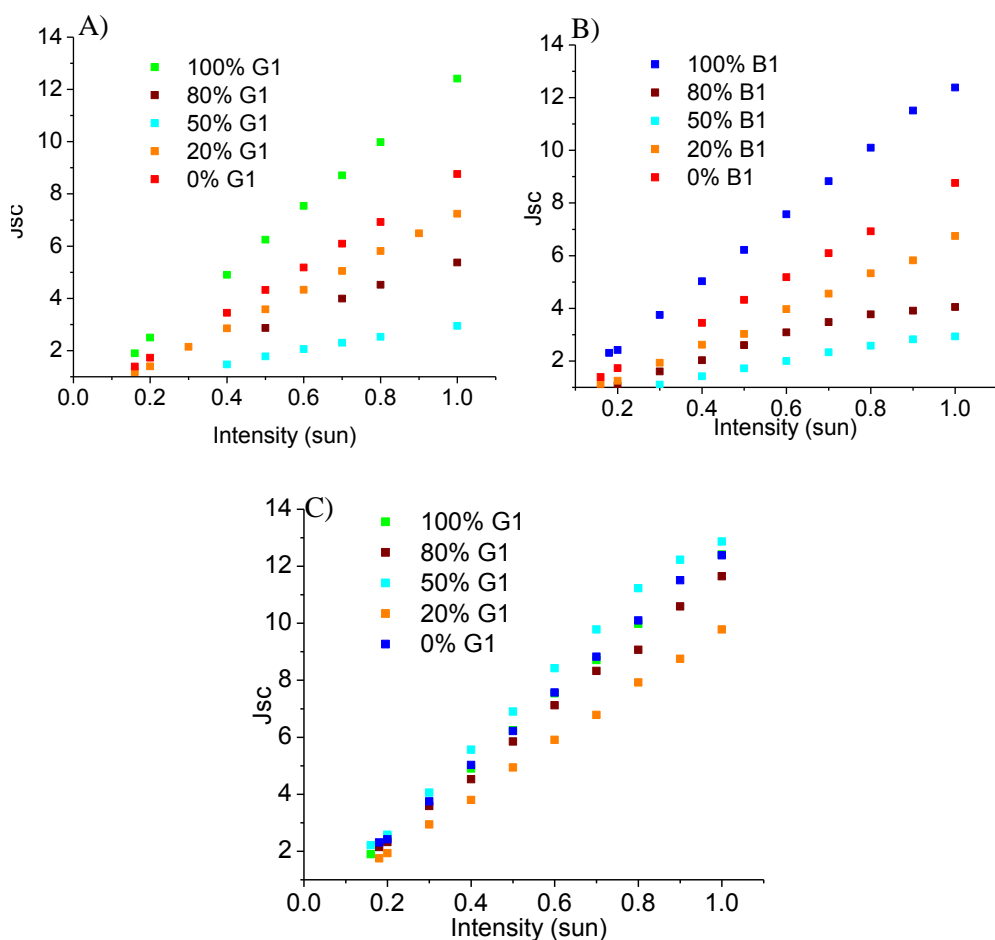


Figure 3-19: Illumination intensity dependence of J_{sc} for all 12 active layers. A) ternary and binary sub-blends for P3HT and G1; B) ternary and binary sub-blends for P3HT and B1; C) ternary and binary sub-blends for B1 and G1

These $J(V)$ values were then used to plot the photocurrent versus effective voltage, which is shown in Figure 3-20 for the B1:G1:PCBM (1:1:4) device. This illustrates how the increase in light intensity, increases the voltage at which the field driven regime appears. This increase in the onset voltage (of the field driven regime) is due to charge recombinations, which are increased by higher free charge carrier densities.

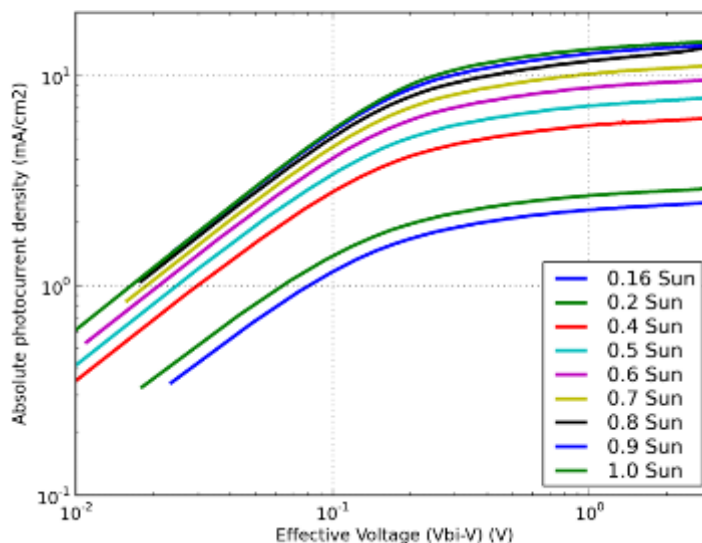


Figure 3-20: Photocurrent density vs. effective voltage at different light intensities for B1:G1 blend (50% G1).[1 Sun=100 mW/cm²]

In the ternary blends that contain P3HT, even at a high drift voltage there is a near square root behaviour in the J_{ph} vs. $(V_{bi}-V)$ curve, which is a sign of a recombination limited regime. This is illustrated in both the P3HT:B1:PCBM (Figure 3-21) and P3HT:G1:PCBM (Figure 3-22) blends, which are shown for various concentrations at 1 sun. It seems that in the P3HT blends the transport mechanism is dominated by a recombination limited regime and not a space charge limited (SCL) regime, occurring due to a large mobility imbalance between electrons and holes. This decrease in hole mobility is attributed to the trapping effect associated with the HOMO level offset of the P3HT and B1 or G1. Moreover, it is distinguishable that recombination losses are more pronounced in the case of a B1 or G1 matrix containing traps given by P3HT (50% and 80% B1 or G1) rather than in the case of a P3HT matrix containing a concentration of LBG polymer (20% B1 or G1). The significance of the traps provided by the higher energy HOMO level of the P3HT dopant in the ternary blend (when $[P3HT] \leq [P2]$) is corroborated by the J_{sc} evolution seen in Figure 3-10 (refer also to section 3.2.1 (“EQE vs. incident photon energy”). However, in the case of the B1:G1:PCBM blends (Figure 3-23) a charge

saturation is reached similar to the binary blends, which provides further evidence of the parallel diode mechanism.

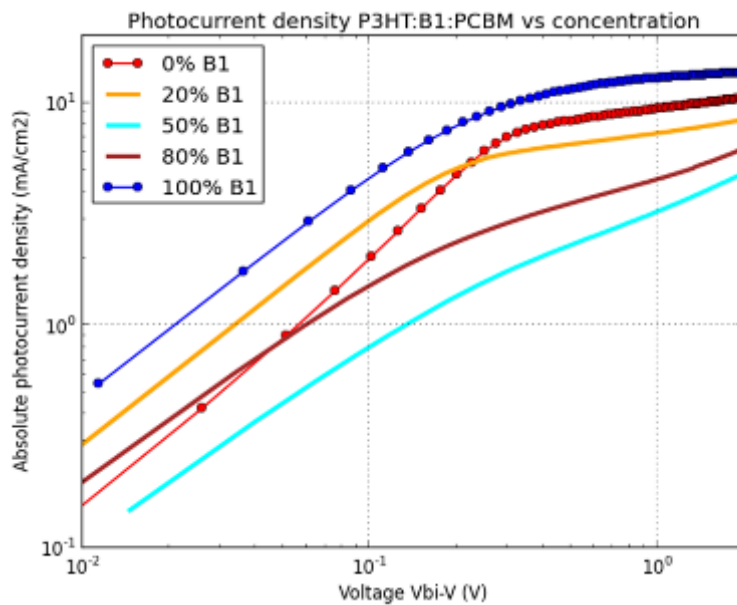


Figure 3-21: J_{ph} vs. $(V_{bi}-V)$ for P3HT:B1:PCBM blend at 1 sun (100 mW/cm²)

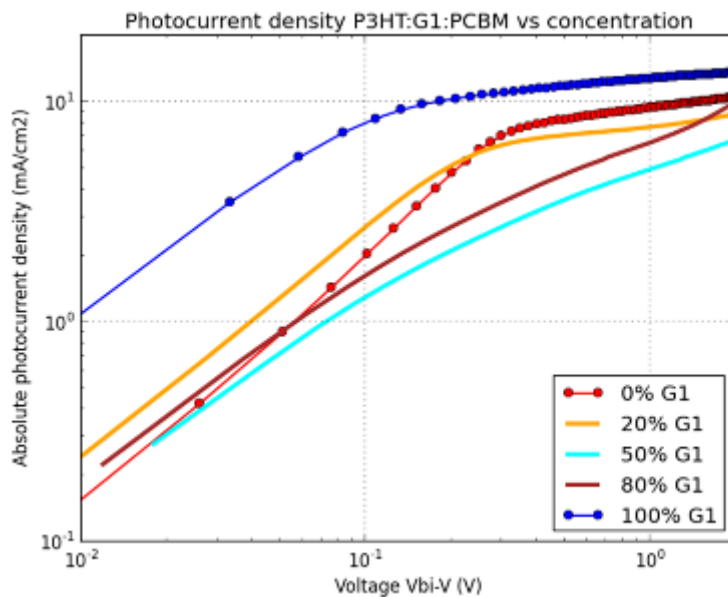


Figure 3-22: J_{ph} vs. $(V_{bi}-V)$ for the P3HT:G1:PCBM blend at 1 sun (100 mW/cm²)

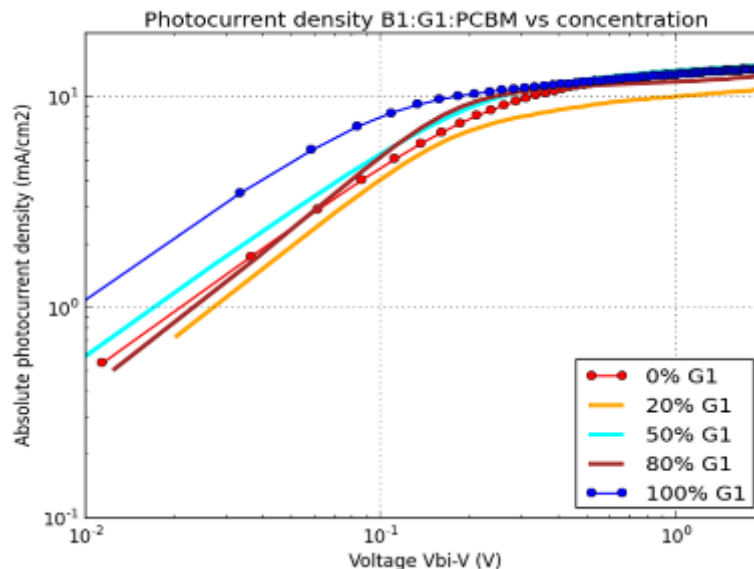


Figure 3-23: J_{ph} vs. $(V_{bi}-V)$ for the B1:G1:PCBM blend at 1 sun (100 mW/cm^2)

3.2.2 Morphology of ternary blend active layers

The morphology of the active layers were investigated by non-contact atomic force microscopy (AFM). This investigation showed the similarity in roughness between the binary blends and the B1:G1:PCBM ternary blend. However, the AFM results also illustrated the discrepancy in surface topology exhibited by the ternary blends containing P3HT.

The three binary blends (polymer:PCBM) had an average topological roughness of 1.94 nm, with the B1:G1:PCBM active layer following suit with a RMS roughness of 3.14 nm. In contrast, the P3HT:B1:PCBM and P3HT:G1:PCBM had a surface roughness of 45.8 nm and 18.6 nm respectively. This discrepancy between the two ternary blends containing P3HT and the B1:G1 ternary blend correlates well with the experimental photovoltaic performance of the active layers.

Table 3-8: RMS roughness (nm) of the AFM topology of the binary active layers and ternary blends with equal donor polymer ratios.

Polymer blend	Roughness – 1 x 1 μm^2 (nm)	Roughness – 3 x 3 μm^2 (nm)
P3HT:PCBM	2.18	4.82
B1:PCBM	1.95	2.56
G1:PCBM	1.70	2.04
<i>P3HT:B1:PCBM</i>	<i>45.8</i>	<i>55.0</i>
<i>P3HT:G1:PCBM</i>	<i>18.6</i>	<i>40.7</i>
B1:G1:PCBM	3.14	3.58

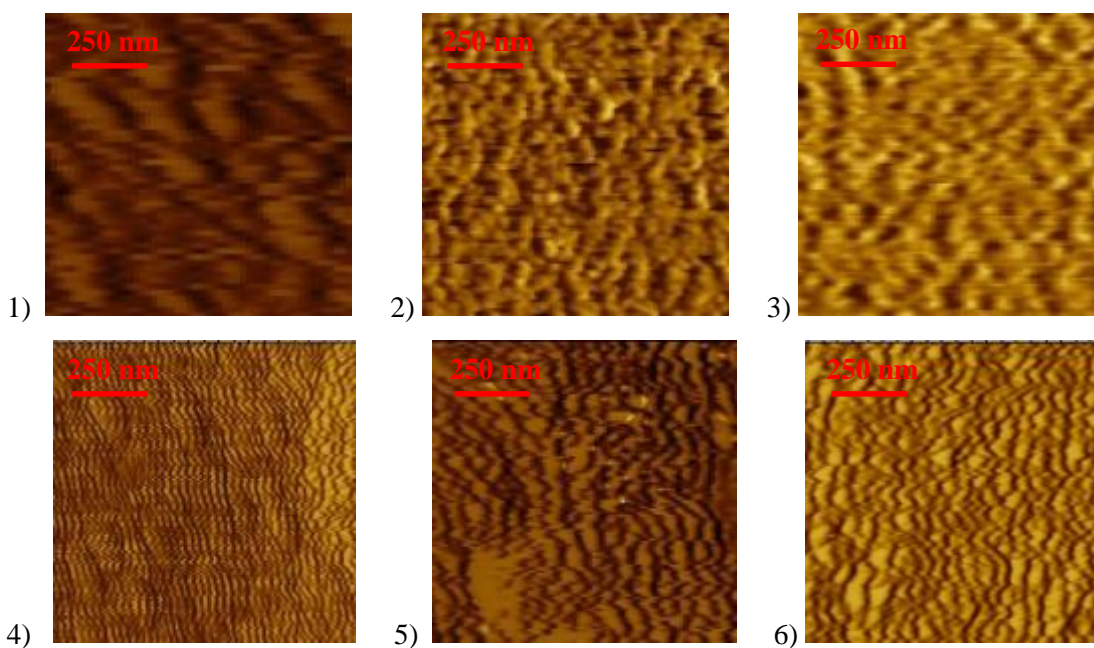


Figure 3-24: AFM phase images (1 x 1 μm^2) of the binary and ternary blends: (1) P3HT:PCBM; (2) B1:PCBM; (3) G1:PCBM; (4) P3HT:B1:PCBM; (5) P3HT:G1:PCBM; (6) B1:G1:PCBM

3.2.3 Equivalent circuit of the parallel diode.

The equivalent circuit of two photodiodes in parallel (Figure 3-26) is used to model the ternary blend's parallel diode mechanism. This model has the potential to calculate the blend ratio of two donor:acceptor domains with the highest PV efficiency. In this equivalent circuit each diode contribution can be adjusted to correspond to the relative area of each donor polymer, with the assumption that the total acceptor concentration is equivalent to both polymer A and polymer B.

Prior to modelling the ternary blend, each individual sub-blend's diode equivalent electric circuit needs to be established (R_s , I_{ph} , R_{sh} and $D1$) by fitting the experimental data for each binary active layer device. As can be seen in Figure 3-26, extra resistances (R_{extra}) have been added to take into account the length of the connectivity inside the electrode from the diode domain area to the collection point of the solar cell.

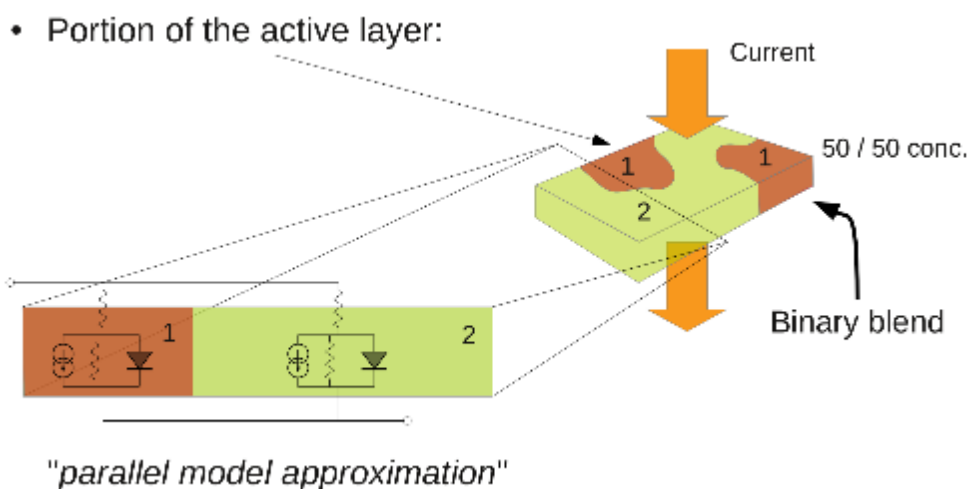


Figure 3-25: Illustration of the parallel diode model to approximate the equivalent circuit in a parallel BHJ polymer solar cell.

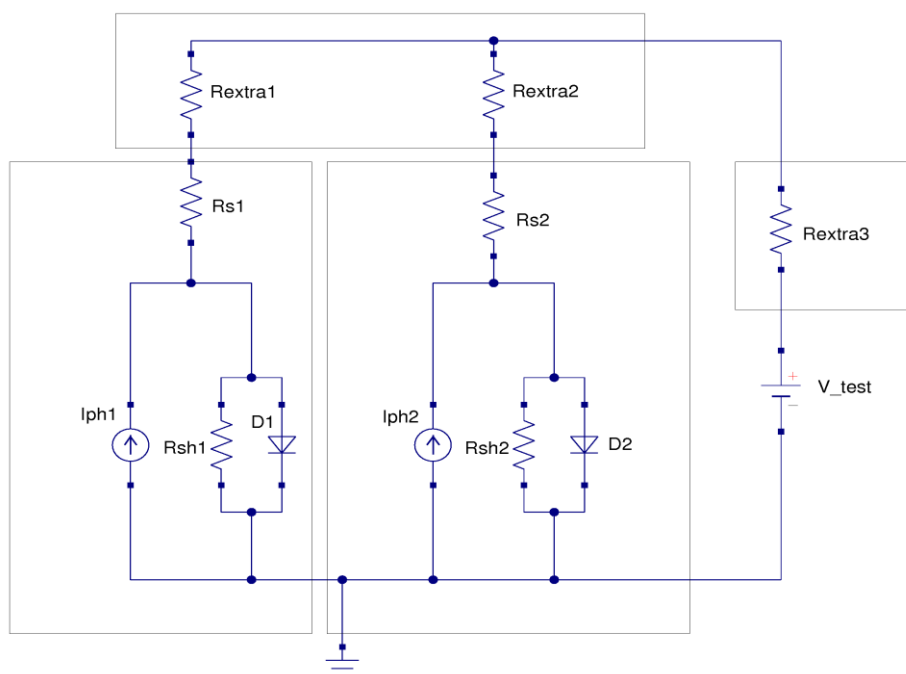


Figure 3-26: Equivalent circuit model of the parallel diode mechanism.

The parallel diode equivalent circuit was used to simulate the $J(V)$ behavior of the ternary blends and are compared to the experimental data for all the P1:P2:PCBM (1:1:4) blends in Figure 3-26. In the case of the P3HT:P2 ternary blends, it was not possible to fit the experimental data to the parallel diode model. Justifiably, because the model implies independent parallel diodes with little trap effects induced by the blend.

However, in the B1:G1:PCBM blends, where trap formation is not expected due to the HOMO level matching of the two polymers, the parallel diode model has provided a reasonably fit of the experimental data. These results are shown in Figure 3-28 for all the B1:G1:PCBM blends which clearly obey the parallel diode model. However, this all electrical model does not reflect the exact configuration of the blend and R_{extra} needed to be used for the fitting. Recently, a more accurate code has been developed at Xlim using a 3D finite element method in order to define the current line cartography in the device. The photogenerated current is produced by a non-linear current source located in the middle depth of the device and matching the device's produced photocurrent. In the future, this model will be

applied to ternary PSCs to more accurately determine the additional series resistances needed in order to predict the parallel connectivity of the binary sub-blends.

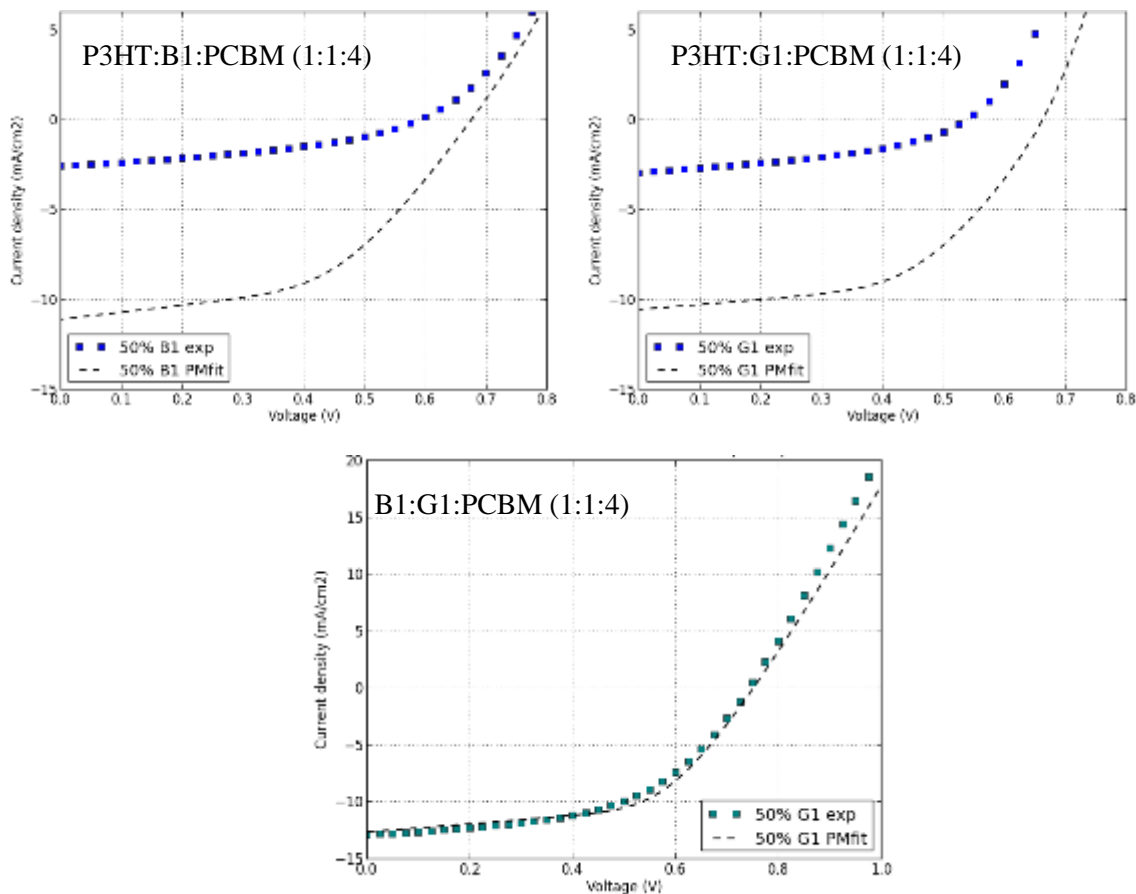


Figure 3-27: Theoretical J(V) curves (dotted line) for the 3 ternary systems at 1:1 polymer ratios (50% P2) using the parallel diode model. The fitted results are compared to the experimental results (blue squares).

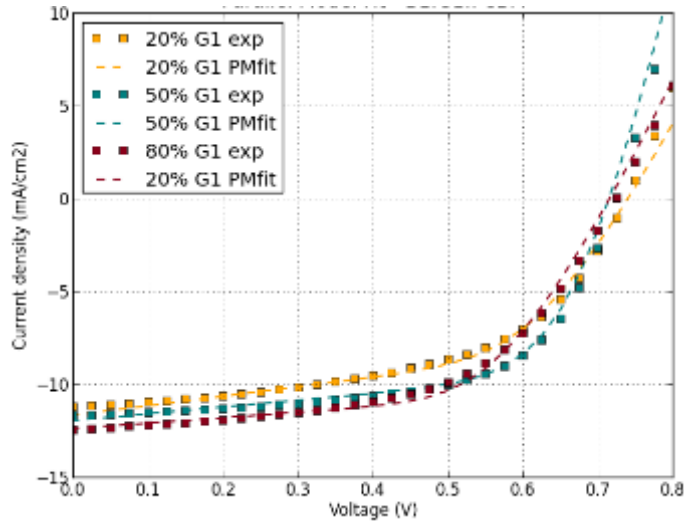


Figure 3-28: Comparison of experimental and modeled J(V) curves for B1:G1:PCBM blends. Experimental results (squares) and parallel diode model fits (dotted line) for 20, 50, and 80 wt% G1 relative to B1.

3.2.4 Mismatch factor of active layers

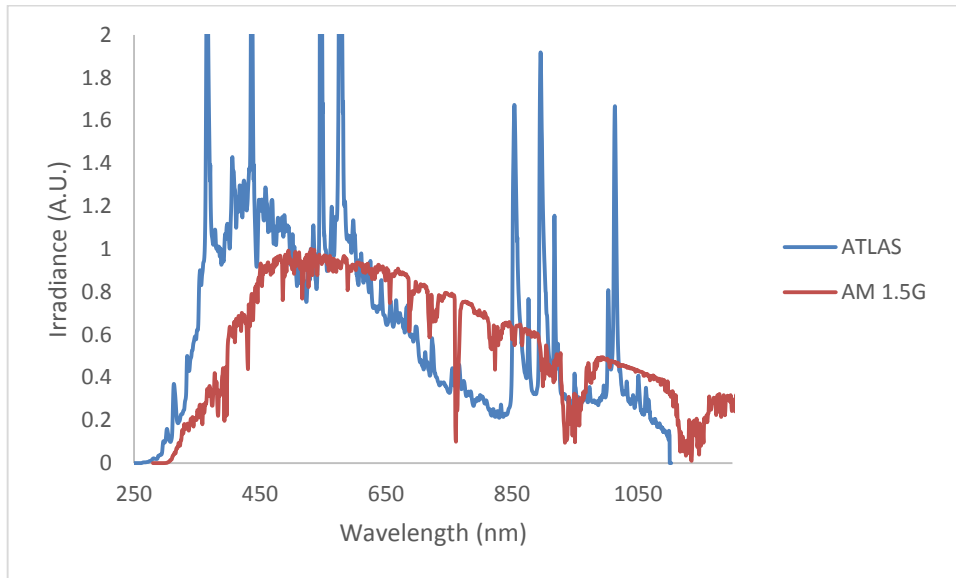


Figure 3-29: Normalized irradiance of the ATLAS solar simulator at Xlim (used through a window in the glovebox) and the irradiance of the sun (AM 1.5G)

To help increase the precision of the solar cell's photovoltaic characterization, a mismatch factor (M) is calculated. This factor is unique for a particular active layer and the corresponding solar simulator. The inherent mismatch in the intensity of the solar simulator (i.e. ATLAS simulator) and

the actual intensity of the sun is shown in Figure 3-29 [104]. Specifically, the mismatch factor is calculated by multiplying the ratio of current in the reference cell (blue) by the ratio of current in the test cell (brown) [105], [106].

$$M = \frac{\int_{\lambda_a}^{\lambda_b} E_{am1.5G} * S_{reference} d\lambda}{\int_{\lambda_a}^{\lambda_b} E_{am1.5G} * S_{reference} d\lambda} * \frac{\int_{\lambda_a}^{\lambda_b} E_{simulator} * S_{test} d\lambda}{\int_{\lambda_a}^{\lambda_b} E_{am1.5G} * S_{test} d\lambda}$$

The sensitivity of a solar cell at a particular wavelength can be described by the current in the cell at that wavelength ($I(\lambda) = S(\lambda) * E(\lambda)$). Where $S(\lambda)$ is the sensitivity of the solar cell in A/W, and $E(\lambda)$ is the irradiance of the light source at a given wavelength.

$$S(\lambda) = \frac{q\lambda}{hc} * EQE (\%)$$

Table 3-9: Calculated mismatch factors (M) for a variety of active layers in inverted devices with the following architecture: PET/ZnO/active layer/PEDOT:PSS/Ag

Active Layer	M
P3HT:[60]PCBM	1.33
B1:[60]PCBM	1.18
G1:[60]PCBM	1.13
B1:[70]PCBM	1.17
G1:[70]PCBM	1.16
P3HT:G1:[60]PCBM (4:1:5)	1.15
P3HT:G1:[60]PCBM (1:1:2)	1.22
P3HT:G1:[60]PCBM (1:4:5)	1.12
B1:G1:[60]PCBM (4:1:5)	1.16
B1:G1:[60]PCBM (1:1:2)	1.17
B1:G1:[60]PCBM (1:4:5)	1.14
B1:G1:[70]PCBM (1:1:2)	1.16

Chapter 4

Conclusions and Future Work

4.1 Functionalized SWCNTs

In the first component of the study, SWCNTs were functionalized with alkyl chains to help increase their dispersive properties in solvents, increase their interaction with the P3HT polymer matrix, and to disrupt the metallic characteristic of the tubes. This was done via an esterification reaction on two purchased tube varieties and with three different primary alcohols. P3HT:PCBM:CNT composite films were characterized and prepared for use as the photoactive layer within inverted solar cell architectures. Primarily based on an AFM study, the CNT doping seemed to increase the active layer's charge transport properties as well as showed some promise to increase the stability of the device. The future work of the project will investigate if improved charge transport can be attained via CNT doping. More specifically, if the doping will enable the fabrication of highly efficient PSCs on large areas with increased active layer thicknesses, which would provide large-area inkjet printing a significant advantage.

4.2 Colour-tuned ternary blend PSCs

Our initial study involved the blending of two donor polymers (red (P3HT), green (G1)) with PC₆₁BM to produce a yellow-brown coloured device. Even though J(V) characteristics of the initial devices exhibited poor efficiencies, the EQE illustrated both polymers' contribution to the PV effect. This led our investigation to test the blend between the same red polymer (P3HT) and a blue polymer (B1) with PC₆₁BM. Unfortunately, this also produced a device with significant trapping. However, with the formation of a ternary blend with the blue (B1) and green (G1) polymer a parallel-like BHJ device was formed. The EQE graphs illustrate these results, in which the EQE of the three ternary blends is compared to the binary systems.

Low efficiencies of ternary devices is explained in terms of transport properties issued from photogenerated current vs. light intensity and bias polarization studies. This physical approach is made in the framework of one polymer ensuring transport whereas the other is responsible for trapping (trap model). Additionally, the parallel diode circuit model approach was implemented in hopes to estimate the best blend combination.

In this study, we have pointed out a necessary condition involving the energy level design of the polymers in order to obtain efficient ternary blend solar cells. However, this is not a sufficient condition, the polymer compatibility, which directly relates to morphology, must also be considered. The future direction of this project will allow for the optimization of ternary blends for their future use in colour-tuned ink-jet printed PSCs.

References

- [1] R. H. Bube, *Photovoltaic Materials, vol. 1 of Series on Properties of Semiconductor Materials*. Imperial College Press, London, 1998.
- [2] P. Yu and M. Cardona, "Electronic Band Structures," in *Fundamentals of Semiconductors*, Springer Berlin Heidelberg, 2010, pp. 17–106.
- [3] D. M. Teegarden, *Polymer chemistry: introduction to an indispensable science*. Arlington, Va.: NSTA Press, National Science Teachers Association, 2004.
- [4] X. Guo, M. Baumgarten, and K. Müllen, "Designing π -conjugated polymers for organic electronics," *Prog. Polym. Sci.*, vol. 38, no. 12, pp. 1832–1908, Dec. 2013.
- [5] C. J. Brabec, Ed., *Organic photovoltaics: concepts and realization*. New York: Springer, 2003.
- [6] N. S. Sariciftci, L. Smilowitz, A. J. Heeger, and F. Wudl, "Photoinduced Electron Transfer from a Conducting Polymer to Buckminsterfullerene," *Science*, vol. 258, pp. 1474–1476, 1992.
- [7] C. W. Tang, "Two-layer organic photovoltaic cell," *Appl. Phys. Lett.*, vol. 48, no. 2, p. 183, 1986.
- [8] S. Morita, A. A. Zakhidov, and K. Yoshino, "Doping effect of buckminsterfullerene in conducting polymer: Change of absorption spectrum and quenching of luminescence," *Solid State Commun.*, vol. 82, no. 4, pp. 249–252, 1992.
- [9] B. C. Thompson and J. M. J. Fréchet, "Polymer–Fullerene Composite Solar Cells," *Angew. Chem. Int. Ed.*, vol. 47, no. 1, pp. 58–77, Jan. 2008.
- [10] Y. Şahin, S. Alem, R. de Bettignies, and J.-M. Nunzi, "Development of air stable polymer solar cells using an inverted gold on top anode structure," *Thin Solid Films*, vol. 476, no. 2, pp. 340–343, Apr. 2005.
- [11] S. E. Shaheen, M. S. White, D. C. Olson, N. Kopidakis, and D. S. Ginley, "Inverted bulk-heterojunction plastic solar cells," *SPIE Newsroom*, vol. 24, 2007.
- [12] G. Hadziioannou and G. G. Malliaras, *Semiconducting polymers 2. 2.*, 2 vols. Weinheim: Wiley-VCH, 2007.
- [13] G. Yu, J. Gao, J. C. Hummelen, F. Wudl, and A. J. Heeger, "Polymer photovoltaic cells: enhanced efficiencies via a network of internal donor-acceptor heterojunctions," *Sci.-AAAS-Wkly. Pap. Ed.*, vol. 270, no. 5243, pp. 1789–1790, 1995.
- [14] P. P. Khlyabich, B. Burkhart, and B. C. Thompson, "Efficient Ternary Blend Bulk Heterojunction Solar Cells with Tunable Open-Circuit Voltage," *J. Am. Chem. Soc.*, vol. 133, no. 37, pp. 14534–14537, Sep. 2011.
- [15] B. Lim, J. T. Bloking, A. Poncec, M. D. McGehee, and A. Sellinger, "Ternary Bulk Heterojunction Solar Cells: Addition of Soluble NIR Dyes for Photocurrent Generation beyond 800 nm," *ACS Appl. Mater. Interfaces*, vol. 6, no. 9, pp. 6905–6913, May 2014.
- [16] T. Ameri, P. Khoram, T. Heumüller, D. Baran, F. Machui, A. Troeger, V. Sgobba, D. M. Guldi, M. Halik, S. Rathgeber, U. Scherf, and C. J. Brabec, "Morphology analysis of near IR sensitized polymer/fullerene organic solar cells by implementing low bandgap heteroanalogue C-/Si-PCPDTBT," *J. Mater. Chem. A*, vol. 2, no. 45, pp. 19461–19472, Sep. 2014.
- [17] M. C. Chen, D. J. Liaw, Y. C. Huang, H. Y. Wu, and Y. Tai, "Improving the efficiency of organic solar cell with a novel ambipolar polymer to form ternary cascade structure," *Sol. Energy Mater. Sol. Cells*, vol. 95, no. 9, pp. 2621–2627, Sep. 2011.
- [18] L. Yang, H. Zhou, S. C. Price, and W. You, "Parallel-like Bulk Heterojunction Polymer Solar Cells," *J. Am. Chem. Soc.*, vol. 134, no. 12, pp. 5432–5435, Mar. 2012.
- [19] P. P. Khlyabich, B. Burkhart, and B. C. Thompson, "Compositional Dependence of the Open-Circuit Voltage in Ternary Blend Bulk Heterojunction Solar Cells Based on Two Donor Polymers," *J. Am. Chem. Soc.*, vol. 134, no. 22, pp. 9074–9077, Jun. 2012.

- [20] Y. (Michael) Yang, W. Chen, L. Dou, W.-H. Chang, H.-S. Duan, B. Bob, G. Li, and Y. Yang, "High-performance multiple-donor bulk heterojunction solar cells," *Nat. Photonics*, vol. 9, no. 3, pp. 190–198, Feb. 2015.
- [21] H. Fu, M. Choi, W. Luan, Y.-S. Kim, and S.-T. Tu, "Hybrid solar cells with an inverted structure: Nanodots incorporated ternary system," *Solid-State Electron.*, vol. 69, pp. 50–54, Mar. 2012.
- [22] L. Yang, L. Yan, and W. You, "Organic Solar Cells beyond One Pair of Donor–Acceptor: Ternary Blends and More," *J. Phys. Chem. Lett.*, vol. 4, no. 11, pp. 1802–1810, Jun. 2013.
- [23] S. Honda, H. Ohkita, H. Benten, and S. Ito, "Multi-colored dye sensitization of polymer/fullerene bulk heterojunction solar cells," *Chem. Commun.*, vol. 46, no. 35, p. 6596, 2010.
- [24] M. Koppe, H.-J. Egelhaaf, G. Dennler, M. C. Scharber, C. J. Brabec, P. Schilinsky, and C. N. Hoth, "Near IR Sensitization of Organic Bulk Heterojunction Solar Cells: Towards Optimization of the Spectral Response of Organic Solar Cells," *Adv. Funct. Mater.*, vol. 20, no. 2, pp. 338–346, Jan. 2010.
- [25] W. Shockley and H. J. Queisser, "Detailed Balance Limit of Efficiency of p-n Junction Solar Cells," *J. Appl. Phys.*, vol. 32, no. 3, p. 510, 1961.
- [26] B. M. van der Ende, L. Aarts, and A. Meijerink, "Lanthanide ions as spectral converters for solar cells," *Phys. Chem. Chem. Phys.*, vol. 11, no. 47, p. 11081, 2009.
- [27] A. K. Pandey and J.-M. Nunzi, "Upconversion injection in rubrene/perylene-diimide-heterostructure electroluminescent diodes," *Appl. Phys. Lett.*, vol. 90, no. 26, p. 263508, 2007.
- [28] Y. Kim, M. Shin, H. Kim, Y. Ha, and C.-S. Ha, "Influence of electron-donating polymer addition on the performance of polymer solar cells," *J. Phys. Appl. Phys.*, vol. 41, no. 22, p. 225101, Nov. 2008.
- [29] M. Campoy-Quiles, Y. Kanai, A. El-Basaty, H. Sakai, and H. Murata, "Ternary mixing: A simple method to tailor the morphology of organic solar cells," *Org. Electron.*, vol. 10, no. 6, pp. 1120–1132, Sep. 2009.
- [30] A. Ojala, H. Bürckstümmer, M. Stolte, R. Sens, H. Reichelt, P. Erk, J. Hwang, D. Hertel, K. Meerholz, and F. Würthner, "Parallel Bulk-Heterojunction Solar Cell by Electrostatically Driven Phase Separation," *Adv. Mater.*, vol. 23, no. 45, pp. 5398–5403, Dec. 2011.
- [31] P. P. Khlyabich, A. E. Rudenko, R. A. Street, and B. C. Thompson, "Influence of Polymer Compatibility on the Open-Circuit Voltage in Ternary Blend Bulk Heterojunction Solar Cells," *ACS Appl. Mater. Interfaces*, p. 140627080606003, Jun. 2014.
- [32] H. Yan, D. Li, Y. Zhang, Y. Yang, and Z. Wei, "Rational Design of Ternary-Phase Polymer Solar Cells by Controlling Polymer Phase Separation," *J. Phys. Chem. C*, vol. 118, no. 20, pp. 10552–10559, May 2014.
- [33] N. Li, P. Kubis, K. Forberich, T. Ameri, F. C. Krebs, and C. J. Brabec, "Towards large-scale production of solution-processed organic tandem modules based on ternary composites: Design of the intermediate layer, device optimization and laser based module processing," *Sol. Energy Mater. Sol. Cells*, vol. 120, pp. 701–708, Jan. 2014.
- [34] R. Lin, M. Wright, K. H. Chan, B. Puthen-Veetil, R. Sheng, X. Wen, and A. Uddin, "Performance improvement of low bandgap polymer bulk heterojunction solar cells by incorporating P3HT," *Org. Electron.*, vol. 15, no. 11, pp. 2837–2846, Nov. 2014.
- [35] L. Lu, T. Xu, W. Chen, E. S. Landry, and L. Yu, "Ternary blend polymer solar cells with enhanced power conversion efficiency," *Nat. Photonics*, vol. 8, no. 9, pp. 716–722, Aug. 2014.
- [36] R. A. Street, D. Davies, P. P. Khlyabich, B. Burkhart, and B. C. Thompson, "Origin of the Tunable Open-Circuit Voltage in Ternary Blend Bulk Heterojunction Organic Solar Cells," *J. Am. Chem. Soc.*, vol. 135, no. 3, pp. 986–989, Jan. 2013.

- [37] R. A. Street, P. P. Khlyabich, A. E. Rudenko, and B. C. Thompson, "Electronic States in Dilute Ternary Blend Organic Bulk Heterojunction Solar Cells," *J. Phys. Chem. C*, p. 141105083220002, Nov. 2014.
- [38] M. O'Connell, Ed., *Carbon nanotubes: properties and applications*. Boca Raton, FL: CRC/Taylor & Francis, 2006.
- [39] J. W. Wilder, L. C. Venema, A. G. Rinzler, R. E. Smalley, and C. Dekker, "Electronic structure of atomically resolved carbon nanotubes," *Nature*, vol. 391, no. 6662, pp. 59–62, 1998.
- [40] S. Saito and A. Zettl, *Carbon Nanotubes: Quantum Cylinders of Graphene: Quantum Cylinders of Graphene*, vol. 3. Elsevier, 2008.
- [41] P. J. Harris and P. J. F. Harris, *Carbon nanotube science: synthesis, properties and applications*. Cambridge University Press, 2009.
- [42] N. W. S. Kam and H. Dai, "Carbon Nanotubes as Intracellular Protein Transporters: Generality and Biological Functionality," *J. Am. Chem. Soc.*, vol. 127, no. 16, pp. 6021–6026, Apr. 2005.
- [43] M. Zheng, A. Jagota, E. D. Semke, B. A. Diner, R. S. Mclean, S. R. Lustig, R. E. Richardson, and N. G. Tassi, "DNA-assisted dispersion and separation of carbon nanotubes," *Nat. Mater.*, vol. 2, no. 5, pp. 338–342, May 2003.
- [44] J. Liu, "Fullerene Pipes," *Science*, vol. 280, no. 5367, pp. 1253–1256, May 1998.
- [45] G. Viswanathan, N. Chakrapani, H. Yang, B. Wei, H. Chung, K. Cho, C. Y. Ryu, and P. M. Ajayan, "Single-step in situ synthesis of polymer-grafted single-wall nanotube composites," *J. Am. Chem. Soc.*, vol. 125, no. 31, pp. 9258–9259, 2003.
- [46] Z. Jin, L. Huang, S. H. Goh, G. Xu, and W. Ji, "Characterization and nonlinear optical properties of a poly (acrylic acid)–surfactant–multi-walled carbon nanotube complex," *Chem. Phys. Lett.*, vol. 332, no. 5, pp. 461–466, 2000.
- [47] R. J. Chen, Y. Zhang, D. Wang, and H. Dai, "Noncovalent Sidewall Functionalization of Single-Walled Carbon Nanotubes for Protein Immobilization," *J. Am. Chem. Soc.*, vol. 123, no. 16, pp. 3838–3839, Apr. 2001.
- [48] M. J. O'Connell, P. Boul, L. M. Ericson, C. Huffman, Y. Wang, E. Haroz, C. Kuper, J. Tour, K. D. Ausman, and R. E. Smalley, "Reversible water-solubilization of single-walled carbon nanotubes by polymer wrapping," *Chem. Phys. Lett.*, vol. 342, no. 3, pp. 265–271, 2001.
- [49] E. Kymakis and G. A. J. Amaratunga, "Single-wall carbon nanotube/conjugated polymer photovoltaic devices," *Appl. Phys. Lett.*, vol. 80, no. 1, p. 112, 2002.
- [50] Z. Li, V. Saini, E. Dervishi, V. P. Kunets, J. Zhang, Y. Xu, A. R. Biris, G. J. Salamo, and A. S. Biris, "Polymer functionalized n-type single wall carbon nanotube photovoltaic devices," *Appl. Phys. Lett.*, vol. 96, no. 3, p. 033110, 2010.
- [51] Y. Kanai and J. C. Grossman, "Role of Semiconducting and Metallic Tubes in P3HT/Carbon-Nanotube Photovoltaic Heterojunctions: Density Functional Theory Calculations," *Nano Lett.*, vol. 8, no. 3, pp. 908–912, Mar. 2008.
- [52] M.-H. Ham, G. L. C. Paulus, C. Y. Lee, C. Song, K. Kalantar-zadeh, W. Choi, J.-H. Han, and M. S. Strano, "Evidence for High-Efficiency Exciton Dissociation at Polymer/Single-Walled Carbon Nanotube Interfaces in Planar Nano-heterojunction Photovoltaics," *ACS Nano*, vol. 4, no. 10, pp. 6251–6259, Oct. 2010.
- [53] A. F. Nogueira, B. S. Lomba, M. A. Soto-Oviedo, C. R. D. Correia, P. Corio, C. A. Furtado, and I. A. Hummelgen, "Polymer Solar Cells Using Single-Wall Carbon Nanotubes Modified with Thiophene Pedant Groups," *J. Phys. Chem. C*, vol. 111, no. 49, pp. 18431–18438, Dec. 2007.
- [54] R. L. Patyk, B. S. Lomba, A. F. Nogueira, C. A. Furtado, A. P. Santos, R. M. Q. Mello, L. Micaroni, and I. A. Hummelgen, "Carbon nanotube–polybithiophene photovoltaic devices with high open-circuit voltage," *Phys. Status Solidi RRL – Rapid Res. Lett.*, vol. 1, no. 1, pp. R43–R45, Jan. 2007.

- [55] B. Pradhan, S. K. Batabyal, and A. J. Pal, "Functionalized carbon nanotubes in donor/acceptor-type photovoltaic devices," *Appl. Phys. Lett.*, vol. 88, no. 9, p. 093106, 2006.
- [56] C. Li, Y. Chen, Y. Wang, Z. Iqbal, M. Chhowalla, and S. Mitra, "A fullerene?single wall carbon nanotube complex for polymer bulk heterojunction photovoltaic cells," *J. Mater. Chem.*, vol. 17, no. 23, p. 2406, 2007.
- [57] J. Arranz-Andrés and W. J. Blau, "Enhanced device performance using different carbon nanotube types in polymer photovoltaic devices," *Carbon*, vol. 46, no. 15, pp. 2067–2075, Dec. 2008.
- [58] S. Berson, R. de Bettignies, S. Bailly, S. Guillerez, and B. Joussetme, "Elaboration of P3HT/CNT/PCBM Composites for Organic Photovoltaic Cells," *Adv. Funct. Mater.*, vol. 17, no. 16, pp. 3363–3370, Nov. 2007.
- [59] E. Kymakis and G. A. Amaratunga, "Carbon nanotubes as electron acceptors in polymeric photovoltaics," *Rev. Adv. Mater. Sci.*, vol. 10, no. 4, pp. 300–305, 2005.
- [60] E. Kymakis, P. Servati, P. Tzanetakis, E. Koudoumas, N. Kornilios, I. Rompogiannakis, Y. Franghiadakis, and G. A. J. Amaratunga, "Effective mobility and photocurrent in carbon nanotube–polymer composite photovoltaic cells," *Nanotechnology*, vol. 18, no. 43, p. 435702, Oct. 2007.
- [61] H. Derbal-Habak, C. Bergeret, J. Cousseau, and J.-M. Nunzi, "Increase of open circuit voltage of polymer bulk heterojunction solar cell by functionalized single walled carbon nanotubes," *Adv. Device Mater.*, p. 2055031615Y.000, Jan. 2015.
- [62] R. Radbeh, E. Parbaile, M. Chakaroun, B. Ratier, M. Aldissi, and A. Moliton, "Enhanced efficiency of polymeric solar cells via alignment of carbon nanotubes," *Polym. Int.*, vol. 59, no. 11, pp. 1514–1519, Nov. 2010.
- [63] S. Berson, R. de Bettignies, S. Bailly, S. Guillerez, and B. Joussetme, "Elaboration of P3HT/CNT/PCBM Composites for Organic Photovoltaic Cells," *Adv. Funct. Mater.*, vol. 17, no. 16, pp. 3363–3370, Nov. 2007.
- [64] J. M. Lee, J. S. Park, S. H. Lee, H. Kim, S. Yoo, and S. O. Kim, "Selective Electron- or Hole-Transport Enhancement in Bulk-Heterojunction Organic Solar Cells with N- or B-Doped Carbon Nanotubes," *Adv. Mater.*, vol. 23, no. 5, pp. 629–633, Feb. 2011.
- [65] J. Geng and T. Zeng, "Influence of Single-Walled Carbon Nanotubes Induced Crystallinity Enhancement and Morphology Change on Polymer Photovoltaic Devices," *J. Am. Chem. Soc.*, vol. 128, no. 51, pp. 16827–16833, Dec. 2006.
- [66] F. C. Krebs, "Fabrication and processing of polymer solar cells: A review of printing and coating techniques," *Sol. Energy Mater. Sol. Cells*, vol. 93, no. 4, pp. 394–412, Apr. 2009.
- [67] C. N. Hoth, S. A. Choulis, P. Schilinsky, and C. J. Brabec, "High Photovoltaic Performance of Inkjet Printed Polymer:Fullerene Blends," *Adv. Mater.*, vol. 19, no. 22, pp. 3973–3978, Nov. 2007.
- [68] C. Turcu, *Radio frequency identification fundamentals and applications, design methods and solutions*. Vukovar: Intech, 2010.
- [69] C. N. Hoth, P. Schilinsky, S. A. Choulis, and C. J. Brabec, "Printing Highly Efficient Organic Solar Cells," *Nano Lett.*, vol. 8, no. 9, pp. 2806–2813, Sep. 2008.
- [70] A. Kamyshny, J. Steinke, and S. Magdassi, "Metal-based inkjet inks for printed electronics," *Open Appl. Phys. J.*, vol. 4, pp. 19–36, 2011.
- [71] S. K. Hau, H.-L. Yip, N. S. Baek, J. Zou, K. O'Malley, and A. K.-Y. Jen, "Air-stable inverted flexible polymer solar cells using zinc oxide nanoparticles as an electron selective layer," *Appl. Phys. Lett.*, vol. 92, no. 25, p. 253301, 2008.
- [72] L. Sun, W. Shen, W. Chen, X. Bao, N. Wang, X. Dou, L. Han, and S. Wen, "Simple solution-processed titanium oxide electron transport layer for efficient inverted polymer solar cells," *Thin Solid Films*, vol. 573, pp. 134–139, Dec. 2014.

- [73] K.-L. Ou, D. Tadytin, K. Xerxes Steirer, D. Placencia, M. Nguyen, P. Lee, and N. R. Armstrong, "Titanium dioxide electron-selective interlayers created by chemical vapor deposition for inverted configuration organic solar cells," *J. Mater. Chem. A*, vol. 1, no. 23, p. 6794, 2013.
- [74] J. Huang, Z. Xu, and Y. Yang, "Low-Work-Function Surface Formed by Solution-Processed and Thermally Deposited Nanoscale Layers of Cesium Carbonate," *Adv. Funct. Mater.*, vol. 17, no. 12, pp. 1966–1973, Aug. 2007.
- [75] M. S. White, D. C. Olson, S. E. Shaheen, N. Kopidakis, and D. S. Ginley, "Inverted bulk-heterojunction organic photovoltaic device using a solution-derived ZnO underlayer," *Appl. Phys. Lett.*, vol. 89, no. 14, p. 143517, 2006.
- [76] S. H. Eom, H. Park, S. H. Mujawar, S. C. Yoon, S.-S. Kim, S.-I. Na, S.-J. Kang, D. Khim, D.-Y. Kim, and S.-H. Lee, "High efficiency polymer solar cells via sequential inkjet-printing of PEDOT:PSS and P3HT:PCBM inks with additives," *Org. Electron.*, vol. 11, no. 9, pp. 1516–1522, Sep. 2010.
- [77] T. Aernouts, T. Aleksandrov, C. Girotto, J. Genoe, and J. Poortmans, "Polymer based organic solar cells using ink-jet printed active layers," *Appl. Phys. Lett.*, vol. 92, no. 3, p. 033306, 2008.
- [78] A. Lange, M. Wegener, C. Boeffel, B. Fischer, A. Wedel, and D. Neher, "A new approach to the solvent system for inkjet-printed P3HT:PCBM solar cells and its use in devices with printed passive and active layers," *Sol. Energy Mater. Sol. Cells*, vol. 94, no. 10, pp. 1816–1821, Oct. 2010.
- [79] C. N. Hoth, S. A. Choulis, P. Schilinsky, and C. J. Brabec, "On the effect of poly(3-hexylthiophene) regioregularity on inkjet printed organic solar cells," *J. Mater. Chem.*, vol. 19, no. 30, p. 5398, 2009.
- [80] V. Fauzia, A. A. Umar, M. M. Salleh, and M. Yahaya, "The effect of solvent on the morphology of an inkjet printed active layer of bulk heterojunction solar cells," *Adv. Nat. Sci. Nanosci. Nanotechnol.*, vol. 2, no. 1, p. 015014, Mar. 2011.
- [81] Y.-H. Lin, P.-C. Yang, J.-S. Huang, G.-D. Huang, I.-J. Wang, W.-H. Wu, M.-Y. Lin, W.-F. Su, and C.-F. Lin, "High-efficiency inverted polymer solar cells with solution-processed metal oxides," *Sol. Energy Mater. Sol. Cells*, vol. 95, no. 8, pp. 2511–2515, Aug. 2011.
- [82] J. Meyer, S. Hamwi, M. Kröger, W. Kowalsky, T. Riedl, and A. Kahn, "Transition Metal Oxides for Organic Electronics: Energetics, Device Physics and Applications," *Adv. Mater.*, vol. 24, no. 40, pp. 5408–5427, Oct. 2012.
- [83] M. T. Greiner, L. Chai, M. G. Helander, W.-M. Tang, and Z.-H. Lu, "Transition Metal Oxide Work Functions: The Influence of Cation Oxidation State and Oxygen Vacancies," *Adv. Funct. Mater.*, vol. 22, no. 21, pp. 4557–4568, Nov. 2012.
- [84] P.-Y. Ho, J.-Y. Sun, S.-H. Kao, C.-Y. Kao, S.-H. Lin, S. Lan, W.-H. Tseng, C.-I. Wu, and C.-F. Lin, "The effects of MoO₃ treatment on inverted PBDTTT-C:PC71BM solar cells," *Sol. Energy Mater. Sol. Cells*, vol. 119, pp. 235–240, Dec. 2013.
- [85] L. Chen, C. Xie, and Y. Chen, "Optimization of the Power Conversion Efficiency of Room Temperature-Fabricated Polymer Solar Cells Utilizing Solution Processed Tungsten Oxide and Conjugated Polyelectrolyte as Electrode Interlayer," *Adv. Funct. Mater.*, vol. 24, no. 25, pp. 3986–3995, Jul. 2014.
- [86] P.-O. Morin, T. Bura, B. Sun, S. I. Gorelsky, Y. Li, and M. Leclerc, "Conjugated Polymers à la Carte from Time-Controlled Direct (Hetero)Arylation Polymerization," *ACS Macro Lett.*, vol. 4, no. 1, pp. 21–24, Jan. 2015.
- [87] C. Bergeret, J. Cousseau, V. Fernandez, J.-Y. Mevellec, and S. Lefrant, "Spectroscopic Evidence of Carbon Nanotubes' Metallic Character Loss Induced by Covalent Functionalization via Nitric Acid Purification," *J. Phys. Chem. C*, vol. 112, no. 42, pp. 16411–16416, Oct. 2008.

- [88] O. Synooka, K.-R. Eberhardt, and H. Hoppe, "Chlorine-free processed high performance organic solar cells," *RSC Adv.*, vol. 4, no. 32, p. 16681, 2014.
- [89] Y. Yao, J. Hou, Z. Xu, G. Li, and Y. Yang, "Effects of Solvent Mixtures on the Nanoscale Phase Separation in Polymer Solar Cells," *Adv. Funct. Mater.*, vol. 18, no. 12, pp. 1783–1789, Jun. 2008.
- [90] J.-F. Chang, B. Sun, D. W. Breiby, M. M. Nielsen, T. I. Sölling, M. Giles, I. McCulloch, and H. Sirringhaus, "Enhanced Mobility of Poly(3-hexylthiophene) Transistors by Spin-Coating from High-Boiling-Point Solvents," *Chem. Mater.*, vol. 16, no. 23, pp. 4772–4776, Nov. 2004.
- [91] K.-S. Chen, H.-L. Yip, C. W. Schlenker, D. S. Ginger, and A. K.-Y. Jen, "Halogen-free solvent processing for sustainable development of high efficiency organic solar cells," *Org. Electron.*, vol. 13, no. 12, pp. 2870–2878, Dec. 2012.
- [92] C.-D. Park, T. A. Fleetham, J. Li, and B. D. Vogt, "High performance bulk-heterojunction organic solar cells fabricated with non-halogenated solvent processing," *Org. Electron.*, vol. 12, no. 9, pp. 1465–1470, Sep. 2011.
- [93] F. Zhang, K. G. Jespersen, C. Björström, M. Svensson, M. R. Andersson, V. Sundström, K. Magnusson, E. Moons, A. Yartsev, and O. Inganäs, "Influence of Solvent Mixing on the Morphology and Performance of Solar Cells Based on Polyfluorene Copolymer/Fullerene Blends," *Adv. Funct. Mater.*, vol. 16, no. 5, pp. 667–674, Mar. 2006.
- [94] R. Mens, F. Demir, G. Van Assche, B. Van Mele, D. Vanderzande, and P. Adriaensens, "Influence of the processing solvent on the photoactive layer nanomorphology of P3HT/PC60BM solar cells," *J. Polym. Sci. Part Polym. Chem.*, vol. 50, no. 5, pp. 1037–1041, Mar. 2012.
- [95] C.-C. Chueh, K. Yao, H.-L. Yip, C.-Y. Chang, Y.-X. Xu, K.-S. Chen, C.-Z. Li, P. Liu, F. Huang, Y. Chen, W.-C. Chen, and A. K.-Y. Jen, "Non-halogenated solvents for environmentally friendly processing of high-performance bulk-heterojunction polymer solar cells," *Energy Environ. Sci.*, vol. 6, no. 11, p. 3241, 2013.
- [96] M. T. Dang, G. Wantz, H. Bejbouji, M. Urien, O. J. Dautel, L. Vignau, and L. Hirsch, "Polymeric solar cells based on P3HT:PCBM: Role of the casting solvent," *Sol. Energy Mater. Sol. Cells*, vol. 95, no. 12, pp. 3408–3418, Dec. 2011.
- [97] J. Jaczewska, A. Budkowski, A. Bernasik, E. Moons, and J. Rysz, "Polymer vs Solvent Diagram of Film Structures Formed in Spin-Cast Poly(3-alkylthiophene) Blends," *Macromolecules*, vol. 41, no. 13, pp. 4802–4810, Jul. 2008.
- [98] F. Machui, S. Langner, X. Zhu, S. Abbott, and C. J. Brabec, "Determination of the P3HT:PCBM solubility parameters via a binary solvent gradient method: Impact of solubility on the photovoltaic performance," *Sol. Energy Mater. Sol. Cells*, vol. 100, pp. 138–146, May 2012.
- [99] K. W. Chou, B. Yan, R. Li, E. Q. Li, K. Zhao, D. H. Anjum, S. Alvarez, R. Gassaway, A. Biocca, S. T. Thoroddsen, A. Hexemer, and A. Amassian, "Spin-Cast Bulk Heterojunction Solar Cells: A Dynamical Investigation," *Adv. Mater.*, vol. 25, no. 13, pp. 1923–1929, Apr. 2013.
- [100] M. T. Dang, L. Hirsch, G. Wantz, and J. D. Wuest, "Controlling the Morphology and Performance of Bulk Heterojunctions in Solar Cells. Lessons Learned from the Benchmark Poly(3-hexylthiophene):[6,6]-Phenyl-C₆₁-butyric Acid Methyl Ester System," *Chem. Rev.*, vol. 113, no. 5, pp. 3734–3765, May 2013.
- [101] P. P. Khlyabich, A. E. Rudenko, B. Burkhart, and B. C. Thompson, "Contrasting Performance of Donor–Acceptor Copolymer Pairs in Ternary Blend Solar Cells and Two-Acceptor Copolymers in Binary Blend Solar Cells," *ACS Appl. Mater. Interfaces*, p. 150126151556005, Jan. 2015.
- [102] S. Kouijzer, W. Li, M. M. Wienk, and R. A. Janssen, "Charge transfer state energy in ternary bulk-heterojunction polymer–fullerene solar cells," *J. Photonics Energy*, vol. 5, no. 1, pp. 057203–057203, 2015.

- [103] G. F. A. Dibb, F. C. Jamieson, A. Maurano, J. Nelson, and J. R. Durrant, "Limits on the Fill Factor in Organic Photovoltaics: Distinguishing Nongeminate and Geminate Recombination Mechanisms," *J. Phys. Chem. Lett.*, vol. 4, no. 5, pp. 803–808, Mar. 2013.
- [104] J. Rostalski and D. Meissner, "Monochromatic versus solar efficiencies of organic solar cells," *Sol. Energy Mater. Sol. Cells*, vol. 61, no. 1, pp. 87–95, 2000.
- [105] V. Shrotriya, G. Li, Y. Yao, T. Moriarty, K. Emery, and Y. Yang, "Accurate Measurement and Characterization of Organic Solar Cells," *Adv. Funct. Mater.*, vol. 16, no. 15, pp. 2016–2023, Oct. 2006.
- [106] J. M. Kroon, M. M. Wienk, W. J. H. Verhees, and J. C. Hummelen, "Accurate efficiency determination and stability studies of conjugated polymer/fullerene solar cells," *Thin Solid Films*, vol. 403–404, pp. 223–228, Feb. 2002.

Appendices A-G

Appendix A

Colour variation of photo-active layers

Binary Active Layer Blends

Images of transmitted light through binary photo-active layer blends. Blends consist of a donor polymer (P3HT, B1, or G1) and a fullerene derivative acceptor (PC₆₁BM, PC₇₁BM, or ICBA).

P3HT:acceptor



P3HT:[70]PCBM



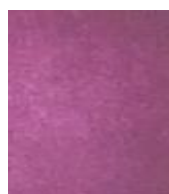
P3HT:ICBA



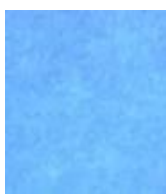
P3HT:[60]PCBM

Figure 0-1: Image of transmitted light through a PET/ITO/ZnO/P3HT:acceptor/PEDOT:PSS substrate.

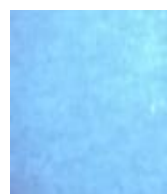
B1:acceptor



B1:[70]PCBM



B1:ICBA



B1:[60]PCBM

Figure 0-2: Image of transmitted light through a PET/ITO/ZnO/B1:acceptor/PEDOT:PSS substrate.

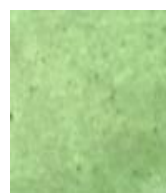
G1:acceptor



G1:[70]PCBM



G1:ICBA



G1:[60]PCBM

Figure 0-3: Image of transmitted light through a PET/ITO/ZnO/G1:acceptor/PEDOT:PSS substrate.

Ternary Active Layer Blends

Images of transmitted light through ternary photo-active layer blends. Blends consist of 1:1 weight % of two donor polymers (P3HT, B1, or G1) and a fullerene derivative acceptor (PC₆₁BM).



P3HT:B1:[60]PCBM



B1:G1:[60]PCBM



P3HT:G1:[60]PCBM

Figure 0-4: Image of transmitted light through a PET/ITO/ZnO/polymer:polymer:acceptor/PEDOT:PSS substrate.

Colourimetry

Colorimetry of the polymer films was conducted via reflectance spectroscopy using an Agilent Cary 300 spectrophotometer. In the following figure, the colour of the films is plotted on a four point reflected colour scale (degree of yellow, red, blue and green).

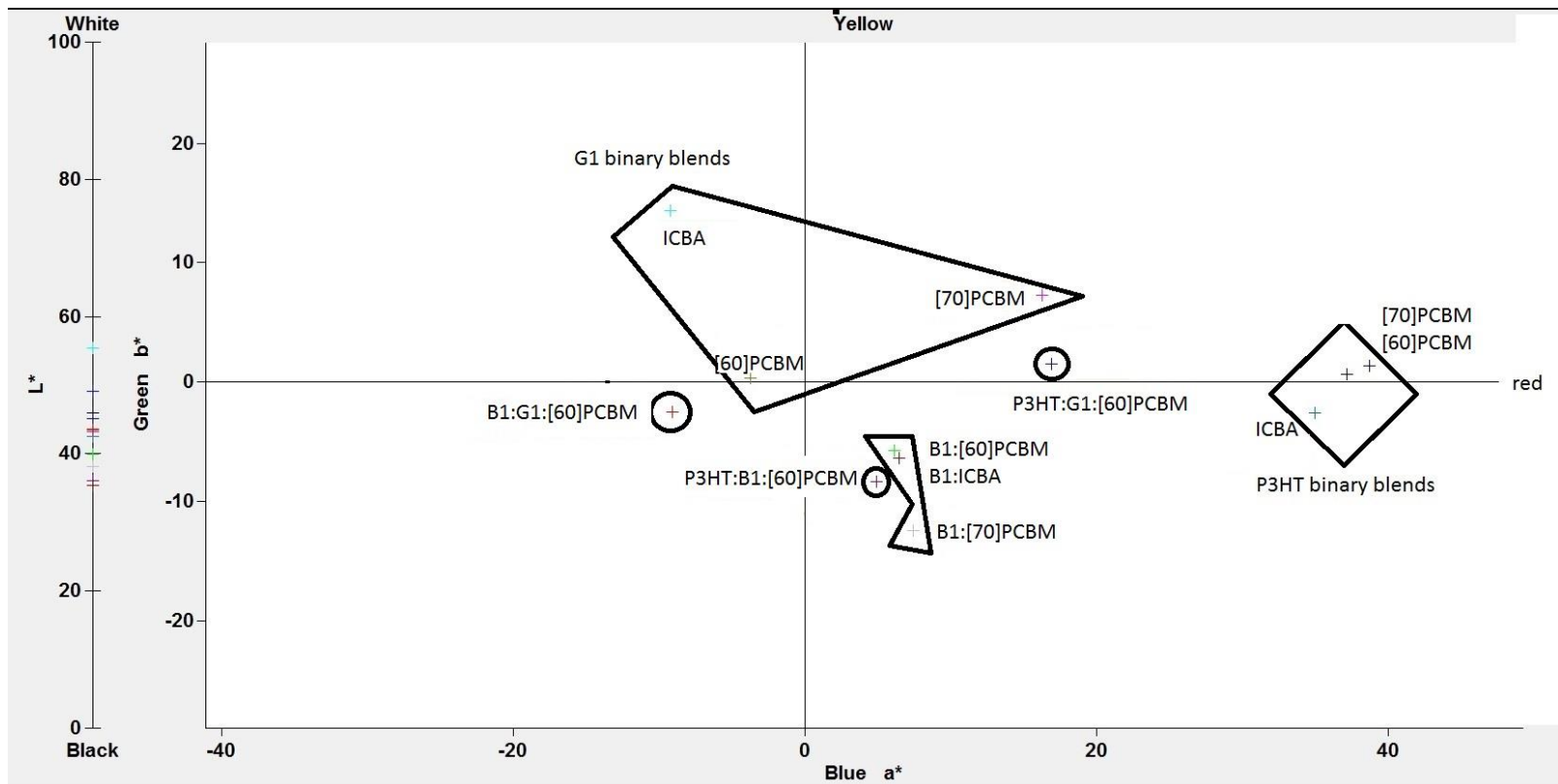


Figure 0-5: Colourimetry of the binary polymer:acceptor blends and the 50% ternary blends (P1:P2:[60]PCBM)

Appendix B

UV-vis Absorption Spectroscopy

Binary blends (P3HT, B1, and G1 with PC₆₁BM, PC₇₁BM, or ICBA)

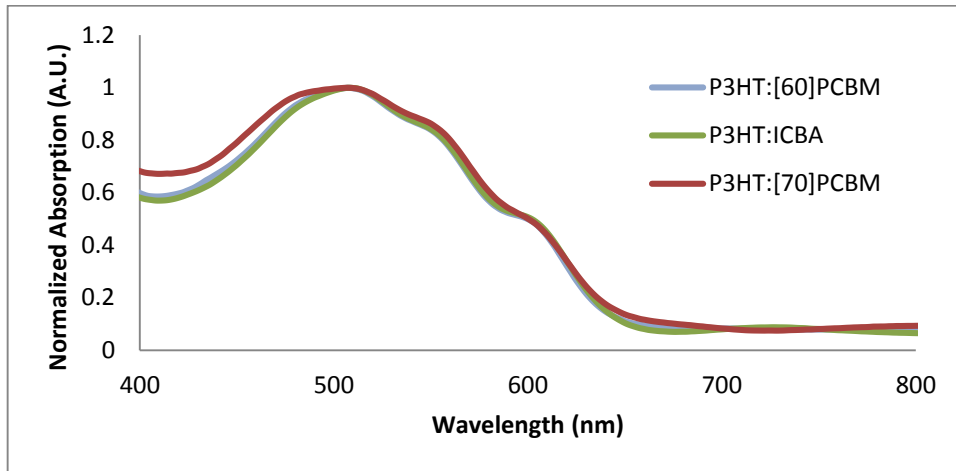


Figure 0-6: UV-vis absorption of P3HT binary active layers with PC₆₁BM, PC₇₁BM, or ICBA.

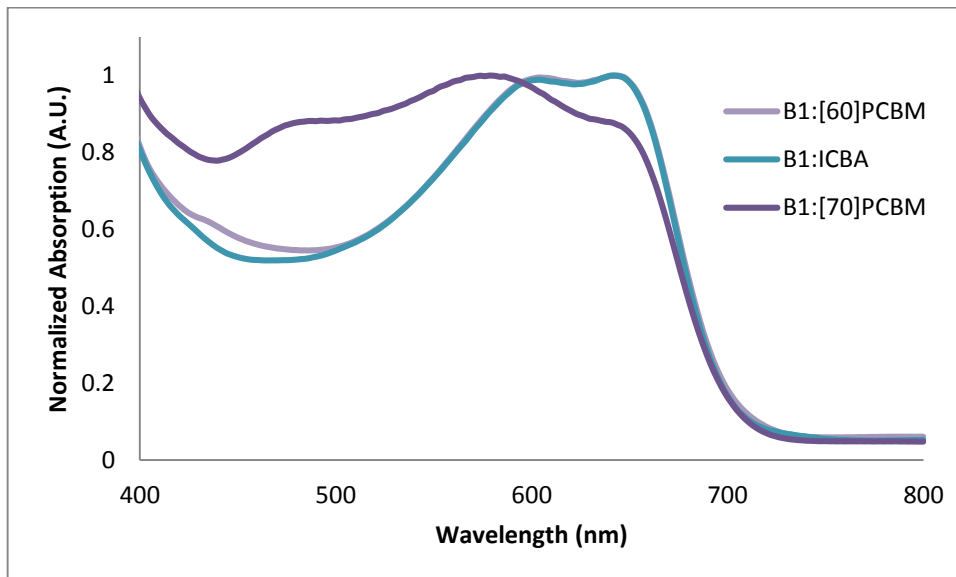


Figure 0-7: UV-vis absorption of B1 binary active layers with PC₆₁BM, PC₇₁BM, or ICBA.

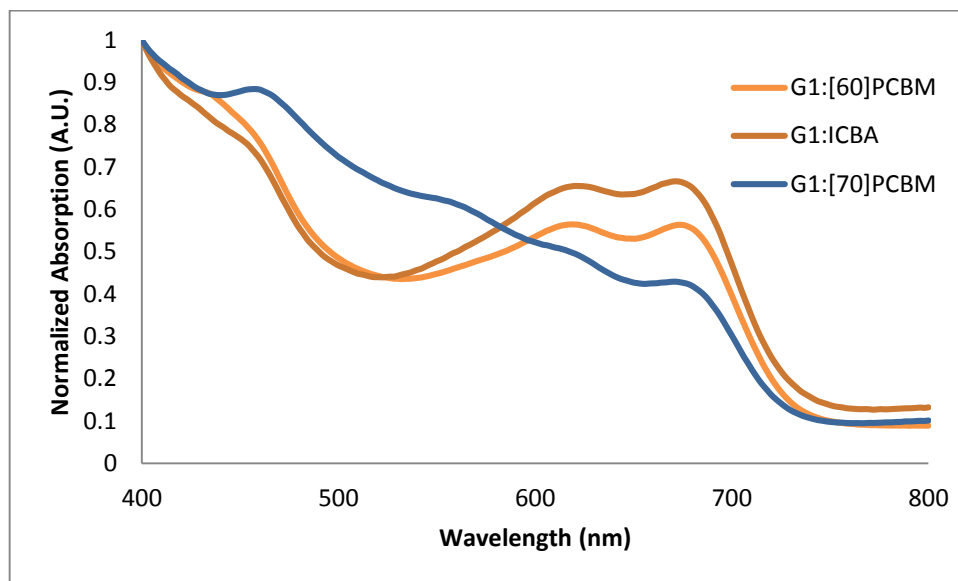


Figure 0-8: UV-vis absorption of G1 binary active layers with PC₆₁BM, PC₇₁BM, or ICBA.

Binary polymer:polymer blends

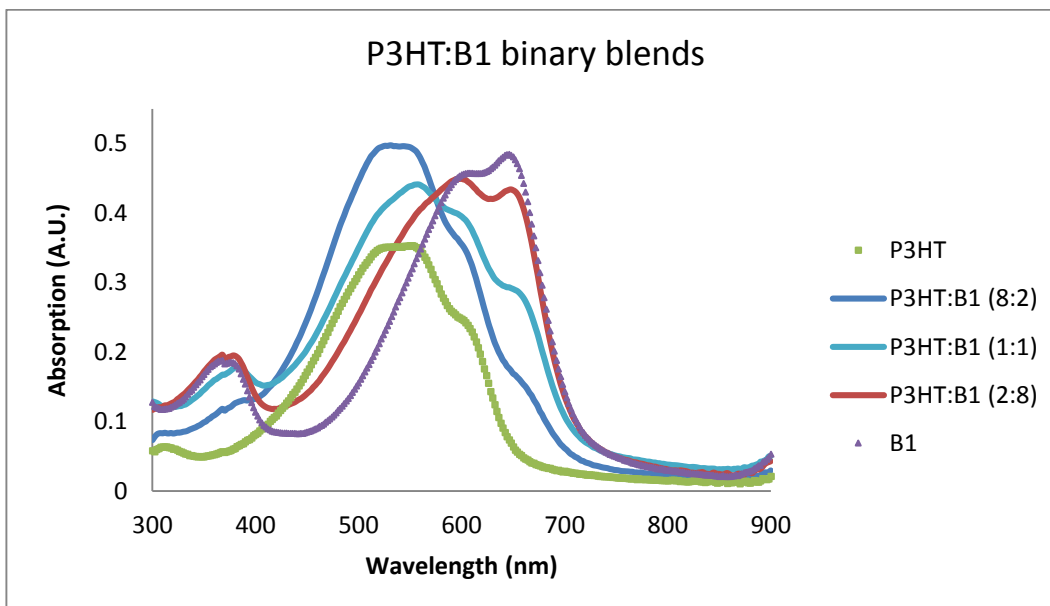


Figure 0-9: UV-vis absorption of P3HT:B1 binary blend films (60 nm films).

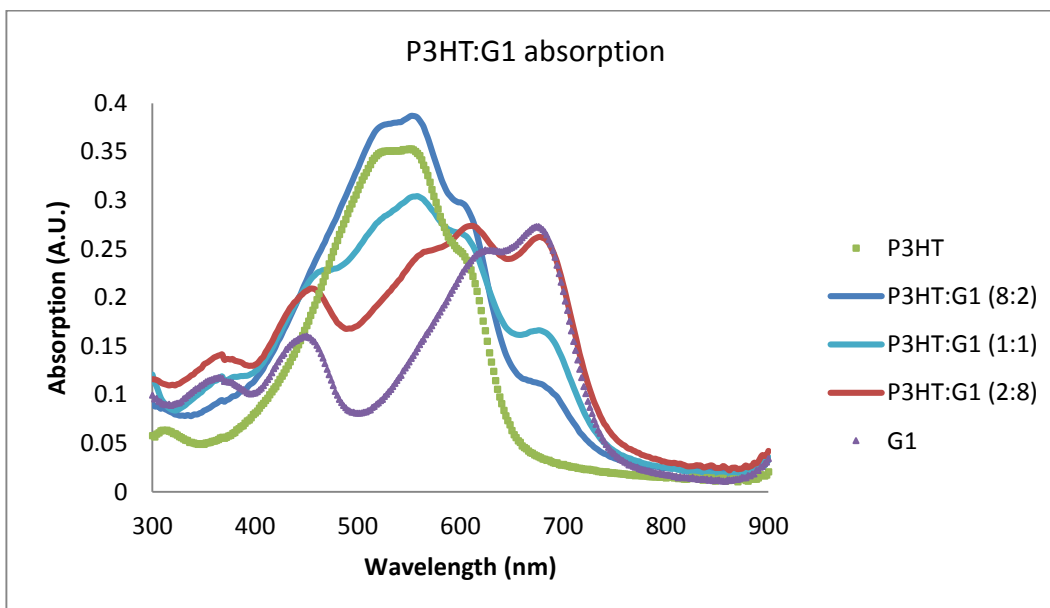


Figure 0-10: UV-vis absorption of P3HT:G1 binary blend films (60 nm films).

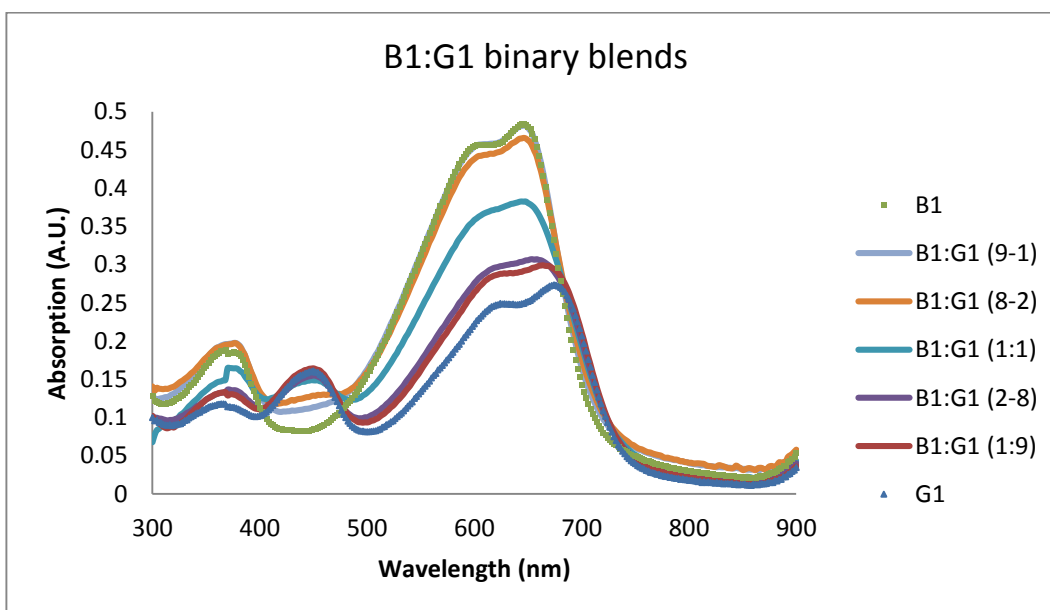


Figure 0-11: UV-vis absorption of B1:G1 binary blend films (60 nm films).

Ternary blends (P3HT, B1, and G1 with PC₆₁BM)

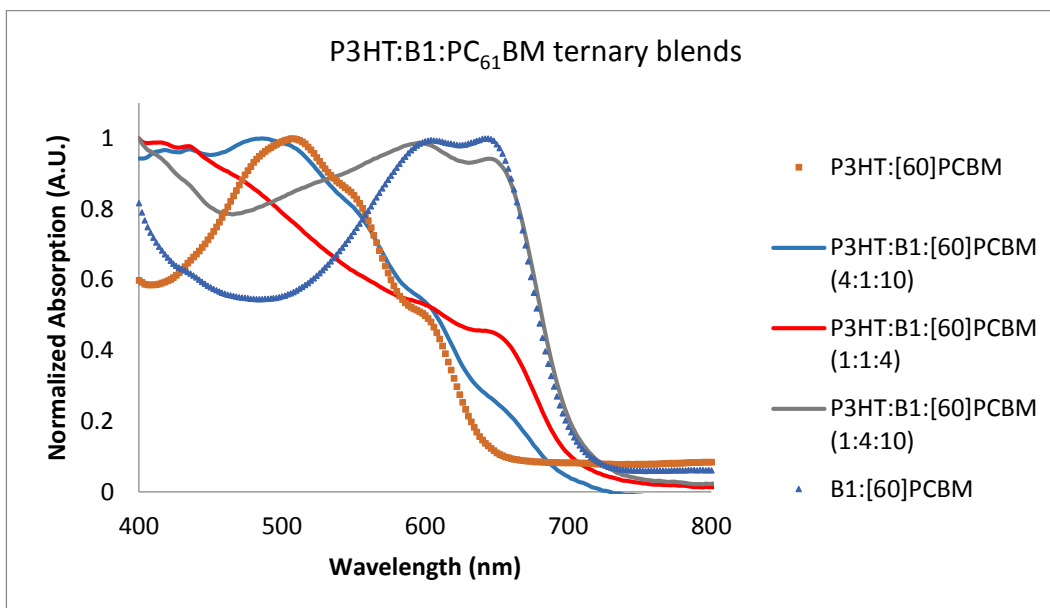


Figure 0-12: UV-vis absorption of P3HT:B1:PC₆₁BM ternary active layers (80%, 50% and 20% relative P3HT:B1 concentrations) and their corresponding binary blends (dotted).

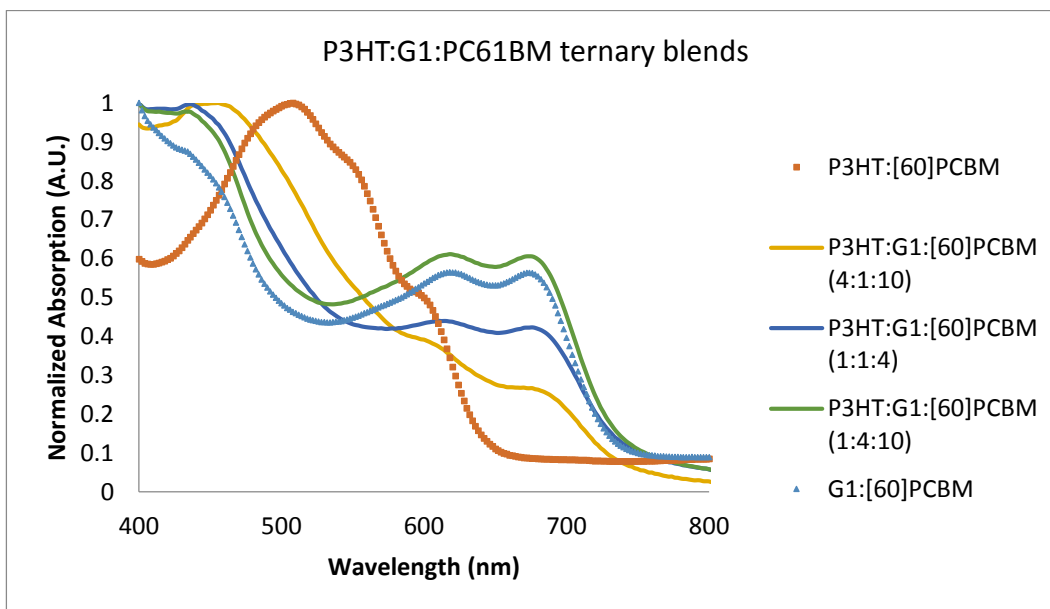


Figure 0-13: UV-vis absorption of P3HT:G1:PC₆₁BM ternary active layers (80%, 50% and 20% relative P3HT:G1 concentrations) and their corresponding binary blends (dotted).

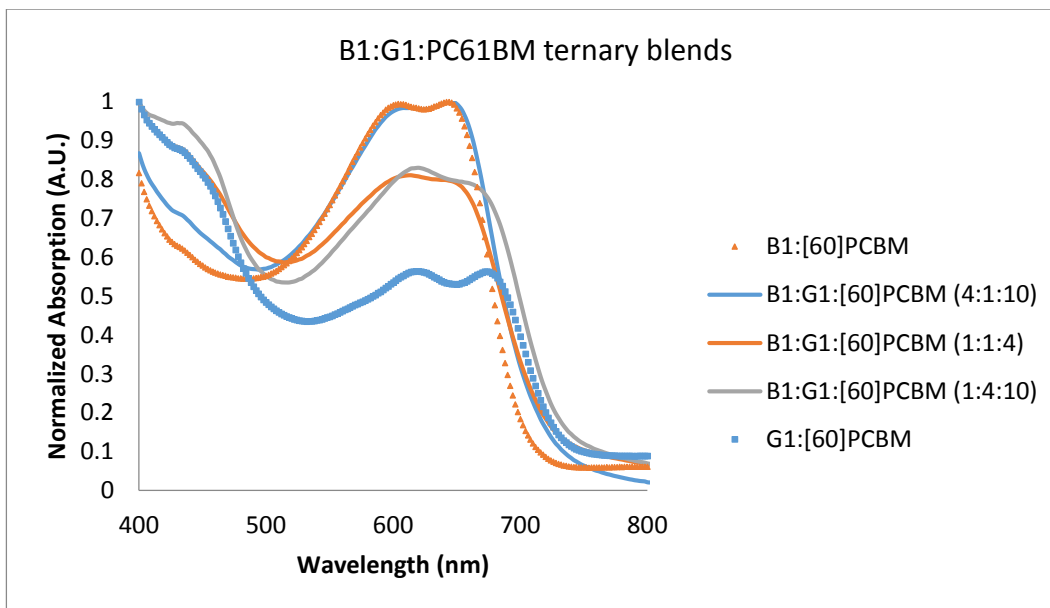


Figure 0-14: UV-vis absorption of B1:G1:PC₆₁BM ternary active layers (80%, 50% and 20% relative B1:G1 concentrations) and their corresponding binary blends (dotted).

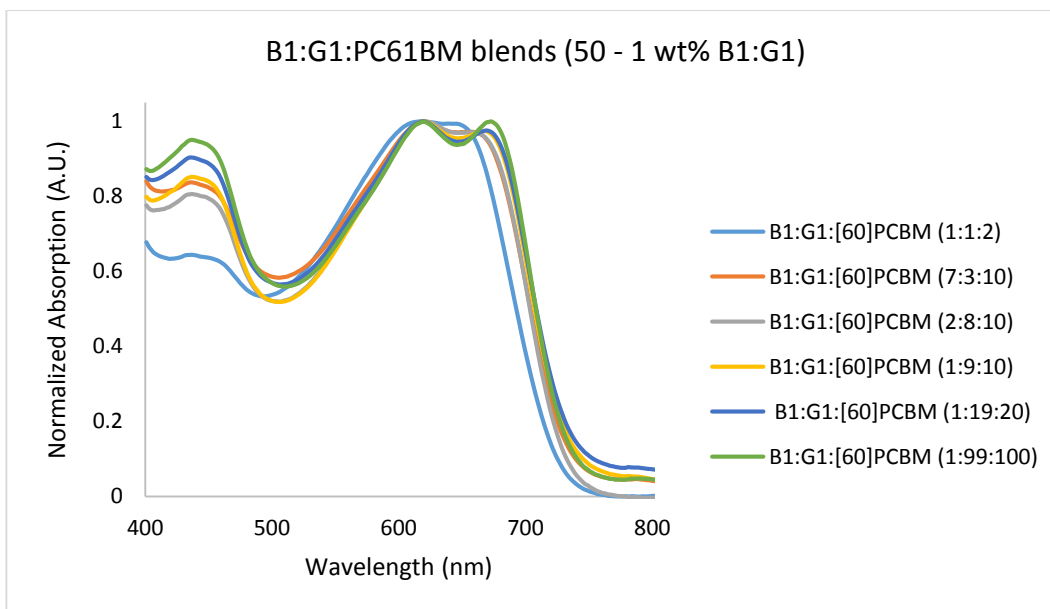


Figure 0-15: UV-vis absorption of B1:G1:PC₆₁BM ternary active layers (50, 30, 20, 10, 5, and 1 wt% relative B1:G1 concentrations).

Appendix C

Photoluminescence Spectroscopy of Polymer Films

Neat polymer films

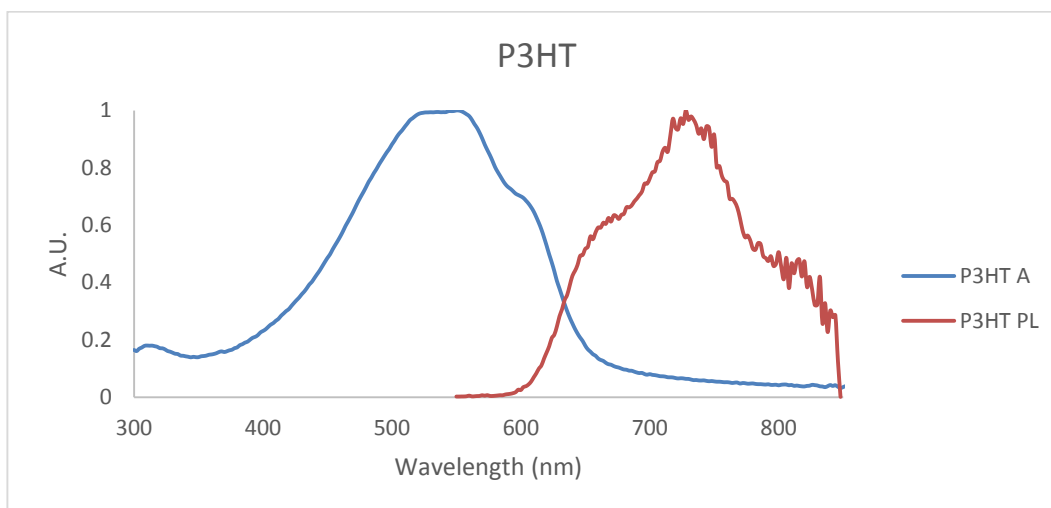


Figure 0-16: UV-vis absorption (A) and emission spectra (PL) of a P3HT film (60 nm). Excitation for photoluminescence was performed by a 509.2 nm laser.

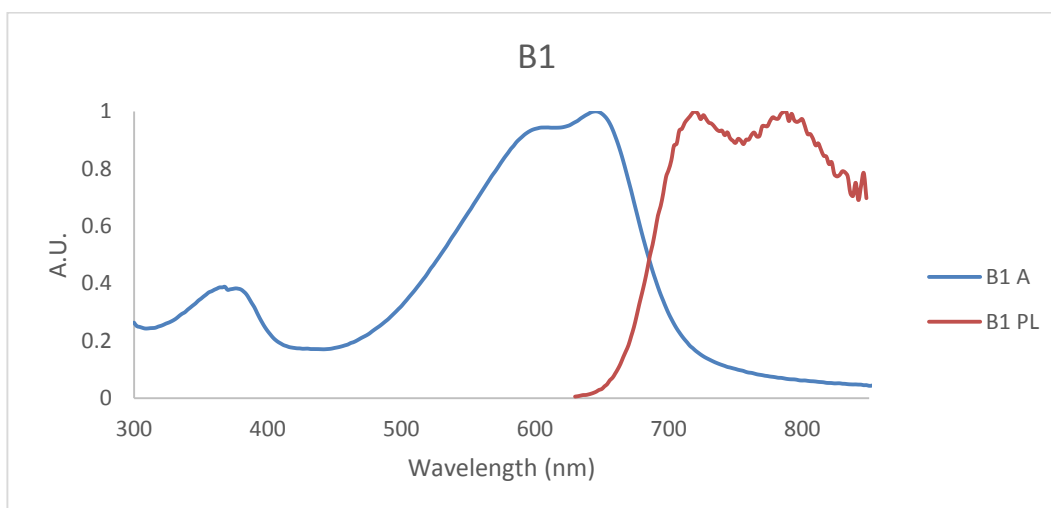


Figure 0-17: UV-vis absorption (A) and emission spectra (PL) of a B1 film (60 nm). Excitation for photoluminescence was performed by a 509.2 nm laser.

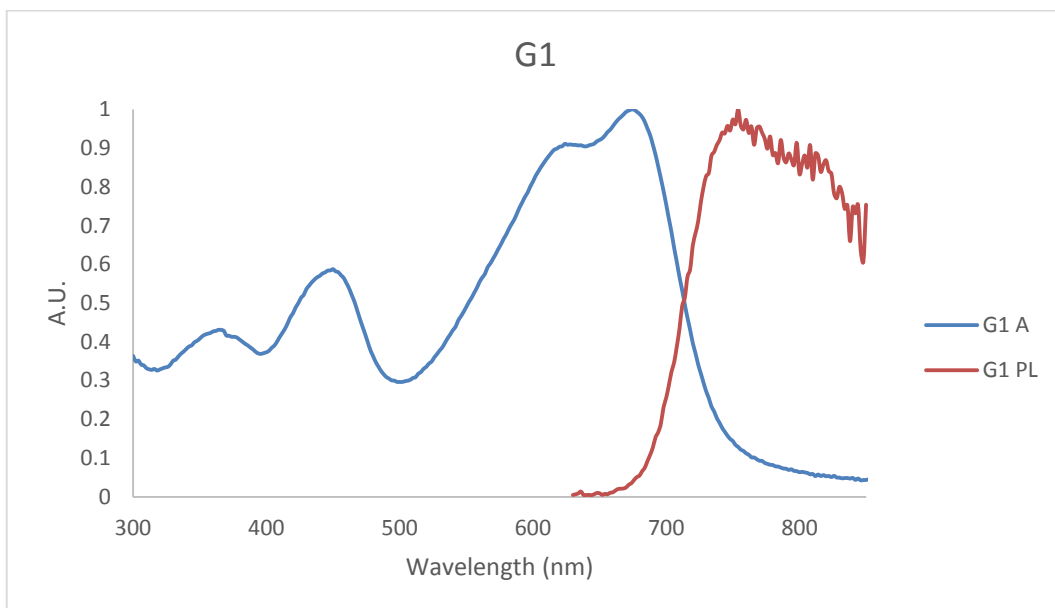


Figure 0-18: UV-vis absorption (A) and emission spectra (PL) of a G1 film (60 nm). Excitation for photoluminescence was performed by a 509.2 nm laser.

Binary polymer:polymer blends

P3HT:B1

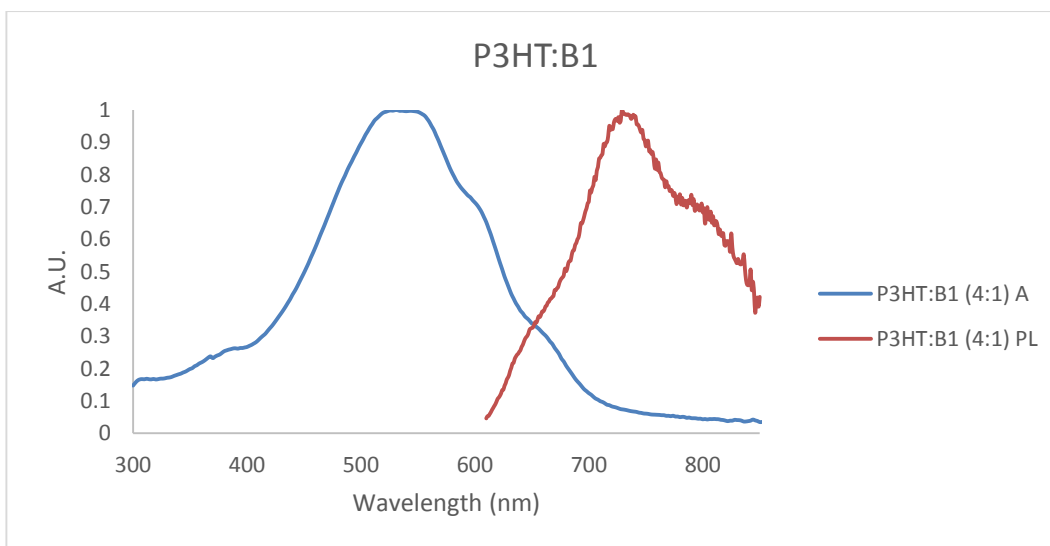


Figure 0-19: UV-vis absorption (A) and emission spectra (PL) of a P3HT:B1 (4:1) film (60 nm). Excitation for photoluminescence was performed by a 509.2 nm laser.

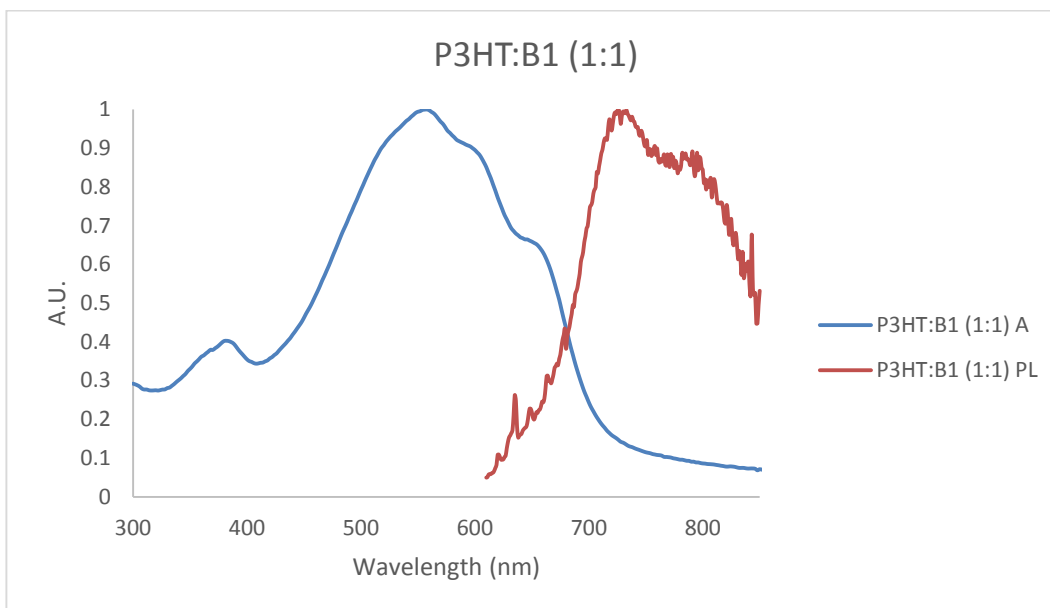


Figure 0-20: UV-vis absorption (A) and emission spectra (PL) of a P3HT:B1 (1:1) film (60 nm). Excitation for photoluminescence was performed by a 509.2 nm laser.

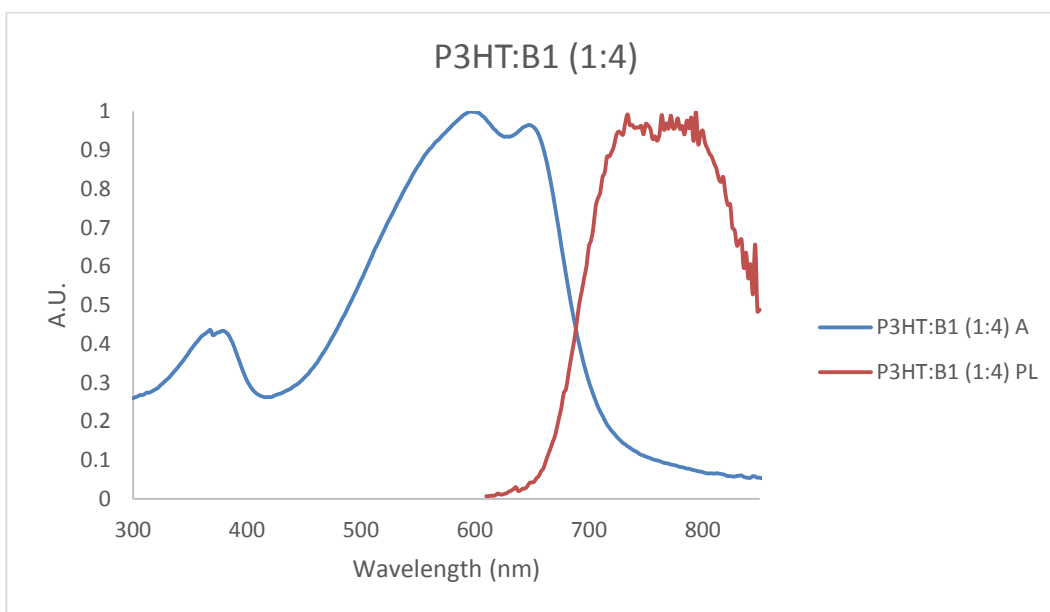


Figure 0-21: UV-vis absorption (A) and emission spectra (PL) of a P3HT:B1 (1:4) film (60 nm). Excitation for photoluminescence was performed by a 509.2 nm laser.

P3HT:G1

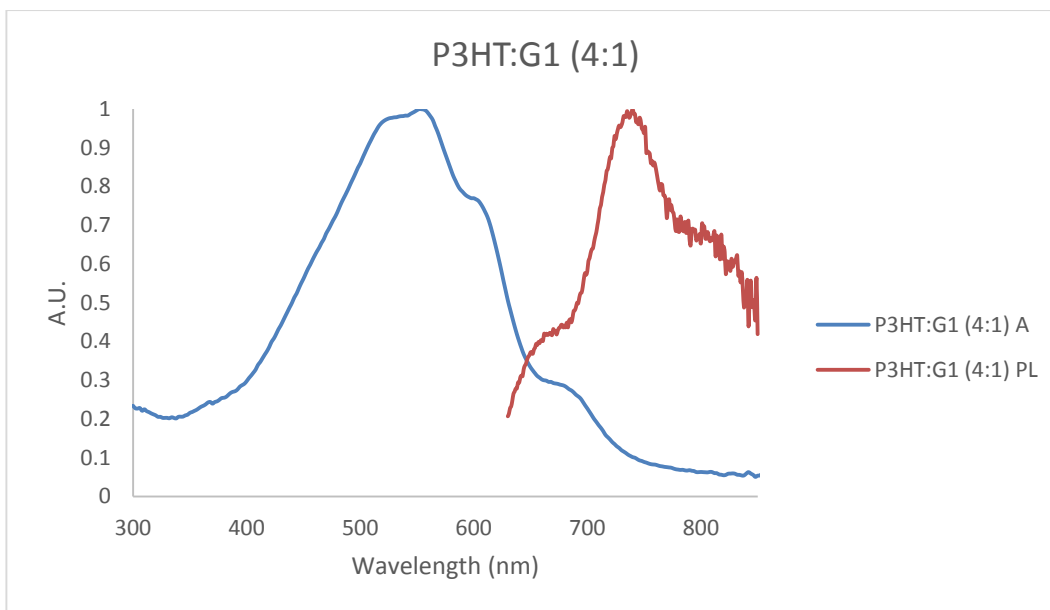


Figure 0-22: UV-vis absorption (A) and emission spectra (PL) of a P3HT:G1 (4:1) film (60 nm). Excitation for photoluminescence was performed by a 509.2 nm laser.

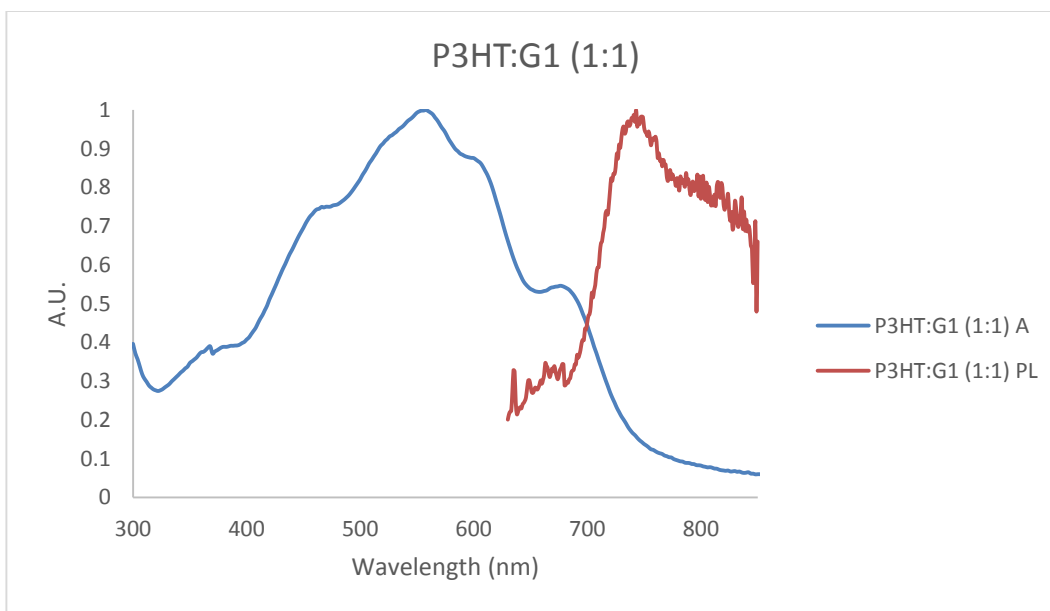


Figure 0-23: UV-vis absorption (A) and emission spectra (PL) of a P3HT:G1 (1:1) film (60 nm). Excitation for photoluminescence was performed by a 509.2 nm laser.

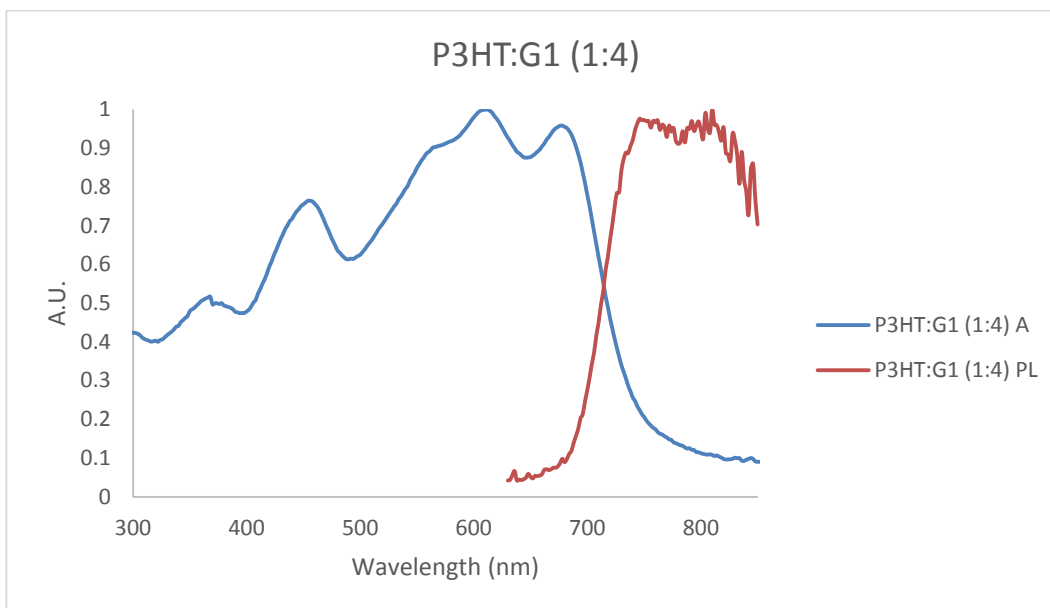


Figure 0-24: UV-vis absorption (A) and emission spectra (PL) of a P3HT:G1 (1:4) film (60 nm). Excitation for photoluminescence was performed by a 509.2 nm laser.

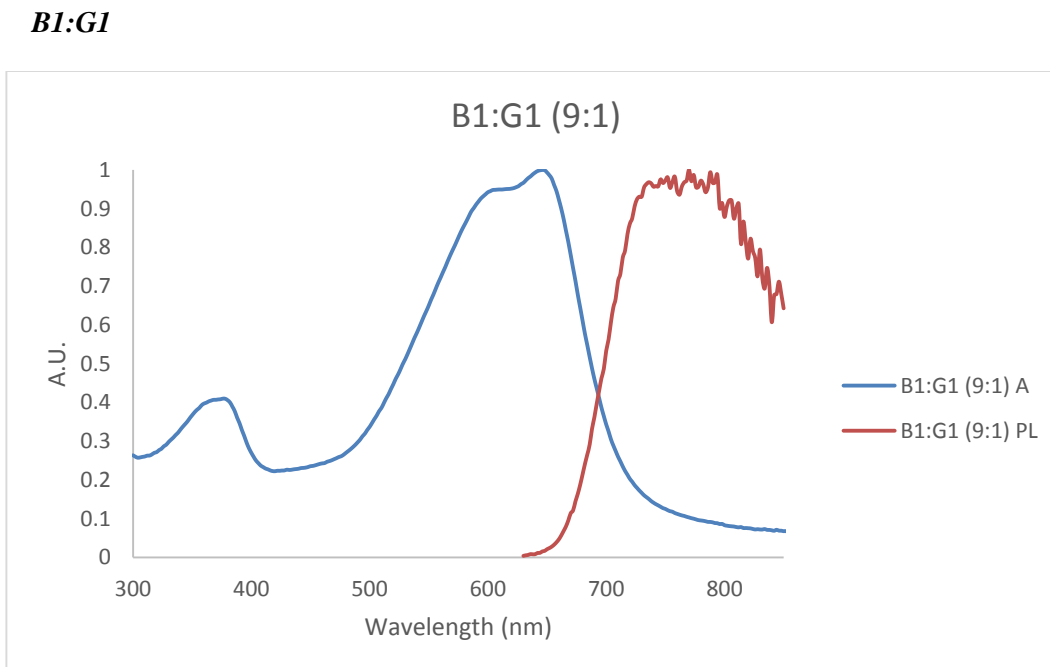


Figure 0-25: UV-vis absorption (A) and emission spectra (PL) of a B1:G1 (9:1) film (60 nm). Excitation for photoluminescence was performed by a 509.2 nm laser.

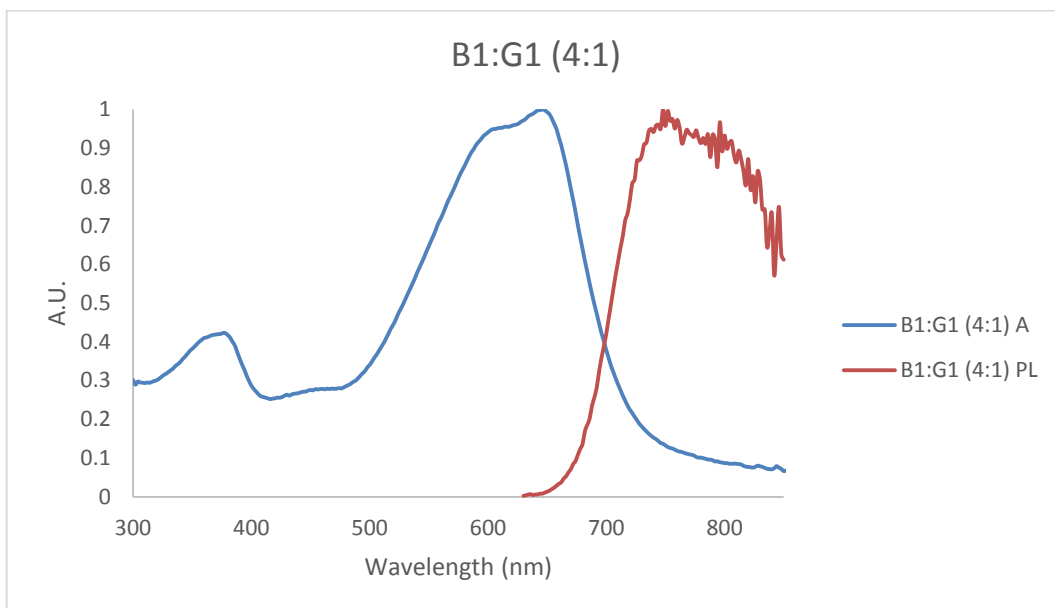


Figure 0-26: UV-vis absorption (A) and emission spectra (PL) of a B1:G1 (4:1) film (60 nm). Excitation for photoluminescence was performed by a 509.2 nm laser.

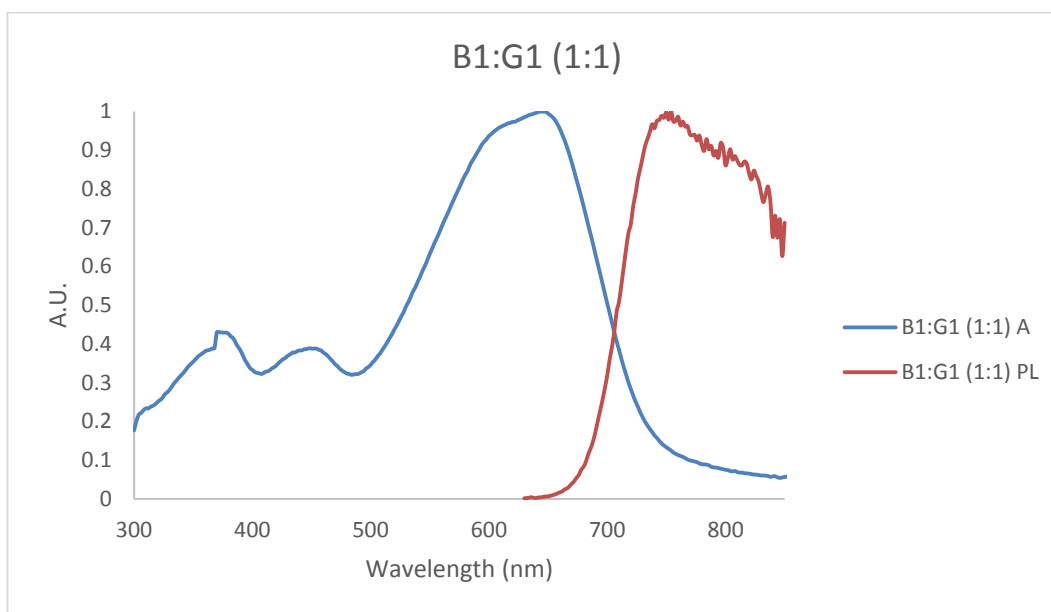


Figure 0-27: UV-vis absorption (A) and emission spectra (PL) of a B1:G1 (1:1) film (60 nm). Excitation for photoluminescence was performed by a 509.2 nm laser.

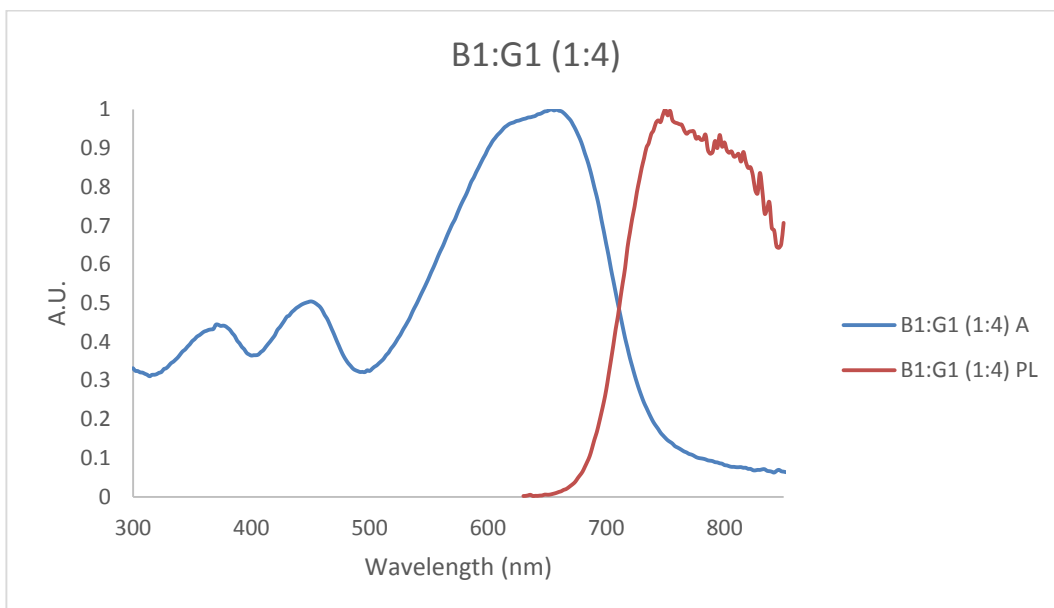


Figure 0-28: UV-vis absorption (A) and emission spectra (PL) of a B1:G1 (1:4) film (60 nm). Excitation for photoluminescence was performed by a 509.2 nm laser.

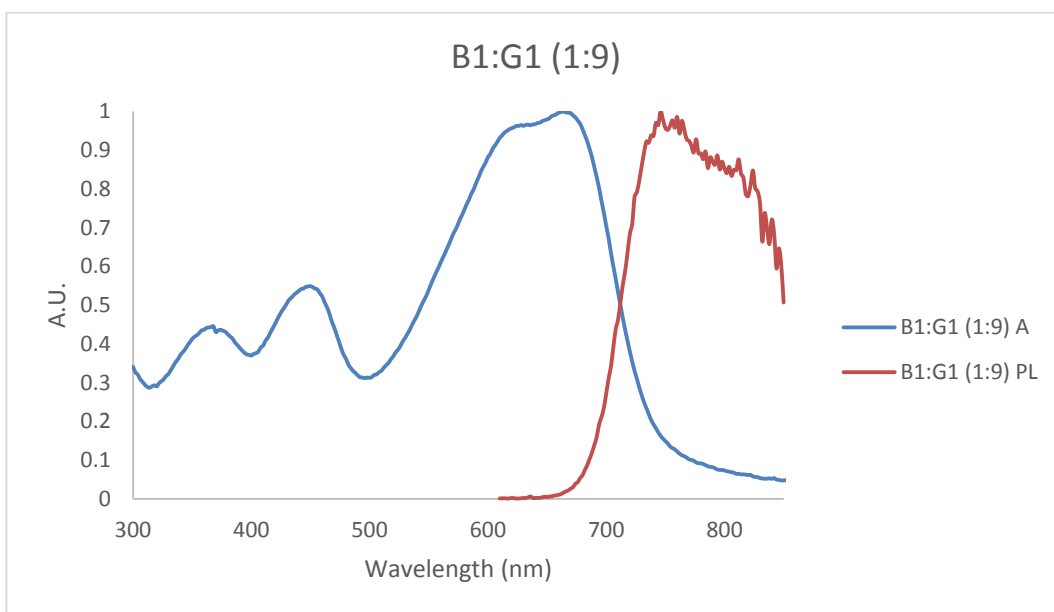


Figure 0-29: UV-vis absorption (A) and emission spectra (PL) of a B1:G1 (1:9) film (60 nm). Excitation for photoluminescence was performed by a 509.2 nm laser.

Time Correlated Single Photon Counting (TCSPC) of polymer films

Time correlated single photon counting (TCSPC) was used to investigate the fluorescent decay of the polymer films. This study was performed at XLIM using an excitation laser (509.2 nm) and observing the decay of the photon emission at 750 nm on an Edinburgh Instruments FLS980 Photoluminescence Spectrometer. The films were deposited via spin coating from 1,2-dichlorobenzene solutions with a total polymer concentration of 10 mg/ml, resulting in 60 nm films (determined by a Brucker Dektak profilometer).

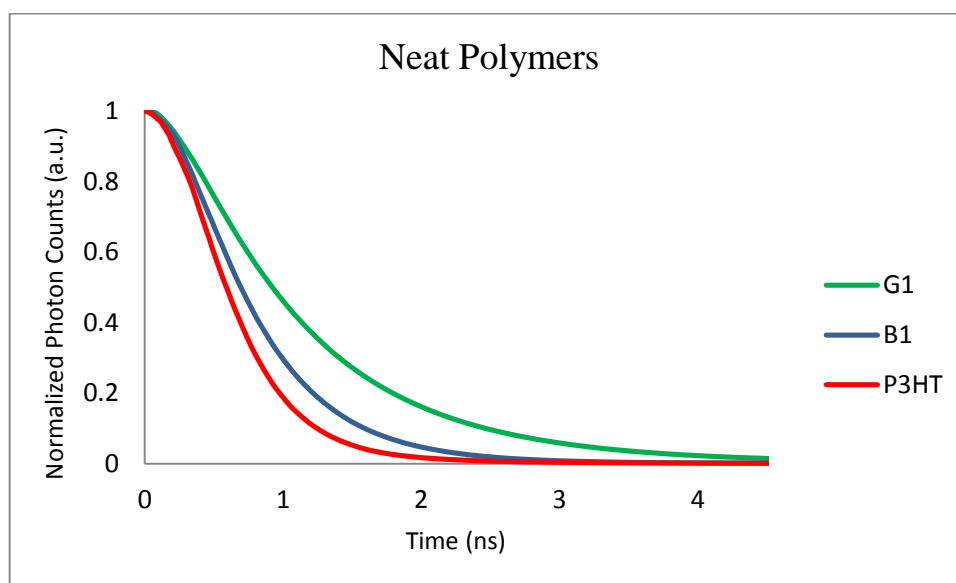


Figure 0-30: Photoluminescence TCSPC at 750 nm of neat P3HT, B1 and G1 polymer films with a 509.2 nm excitation laser.

P3HT:B1 blends

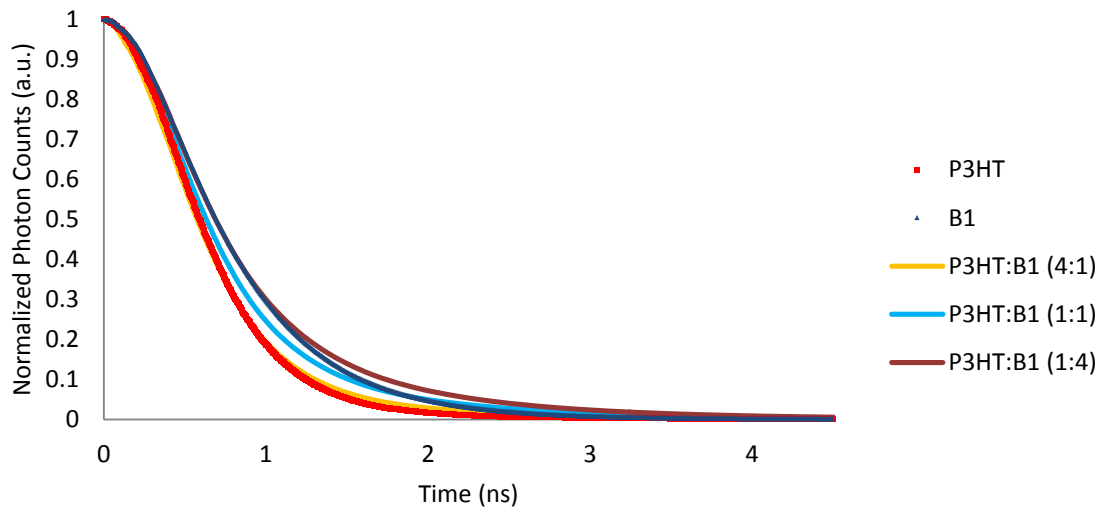


Figure 0-31: Photoluminescence TCSPC at 750 nm of neat P3HT and B1 films and their binary blends (P3HT:B1) with a 509.2 nm excitation laser.

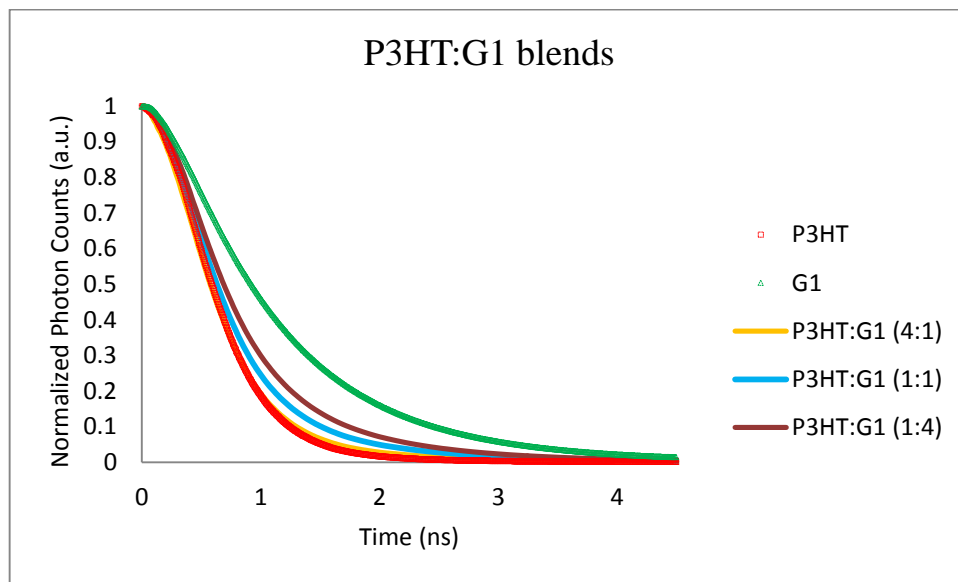


Figure 0-32: Photoluminescence TCSPC at 750 nm of neat P3HT and G1 films and their binary blends (P3HT:G1) with a 509.2 nm excitation laser.

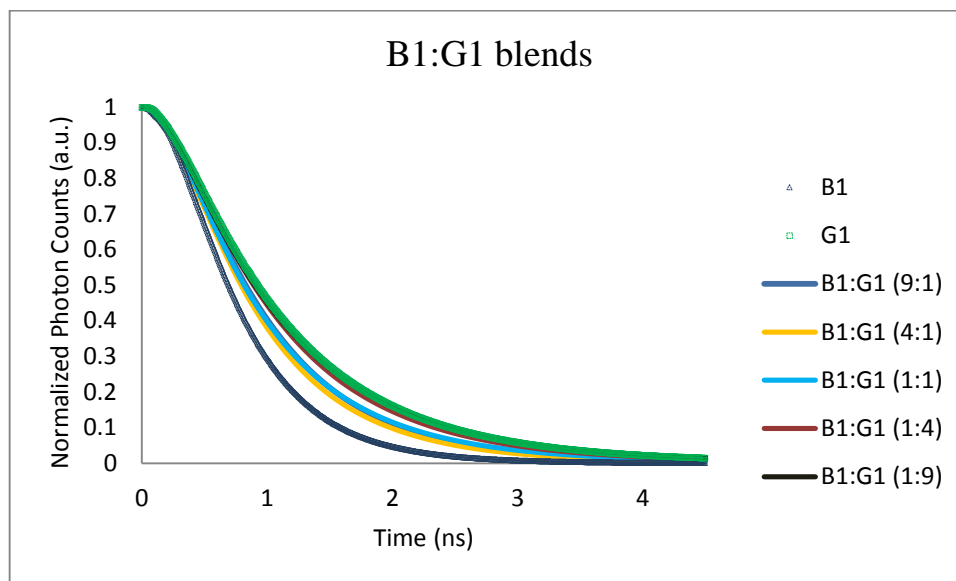


Figure 0-33: Photoluminescence TCSPC at 750 nm of neat B1 and G1 films and their binary blends (B1:G1) with a 509.2 nm excitation laser.

Appendix D

Comparison of EQE and active layer absorption.

Binary blends

P3HT

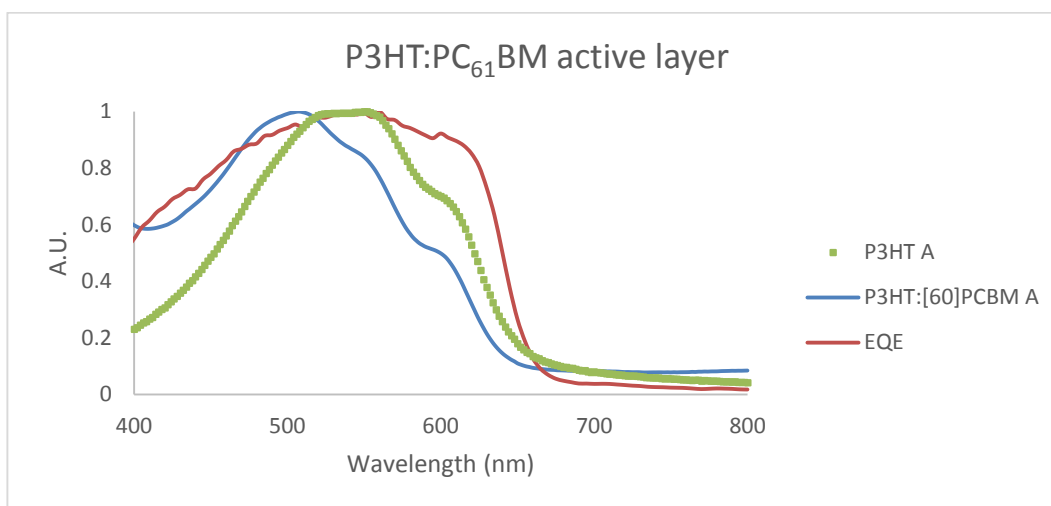


Figure 0-34: Comparison of the UV-visible optical absorption (A) of a P3HT and P3HT:PC₆₁BM film with the external quantum efficiency (EQE) of a solar cell with a P3HT:PC₆₁BM active layer.

B1

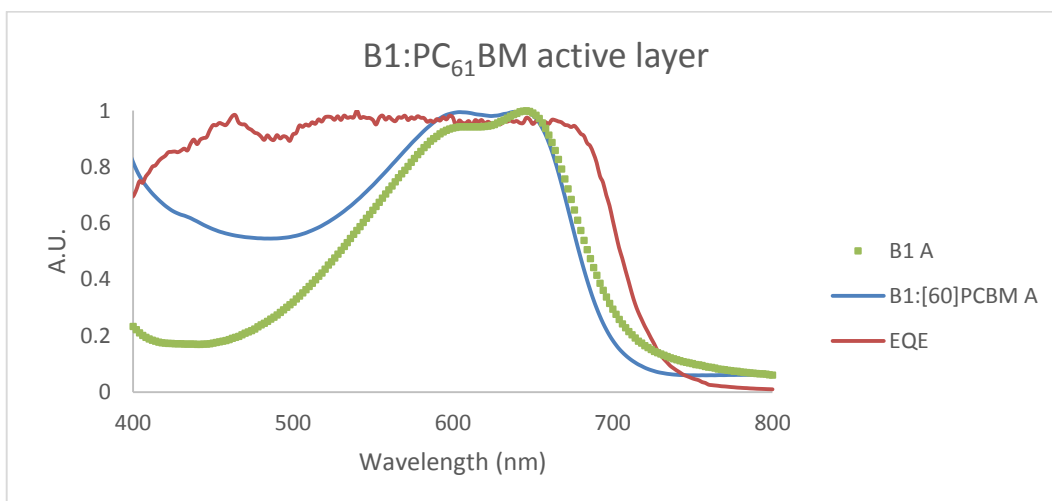


Figure 0-35: Comparison of the UV-visible optical absorption (A) of a B1 and B1:PC₆₁BM film with the external quantum efficiency (EQE) of a solar cell with a B1:PC₆₁BM active layer.

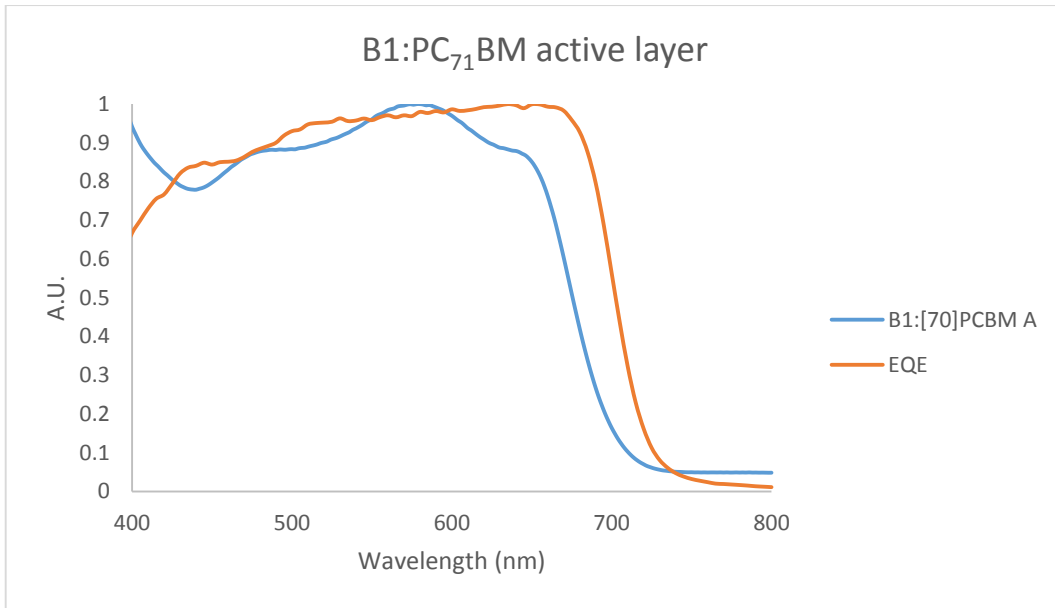


Figure 0-36: Comparison of the UV-visible optical absorption (A) of a B1:PC₇₁BM film with the external quantum efficiency (EQE) of a solar cell with a B1:PC₇₁BM active layer.

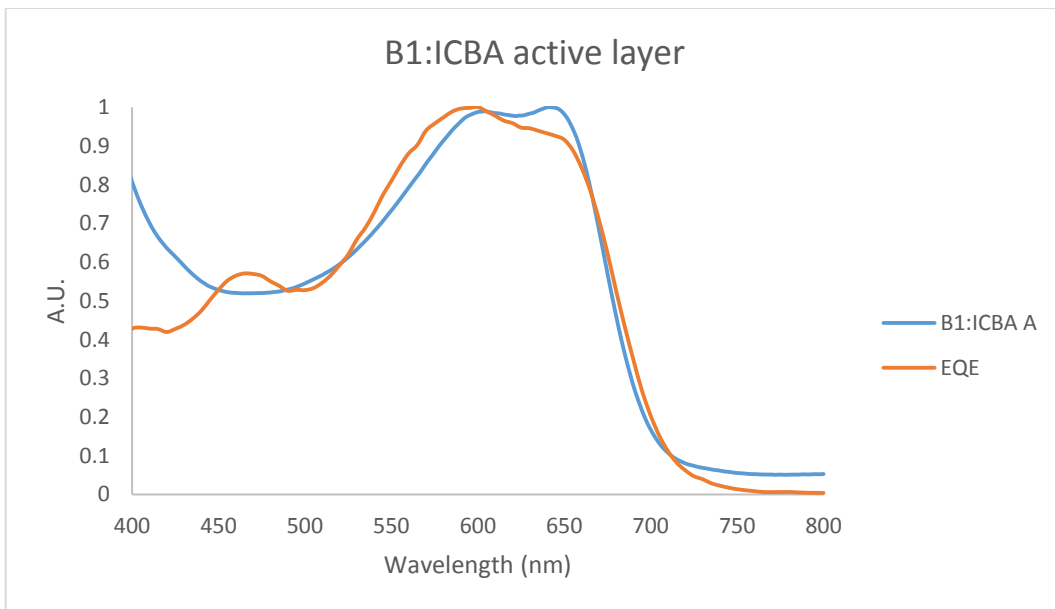


Figure 0-37: Comparison of the UV-visible optical absorption (A) of a B1:ICBA film with the external quantum efficiency (EQE) of a solar cell with a B1:ICBA active layer.

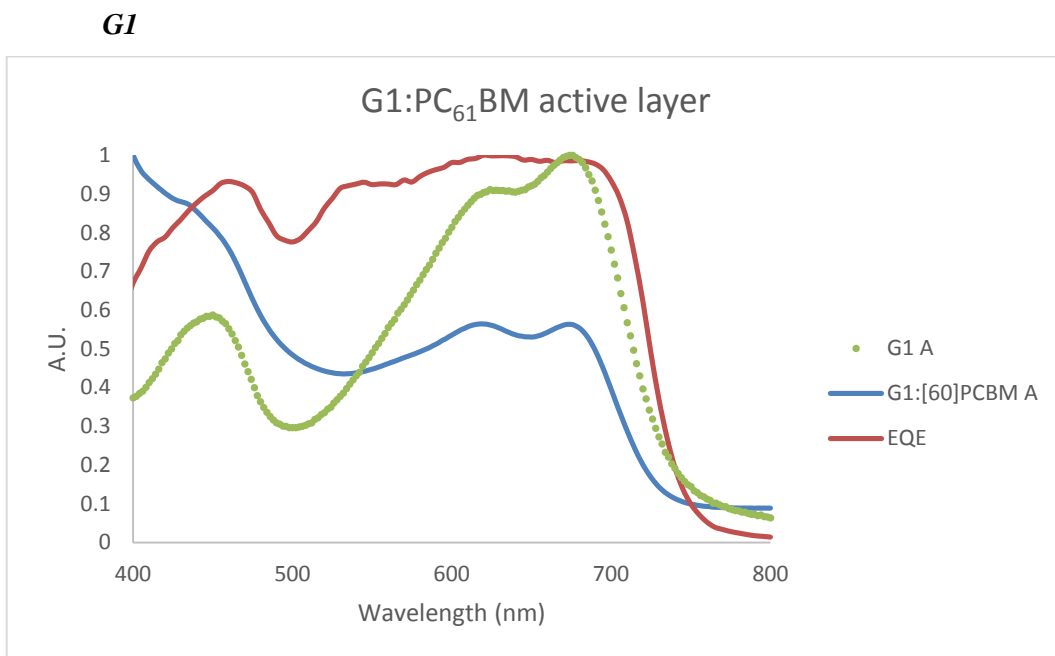


Figure 0-38: Comparison of the UV-visible optical absorption (A) of a G1 and G1:PC₆₁BM film with the external quantum efficiency (EQE) of a solar cell with a G1:PC₆₁BM active layer.

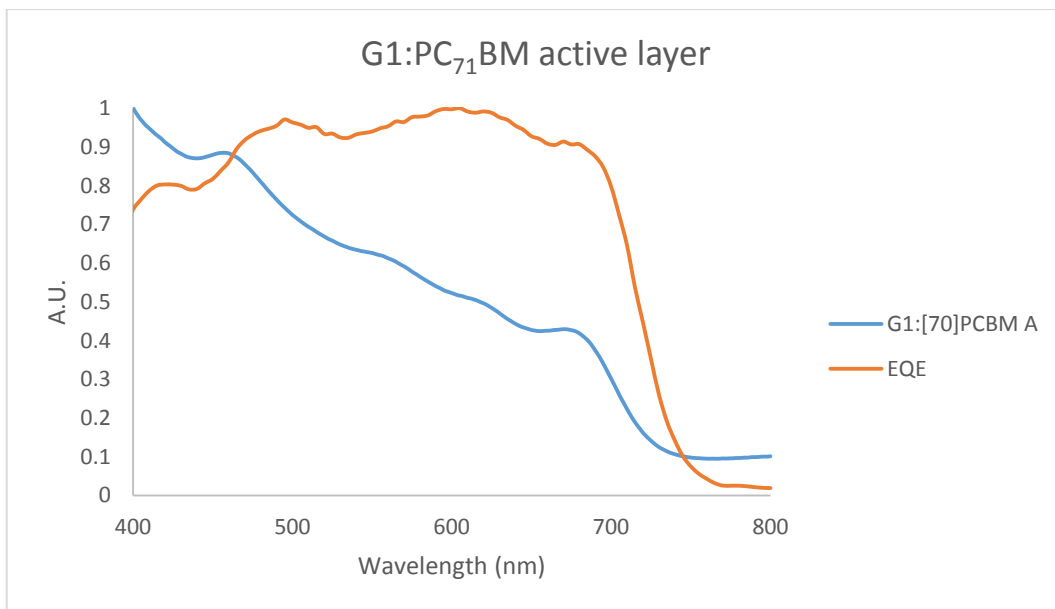


Figure 0-39: Comparison of the UV-visible optical absorption (A) of a G1:PC₇₁BM film with the external quantum efficiency (EQE) of a solar cell with a G1:PC₇₁BM active layer

Ternary blends

P3HT:B1:PC₆₁BM

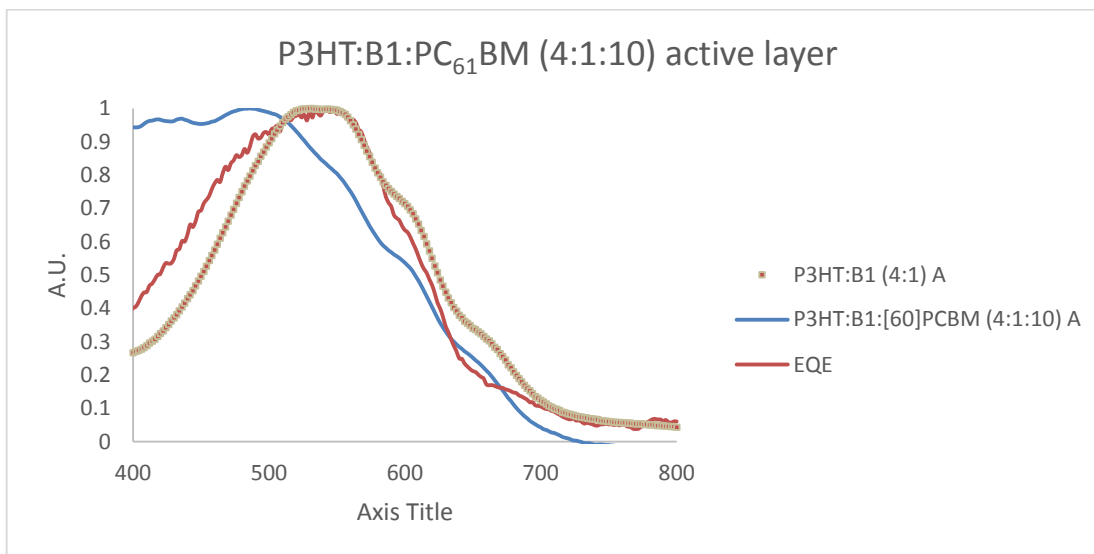


Figure 0-40: Comparison of the UV-visible optical absorption (A) of a P3HT:B1 (4:1) and P3HT:B1:PC₆₁BM (4:1:10) film with the external quantum efficiency (EQE) of a solar cell with a P3HT:B1:PC₆₁BM (4:1:10) active layer.

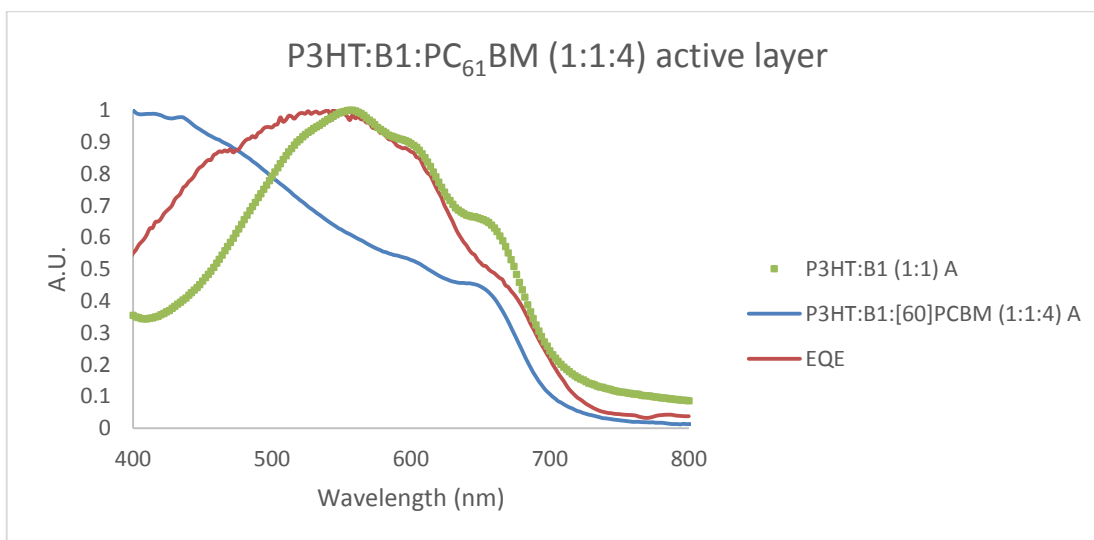


Figure 0-41: Comparison of the UV-visible optical absorption (A) of a P3HT:B1 (1:1) and P3HT:B1:PC₆₁BM (1:1:4) film with the external quantum efficiency (EQE) of a solar cell with a P3HT:B1:PC₆₁BM (1:1:4) active layer.

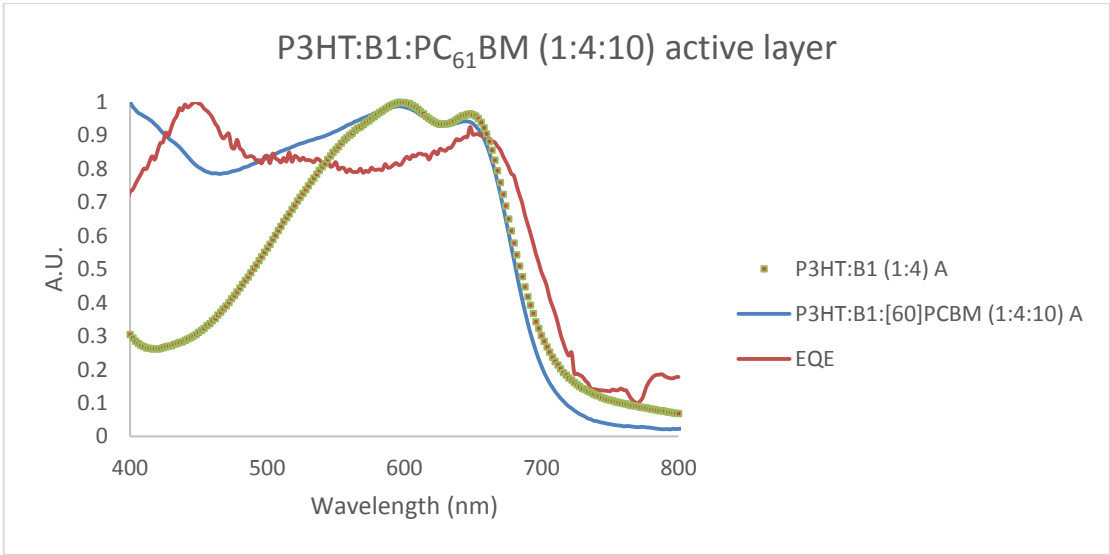


Figure 0-42: Comparison of the UV-visible optical absorption (A) of a P3HT:B1 (1:4) and P3HT:B1:PC₆₁BM (1:4:10) film with the external quantum efficiency (EQE) of a solar cell with a P3HT:B1:PC₆₁BM (1:4:10) active layer.

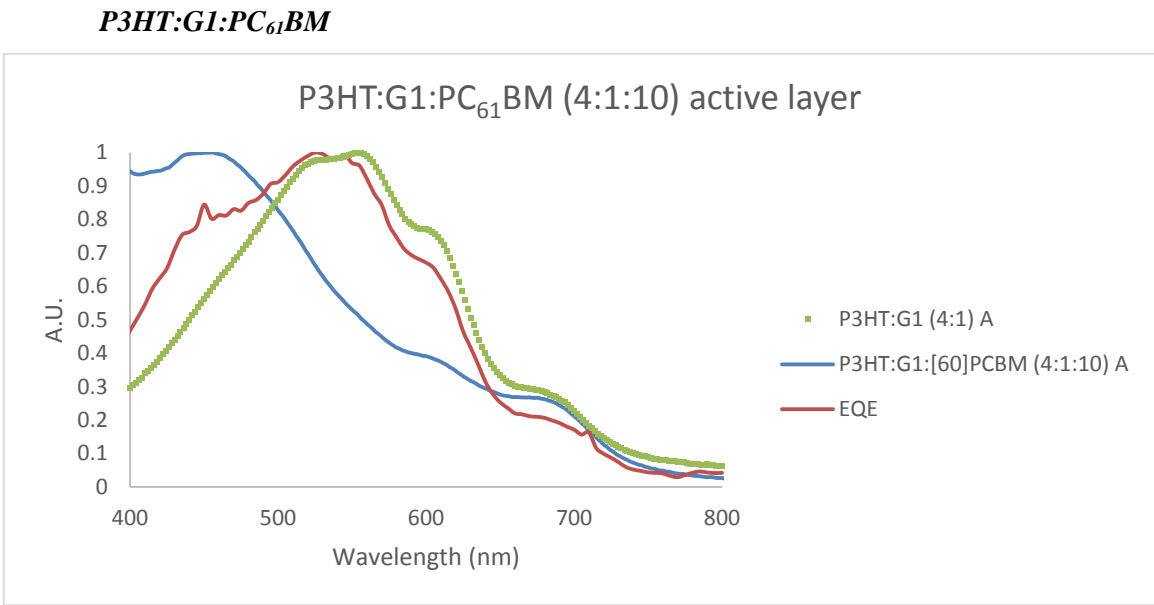


Figure 0-43: Comparison of the UV-visible optical absorption (A) of a P3HT:G1 (4:1) and P3HT:G1:PC₆₁BM (4:1:10) film with the external quantum efficiency (EQE) of a solar cell with a P3HT:G1:PC₆₁BM (4:1:10) active layer.

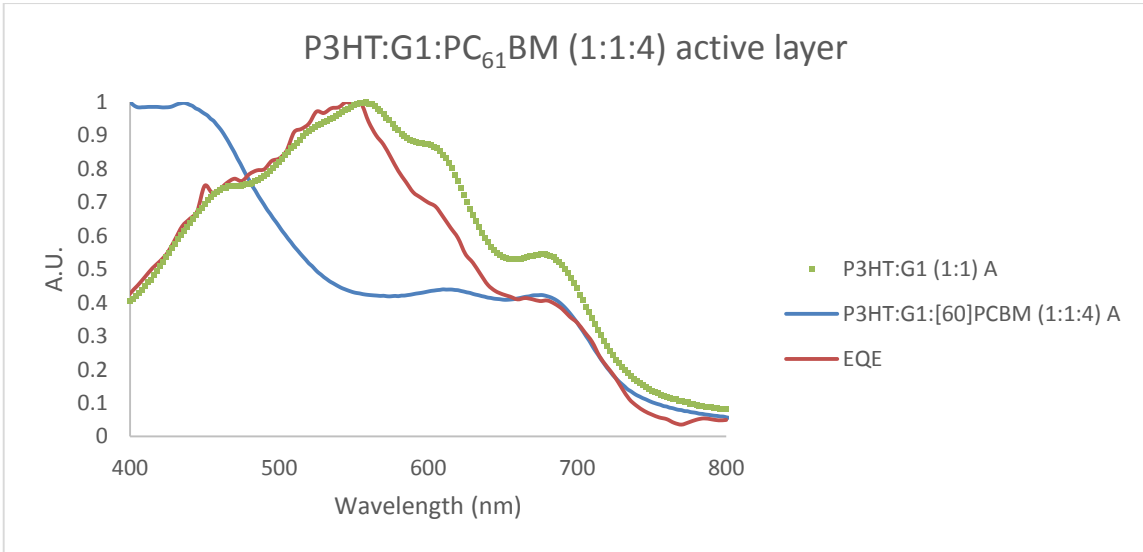


Figure 0-44: Comparison of the UV-visible optical absorption (A) of a P3HT:G1 (1:1) and P3HT:G1:PC₆₁BM (1:1:4) film with the external quantum efficiency (EQE) of a solar cell with a P3HT:G1:PC₆₁BM (1:1:4) active layer.

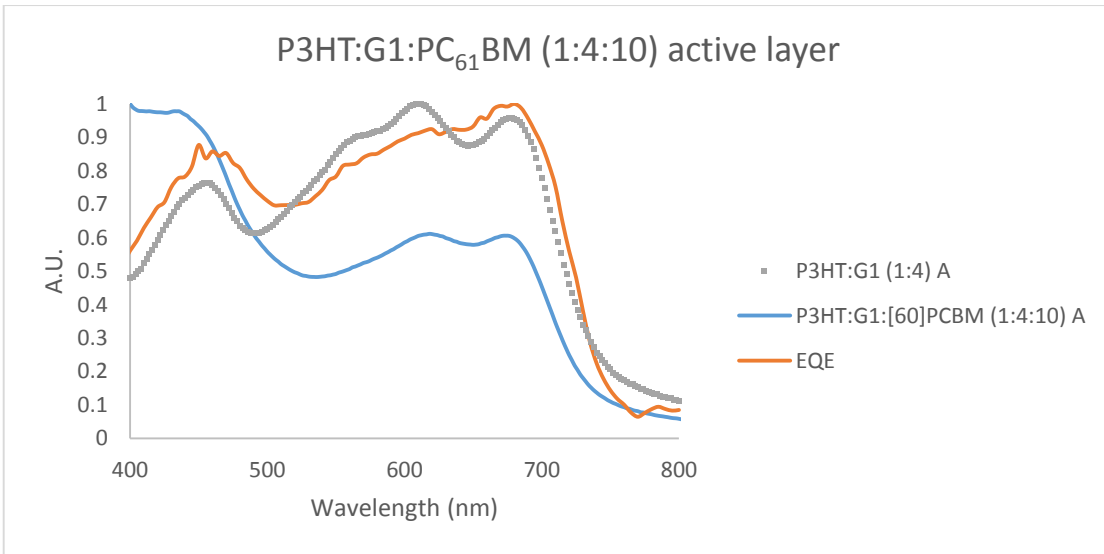


Figure 0-45: Comparison of the UV-visible optical absorption (A) of a P3HT:G1 (1:4) and P3HT:G1:PC₆₁BM (1:4:10) film with the external quantum efficiency (EQE) of a solar cell with a P3HT:G1:PC₆₁BM (1:4:10) active layer.

B1:G1:PC₆₁BM

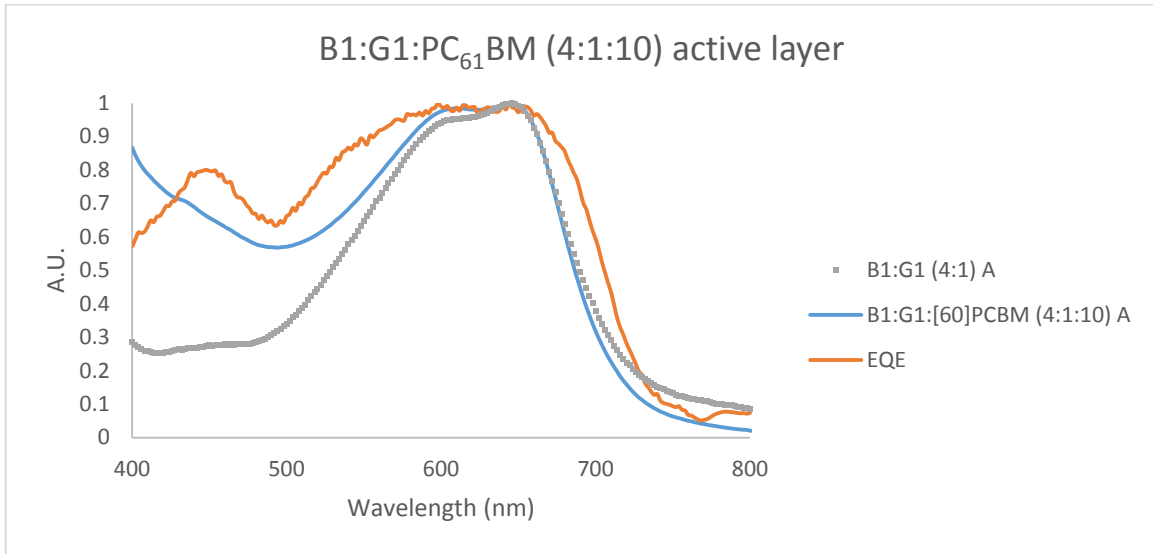


Figure 0-46: Comparison of the UV-visible optical absorption (A) of a B1:G1 (4:1) and B1:G1:PC₆₁BM (4:1:10) film with the external quantum efficiency (EQE) of a solar cell with a B1:G1:PC₆₁BM (4:1:10) active layer.

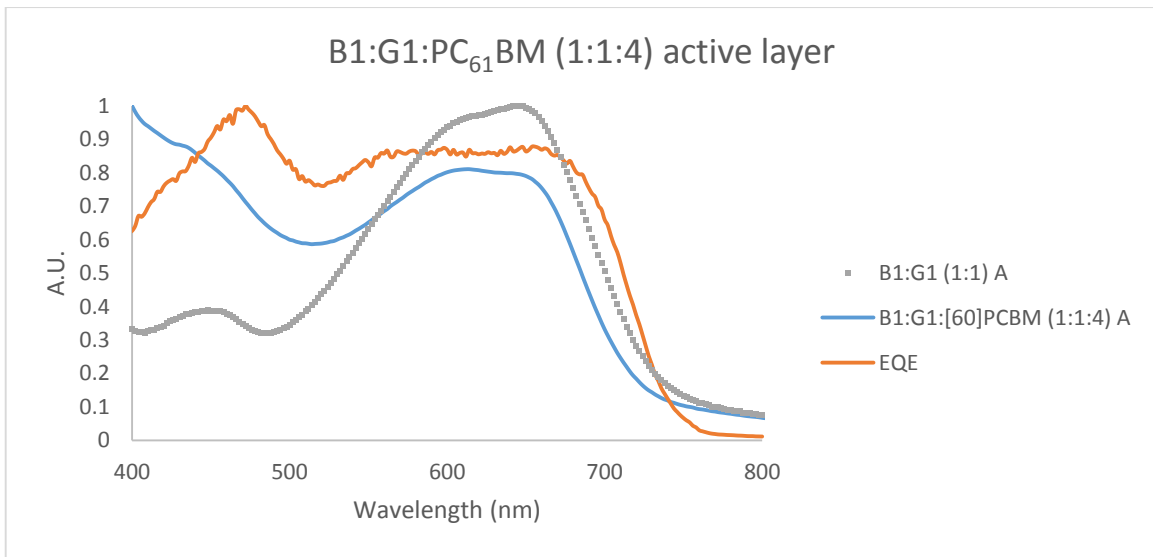


Figure 0-47: Comparison of the UV-visible optical absorption (A) of a B1:G1 (1:1) and B1:G1:PC₆₁BM (1:1:4) film with the external quantum efficiency (EQE) of a solar cell with a B1:G1:PC₆₁BM (1:1:4) active layer.

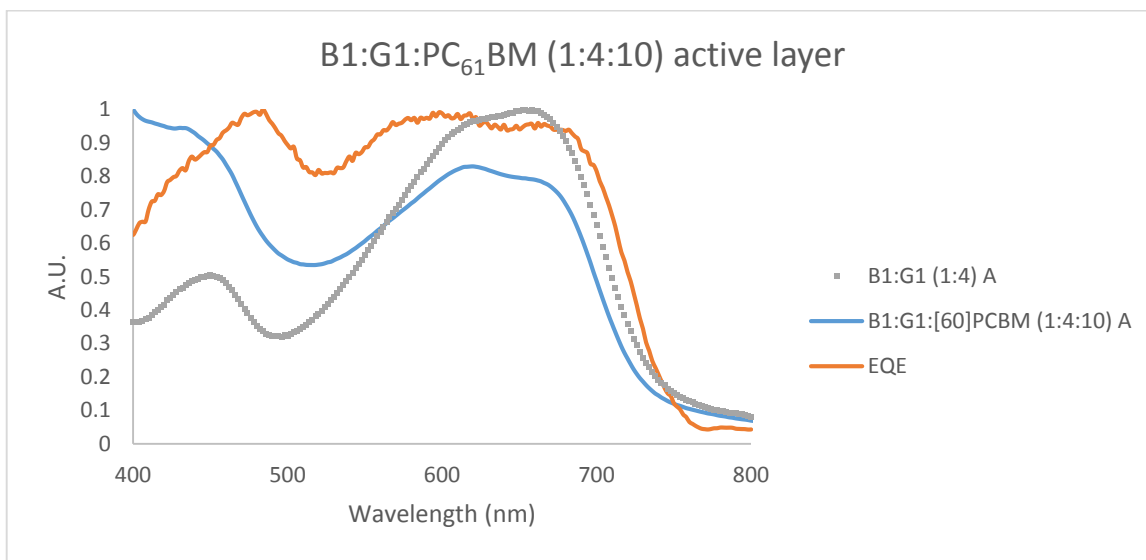


Figure 0-48: Comparison of the UV-visible optical absorption (A) of a B1:G1 (1:4) and B1:G1:PC₆₁BM (1:4:10) film with the external quantum efficiency (EQE) of a solar cell with a B1:G1:PC₆₁BM (1:4:10) active layer.

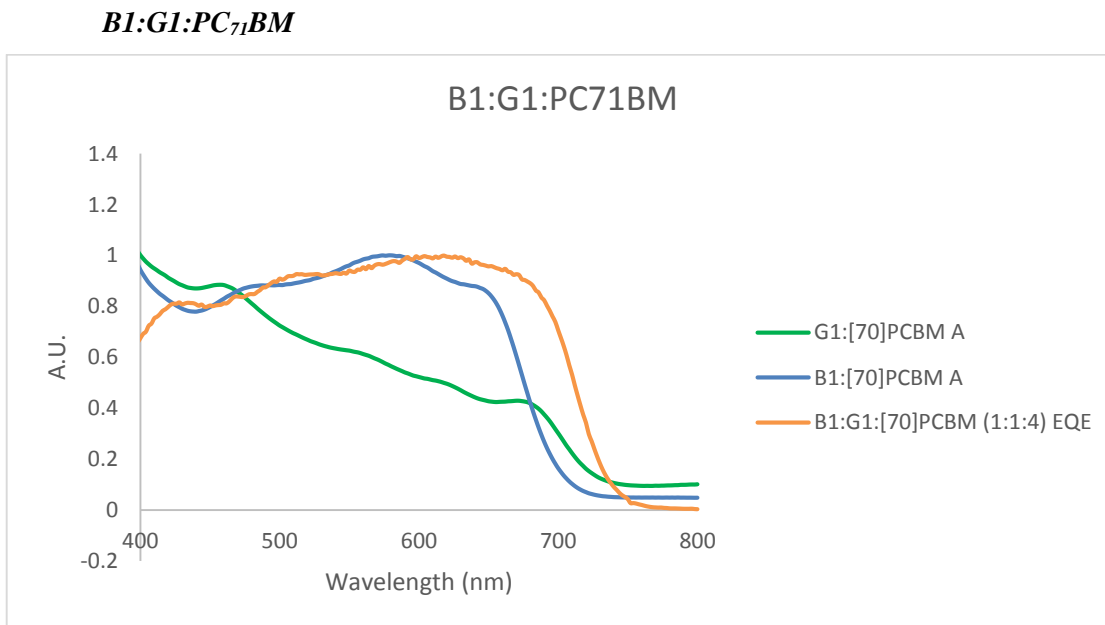


Figure 0-49: Comparison of the UV-visible optical absorption (A) of a B1:PC₇₁BM (blue dots) and G1:PC₇₁BM (green dots) film with the external quantum efficiency (EQE) of a solar cell with a B1:G1:PC₇₁BM (1:1:4) active layer.

Appendix E

J(V) characteristics of photo-active layer blends

J(V) characteristics of cells with 0.18 cm² active area

Table 0-1 J(V) characteristics of 0.18 cm² PV devices on plastic with the following architecture: PET/ITO/ZnO/active layer/PEDOT:PSS/Ag

Active Layer	V _{oc} (V)	J _{sc} (mA/cm ²)	FF (%)	PCE (%)
P3HT:[60]PCBM (1:0.8)	0.55	8.18	53.0	2.39
B1:[60]PCBM (1:1.5)	0.77	11.07	53.7	4.56
G1:[60]PCBM (1:2)	0.71	13.72	59.4	5.78
B1:[70]PCBM (1:1.5)	0.78	11.80	48.2	4.45
G1:[70]PCBM (1:2)	0.76	14.04	62.7	6.67
P3HT:G1:[60]PCBM (4:1:10)	0.54	7.35	53.0	2.10
P3HT:G1:[60]PCBM (1:1:4)	0.56	4.34	40.1	0.97
P3HT:G1:[60]PCBM (1:4:10)	0.62	5.83	37.7	1.37
B1:G1:[60]PCBM (4:1:10)	0.73	11.18	53.8	4.40
B1:G1:[60]PCBM (1:1:4)	0.72	11.08	64.8	5.16
B1:G1:[60]PCBM (1:4:10)	0.73	12.55	63.6	5.82
P3HT:B1:[60]PCBM (4:1:10)	0.57	5.31	54.6	1.64
P3HT:B1:[60]PCBM (1:1:4)	0.60	2.71	39.9	0.65
P3HT:B1:[60]PCBM (1:4:10)	0.66	4.20	38.9	1.07
G1:G1:[70]PCBM (1:1:4)	0.73	12.62	51.7	4.75

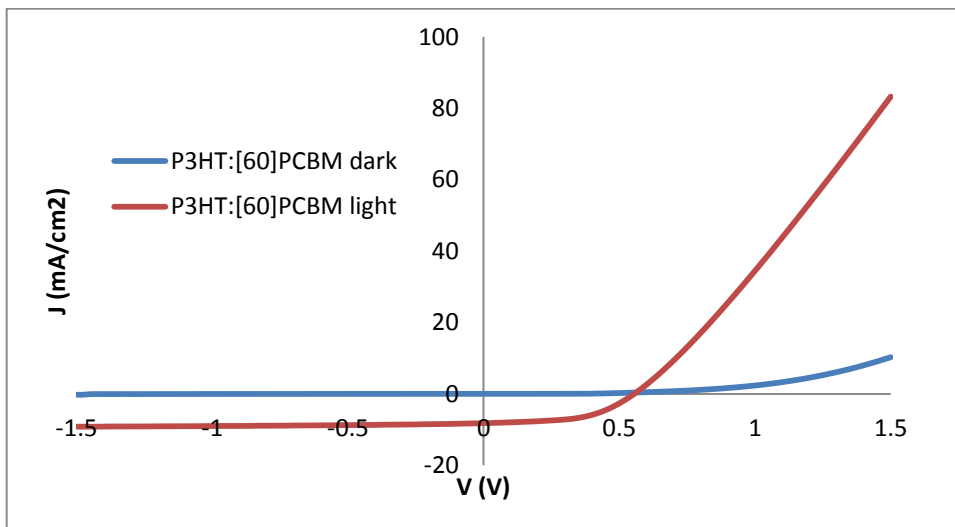
J(V) characteristics of cells with 2 cm² active area

Table 0-2: J(V) characteristics of 2 cm² PV devices on plastic with the following architecture: PET/ITO/ZnO/active layer/PEDOT:PSS/Ag

Active Layer	V _{oc} (V)	J _{sc} (mA/cm ²)	FF (%)	PCE (%)
P3HT:[60]PCBM	0.53	6.73	47.2	1.70
B1:[60]PCBM	0.69	10.08	39.9	2.79
G1:[60]PCBM	0.74	12.77	50.8	4.79
P3HT:[70]PCBM	0.54	7.00	32.9	1.24
G1:[70]PCBM	0.74	10.47	36.9	2.84
P3HT:G1:[60]PCBM (4:1:10)	0.49	4.07	26.5	0.53
B1:G1:[70]PCBM (1:1:4)	0.73	9.53	35.2	2.44

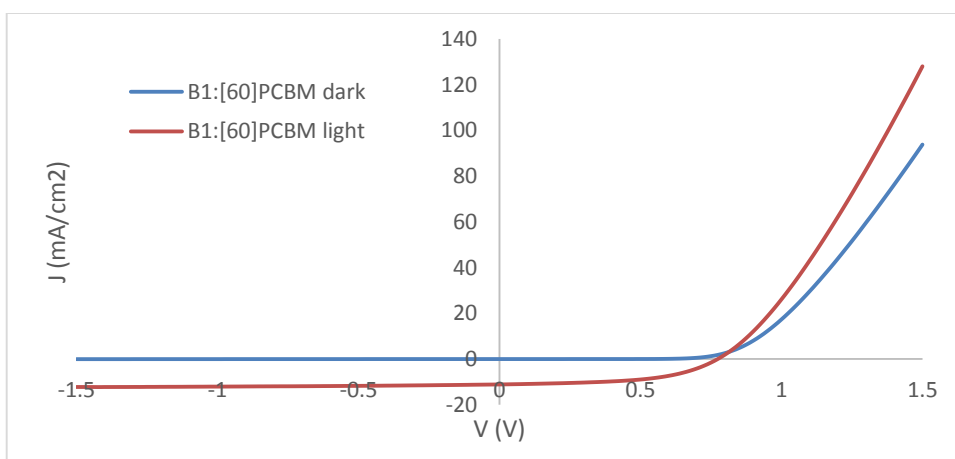
J(V) curves

0.18 cm² active areas



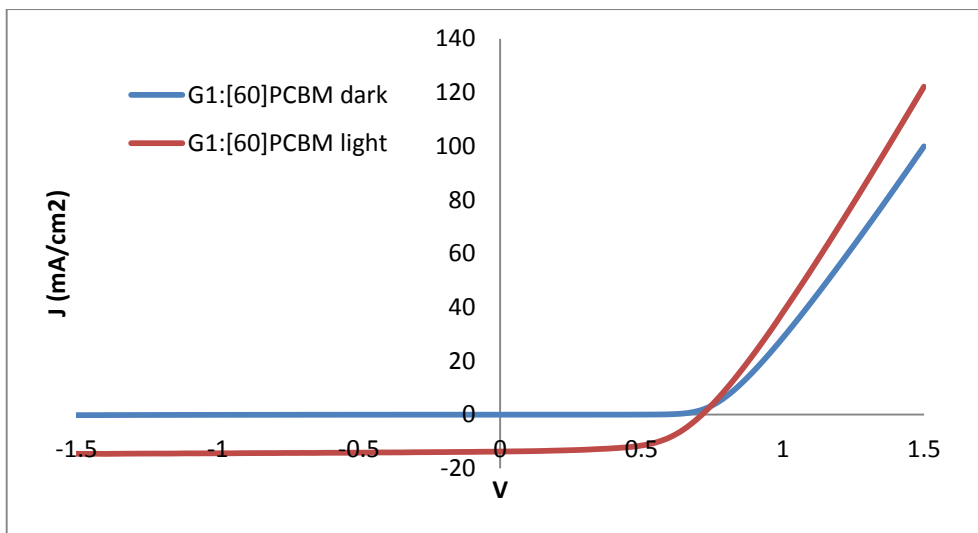
V _{oc} (V)	J _{sc} (mA/cm ²)	FF (%)	PCE (%)	R series (Ω)	R shunt (Ω)
0.55	8.18	53.0	2.39	106.3	2704.2

Figure 0-50: J(V) curve and characteristics for a PSC on plastic with the following architecture: PET/ITO/ZnO/P3HT:PC₆₁BM/PEDOT:PSS/Ag



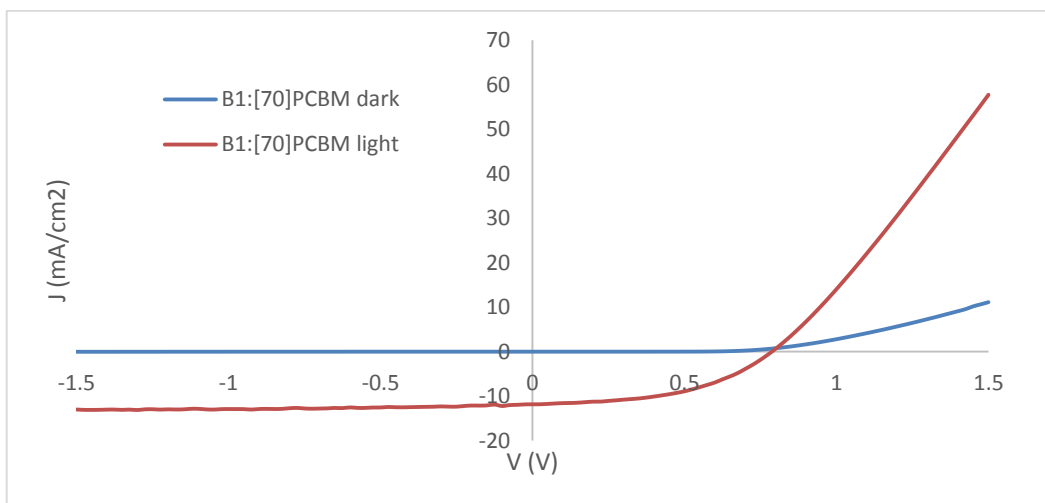
V _{oc} (V)	J _{sc} (mA/cm ²)	FF (%)	PCE (%)	R series (Ω)	R shunt (Ω)
0.77	11.07	53.7	4.56	79.1	2982.3

Figure 0-51: J(V) curve and characteristics for a PSC on plastic with the following architecture: PET/ITO/ZnO/B1:PC₆₁BM/PEDOT:PSS/Ag



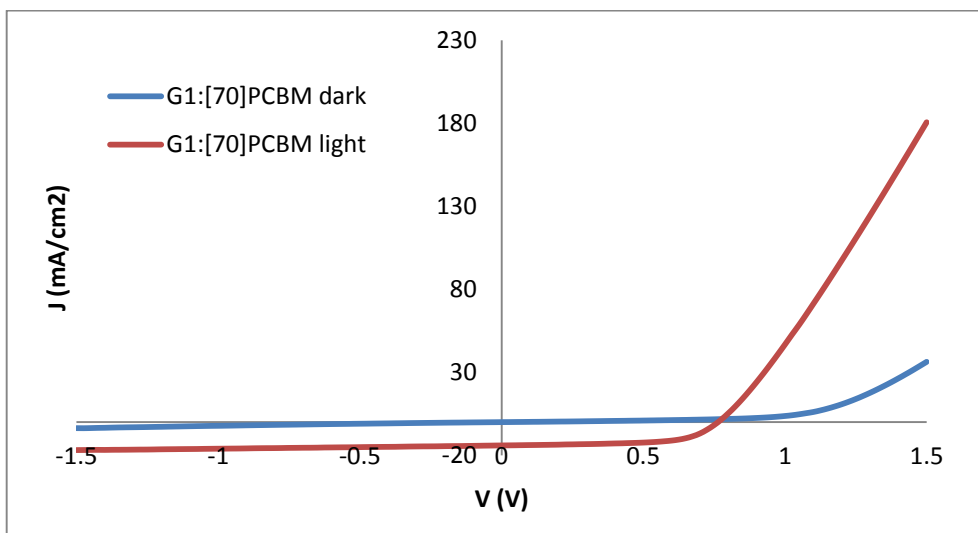
V_{oc} (V)	J_{sc} (mA/cm ²)	FF (%)	PCE (%)	R series (Ω)	R shunt (Ω)
0.71	13.72	59.4	5.78	55.3	4290.1

Figure 0-52: J(V) curve and characteristics for a PSC on plastic with the following architecture: PET/ITO/ZnO/G1:PC₆₁BM/PEDOT:PSS/Ag



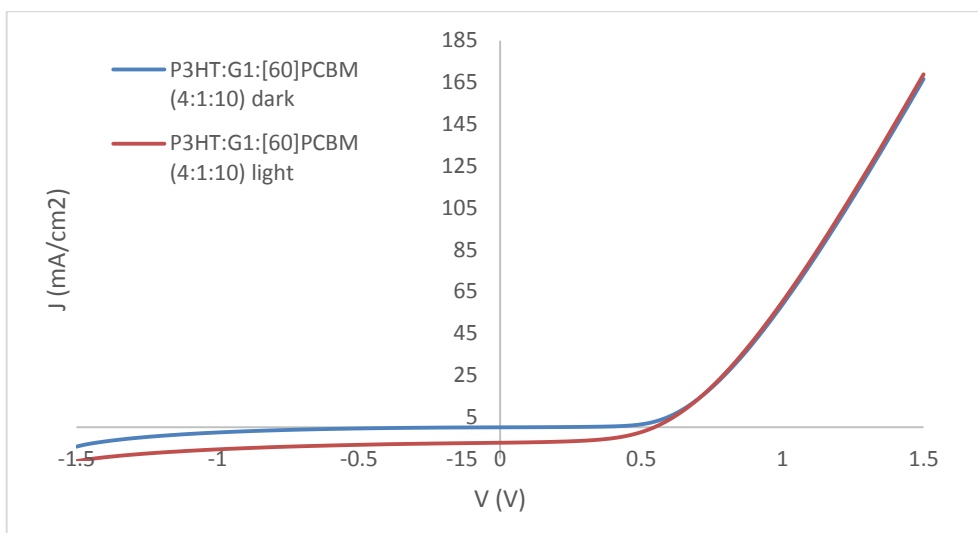
V_{oc} (V)	J_{sc} (mA/cm ²)	FF (%)	PCE (%)	R series (Ω)	R shunt (Ω)
0.78	11.80	48.2	4.45	112.8	2609.5

Figure 0-53: J(V) curve and characteristics for a PSC on plastic with the following architecture: PET/ITO/ZnO/B1:PC₇₁BM/PEDOT:PSS/Ag



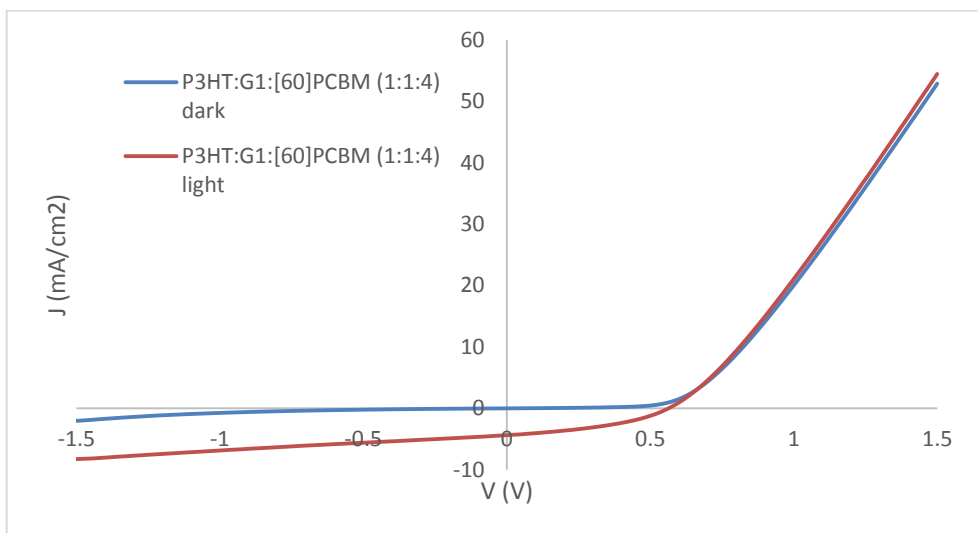
V_{oc} (V)	J_{sc} (mA/cm ²)	FF (%)	PCE (%)	R series (Ω)	R shunt (Ω)
0.76	14.04	62.7	6.67	39.9	2422.3

Figure 0-54: J(V) curve and characteristics for a PSC on plastic with the following architecture: PET/ITO/ZnO/G1:PC₇₁BM/PEDOT:PSS/Ag



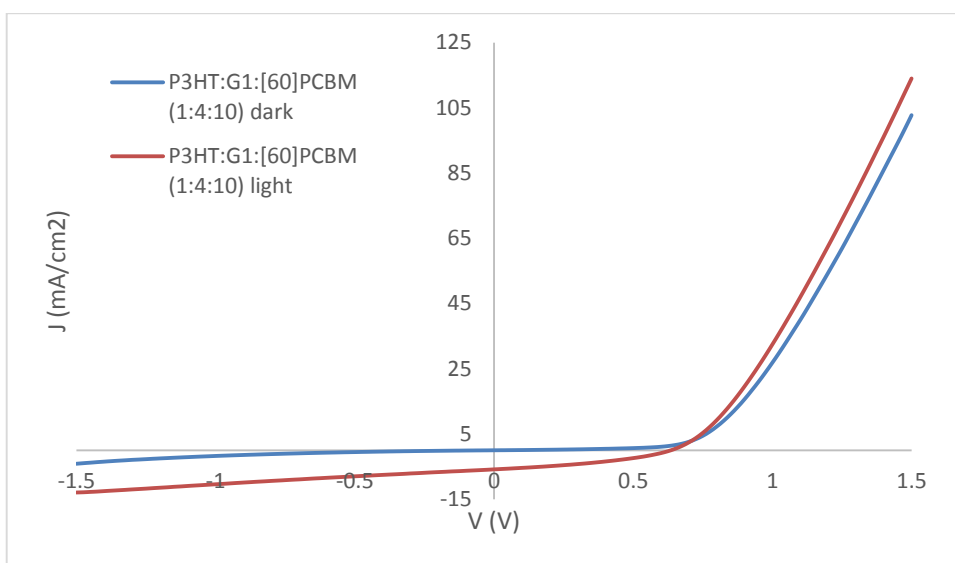
V_{oc} (V)	J_{sc} (mA/cm ²)	FF (%)	PCE (%)	R series (Ω)	R shunt (Ω)
0.54	7.35	53.0	2.10	92.8	3084.4

Figure 0-55: J(V) curve and characteristics for a PSC on plastic with the following architecture: PET/ITO/ZnO/P3HT:G1:PC₆₁BM (4:1:10)/PEDOT:PSS/Ag



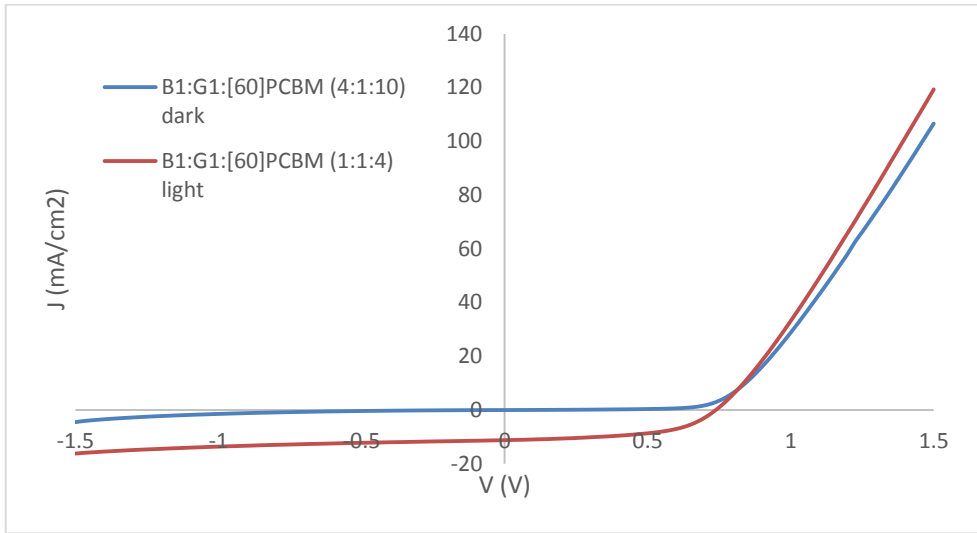
V_{oc} (V)	J_{sc} (mA/cm ²)	FF (%)	PCE (%)	R series (Ω)	R shunt (Ω)
0.56	4.34	40.1	0.97	220.3	1827.0

Figure 0-56: J(V) curve and characteristics for a PSC on plastic with the following architecture: PET/ITO/ZnO/P3HT:G1:PC₆₁BM (1:1:4)/PEDOT:PSS/Ag



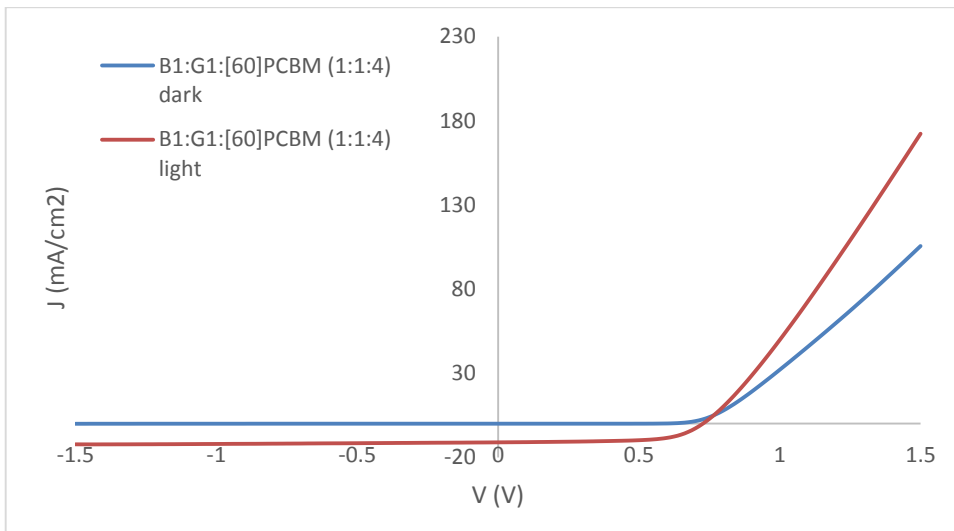
V_{oc} (V)	J_{sc} (mA/cm ²)	FF (%)	PCE (%)	R series (Ω)	R shunt (Ω)
0.62	5.83	37.7	1.37	204.9	1256.7

Figure 0-57: J(V) curve and characteristics for a PSC on plastic with the following architecture: PET/ITO/ZnO/P3HT:G1:PC₆₁BM (1:4:10)/PEDOT:PSS/Ag



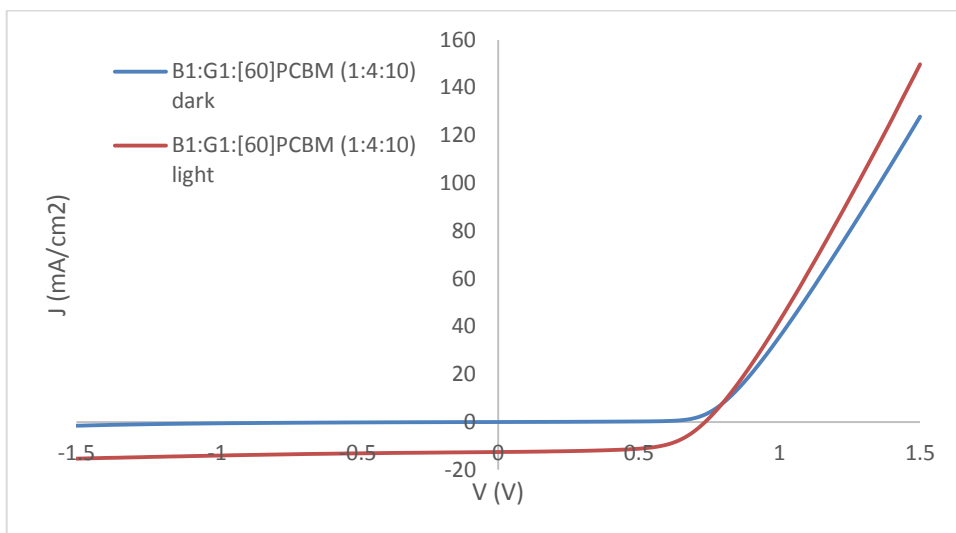
V_{oc} (V)	J_{sc} (mA/cm ²)	FF (%)	PCE (%)	R series (Ω)	R shunt (Ω)
0.73	11.18	53.8	4.40	63.9	2352.03

Figure 0-58: J(V) curve and characteristics for a PSC on plastic with the following architecture: PET/ITO/ZnO/B1:G1:PC₆₁BM (4:1:10)/PEDOT:PSS/Ag



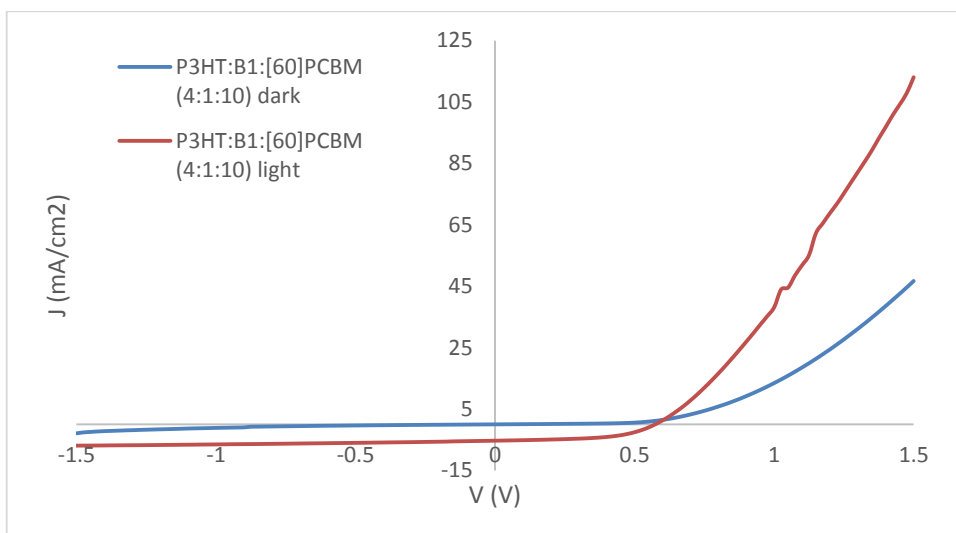
V_{oc} (V)	J_{sc} (mA/cm ²)	FF (%)	PCE (%)	R series (Ω)	R shunt (Ω)
0.72	11.08	64.8	5.16	50.0	4482.6

Figure 0-59: J(V) curve and characteristics for a PSC on plastic with the following architecture: PET/ITO/ZnO/B1:G1:PC₆₁BM (1:1:4)/PEDOT:PSS/Ag



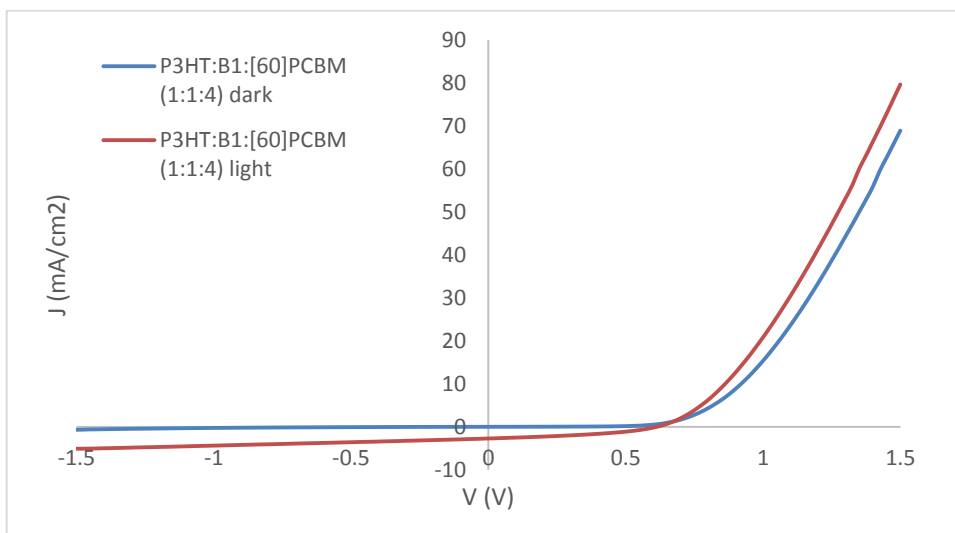
V_{oc} (V)	J_{sc} (mA/cm ²)	FF (%)	PCE (%)	R series (Ω)	R shunt (Ω)
0.73	12.55	63.6	5.82	53.8	5012.9

Figure 0-60: J(V) curve and characteristics for a PSC on plastic with the following architecture: PET/ITO/ZnO/B1:G1:PC₆₁BM (1:4:10)/PEDOT:PSS/Ag



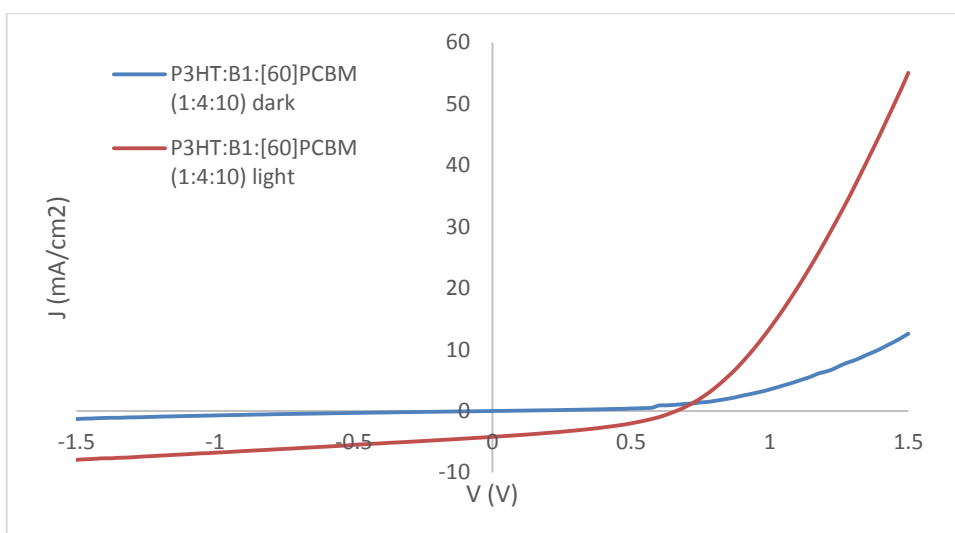
V_{oc} (V)	J_{sc} (mA/cm ²)	FF (%)	PCE (%)	R series (Ω)	R shunt (Ω)
0.57	5.31	54.6	1.64	123.5	3375.4

Figure 0-61: J(V) curve and characteristics for a PSC on plastic with the following architecture: PET/ITO/ZnO/P3HT:B1:PC₆₁BM (4:1:10)/PEDOT:PSS/Ag



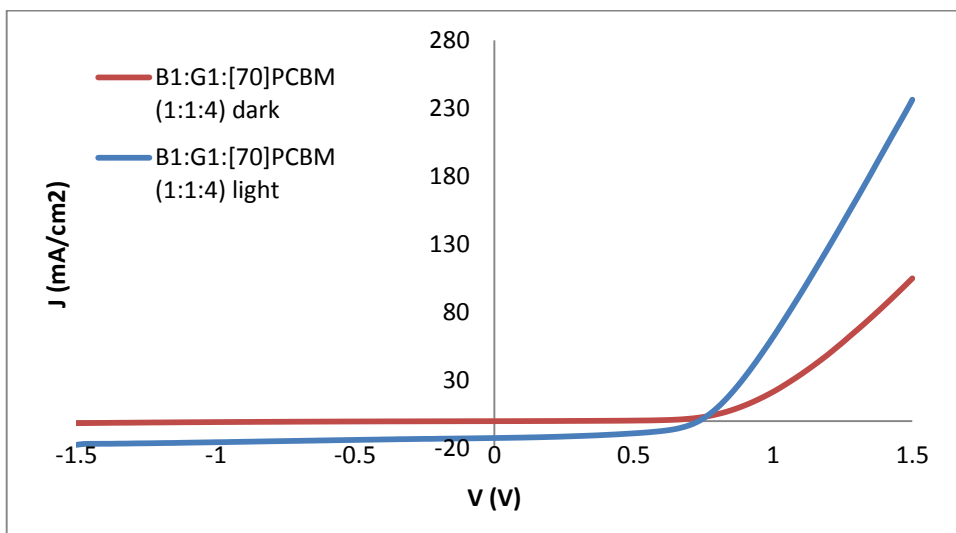
V_{oc} (V)	J_{sc} (mA/cm ²)	FF (%)	PCE (%)	R series (Ω)	R shunt (Ω)
0.60	2.71	39.9	0.65	308.8	2778.2

Figure 0-62: J(V) curve and characteristics for a PSC on plastic with the following architecture: PET/ITO/ZnO/P3HT:B1:PC₆₁BM (1:1:4)/PEDOT:PSS/Ag



V_{oc} (V)	J_{sc} (mA/cm ²)	FF (%)	PCE (%)	R series (Ω)	R shunt (Ω)
0.66	4.20	38.9	1.07	316.1	1904.7

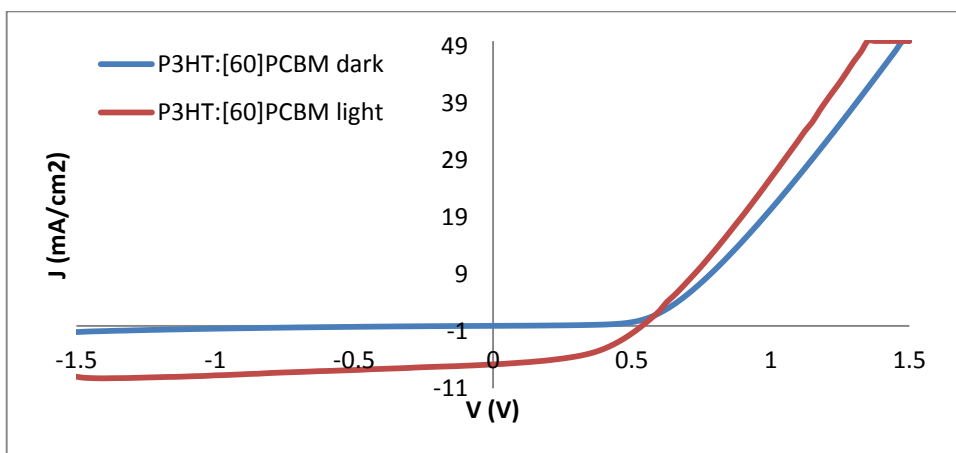
Figure 0-63: J(V) curve and characteristics for a PSC on plastic with the following architecture: PET/ITO/ZnO/P3HT:B1:PC₆₁BM (1:4:10)/PEDOT:PSS/Ag



V_{oc} (V)	J_{sc} (mA/cm ²)	FF (%)	PCE (%)	R series (Ω)	R shunt (Ω)
0.73	12.62	51.7	4.75	54.0	1812.4

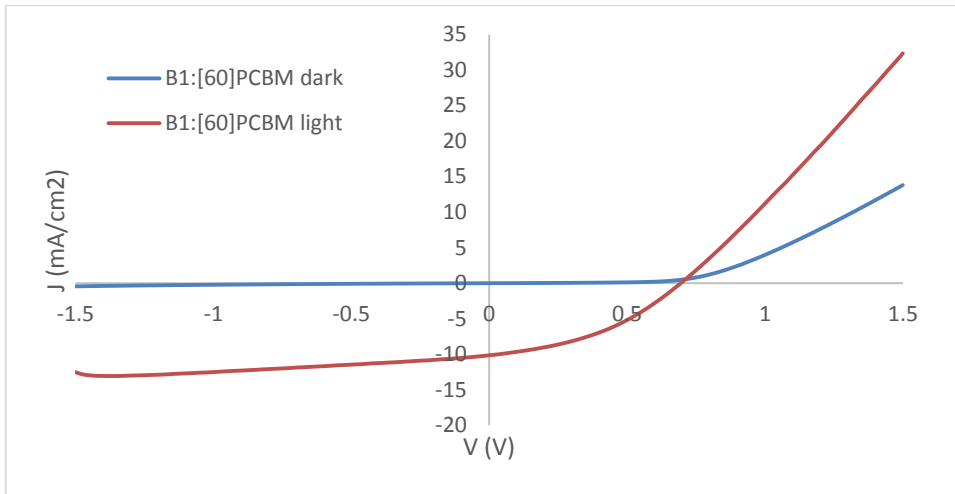
Figure 0-64: J(V) curve and characteristics for a PSC on plastic with the following architecture: PET/ITO/ZnO/B1:G1:PC₇₁BM (1:1:4)/PEDOT:PSS/Ag

2 cm² active areas



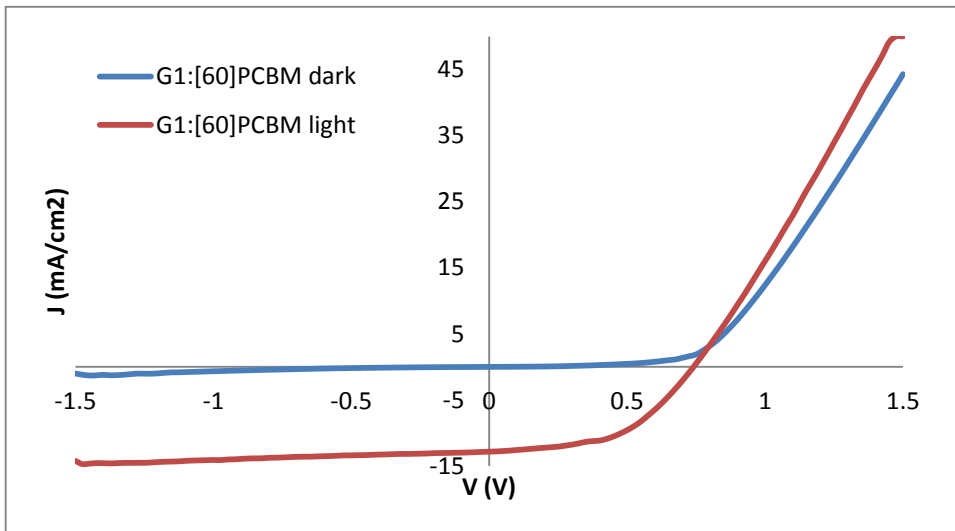
V_{oc} (V)	J_{sc} (mA/cm ²)	FF (%)	PCE (%)	R series (Ω)	R shunt (Ω)
0.53	6.73	47.2	1.70	13.6	182.5

Figure 0-65: J(V) curve and characteristics for a 2 cm² PSC on plastic with the following architecture: PET/ITO/ZnO/P3HT:PC₆₁BM/PEDOT:PSS/Ag



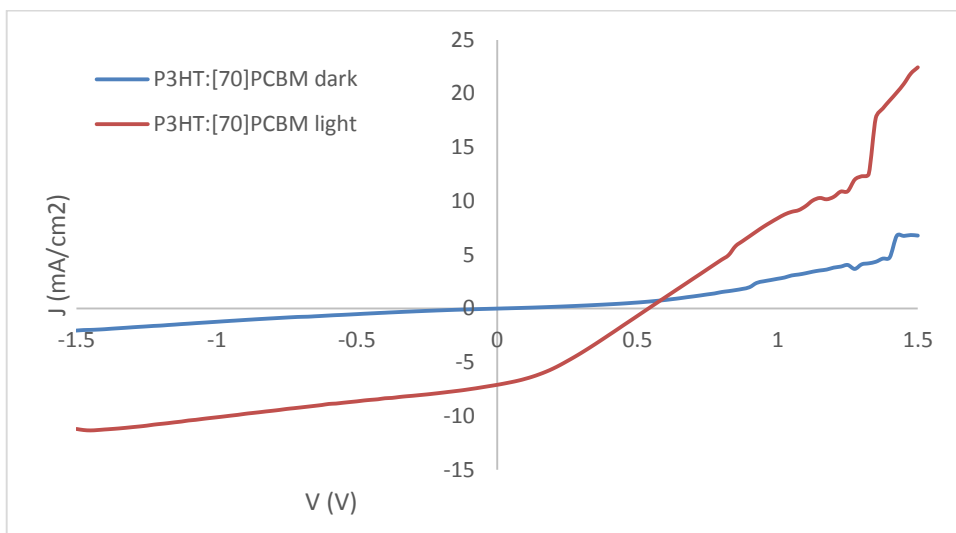
V_{oc} (V)	J_{sc} (mA/cm ²)	FF (%)	PCE (%)	R series (Ω)	R shunt (Ω)
0.69	10.08	39.9	2.79	15.6	116.5

Figure 0-66: J(V) curve and characteristics for a 2 cm² PSC on plastic with the following architecture: PET/ITO/ZnO/B1:PC₆₁BM/PEDOT:PSS/Ag



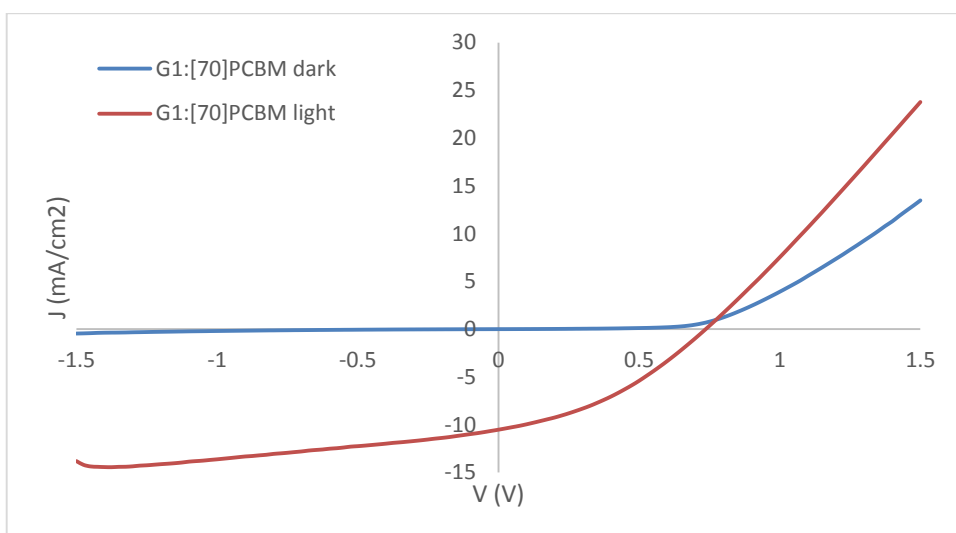
V_{oc} (V)	J_{sc} (mA/cm ²)	FF (%)	PCE (%)	R series (Ω)	R shunt (Ω)
0.74	12.77	50.8	4.79	9.3	249.6

Figure 0-67: J(V) curve and characteristics for a 2 cm² PSC on plastic with the following architecture: PET/ITO/ZnO/G1:PC₆₁BM/PEDOT:PSS/Ag



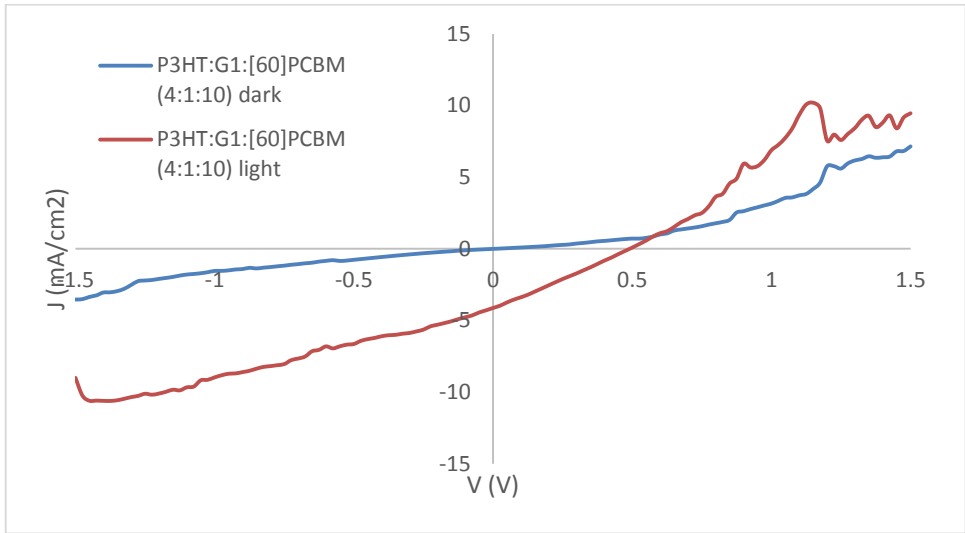
V_{oc} (V)	J_{sc} (mA/cm ²)	FF (%)	PCE (%)	R series (Ω)	R shunt (Ω)
0.54	7.00	32.9	1.24	28.6	97.0

Figure 0-68: J(V) curve and characteristics for a 2 cm² PSC on plastic with the following architecture: PET/ITO/ZnO/P3HT:PC₇₁BM/PEDOT:PSS/Ag



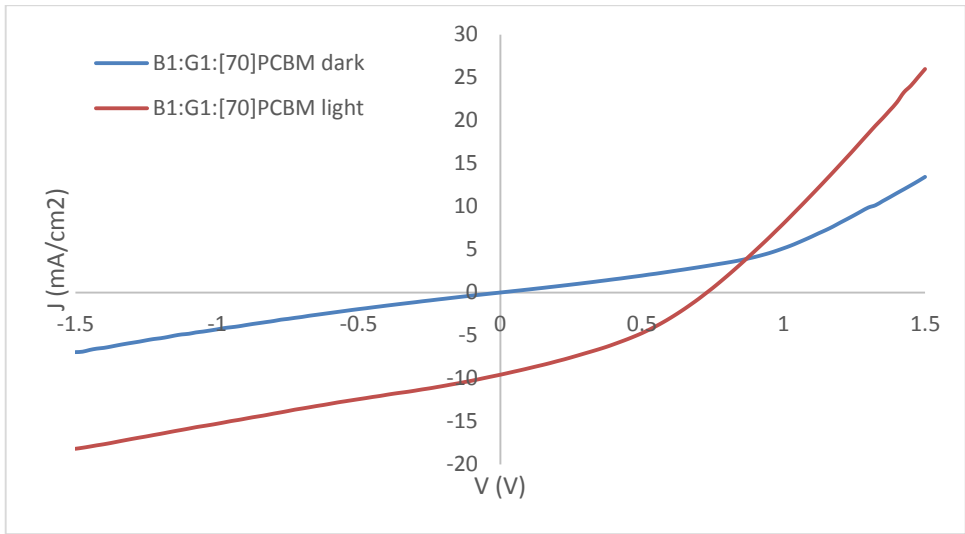
V_{oc} (V)	J_{sc} (mA/cm ²)	FF (%)	PCE (%)	R series (Ω)	R shunt (Ω)
0.74	10.47	36.9	2.84	19.3	95.3

Figure 0-69: J(V) curve and characteristics for a 2 cm² PSC on plastic with the following architecture: PET/ITO/ZnO/G1:PC₇₁BM/PEDOT:PSS/Ag



V_{oc} (V)	J_{sc} (mA/cm ²)	FF (%)	PCE (%)	R series (Ω)	R shunt (Ω)
0.49	4.07	26.5	0.53	51.5	72.2

Figure 0-70: J(V) curve and characteristics for a 2 cm² PSC on plastic with the following architecture: PET/ITO/ZnO/P3HT:G1:PC₆₁BM/PEDOT:PSS/Ag



V_{oc} (V)	J_{sc} (mA/cm ²)	FF (%)	PCE (%)	R series (Ω)	R shunt (Ω)
0.73	9.53	35.2	2.44	19.7	69.9

Figure 0-71: J(V) curve and characteristics for a 2 cm² PSC on plastic with the following architecture: PET/ITO/ZnO/B1:G1:PC₇₁BM/PEDOT:PSS/Ag

Intensity variation of ternary blends

A study to investigate the effect of illumination intensity was performed on all active layer blends with the following architecture:

PET/ITO/ZnO/fullerene blend/PEDOT:PSS/Ag

The blends were:

- P3HT:[60]PCBM
- B1:[60]PCBM
- G1:[60]PCBM
- P3HT:G1:[60]PCBM (4:1:10), (1:1:4), (1:4:10)
- P3HT:B1:[60]PCBM (4:1:10), (1:1:4), (1:4:10)
- B1:G1:[60]PCBM (4:1:10), (1:1:4), (1:4:10)

Included herein is an example of the intensity study results for P3HT:[60]PCBM, G1:[60]PCBM, P3HT:G1:[60]PCBM (1:1:4), P3HT:B1:[60]PCBM (1:1:4) and B1:G1:[60]PCBM (1:1:4)

Table 0-3: J(V) characteristics for a P3HT:[60]PCBM cell as illumination intensity is varied

Si Ref	With MM (1.25)	Vmpp (V)	Jmpp (mA/cm ²)	MPP (mW/cm ²)	Voc (V)	Jsc (mA/cm ²)	FF (%)	n (%) (with MM)	Rs (Ω)	Rsh (Ω)
0.15	18.8	0.35	1.05	0.37	0.46	1.39	57.6	1.97	268.13	10165.39
0.2	25	0.38	1.26	0.47	0.47	1.73	58.3	1.88	247.61	9080.56
0.4	50	0.38	2.62	0.98	0.50	3.45	57.3	1.96	149.27	4453.45
0.5	62.5	0.38	3.31	1.24	0.51	4.32	56.8	1.98	110.95	3735.84
0.6	75	0.38	4.00	1.50	0.51	5.18	56.3	2.00	105.85	3250.33
0.7	87.5	0.38	4.71	1.77	0.52	6.09	55.6	2.02	102.81	2860.02
0.8	100	0.38	5.38	2.02	0.53	6.92	55.1	2.02	99.80	2750.32
1.0	125	0.38	6.91	2.59	0.54	8.76	54.3	2.07	83.17	2339.97

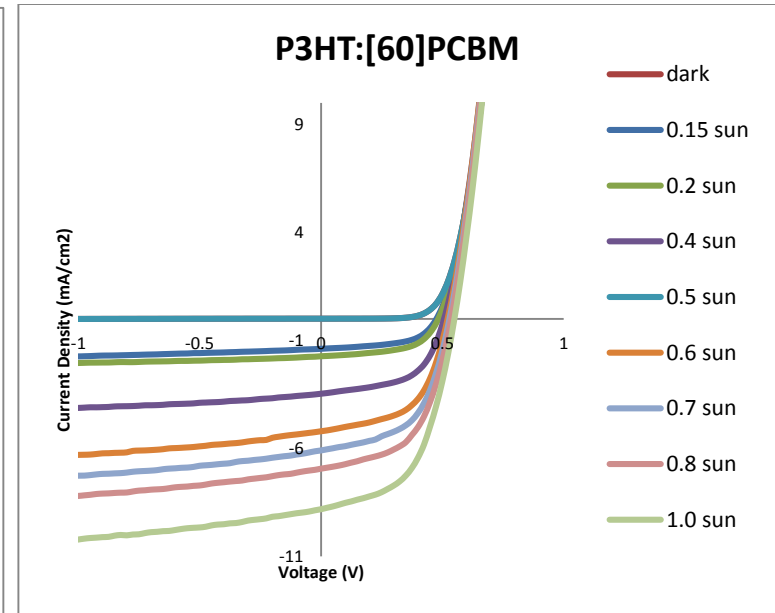
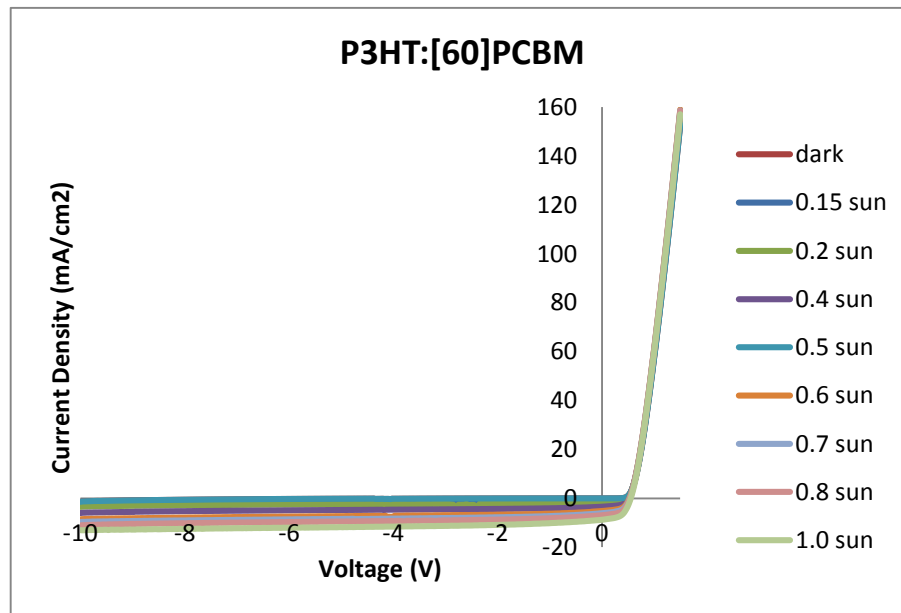


Table 0-4: J(V) characteristics for a G1:[60]PCBM cell as illumination intensity is varied

Si Ref	With MM (1.14)	Vmpp (V)	Jmpp (mA/cm ²)	MPP (mW/cm ²)	Voc (V)	Jsc (mA/cm ²)	FF (%)	n (%) (with MM)	Rs (Ω)	Rsh (Ω)
0.15	17.1	0.55	1.63	0.89	0.67	1.90	70.1	5.20	102.16	41161.40
0.2	22.8	0.58	2.04	1.17	0.68	2.50	69.5	5.13	94.08	30816.08
0.4	45.6	0.58	4.01	2.31	0.69	4.90	67.9	5.07	75.33	13000.21
0.5	57	0.58	5.08	2.92	0.70	6.25	66.3	5.12	51.24	9181.68
0.6	68.4	0.58	6.20	3.57	0.71	7.54	66.5	5.22	49.76	6240.90
0.7	79.8	0.60	6.86	4.12	0.72	8.71	65.8	5.16	48.97	4839.54
0.8	91.2	0.60	7.92	4.75	0.73	9.98	65.3	5.21	37.75	3843.32
1.0	114.0	0.60	9.98	5.99	0.75	12.41	64.7	5.25	38.92	3021.88

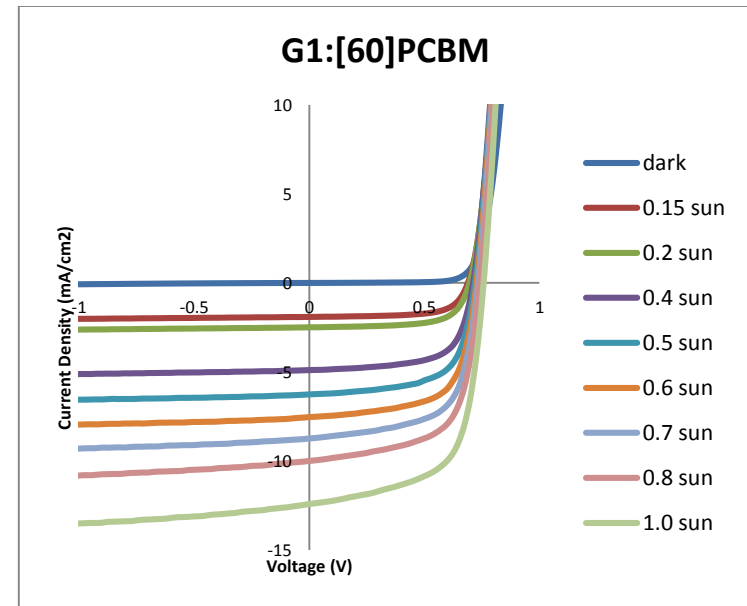
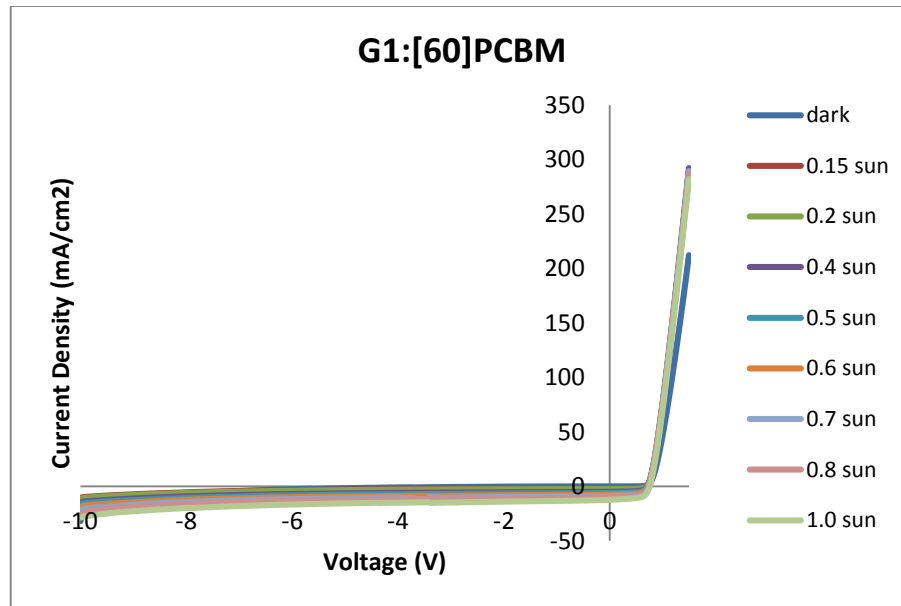


Table 0-5: J(V) characteristics for a P3HT:G1:[60]PCBM cell as illumination intensity is varied

Si Ref	No MM	Vmpp (V)	Jmpp (mA/cm ²)	MPP (mW/cm ²)	Voc (V)	Jsc (mA/cm ²)	FF (%)	n (%) (with MM)	Rs (Ω)	Rsh (Ω)
0.2	20	0.30	0.49	0.15	0.44	0.81	41.0	0.75	866.82	6466.90
0.4	40	0.33	0.85	0.28	0.47	1.47	40.4	0.7	503.18	3570.74
0.5	50	0.33	1.09	0.36	0.48	1.78	41.5	0.72	345.82	3183.65
0.6	60	0.33	1.27	0.41	0.48	2.06	41.2	0.68	330.72	2784.02
0.7	70	0.35	1.36	0.48	0.49	2.30	42.6	0.69	317.62	2607.28
0.8	80	0.35	1.55	0.54	0.50	2.53	42.8	0.68	309.83	2450.95
1.0	100	0.38	1.75	0.66	0.52	2.95	42.4	0.66	268.38	2190.14

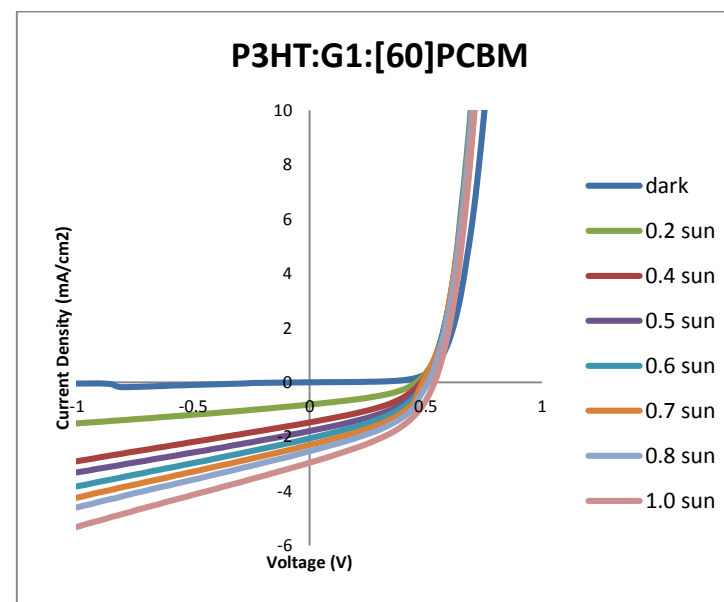
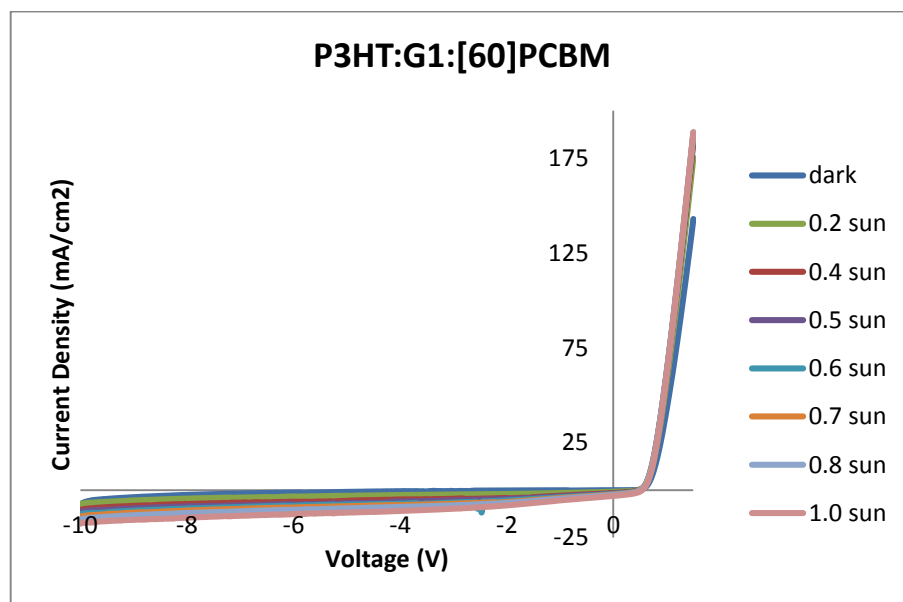


Table 0-6: J(V) characteristics for a P3HT:B1:[60]PCBM cell as illumination intensity is varied

Si Ref	Intensity ((mW/cm ²))	Vmpp (V)	Jmpp (mA/cm ²)	MPP (mW/cm ²)	Voc (V)	Jsc (mA/cm ²)	FF (%)	n (%)	Rs (Ω)	Rsh (Ω)
0.16	16	0.35	0.39	0.14	0.48	0.62	45.7	0.14	882.9	12430.3
0.2	20	0.35	0.48	0.17	0.49	0.76	45.1	0.17	823.2	9848.3
0.3	30	0.35	0.71	0.25	0.51	1.10	44.2	0.25	552.6	6639.1
0.4	40	0.35	0.92	0.32	0.52	1.42	43.7	0.32	501.8	5157.7
0.5	50	0.33	1.04	0.34	0.50	1.72	39.0	0.34	448.7	3307.6
0.6	60	0.35	1.30	0.46	0.53	2.00	43.0	0.46	337.2	3601.1
0.7	70	0.38	1.42	0.53	0.54	2.33	42.7	0.53	324.7	3084.0
0.8	80	0.38	1.58	0.59	0.54	2.59	42.2	0.59	325.6	2759.9
0.9	90	0.38	1.73	0.65	0.55	2.82	41.6	0.65	267.9	2495.5
1.0	100	0.38	1.82	0.68	0.57	2.93	41.2	0.68	295.7	2425.7

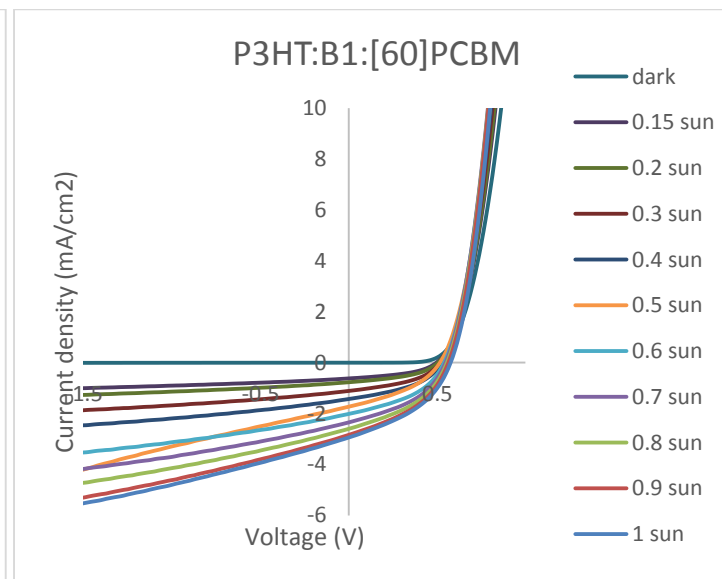
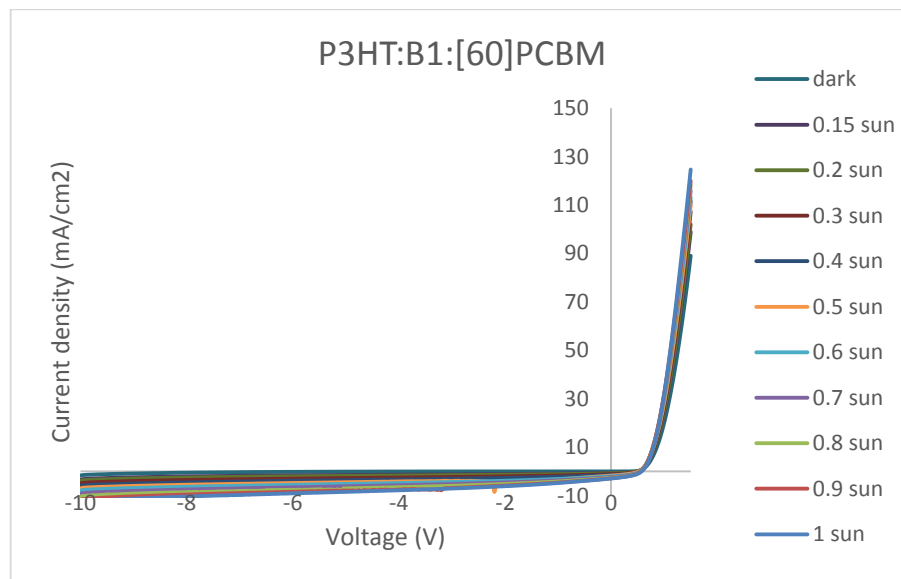
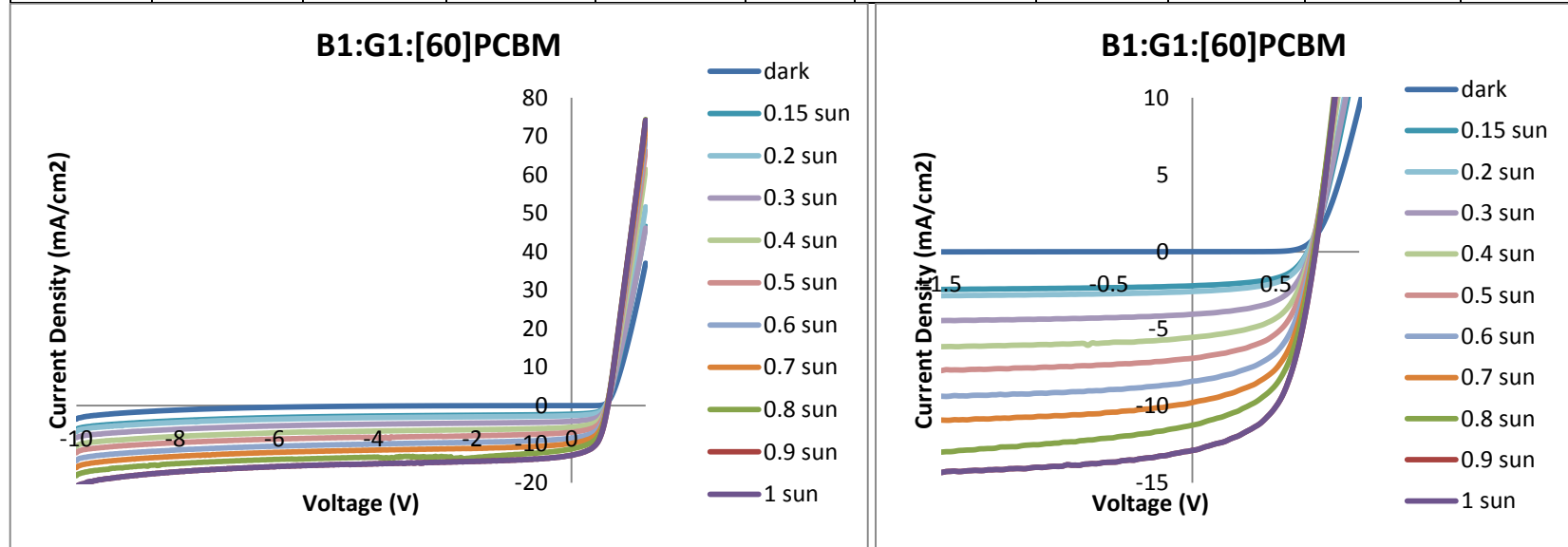


Table 0-7: J(V) characteristics for a B1:G1:[60]PCBM cell as illumination intensity is varied

Si Ref	Intensity (mW/cm ²)	V _{mpp} (V)	J _{mpp} (mA/cm ²)	MPP (mW/cm ²)	V _{oc} (V)	J _{sc} (mA/cm ²)	FF (%)	n (%)	R _s (Ω)	R _{sh} (Ω)
0.16	16	0.53	1.65	0.86	0.68	2.21	57.4	5.38	241.6	13972.3
0.2	20	0.53	1.92	1.01	0.68	2.58	57.2	5.05	211.3	11949.3
0.3	30	0.53	3.05	1.60	0.70	4.06	56.2	5.33	185.5	7800.5
0.4	40	0.53	4.14	2.17	0.70	5.56	55.7	5.43	137.0	4963.9
0.5	50	0.53	5.10	2.68	0.71	6.90	54.9	5.36	104.6	4040.1
0.6	60	0.53	6.27	3.29	0.71	8.42	54.7	5.48	94.3	3318.8
0.7	70	0.53	7.27	3.82	0.72	9.78	54.2	5.46	87.5	2757.4
0.8	80	0.53	8.26	4.34	0.72	11.23	53.4	5.43	81.4	2210.2
0.9	90	0.53	9.10	4.78	0.73	12.23	53.6	5.31	79.0	2213.8
1.0	100	0.53	9.65	5.07	0.73	12.87	53.7	5.07	79.0	2249.9



Appendix F

Thermogravimetric analysis (TGA) of esterified SWCNTs.

Unidym SWCNTs (esterified tubes and reference)

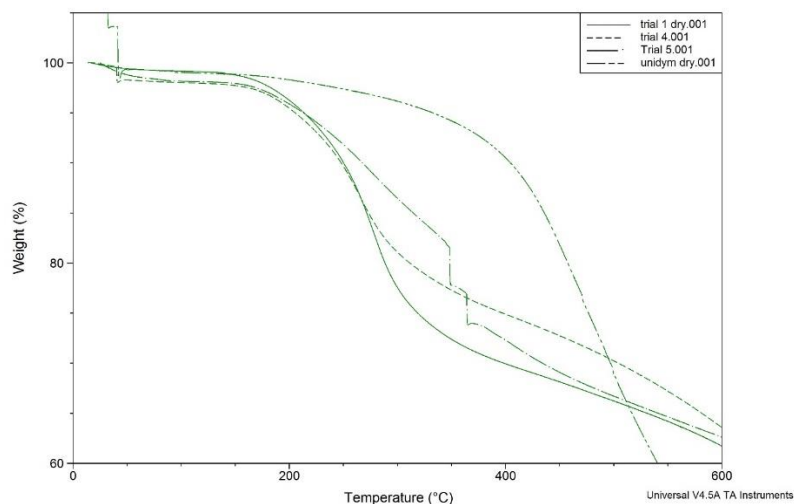


Figure 0-72: TGA results for Unidym SWCNTs: non-esterified reference (*unidym dry*), and those esterified with 1-decanol (*trial 1, solid*), 1-dodecanol (*trial 5, - - -*), and 1-tetradecanol (*trial 4, - - -*).

BuckyUSA SWCNTs (esterified tubes and reference)

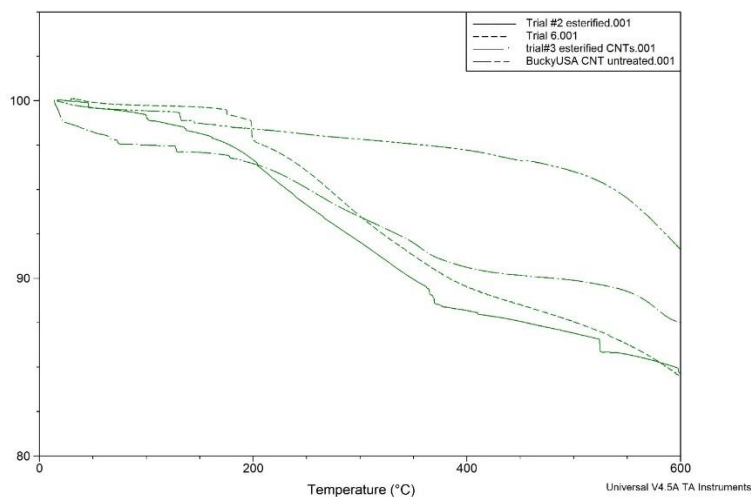


Figure 0-73: TGA results for BuckyUSA SWCNTs: non-esterified reference (*BuckyUSA CNT untreated*), and those esterified with 1-decanol (*trial 6, - - -*), 1-dodecanol (*trial 2, solid*), and 1-tetradecanol (*trial 3, - - -*).

Comparison of both varieties esterified with 1-decanol

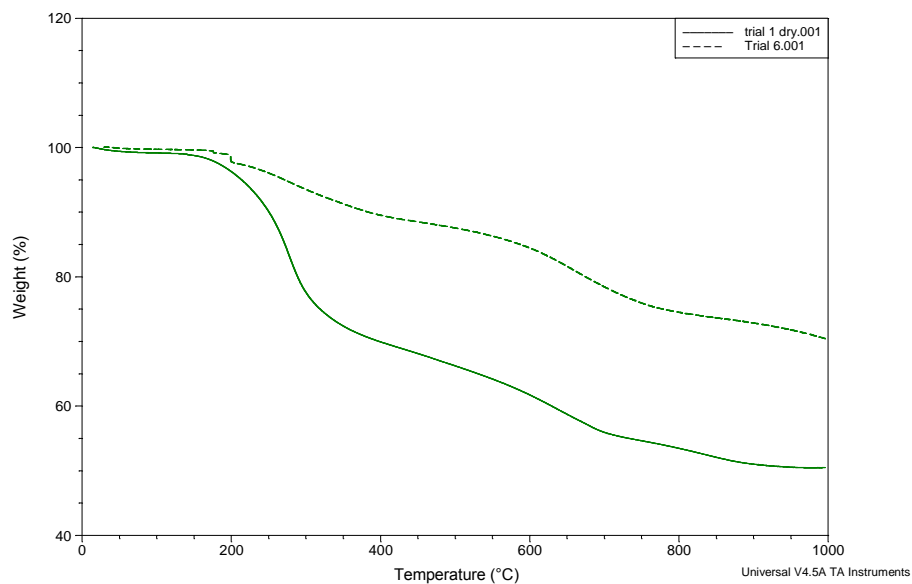


Figure 0-74: TGA results for SWCNTs esterified with 1-decanol: Unidym (*trial 1*) and BuckyUSA (*trial 6*).

Comparison of both varieties esterified with 1-dodecanol

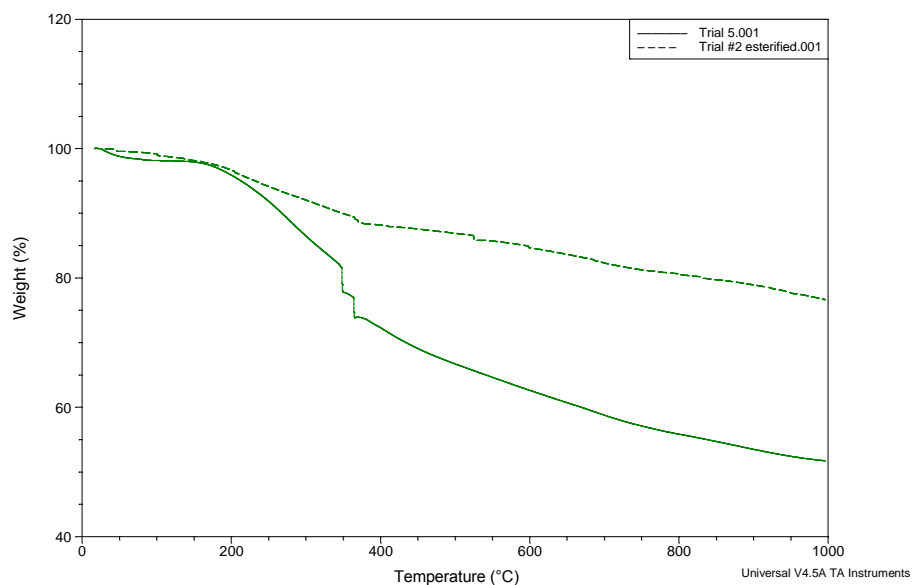


Figure 0-75: TGA results for SWCNTs esterified with 1-dodecanol: Unidym (*trial 5*) and BuckyUSA (*trial 2*).

Comparison of both varieties esterified with 1-tetradecanol

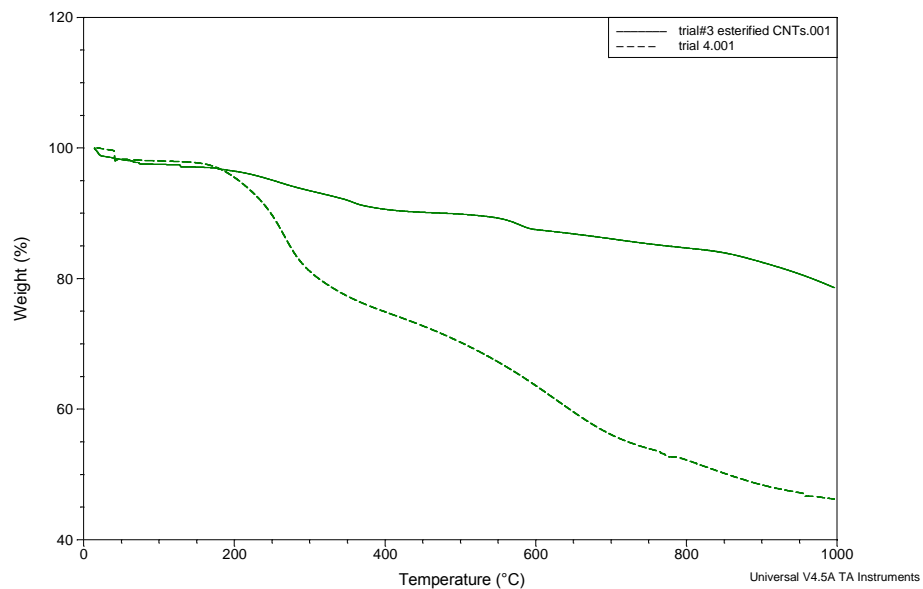


Figure 0-76: TGA results for SWCNTs esterified with 1-decanol: Unidym (*trial 4*) and BuckyUSA (*trial 3*).

Visual solubility test of functionalized single-walled carbon nanotubes (f-SWCNTs)

A selection of the available CNTs were mixed with chloroform (5 mg/15 ml) to observe the relative rate of sedimentation. Vials are numbered from left to right (1-5) and were let to sit after a fifteen minute sonication. Images are labelled with respect to time after initial sonication.

Vial 1: Unidym SWCNTs as received

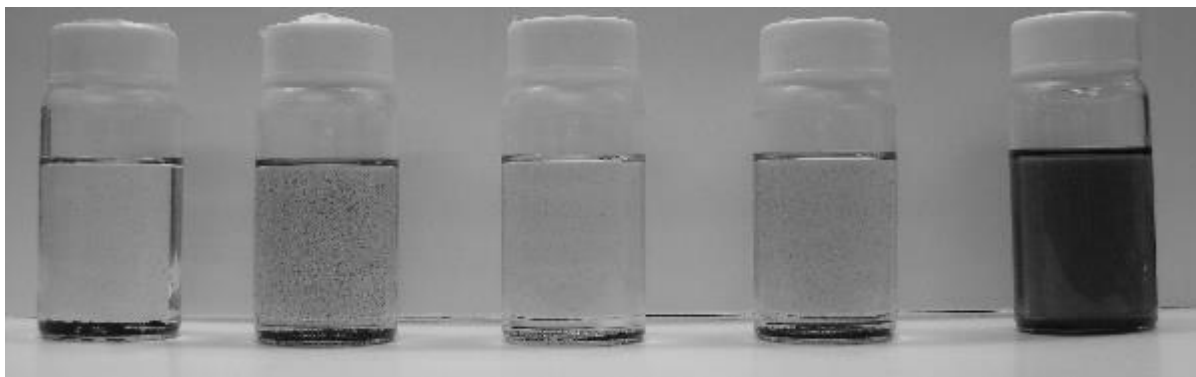
Vial 2: f-SWCNTs (Unidym, R = 10)

Vial 3: f-SWCNTs (BuckyUSA, R = 12)

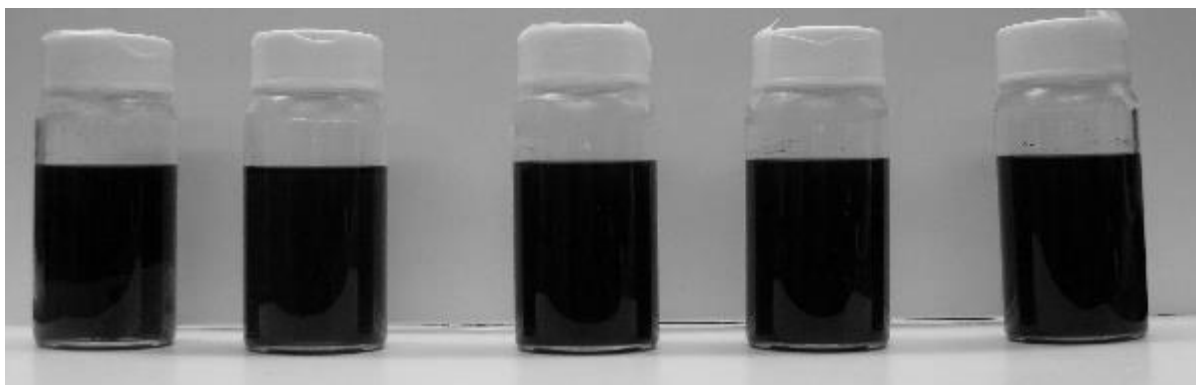
Vial 4: f-SWCNTs (BuckyUSA, R = 14)

Vial 5: BuckyUSA SWCNTs as received

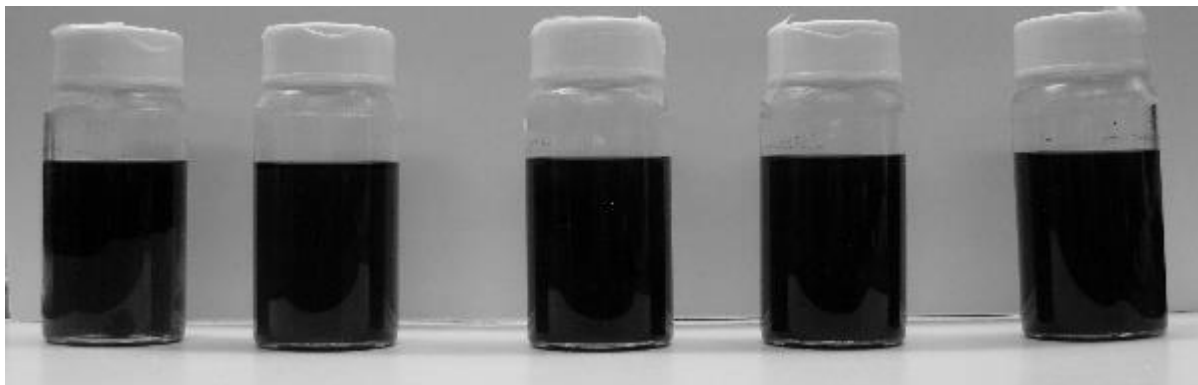
Pre-sonication



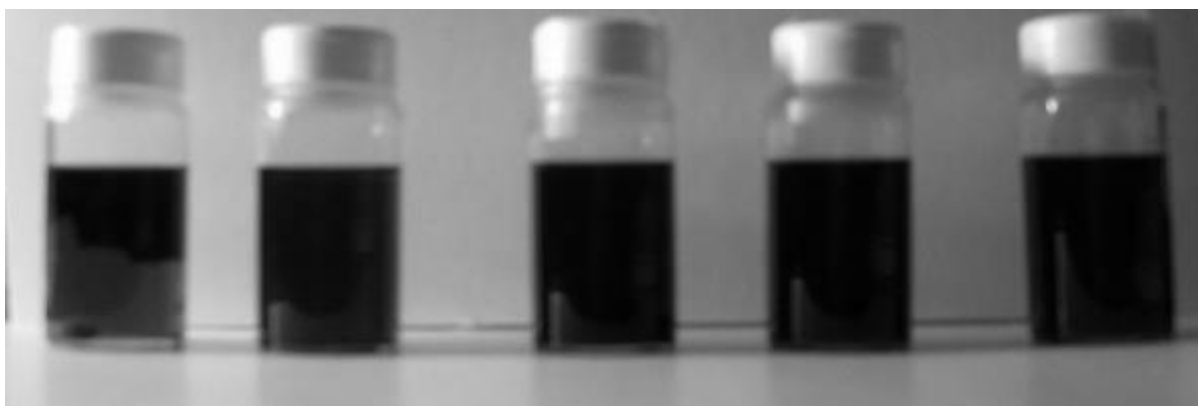
1 min



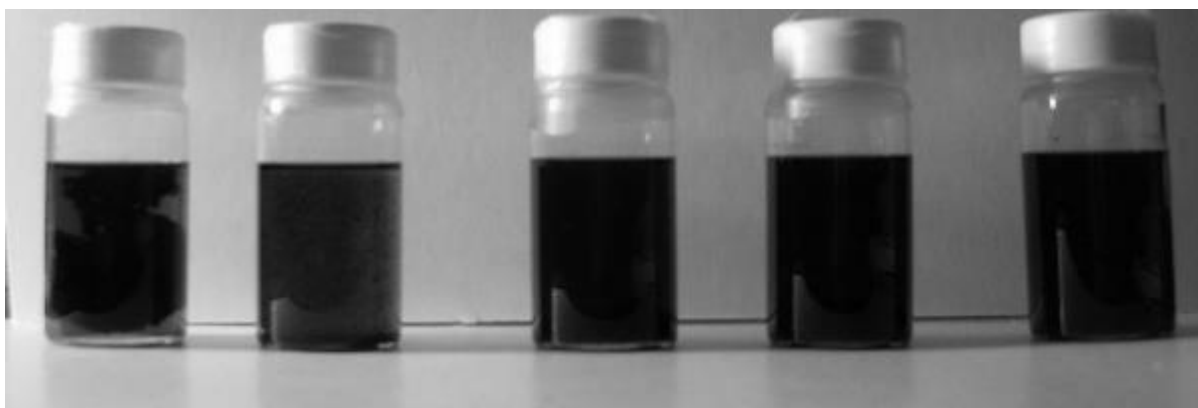
10 min



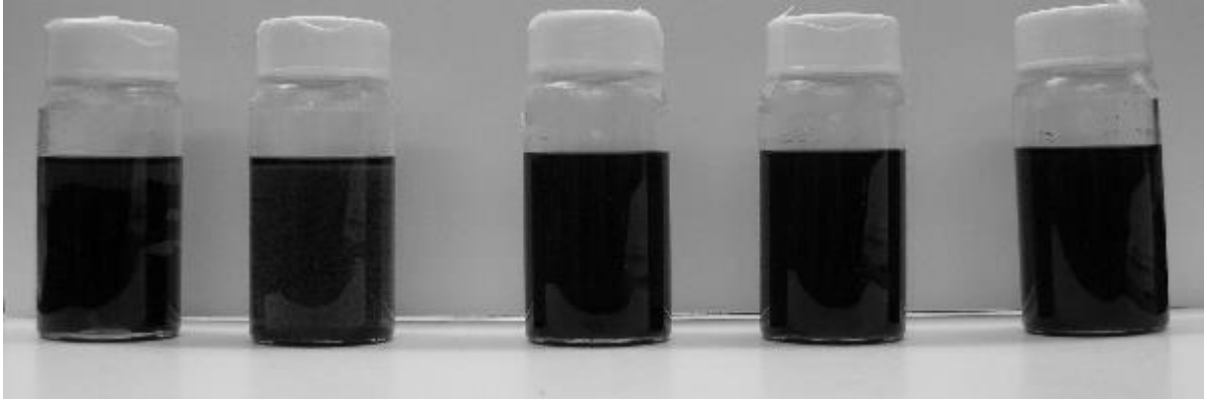
31 min



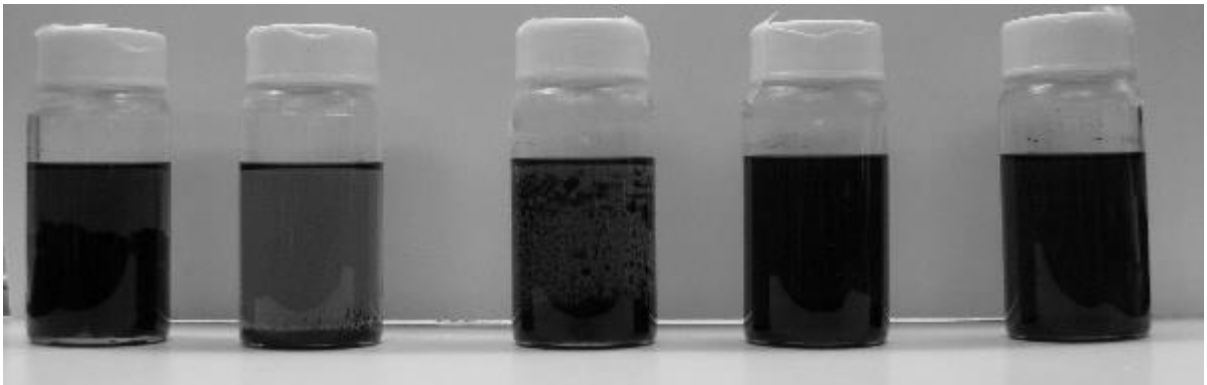
61 min



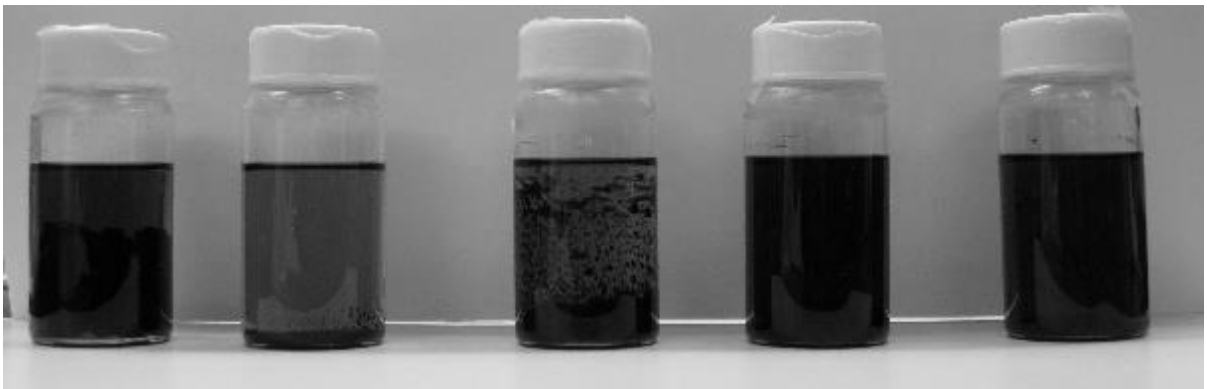
81 min



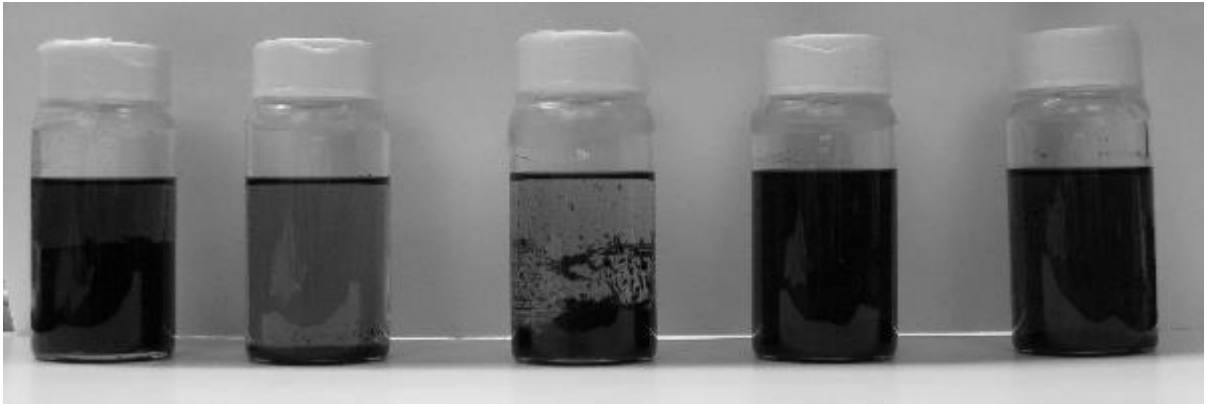
1036 min



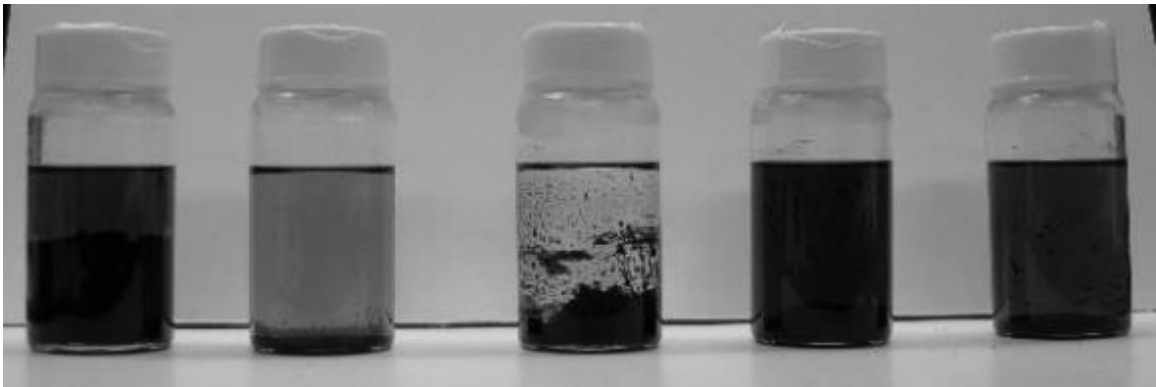
1486 min



2371 min



5491 min



Appendix G

Preliminary effects of CNT doping

Effects of CNT doping on P3HT fluorescence decay

Time Correlated Single Photon Counting (TCSPC) was used to determine fluorescence decay lifetime of P3HT films with increasing CNT concentration. The measurements were performed at the University of Montreal in the laboratory of Prof. Carlos Silva.

Six P3HT films were analyzed via TCSPC, with a pump source of 379 nm and decay being measured at 730 nm. The functionalized SWCNT (f-SWCNT) chosen were the Unidym CNTs functionalized with the 14 member carbon chain (DoF = 1.7 %).

Analyzed films: neat P3HT, P3HT:Unidym control (1 wt%) and four films with P3HT doped with the functionalized (R=14) Unidym SWCNTs (0.2, 0.5, 1, and 2 wt%).

The results indicated that the CNTs increased the fluorescence lifetime of the P3HT. Furthermore, this provides some evidence of an optimal CNT doping concentration and an increased charge carrier lifetime with the presence of CNT (0.5, 1 wt%).

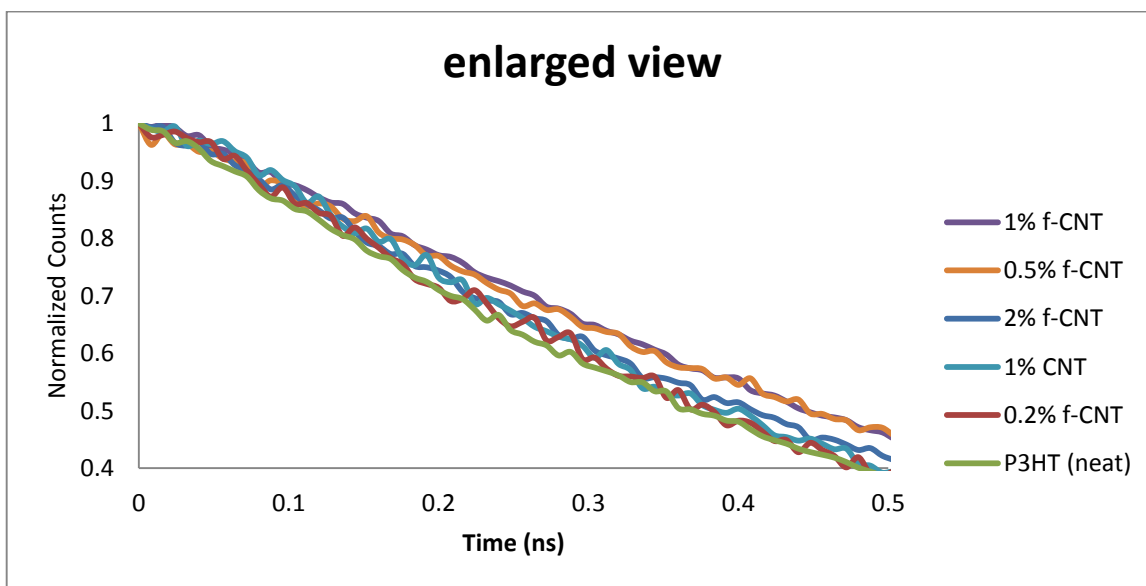
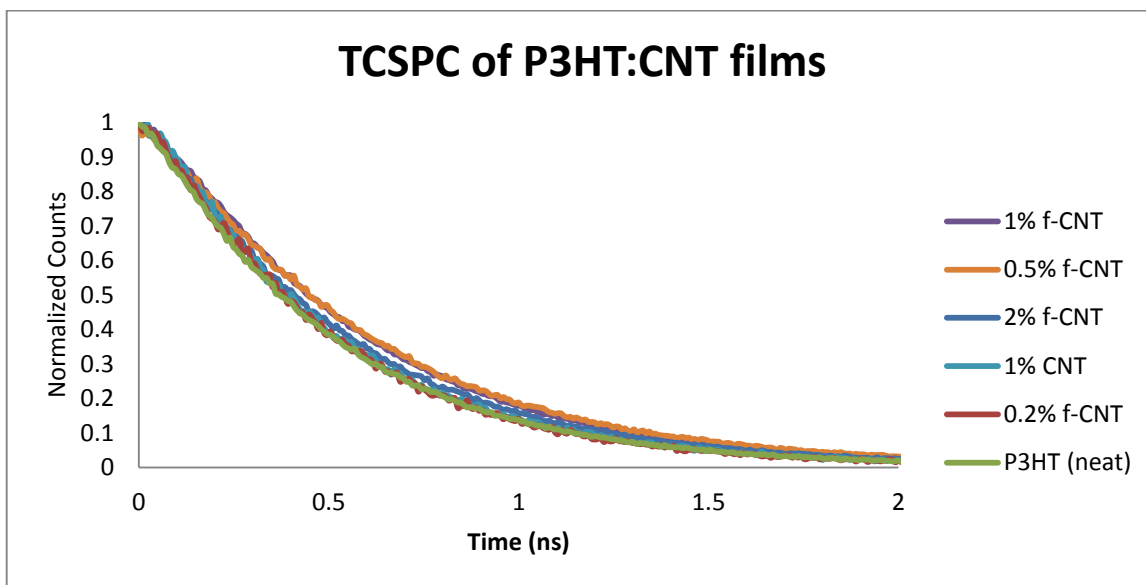


Figure 0-77: Photoluminescence TCSPC of P3HT films with various functionalized SWCNT concentrations (wt%) at 730 nm.

Stability investigation of CNT-doped PSCs

The P3HT:PCBM active layer was doped with either of the three Unidym functionalized SWCNTs (R=10, 12, or 14). The devices in this case were non-annealed with the following architecture:

ITO/ZnO (np)/P3HT:PCBM:CNT (0.2 wt % to P3HT+PCBM)/PEDOT:PSS (F010)/Ag

Following initial J(V) characterization, the devices were placed under constant illumination and characterized every two minutes. [Annealed devices, with and without CNTs exhibited similar stabilities].

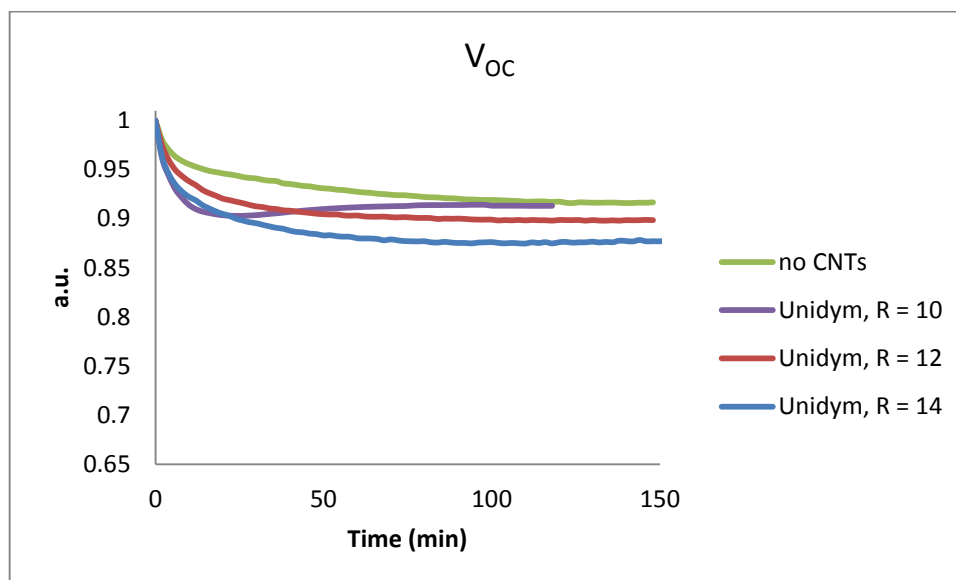


Figure 0-78: Evolution of V_{OC} of CNT-doped PSCs under constant illumination.

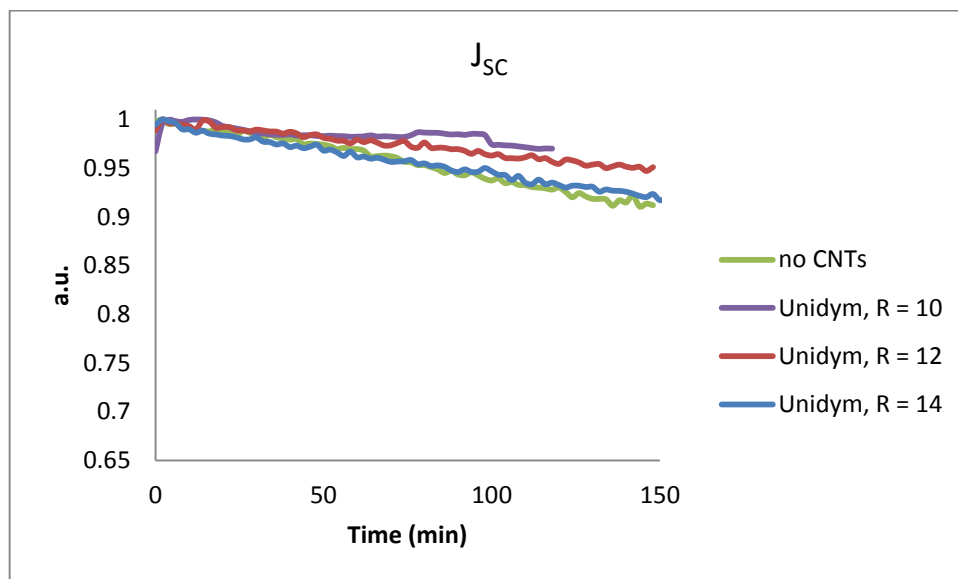


Figure 0-79: Evolution of J_{sc} of CNT-doped PSCs under constant illumination.

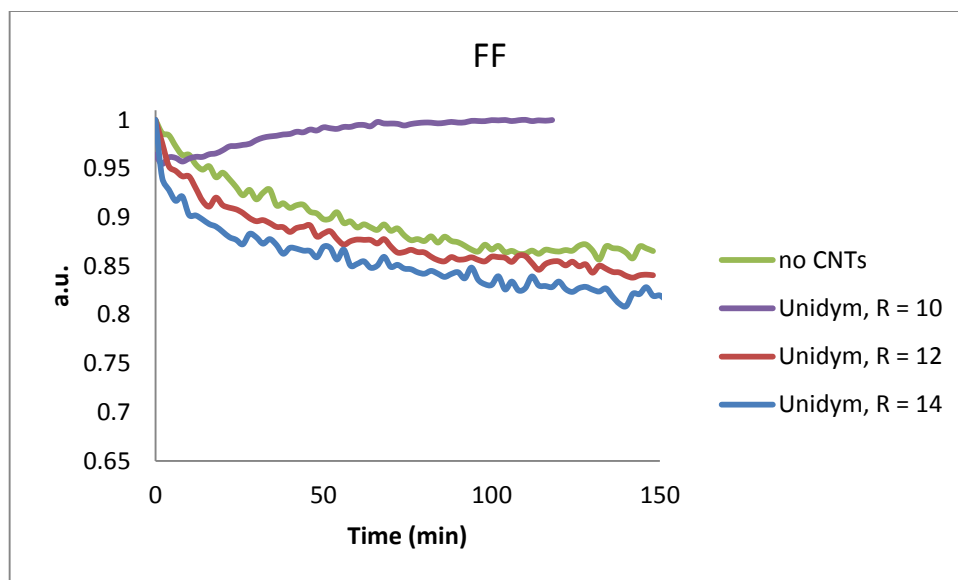


Figure 0-80: Evolution of the FF of CNT-doped PSCs under constant illumination.

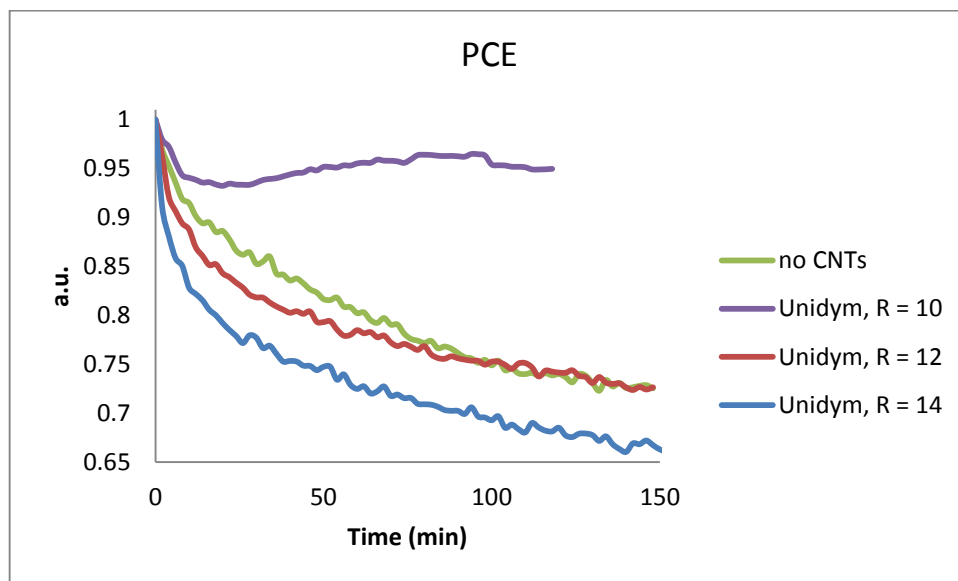


Figure 0-81: Evolution of the efficiency of CNT-doped PSCs under constant illumination.